

3D PRINTED CONCRETE: MULTISCALE MECHANICAL
CHARACTERIZATION AND COMPUTATIONAL MODELING

A THESIS SUBMITTED TO
THE GRADUATE SCHOOL OF NATURAL AND APPLIED SCIENCES
OF
MIDDLE EAST TECHNICAL UNIVERSITY

BY

ALPER TUNGA BAYRAK

IN PARTIAL FULFILLMENT OF THE REQUIREMENTS
FOR
THE DEGREE OF MASTER OF SCIENCE
IN
CIVIL ENGINEERING

JANUARY 2024

Approval of the thesis:

**3D PRINTED CONCRETE: MULTISCALE MECHANICAL
CHARACTERIZATION AND COMPUTATIONAL MODELING**

submitted by **ALPER TUNGA BAYRAK** in partial fulfillment of the requirements
for the degree of **Master of Science in Civil Engineering, Middle East Technical
University** by,

Prof. Dr. Halil Kalıpçılar
Dean, Graduate School of **Natural and Applied Sciences**

Prof. Dr. Erdem Canbay
Head of the Department, **Civil Engineering**

Prof. Dr. Afşin Sarıtaş
Supervisor, **Civil Engineering, METU**

Assoc. Prof. Dr. Çağla Akgül
Co-Supervisor, **Civil Engineering, METU**

Examining Committee Members:

Prof. Dr. Eray Baran
Civil Engineering, METU

Prof. Dr. Afşin Sarıtaş
Civil Engineering, METU

Assoc. Prof. Dr. Çağla Akgül
Civil Engineering, METU

Assoc. Prof. Dr. Hüsnü Dal
Mechanical Engineering, METU

Prof. Dr. Lutfullah Turanlı
Civil Engineering, Ankara Yıldırım Beyazıt University

Date: 26.01.2024

I hereby declare that all information in this document has been obtained and presented in accordance with academic rules and ethical conduct. I also declare that, as required by these rules and conduct, I have fully cited and referenced all material and results that are not original to this work.

Name, Surname : Alper Tunga Bayrak

Signature :

ABSTRACT

3D PRINTED CONCRETE: MULTISCALE MECHANICAL CHARACTERIZATION AND COMPUTATIONAL MODELING

Bayrak, Alper Tunga
Master of Science, Civil Engineering
Supervisor: Prof. Dr. Afşin Sarıtaş
Co-Supervisor: Assoc. Prof. Dr. Çağla Akgül

January 2024, 251 pages

This thesis presents a comprehensive exploration of the physical, mechanical, and thermal properties of 3D Printed Concrete (3DPC) structures across micro, meso, and macrostructural scales. The central focus is the analysis of full-scale walls under rigorous mechanical tests, revealing a notable and novel discovery: the mechanical properties —compressive strength, elastic modulus, and tensile strength— of the lower part of the 3DPC walls enhanced by up to 108%, 53%, and 100%, respectively, compared to the upper parts. This novel and dominant elevation effect on mechanical properties surpasses the previously known anisotropic behavior in 3DPC.

The investigation extends to material modeling, introducing the Continuum Damage Plasticity Model (CDPM) for cyclic loading of concrete. The numerical implementation using the Backward-Euler method is meticulously examined. Micro and meso scales are scrutinized using computed tomograms (CT), shedding light on anisotropic behavior due to porosity and interlayer effects through finite element methods by using CDPM and traction-separation laws.

The macrostructural assessment involves subjecting 3DPC walls to lateral loads up to failure for earthquake performance. Digital image correlation method is used to evaluate displacement counters and fracture behavior of these walls. The

contributions of individual components, including truss and web elements, are thoroughly examined using finite element simulations.

This thesis not only expands the understanding of the anisotropic behavior of 3DPC but reveals a novel and more dominant elevation effect on mechanical properties. These findings contribute significantly to existing knowledge and bear important implications for future research and practical applications in the realm of 3DPC.

Keywords: 3D Printed Concrete, Continuum Damage Plasticity Model, Mechanical and Thermal Anisotropy, Multi-Scale Modelling of Concrete, Structural Assessment

ÖZ

3B BASKILI BETON: ÇOK ÖLÇEKLİ MEKANİK KARAKTERİZASYON VE HESAPLAMALI MODELLEME

Bayrak, Alper Tunga
Yüksek Lisans, İnşaat Mühendisliği
Tez Yöneticisi: Prof. Dr. Afşin Sarıtaş
Ortak Tez Yöneticisi: Doç. Dr. Çağla Akgül

Ocak 2024, 251 sayfa

Bu yüksek lisans tezi, mikro, mezo ve makro yapısal ölçeklerde 3B Baskılı Beton (3BBB) yapıların fiziksel, mekanik ve termal özelliklerinin kapsamlı bir araştırmasını sunmaktadır. Tezin ana odağı, özenli mekanik testler altında tam ölçekli duvarların analizleri olup dikkate değer ve yeni bir keşfi ortaya çıkarmaktadır: 3BBB duvarlarının alt kısmının mekanik özellikleri (basınç dayanımı, elastik modül ve çekme dayanımı) üst kısımlara kıyasla sırasıyla %108, %53 ve %100'e kadar artmıştır. Bu yeni ve baskın yükseklik etkisinin mekanik özellikler üzerindeki etkisi, 3BBB malzemesinde daha önce bilinen anizotropik davranışı domine etmektedir.

Araştırma, çevrimsel beton yüklemesi için Sürekli Hasar Plastiklik Modelini (CDPM) sunarak malzeme modellemeye de uzanmaktadır. Geriye doğru Euler yöntemi kullanılarak yapılan sayısal uygulama titizlikle incelenmiştir. Mikro ve mezo ölçekler, bilgisayarlı tomografiler (BT) kullanılarak incelenmekte, CDPM ve çekme-ayırma yasaları kullanılarak sonlu eleman yöntemleri aracılığıyla gözeneklilik ve ara katman etkilerinden kaynaklanan anizotropik davranışa ışık tutulmaktadır.

Makro yapısal deęerlendirme, 3BBB duvarların deprem performansı için kırılmaya kadar yanal yüklere maruz bırakılmasını içerir. Bu duvarların yer deęiştirme ölçümlerini ve kırılma davranışını deęerlendirmek için dijital görüntü korelasyonu yöntemi kullanılmaktadır. Kafes ve gövde elemanları dahil olmak üzere münferit bileşenlerin katkıları, sonlu eleman simülasyonları kullanılarak kapsamlı bir şekilde incelenmiştir.

Bu tez, sadece 3BBB malzemesinin anizotropik davranışı hakkındaki anlayışı genişletmekle kalmaz, daha da önemlisi mekanik özellikler üzerinde yeni ve daha baskın bir yükseklik etkisini ortaya çıkarır. Bulgular, mevcut bilgiye önemli ölçüde katkıda bulunmakta olup, 3BBB alanında gelecekteki araştırmalar ve pratik uygulamalar için sonuçlar doğurmaktadır.

Anahtar Kelimeler: 3B Baskılı Beton, Sürekli Hasar Plastisite Modeli, Mekanik ve Termal Anizotropi, Betonun Çok Ölçekli Modellenmesi, Yapısal Deęerlendirme

To my cherished family, my dearest friends, and my love

ACKNOWLEDGMENTS

I am deeply grateful to my advisors, Prof. Dr. Afşin Sarıtaş and Assoc. Prof. Dr. Çağla Akgül, for their unwavering support and guidance throughout my research journey. Their expertise, encouragement, and belief in my potential were instrumental in shaping this thesis. Prof. Dr. Sarıtaş's insightful feedback and mentorship challenged me to think critically and independently, while Dr. Akgül's collaborative spirit and hands-on assistance were invaluable in navigating the research process. Special thanks also goes to Prof. Dr. Eray Baran for his invaluable guidance and equipment support, which were crucial for the completion of this research. Additionally, I am grateful to Assoc. Prof. Dr. Serdar Göktepe, whose encouragement and open-door policy facilitated my personal and academic development throughout my studies.

I would like to express my heartfelt appreciation to my friends and colleagues, particularly those within the 3DPC project, and to Dr. Nefize Shaban, Dr. Sepehr Seyyedean, Erman Tunçer, and Burak Talha Kılıç for their invaluable assistance. The technical support of Osman Keskin, Murat Demirel, and Cuma Yıldırım is also gratefully acknowledged. This work was funded by TUBİTAK for the 3DPC project (120N990), and I am thankful to the project leader, Assoc. Prof. Dr. Çağla Akgül, for the opportunity to contribute to it.

I owe immense gratitude to my pillars of strength: my parents, Kadriye and İsmail Bayrak, and my siblings, Ayça and Mehmet Bayrak, for their unwavering love and encouragement. To my dearest friends, Behram Sarıkaya, Çağlar Yıldız, Samet Akyıldız, Enes Ekici, Yusuf Çoğan, and Ömer Bulut, your presence, unwavering friendship, and infectious joy have fueled my journey.

Lastly, I extend my deepest thanks to Bengi Başar. Her unwavering support and encouragement have been the wind beneath my wings. She knows my struggles

intimately and has been there to lift me up. I am forever grateful for her presence and love.

TABLE OF CONTENTS

ABSTRACT	v
ÖZ.....	vii
ACKNOWLEDGMENTS	x
TABLE OF CONTENTS	xii
LIST OF TABLES	xvi
LIST OF FIGURES	xvii
CHAPTERS	
1 INTRODUCTION	1
1.1 Current Practices in 3D Printed Concrete Structures.....	2
1.2 The Mechanics of 3D Printed Concrete.....	8
1.3 Objective and Scope	16
1.4 Limitations	17
1.5 Organization of Thesis.....	18
2 CONTINUUM DAMAGE PLASTICITY MODEL FOR CONCRETE UNDER CYCLIC LOADING	21
2.1 Mechanical Behavior of Concrete	21
2.2 Literature Review	22
2.3 Constitutive Theory for Continuum Damage Plasticity Model	27
2.3.1 Plastic-Damage Model	28
2.3.2 Evolution of Damage and Stiffness Degradation	29
2.3.3 Flow Rule and Yield Function	34
2.4 Numerical Implementation	36

2.4.1	Stress Update Algorithm for Continuum Damage Plasticity	36
2.4.2	Return-Mapping Algorithm and Spectral Decomposition	38
2.4.3	Linearizing the Equations Governing Damage Evolution	39
2.4.4	Summary of Update Algorithm for CDPM	43
2.5	Validation of CDPM Available in ABAQUS	45
3	MECHANICAL AND THERMOPHYSICAL PROPERTIES OF 3-D PRINTED CONCRETE THROUGHOUT A FULL-SCALE WALL	49
3.1	Introduction	49
3.2	Materials and Sample Preparation	54
3.2.1	Raw Materials and Mix Design	54
3.2.2	Printing Process and Sample Preparation	55
3.3	Experimental Program	59
3.3.1	Physical Properties	60
3.3.2	Mechanical Properties	61
3.3.3	Thermophysical Properties	61
3.4	Results and Discussions	63
3.4.1	Physical Properties	63
3.4.2	Mechanical Properties	69
3.4.3	Thermophysical Properties	78
3.5	Further Discussions	80
3.5.1	Factors Beyond Self-Weight	80
3.5.2	Additional Experimental Insights	81
3.6	Conclusion	83

4	EXPLORING THE FABRIC: MICRO AND MESO SCALE INVESTIGATION OF POROSITY AND INTERLAYER EFFECTS IN 3D PRINTED CONCRETE	87
4.1	Introduction.....	87
4.2	Mix Design and Sample Preparation	93
4.2.1	Mix Design	93
4.2.2	Sample Preparation.....	94
4.3	Computed Tomography (CT) Analysis	96
4.3.1	CT Analysis Procedures	96
4.3.2	CT Analysis Results	97
4.4	Numerical Analysis Strategies.....	104
4.4.1	Approach 1: Simplification of Porosities as Imperfections.....	105
4.4.2	Approach 2: Interface Model Using Traction and Separation Law.	111
4.5	Results & Discussion	115
4.5.1	Approach 1: Simplification of Porosities as Imperfections.....	116
4.5.2	Approach 2: Interface Model Using Traction and Separation Law.	123
4.6	Crack Propagation and Failure Mechanism: A Comparative Analysis ..	128
4.7	Conclusion	135
5	MACRO/STRUCTURAL LEVEL STUDY: STRUCTURAL RESPONSE AND FAILURE MECHANISMS OF UNREINFORCED 3D PRINTED CONCRETE WALLS UNDER MONOTONIC LATERAL LOADS	139
5.1	Introduction.....	139
5.2	Experimental Program	142
5.2.1	Raw Materials and Mix Design.....	142
5.2.2	Mechanical Properties of 3D Printed Concrete Walls.....	142

5.2.3	Specimen Design and Building Procedures	144
5.2.4	Test Setup and Instrumentation	146
5.2.5	Loading Configurations	149
5.2.6	Measurements and Digital Image Correlation (DIC).....	150
5.3	Experimental Results and Discussion	151
5.3.1	Load-Displacement Curves of the Walls	151
5.3.2	Failure Modes of the Walls.....	163
5.3.3	Discussion of Factors Influencing Performance	173
5.4	Numerical Simulation of 3DPC Wall 25-150-100.....	177
5.4.1	Model Details, Parameters and Boundary Conditions	178
5.4.2	Numerical Simulation Results and Discussions	185
5.5	Conclusions and Discussion.....	199
5.6	Suggestions for future research.....	203
6	CONCLUSION.....	205
	REFERENCES	211
	APPENDICES	
A.	Concrete Damage Plasticity Model (CDPM) – ABAQUS UMAT.....	229
B.	Concrete Damage Plasticity Model (CDPM) – FEAP UMAT	241

LIST OF TABLES

TABLES

Table 2.1. Material Parameters for the Numerical Tests	46
Table 3.1. Properties of Used Monofilament Polypropylene Fibers	55
Table 3.2. Tests on Hardened Concrete ^(†)	59
Table 3.3. Water Absorption, Density, and Permeable Voids per ASTM C642.....	63
Table 3.4. Definition of the Densities and Voids Ratio Related to Figure 3.9.....	65
Table 3.5. Water Penetration Depths of the Cast and Printed Specimens.....	67
Table 3.6. Thermophysical Properties of the Printed and Cast Specimens.....	78
Table 4.1. Mechanical Properties of Printed and Cast Concrete	94
Table 4.2. CT Scans on Hardened Concrete.....	96
Table 4.3. %Porosity from CT Scans: (Left) μ -CT and (Right) Macro-CT.....	101
Table 4.4. Cross-Sectional Views (XY, YZ, and XZ planes) of Porosities in 3D Reconstructed Macro-CT Analysis Results for Printed and Cast Concrete Samples	103
Table 4.5. Visualization of Smoothened Porosity in U_z and L_z Samples and Simplified Geometries.....	106
Table 4.6. Used Material Properties	109
Table 4.7. Traction-Separation Law Parameters for Interlayer and Interstrip Modeling.....	115
Table 5.1. Mechanical Properties of Printed and Cast Concrete	144
Table 5.2. Printing Procedure and Printed Walls	145
Table 5.3. Wall Properties and Performance Metrics.....	174
Table 5.4. The Key Parameters Defining the CDPM Material Model and Its Logic	182
Table 5.5. Applied Load, Members' Reaction Forces and Percentage Contributions	198

LIST OF FIGURES

FIGURES

Figure 1.1. Schematics of the Production Line for Parts Printed by Industrial Robotic Arms Using the Contour Crafting Technique [11].....	3
Figure 1.2. Structures Produced by Winsun Company in China: (a) 300 m ² Single Story Buildings with a Cost of 4800\$ [12], and (b) Five Story Building	3
Figure 1.3. (a) The Material Used to Build the Yaroslavi House is a Cement-Based Mix Called M-300 Sand Concrete. [13]; (B) The First 3DPC Structure in Turkey Built by ISTON; (C) The First 3D Printed Footbridge of Alcobendas [14]	4
Figure 1.4. Office of the Future- 3D Printed Office; a Fully Functional Building with Electricity, Water, Telecommunications and Even Air Conditioning Systems [17].....	5
Figure 1.5. Apis Cor's 3D-Printing Machine was Moved About the Site Using a Crane to Re-Position it so it Could Build Different Parts of the Building [19].....	6
Figure 1.6. The Entire Construction Cost was Around \$10,000 and it can Withstand Temperatures as low as -35°C. This Type of Technology can Provide an Alternative to Traditional Construction Methods, Thereby Creating Affordable Housing [21]	6
Figure 1.7. The Building Printed by the Winsun Company [23].....	7
Figure 1.8. 3DPC Structures Built as Part of the ACES Project Carried Out by the US Army Corps of Engineers [24].....	7
Figure 1.9. A Study On Early Age Mechanical Behavior of 3D Printed Concrete [25].....	8
Figure 1.10. Comparing Experimental Findings with the Numerical Model [25]....	9
Figure 1.11. A study by Feng et al. [28] on Mechanical Properties of Structures 3D Printed Powders	10
Figure 1.12. A Study on Continuous Fibers in a Cementitious Matrix [32].....	12
Figure 1.13. A Study on Penetration Reinforcing Method for 3DPC [33]	13
Figure 1.14. Results of Penetration Reinforcing Method for 3DPC [33]	14

Figure 1.15. The Used Wall Samples; (a) The Flat Wall, (b) The Diamond Wall [34]	15
Figure 1.16. Experimental Results [34].....	16
Figure 2.1. The Stress-Strain Curves Describing the Behavior of a Concrete Under (A) Monotonic and (B) Cyclic Compressive Loading [35].....	22
Figure 2.2. $\sigma - \epsilon_p$ Relationship in (a) Tension, (b) Compression [41]	30
Figure 2.3. Stiffness Recovery Effect.....	33
Figure 2.4. Lubliner Yield Function [41] in (a) Plane Stress Space, (b) Octahedral Plane, and (c) Meridian Plane	35
Figure 2.5. Comparison of Numerical Results and Experimental Data for (a) Uniaxial Monotonic Tensile Behavior, (b) Uniaxial Monotonic Compressive Behavior, (c) Cyclic Tensile Behavior, and (d) Cyclic Compressive Behavior.....	47
Figure 3.1. The First 3D Printed Structure in Turkey, ISTON.....	54
Figure 3.2. Particle Size Distribution of Fine Aggregates.....	55
Figure 3.3. (a) Printing Process and (b) Printing Paths of the Walls (Not to Scale. Red Arrows: First Path; Green Arrows: Reverse Path; Stars: Start and End Points.)	56
Figure 3.4. Images Showing (a) Coring Directions (Dimensions in cm), (b-d) Coring of Wall-1 in X (Printing), Y (Deposition) and Z (Translation) Directions, (e) Cored Wall, and (f) Cored Micro-CT Sample	57
Figure 3.5. Tests Conducted on Wall-1 Cores (The Center of the UZ1-9, UZ10-14, LZ1-6, and LZ7-14 Cores were Located at 49.5 cm, 64.5 cm, 171 cm, and 186 cm from the Top of Wall-1, Respectively.).....	58
Figure 3.6. Beams from Wall-2 and -3 (Beam Top Surfaces were Marked with Yellow, Blue, and Green for B1, B2, and B3, Respectively. Dimensions in cm.)..	58
Figure 3.7. Schematic Representation of (a) Cylindrical, (b) Four-Point Bending and (c) Direct Shear Samples (Dimensions are in cm. in (c), Shear Failure Expected Interlayers are Marked with Blue.).....	61
Figure 3.8. The Standard Module TPS Setup with a Kapton 8563 Sensor	63

Figure 3.9. Representative Figure Illustrating Permeable and Impermeable Voids in: (a) Upper Layers and (b) Lower Layers (Blue: Permeable Voids, White: Impermeable Voids, and Grey: Solid Volume)	65
Figure 3.10. Capillary Rise Results of Cast and Printed Specimens	66
Figure 3.11. Cross-Sections of the Specimens Subjected to Water Penetration Tests: (a) U_{Y-D8} and (b) U_{Z2}	68
Figure 3.12. Compressive Strength of the Cast and Printed Specimens.....	70
Figure 3.13. Failure Modes (Fracture Patterns) of Upper and Lower Specimens Under Compression	71
Figure 3.14. Results of (a) Elastic Modulus and (b) Poisson's Ratio in Cast and Printed Specimens.....	72
Figure 3.15. Lateral Strain Versus Axial Strain Graph for Type U_Z Specimens	73
Figure 3.16. Correlation Between Volume of Permeable Pore Space (%) and (a) Compressive Strength (MPa) and (b) Elastic Modulus (GPa).....	73
Figure 3.17. Splitting Tensile Strength Results of Cast and Printed Specimens	75
Figure 3.18. The Split Specimens Located at Upper and Lower Part of Wall-1	75
Figure 3.19. Flexural Strength for the Cast and Printed Beams Estimated from Four-Point Bending Tests	77
Figure 3.20. The Triaxial Anisotropic Thermal Conductivities	80
Figure 3.21. A Comparison of the Initially Printed Concrete with U and L Samples	82
Figure 4.1. Impact of Printing Parameters on Bond Strength: (a) Varying Time Gap, (b) Printing Speed, and (c) Nozzle Standoff Distance [113].....	88
Figure 4.2. Challenges Arising from Using Circular and Square Nozzles: (a) Voids Between the Circular Bead Layers [4], (b) Misalignment of Bead Layers due to the Nozzle [4], and (c) Schematic Illustration Depicting the Flow of Printed Mortar Through the Circular Nozzle Problems [118].....	89
Figure 4.3. Example Figures of Void Formation Between Layers due to the Use of Circular Nozzle (Taken from (a) [122], (b)-(c) [78], and (d) [31])	90

Figure 4.4. Sample Printed by Rectangular Nozzle at (a) 1-Min Time-Gap, (b) 5-Min Time-Gap, (c) 10-Min Time-Gap, and (d) 20-Min Time-Gap, Illustrating the Impact of Time-Gap on Printed Samples [79]	91
Figure 4.5. The Cross-Sectional Geometries Achieved by the (a) Rectangular and (b) Circular Nozzles [121].....	91
Figure 4.6. (a) Cored CT-Samples, (b) Micro CT Sample, and (c) the Location of Micro CT sample Highlighted by Red (Blue is a Concrete Filament)	95
Figure 4.7. (Top) μ -CT Slices and (Bottom) Reconstructed Cross Sections of Cast, $U_Y, L_Y \varnothing 0.75\text{cm}$ Samples - ⁽⁺⁾ Dashed Red Lines Mark the Location of the Selected Slice	98
Figure 4.8. Pore Size Distribution Estimated on μ -CT Samples (*) The Pore Size is Expressed as an Equivalent Diameter Obtained from a Circumscribed Sphere of Equal Volume to That of the Pore	99
Figure 4.9. Porosity Distribution Along Printed Specimens' Height	99
Figure 4.10. 3D Reconstructed μ -CT Analysis Results for Cast and Printed Concrete Samples (Each Edge of the Cubes is 4.5 mm – Pores are Highlighted by Cyan Color)	100
Figure 4.11. (Top) Macro-CT Slices and (Bottom) Reconstructed Cross Sections of Cast, $U_Z, L_Z \varnothing 10\text{cm}$ Specimens: (*) The Transparent Red and Black Areas Indicate the ROI-1 (Including Interstrip) and ROI-2 (Excluding Interstrip), Respectively. ⁽⁺⁾ Dashed Red Lines Mark the Location of the Selected Slice.	101
Figure 4.12. Thickness Analysis Results of Macro-CT Scans. (a) Cast and Printed Concrete, (b) U_Z , (c) U_X , (d) L_Z , (e) L_X Macro-CT Scans	102
Figure 4.13. (a) Schematic Representation of Sampling Procedure and Pore Simplification in the Printed Wall and (b) Cored Samples in a CAD Environment	108
Figure 4.14. Generated Stress-Strain Curves in (a) Compression and (b) Tension	110
Figure 4.15. Generated Meshes for the Samples	110

Figure 4.16. (a) Typical Traction-Separation Model, and (b) Illustration of Mixed-Mode Softening [138]	113
Figure 4.17. Generated Meshes for the Samples	114
Figure 4.18. Comparison Between Experimental and Numerical Results of Compressive Strength, Elastic Modulus, and Poisson's Ratio for the Upper and Lower Samples in the First Approach	116
Figure 4.19. Isosurface Illustrations of Mises Stress Distribution in Fully Elastic State for (a) Upper Samples, and (b) details of U_Z sample	118
Figure 4.20. Compressive and Tensile Damage, and Plastic Strain Evolution on Cast and Upper Samples at Their Respective Ultimate Loads	120
Figure 4.21. Compressive and Tensile Damage, and Plastic Strain Evolution on Lower Samples at Their Respective Ultimate Loads	121
Figure 4.22. Isosurface Illustrations of Damage and Plastic Strain Distribution in Upper Samples at Equivalent Damage and Plastic Strain Levels	123
Figure 4.23. Comparison Between Experimental and Numerical Results of Compressive Strength, Elastic Modulus, and Poisson's Ratio in the Second Approach	124
Figure 4.24. QUADSCRT, MMIXDME, and Stiffness Degradation on Upper Samples at Their Respective Ultimate Loads	126
Figure 4.25. QUADSCRT, MMIXDME, and Stiffness Degradation on Lower Samples at Their Respective Ultimate Loads	127
Figure 4.26. Diagonal Shear Failure in the Interstrip of L_X sample	127
Figure 4.27. Comparative Analysis of U_X Sample Failure Modes	129
Figure 4.28. Comparative Analysis of U_{Y-S} Sample Failure Modes (Approach 2)	130
Figure 4.29. Comparative Analysis of U_{Y-D} Sample Failure Modes (Approach 2)	130
Figure 4.30. Comparative Analysis of U_Z Sample Failure Modes (Approach 2)	131
Figure 4.31. Comparative Analysis of U_{Y-S} Sample Failure Modes (Approach 1)	132

Figure 4.32. Comparative Analysis of U_{Y-D} Sample Failure Modes (Approach 1)	133
Figure 4.33. Crack Propagation within the Concrete Flament in U_Z Sample (Approach 1)	134
Figure 4.34. Comparative Analysis of U_Z Sample Failure Modes (Approach 1)	135
Figure 5.1. Images Showing (a) Cored Wall, (b) Coring Directions (Coring of Wall-1 in X, Y and Z), and (c) Schematic of Cylindrical Samples and the Experiments (Dimensions are in cm)	143
Figure 5.2. Experimental Setup Details	147
Figure 5.3. Modified Experimental Setup Details	148
Figure 5.4. Wall Surface Preparation for Digital Image Correlation (DIC)	150
Figure 5.5. Lateral Load – Top Displacement Measured from Load-Cell and LVDT #2	153
Figure 5.6. Lateral Load – Uplift Displacement Measured from Load-Cell and LVDT #7	154
Figure 5.7. Lateral Load vs. Induced Strain/Force in the Bars	155
Figure 5.8. Lateral Displacement Profiles	156
Figure 5.9. Comparisons of the Lateral Displacement Profiles of the Walls at (a) 80 kN Lateral Load, and (b) Ultimate Lateral Load Applied to the Wall	157
Figure 5.10. Comparison of Initial and Deformed Surface Patterns for the Walls (a) 25-150-100, (b) 25-100-100, (c) 25-100-100, and (d) 25-100-150	158
Figure 5.11. Calculation Procedure of Net Lateral Deformation	161
Figure 5.12. Lateral Load – Net Lateral Deformation Derived from LVDT Measurements	162
Figure 5.13. Lateral Load – Net Lateral Deformation Derived from DIC Measurements	163
Figure 5.14. Crack Propagation Process: (a) Initial Undamaged Wall Configuration, (b) First Sudden Crack, (c) Second Continuous Crack, and (d) Brittle Diagonal Failure of the Front Face	164

Figure 5.15. Sudden Diagonal Crack Propagation of the Wall 25-100-150 Captured by DIC.....	166
Figure 5.16. Key Images and Notes from Fractured Walls: Walls (a) 30-150-100, (b) 25-150-100, and (c) 20-150-100	167
Figure 5.17. Crack Propagation Process: (a) Initial Undamaged Wall Configuration, (b) First Sudden Crack, and (c) Second Sudden Crack	168
Figure 5.18. Crack Propagation Process: (a) Initial Damaged Wall from the First Test, (b) Brittle Diagonal Failure of the Front Face, and (c) Brittle Diagonal Failure of the Front Face Captured by DIC.....	170
Figure 5.19. Key Images and Notes from Fractured Wall 25-100-100: (a) Initial Test Setup, and (b) Modified Test Setup	171
Figure 5.20. Crack Propagation Process: (a) Initial Undamaged Wall Configuration, (b) First Crack Propagation, and (c) Second Crack Propagation.....	172
Figure 5.21. Key Images and Notes from Fractured Wall 25-100-150	173
Figure 5.22. Numerical Simulation Model Details: (a) the Experimental Setup, (b) Wall Details, (c) Mesh Details of the Wall, and (d) Mesh Details of the Tension Bar System	179
Figure 5.23. Interlayer Observations During Wall Demolition: (a) Upper Portion and (b) Lower Portion	181
Figure 5.24. Stress-Strain Curves in (a) Compression and (b) Tension	183
Figure 5.25. Material Model Assignments for Wall 25-150-100 - (a) Wall-CDPM-1, (b) Wall-CDPM-5, (c) Wall-CDPM-CAST, and (d) Wall-CDPM-Segmented	184
Figure 5.26. Comparison of DIC and Numerical Simulation Results for (a) Wall-CDPM-1, (b) Wall-CDPM-5, (c) Wall-CDPM-CAST, and (d) Wall-CDPM-Segmented.....	186
Figure 5.27. Compressive and Tensile Damage Distribution for Different CDPM Walls: (a) CDPM-1, (b) CDPM-5, (c) CDPM-CAST, and (d) CDPM-Segmented	189
Figure 5.28. Tensile Damage (Fracture) Propagation during the Analysis for the Wall-CDPM-Segmented	191

Figure 5.29. Plastic Strain Distribution for the Front and Back Face of the Wall	192
Figure 5.30. Comparison of Numerical Result from ABAQUS and Experimental Result from DIC Considering the Maximum Principal Strain Distribution.....	192
Figure 5.31. Shear Stress Distribution Contour on Wall Cross-Section for Various Load Levels and Elevations.....	195
Figure 5.32. Shear Force Distribution and Load Transfer Mechanisms within Mid-Height (500 mm) of Wall-25-150-100 Analyzed using CDPM-Segmented Model	196
Figure 5.33. The Reaction Forces and Percentage Contributions of Each Member	199

CHAPTER 1

INTRODUCTION

Additive manufacturing (AM), also known as three-dimensional printing, was introduced in 1986 [1]. The logic of this technique is to construct a three-dimensional object layer-by-layer addition of a raw material, which creates freeform structures through a rapid prototyping system.

Although AM has been widely applied in different fields such as biomedical materials, aerospace, prototyping, and automotive industries, the progress of AM in the construction industry was very slow in spite of its advantages. AM technology is open to improvement, and when it becomes commercially applicable in the construction industry, with admitted/approved specifications/standards, it brings many advantages together. Increased construction speed; decreased labor, material usage, waste production and CO₂ emission, and safer construction in terms of injury and fatal accidents are commonly cited potential benefits of three dimensional printed concrete (3DPC) [2,3]. One of the most important benefits of 3DPC is to construct a structure, even a complex one, without using formworks and reducing the waste production. Therefore, the 3DPC method deduces two important items of the construction industry: The total formwork cost (the material and the labor cost) and the installation time of the formwork.

The cost of the formwork is generally estimated around sixty percent of the total concrete work of the construction and the formwork installation time is between fifty and seventy percent of the total construction time [2,4–7]. The study done by Batikha et al. showed that compared to the other construction methods which are prefabricated modular construction, cold formed steel-based construction, hot rolled steel-based construction and reinforced concrete-based construction, 3DPC is the most economical construction method. Also, 3DPC is the most sustainable

construction method (almost the same as the cold-formed steel-based construction method) in terms of CO₂ emission, and the fastest one after the prefabricated modular construction method [8].

On the other hand, the research about 3DPC mostly focuses on developing and improving the material and application methods such as the mechanical performance of the used material and reinforcement integrations [9]. On the contrary, there is a few studies about structural performance of the 3DPC structures, and there is no study about earthquake performance of 3DPC structures in the literature. This causes a viability problem for 3DPC structure. Bos et al.[10] studied that viability of 3DPC structures and the approval process of 3DPC structures. It was found that lack of the regulatory framework for expedient approval, structural application of 3DPC is limited. The standardization of constructing the 3DPC structures is an important issue to ease the application progress of 3DPC structure. Therefore, it is crucial to understand 3DPC structures thoroughly before standardization.

In this chapter, a comprehensive review of existing literature on current practices in 3DPC structures are undertaken. Then, mechanics of 3DPC are meticulously analyzed, establishing a foundational understanding for the research objectives and scope, which are subsequently presented. Finally, a roadmap is provided for navigating the forthcoming chapters.

1.1 Current Practices in 3D Printed Concrete Structures

Architect James Bruce Gardiner is one of the chief architects behind several significant projects designed to be constructed using 3D printing technologies. The FreeFAB Tower Project was the first project in history to be designed for production using 3D printing techniques. In this project, a hybrid approach combining modular and 3D manufacturing was planned [11]. This project served as a starting point for Winsun, which has since executed numerous large-scale 3D manufacturing projects. Additionally, it set an example for the use of multi-axis robotic arms in 3D

construction. Companies like MX3D and Branch Technology have followed in the footsteps of this project, continuing to achieve success with their current projects. Figure 1.1 illustrates a sketch of the production line for the printers to be used in the manufacturing of the FreeFAB project.

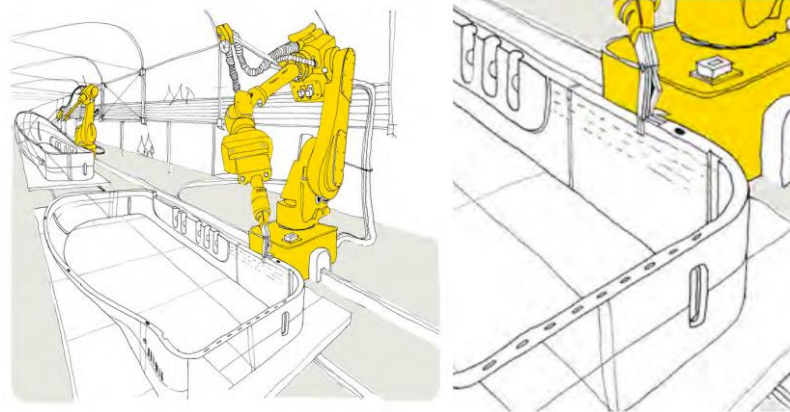


Figure 1.1. Schematics of the Production Line for Parts Printed by Industrial Robotic Arms Using the Contour Crafting Technique [11]

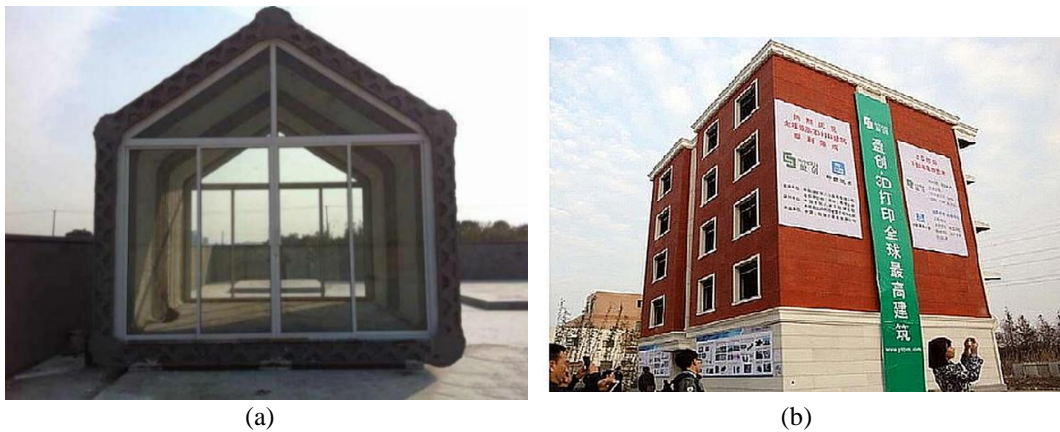


Figure 1.2. Structures Produced by Winsun Company in China: (a) 300 m² Single Story Buildings with a Cost of 4800\$ [12], and (b) Five Story Building

Figure 1.2-a shows the low-cost structure produced by Winsun with a concrete printer. The company built the structure by transporting the prefabricated parts manufactured with a 3D concrete printer to the construction site and assembling the parts. It has been stated that the company reduces the construction costs up to 80%

in this way. In 2014, the company kept the cost of one-story buildings produced in one day in China below \$5,000. Additionally, the firm built a 5-storey building with the same method, Figure 1.2-b. Winsun company also has projects that it carries out by sending prefabricated elements to Dubai in this way.

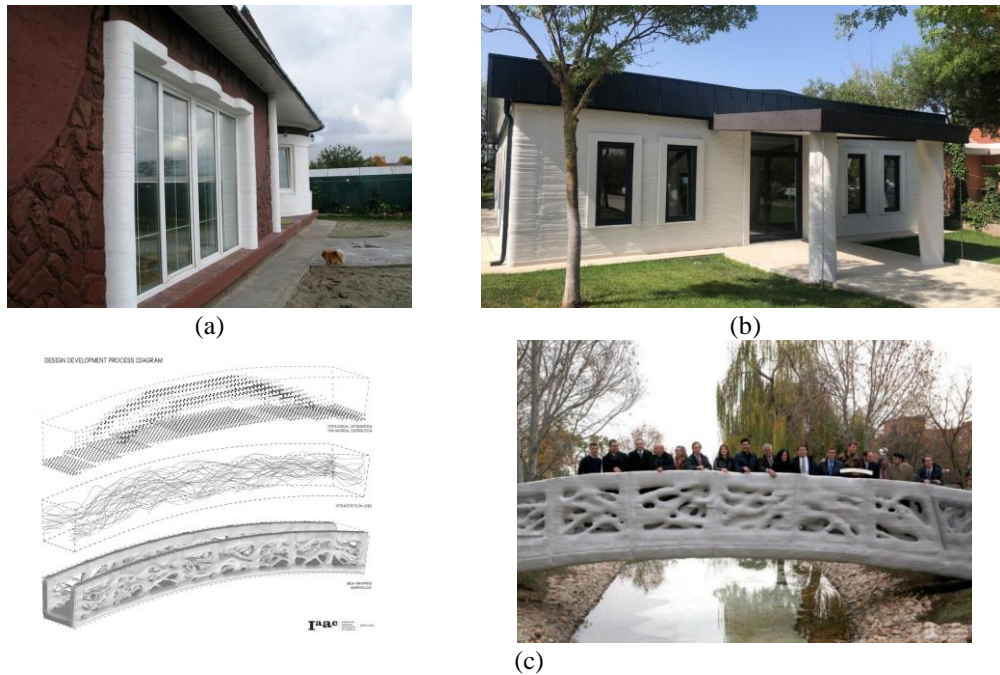


Figure 1.3. (a) The Material Used to Build the Yaroslavi House is a Cement-Based Mix Called M-300 Sand Concrete. [13]; (B) The First 3DPC Structure in Turkey Built by ISTON; (C) The First 3D Printed Footbridge of Alcobendas [14]

The first residential project built was 298.5 m², under the name Yaroslavi, in Russia. In 2015, around 600 pieces of Yaroslavi were produced at the factory and assembled on site. The residence shown in Figure 1.3-a was not built for presentation purposes only; There are people living in it today. On the other hand, the first 3DPC structure in Turkey built by ISTON shown in Figure 1.3-b. The load-bearing system of this structure consisted of RC columns for analysis and design purposes, where the RC columns were constructed without the need for formwork due to the printed 3DPC walls. In 2016, the first 3D printed pedestrian bridge in the world was opened in the urban park of Castilla-La Mancha in Madrid, Spain. The total length of the bridge is 12 meters and the width is 1.75 meters, and it was printed in micro-reinforced concrete. The architectural design was made by the Institute of Advanced

Architecture of Catalonia (IAAC). The 3D printer used to build the pedestrian bridge was produced by D-Shape. In Figure 1.3-c, the diagram related to the design and 3D modeling phase and the photograph in use after manufacturing are presented [15].

An office named as Office of the Future, designed by Gensler, and manufactured by Winsun, one of the leading companies in the industry, went down in history as the first commercial building constructed by using 3D printing technology. In this way, it has succeeded in reducing labor costs and manufacturing waste by 30%. All parts of the office building shown in Figure 1.4 took only 17 days to print, and it took an additional 2 days to assemble the printed parts [16].



Figure 1.4. Office of the Future- 3D Printed Office; a Fully Functional Building with Electricity, Water, Telecommunications and Even Air Conditioning Systems [17]

Apis Cor's record-breaking project for Municipality of Dubai is the largest 3D-printed building to date shown in Figure 1.5. The 650 square meter area on two floors was printed by Apis Cor's self-developed printer. The building sits on conventional foundations, and the 3D-printed formwork for the columns was reinforced with concrete and rebar. The roof and window are still in situ with conventional solutions. The company has also won NASA's 3D printed Habitat Competition in 2019, together with SEArch+, bringing space inhabitation one step closer [18].



Figure 1.5. Apis Cor's 3D-Printing Machine was Moved About the Site Using a Crane to Re-Position it so it Could Build Different Parts of the Building [19]

Another project of Apis Cor that has impacted the industry is a building located in the town of Stupino near Moscow. One of the biggest reasons why the project is special is that all the main components were constructed on site. This reduced transporting and assembly costs, and the total 3D printing time took only 24 hours. Using a mixture of solid elements and liquid polyurethane, Apis Cor has carried out on-site printing with this material with thermal insulation properties [20]. Figure 1.6 shows a phase from this 24-hour construction process.



Figure 1.6. The Entire Construction Cost was Around \$10,000 and it can Withstand Temperatures as low as -35°C . This Type of Technology can Provide an Alternative to Traditional Construction Methods, Thereby Creating Affordable Housing [21]

Approximately 400 m^2 2-storey villa shown in Figure 1.7 was built on site with a 3D printer. The construction took approximately 45 days. The walls of the villa have 25

cm thickness and are made of approximately 20 tons of C30-grade concrete. The production process of the building, which shown in Figure 1.7 as finished, is different from other 3DPC buildings, and the entire printing process took place on site [22].



Figure 1.7. The Building Printed by the Winsun Company [23]

In the ACES project, which is carried out by the US Army Corps of Engineers, about 3DPC construction, it is aimed to investigate fast construction methods in the field for custom-designed expeditionary structures by using concrete sourced from locally available materials in order to meet the needs of the army. As a result of the field trials, it was stated that the chevron type (Figure 1.8) geometry of the walls provides the most suitable form for structural stability and against cracking. It is among the results of the project that it is important to determine the behavior of these structures against earthquake loads, but in this respect, no data related to the outputs of the project was found.



Figure 1.8. 3DPC Structures Built as Part of the ACES Project Carried Out by the US Army Corps of Engineers [24]

Having explored several groundbreaking 3DPC projects, it becomes evident that this innovative construction method is poised to redefine the industry. To fully grasp its

transformative potential, it is essential to delve into a concise review of the key mechanical properties that underpin the structural integrity and functionality of 3DPC.

1.2 The Mechanics of 3D Printed Concrete

Research on 3DPC has recently intensified, with a focus primarily on application methods, material development, mechanical performance of existing materials, and the integration of elements such as reinforcement and fibers. However, there have been very few studies on the structural system of 3D printed concrete and reinforced concrete structures, and no studies have addressed seismic/earthquake performance. In this context, various studies, experiments, and examples are discussed below.

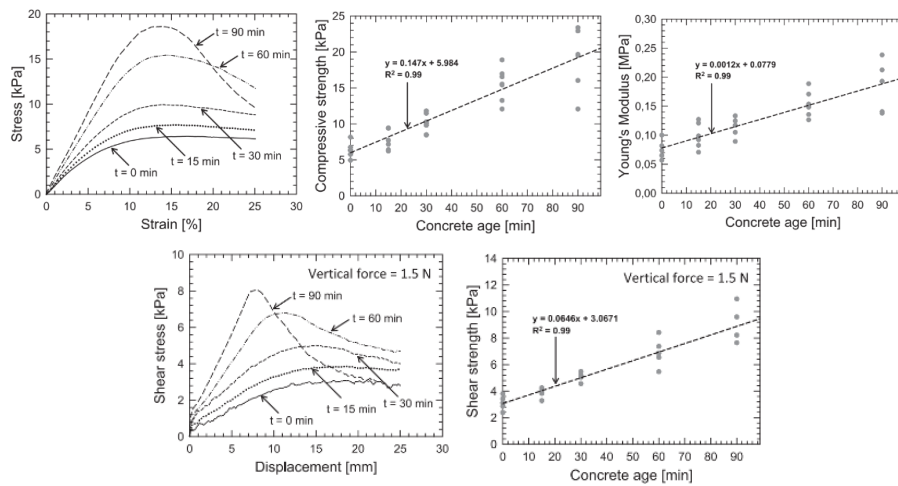


Figure 1.9. A Study On Early Age Mechanical Behavior of 3D Printed Concrete [25]

In a study conducted in 2018 [25], the mechanical behavior of uncured 3D-printed concrete was investigated. Samples, whose initial setting time was approximately 2 hours as measured by standard Vicat testing, underwent uniaxial compression and direct shear tests at 0, 15, 30, 60, and 90 minutes. These tests were conducted following ASTM D2166 [26] and ASTM D3080 [27] standards:

- In uniaxial compression test, force/displacement graphs were created during the test. Stress values were continuously calculated using the changing

surface area, and linear correlations were established between the concrete's strength/elastic modulus and age using average values.

- In direct shear test, the same procedures were applied for, and a linear correlation was established between the concrete's shear strength and age. The test results are summarized in the graphs below (Figure 1.9).
- Experiment is compared with the numerical model. The aim of the analysis is to observe the structural behavior and failure-deformation mode of uncured 3D-printed concrete during production. The data obtained from the experiments were used in the numerical model. Both the experiments and numerical analyses used cylindrical models with the same dimensions. The analyses were conducted considering the 3D printer's printing time, layer formation time, and material density. It was observed that the deformation-failure mode in both numerical analyses and experiments was a combination of cylindrical buckling and material yielding. The results of numerical analyses and experiments are shown in the Figure 1.10.

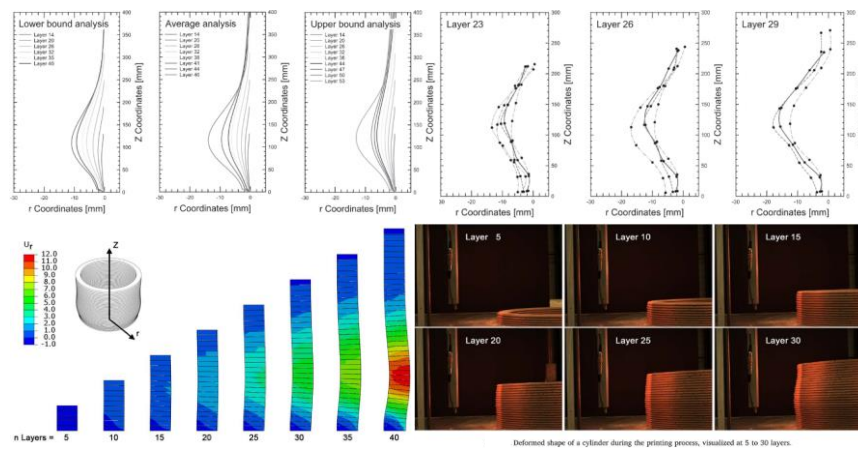


Figure 1.10. Comparing Experimental Findings with the Numerical Model [25]

For the hardened concrete, the variation of compressive, tensile, and shear strength, as well as the failure type of 3D-printed samples, was investigated [28] in relation to the printing direction, emphasizing the importance of the compression direction. The results were used in the numerical analysis of 3D-printed structures. Figure 1.11-a

illustrates the printing directions. The printing process occurs in a straight line from A1 to B1 (in the X direction), and after B1, it proceeds from B2 to A2 without spraying (in the Y direction). Once all strips to be compressed in the Y direction are completed, the process moves to the next layer (in the Z direction), and the printing continues in the next layer. Uniaxial compression tests and bending tests were performed in different directions on the samples. The results of uniaxial compression tests for 50x50x50 mm samples (Figure 1.11-b) yielded average strengths of 16.8, 11.6, and 13.2 MPa when compression was applied in the X, Y, and Z directions, respectively. This test result indicates that the compressive strength in the X direction is greater than that in the Y and Z directions, suggesting that 3D-printed samples exhibit anisotropic behavior. The inference drawn is that the bond between strips created in a short time is stronger than the bond between strips created over a longer period. The bending test (Figure 1.11-c) was conducted in accordance with the National Chinese Standards [29]. For bending strength, the initial fracture force obtained from linear elastic analysis was used. The average bending strengths were found to be 4.12 MPa in the Z direction and 0.365 MPa in the X direction.

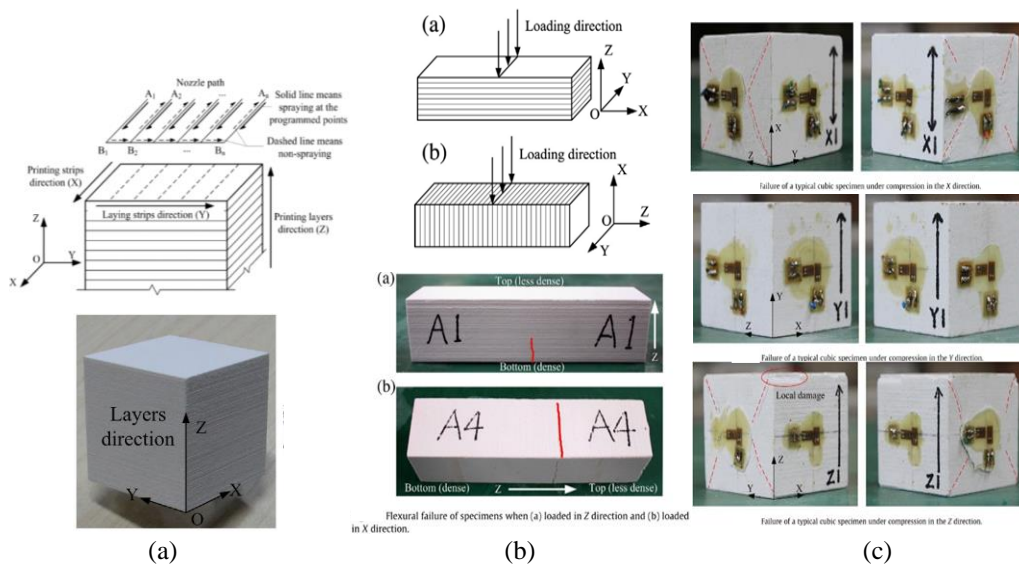


Figure 1.11. A study by Feng et al. [28] on Mechanical Properties of Structures 3D Printed Powders

In a similar study conducted in 2019 [30], it was concluded that the strength of the bond between layers is directly related to the layer formation time. In this study, it was observed that the strength properties of 3DPC samples produced in a short time varied very little depending on the direction, but for 3DPC samples produced over a longer time, the interlayer bond strength decreased. This article recommends paying attention to printing times in such studies and suggests the creation of specifications related to this aspect.

Panda et al. [31] evaluated geopolymer mortar reinforced with different lengths and percentages of glass fibers. The lengths of the fibers used were 3, 6, and 8 mm, and the usage percentages were 0.25%, 0.5%, 0.75%, and 1%. In this context, bending and compressive tests were conducted in different 3D printing directions according to BS EN 196-1:2016 standards. In addition, tensile tests were also performed, and these tests were conducted in two different directions. The results of the experiments showed that the glass fiber reinforcement did not provide a significant improvement in compressive strength. However, it was observed that the tensile and flexural strength increased significantly with an increasing percentage of glass fiber. Nevertheless, the interlayer strength could not be greatly increased with the glass fiber used. Therefore, the increase in tensile strength perpendicular to the 3D printing direction was less than the increase in tensile strength in the other direction.

Ducoulombier et al. [32] studied integration of continuous fibers into additive concrete manufacturing. In this process, unlike the commonly used extrusion-based 3D printers, a continuous 3D printing process was performed using flow-based pultrusion with fibers. The 3D printing method in this research was developed and compared with other methods. In addition, tensile tests were conducted to evaluate the mechanical performance of the structure. Tensile tests were performed on specimens with dimensions suitable for compression. The results of the experiments showed that the continuously fiber-reinforced concrete exhibited ductile behavior. Figure 1.12-a illustrates the printing process, Figure 1.12-b shows the test results, and the experimental outcome along with the sample used are presented. The study pointed out that anisotropic materials are generally not preferred in civil engineering

applications but highlighted some applications where anisotropy could be desired, such as concrete cage systems and layer-wise plates. The author drew attention to these applications, emphasizing the need for innovative structural designs.

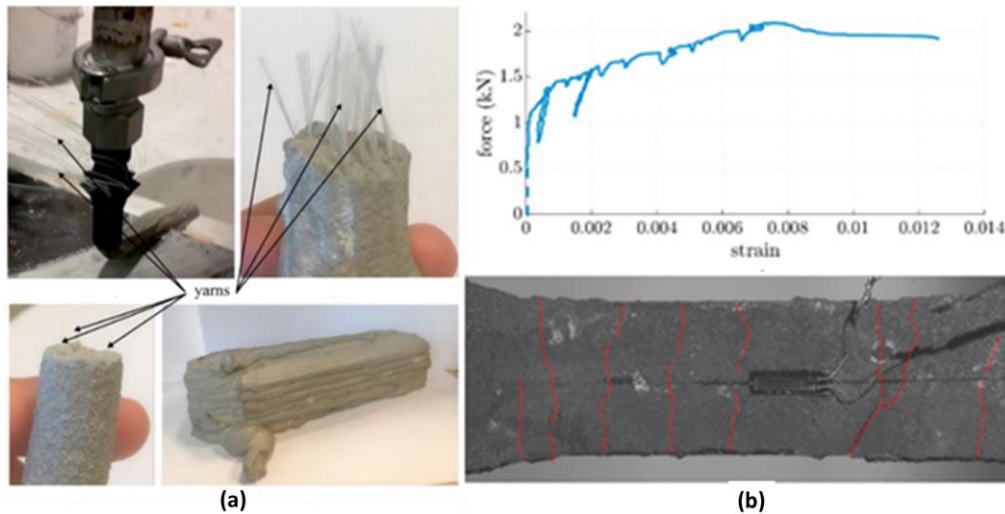


Figure 1.12. A Study on Continuous Fibers in a Cementitious Matrix [32]

In a study conducted by Marchment & Sanjayan [33], an attempt was made to integrate steel mesh into 3D concrete printing. The researcher aimed to continuously place steel mesh within the concrete during the printing process. Therefore, the flexibility of the steel mesh is essential to enable it to be rolled into the concrete during the printing process without hindrance. For this study, 6x6 mm galvanized steel mesh was selected, with a height of 26 mm, as shown in Figure 1.13-a. The results of uniaxial tensile tests conducted on a single wire of the mesh are also presented in Figure 1.13-a. Figure 1.13-b illustrates how the mesh should be placed within the concrete layers and attempts to illustrate the integration process of the mesh. In this context, it is necessary to leave a specific lap length to ensure that the mesh embedded entirely within the concrete is also connected to the concrete in the layer above.

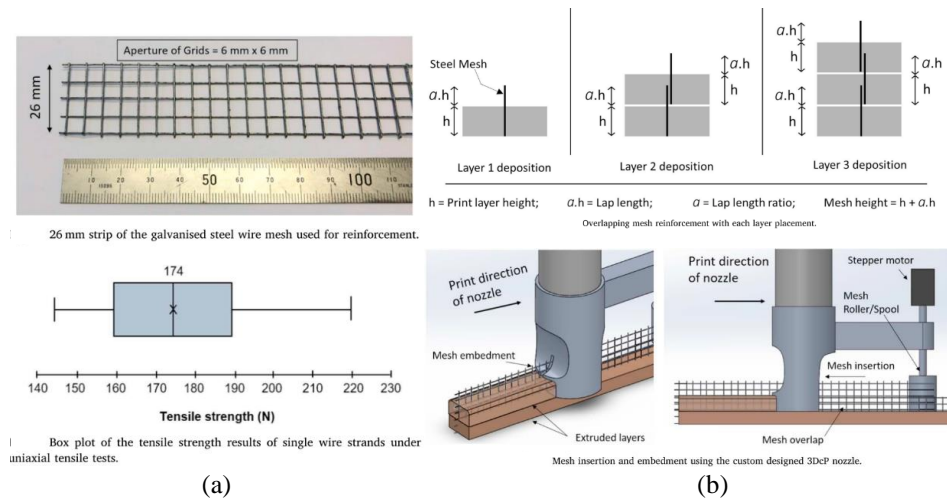


Figure 1.13. A Study on Penetration Reinforcing Method for 3DPC [33]

Tensile and three-point bending tests were conducted to examine the mechanical performance of the steel mesh-reinforced 3D printed concrete produced using this method. The preparation of the specimens took into account the printing time, and the tests were performed on the 7th day.

- Compressive strength test: 25x25x25 mm cast specimens and 30x30x30 mm 3D printed specimens are used in this test. Vibration was applied to the specimens created by the conventional method, resulting in a lower void ratio in the specimens compared to the 3D printed ones. The test results are summarized in Figure 1.14-a.
- Three-point bending test (ASTM C-293): This test included 6 specimens reinforced with steel mesh and 3 control specimens (unreinforced) 3D printed concrete. The specimens were created by cutting the printed concrete into lengths of 45 mm, as seen in Figure 1.14-b, and the test setup is shown in Figure 1.14-c. In this test, the bending moment strength, moment capacity, and bending bond strength were calculated using the moment value at the point where cracking occurred. This is because the expected crack location is within the layer-to-layer region rather than where the moment reaches its maximum value. The test results and crack patterns in the specimens are summarized in Figure 1.14-d. The terms 'R' and 'C' represent specimens

reinforced with galvanized steel mesh and unreinforced specimens, respectively. As expected, the initial crack locations in the bending tests occurred between the layers. As a result, the study observed that the cause of failure in the specimens produced using the method in the paper was the rupture of the mesh, indicating that the adhesion between the steel mesh and concrete was sufficiently good. The steel mesh reinforcement increased the bending moment strength by 170% to 290% in 3D printed concrete.

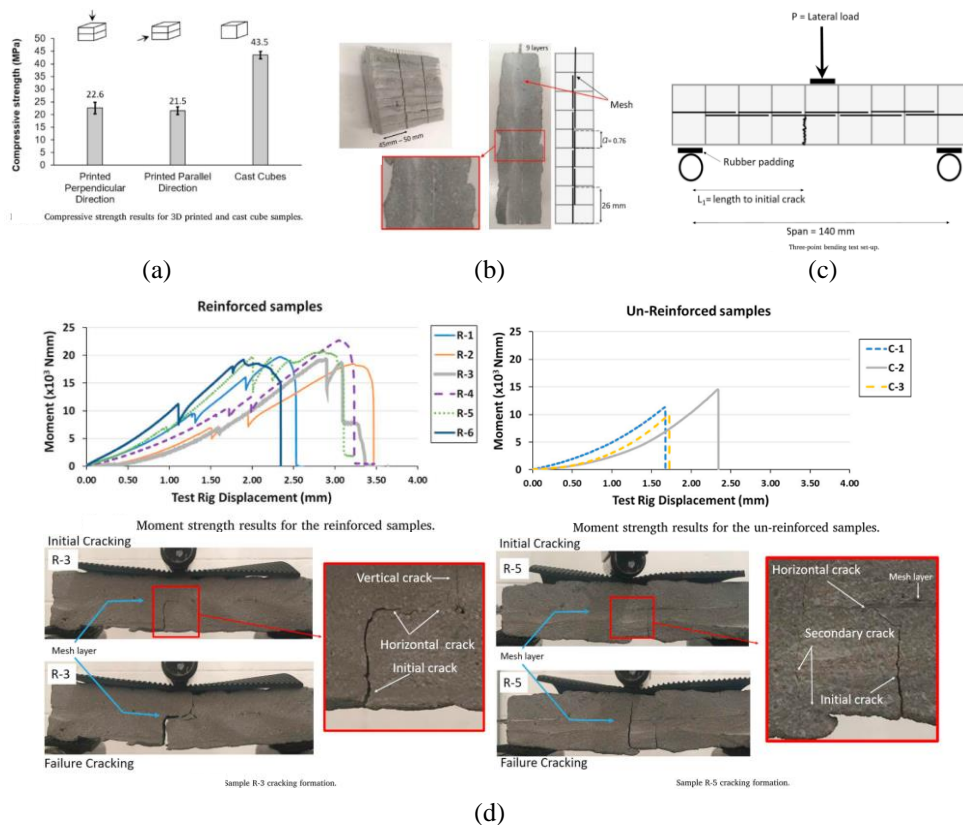


Figure 1.14. Results of Penetration Reinforcing Method for 3DPC [33]

Load-bearing walls are among the most crucial structures in 3D-printed concrete buildings. However, there is currently no standard or optimized geometry for these walls. It is an architectural expectation that load-bearing walls are designed flexibly. In a study conducted in 2021 by Daungwilailuk et al. [34], large-scale wall specimens with two different designs were identified, and uniaxial compressive tests were performed to observe the behavior of the walls during the tests. Finite element

analyses were also conducted. One of the models used in the experiments, a double-layered wall with an inner truss, represented a flat wall, while the other, a diamond wall or waving design wall, represented a diamond-shaped wall. The geometric characteristics of the specimens are summarized in the Figure 1.15. Additionally, the maximum and minimum depth of the diamond wall are 12.5 cm and 6 cm, respectively, and only one surface has a wavy pattern. The reason for the other surface to be flat is the necessity for the structure to remain stable during printing.

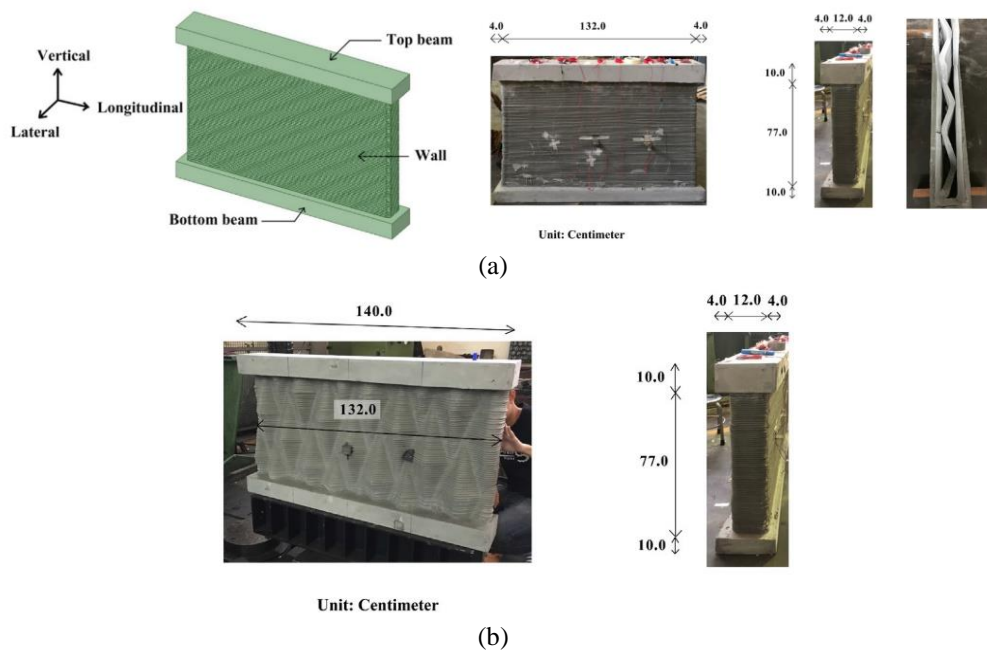


Figure 1.15. The Used Wall Samples; (a) The Flat Wall, (b) The Diamond Wall [34]

The uniaxial loading test was conducted manually at an approximate rate of 45-55 kN/min, and it continued until the test specimens fractured. As a result of the tests, the characteristic behavior of the flat wall remained unchanged when combined with the diamond wall. However, there were larger fluctuations in strain values in the diamond wall's unit deformation, and this was due to the trusses inside the flat wall. Figure 1.16 illustrate the horizontal and vertical displacements in both the flat and diamond walls. The horizontal displacement of the flat wall fluctuated between -1 and 1 mm. This fluctuation indicates that the specimen bowed during the test. The horizontal displacement of the diamond wall reached levels of 4 mm, which is

approximately 400% higher than what the flat wall achieved. Additionally, extreme strains on the front surface and extreme compression unit deformations on the rear surface of the diamond wall were observed. Therefore, the diamond wall fractured due to strain, force, and buckling. In conclusion, it can be stated that the shape of the wall significantly affected crack formation and mechanical performance. It was understood that the pits in the diamond wall were weak points of the structure, and the inner trusses in the flat wall mitigated deformation and damage. Additionally, numerical analyses were conducted on the flat wall without the use of inner trusses. The results of these analyses indicated that the absence of inner trusses could pose a risk of torsional failure. In summary, it can be concluded that the wall pattern significantly affected the load-carrying capacity of the wall. High tensile strains were observed in the pits/tips of the diamond wall, leading to cracking and spalling in the concrete. Furthermore, the inner trusses acted as braces for the wall, reducing its curvature and preventing torsional failure. Finally, the strain gauges exhibited both positive and negative values at the same location and in the same direction. This was due to wall bowing and the deformation of the compressed concrete.

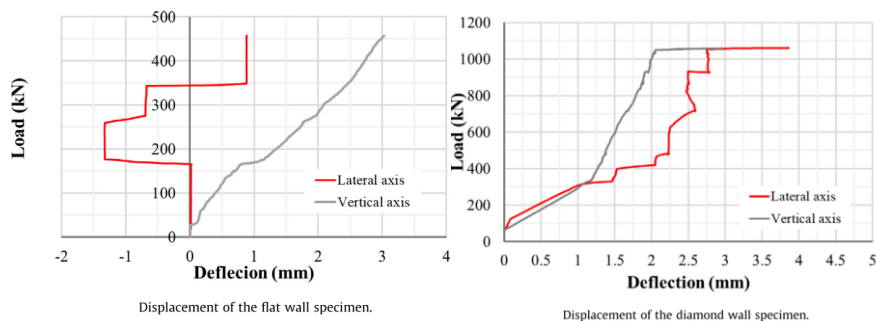


Figure 1.16. Experimental Results [34]

1.3 Objective and Scope

This thesis aims to address a critical gap in the current understanding of 3DPC wall performance under lateral loads, such as those experienced during earthquakes. While the literature review revealed that there are no studies in this direction and there are very few studies on the evaluation of structural performance of 3DPC.

Despite the limited research on the evaluation of structural performance, notable construction activity has been observed in the field. Therefore, a comprehensive investigation of 3DPC wall performance has been undertaken, systematically addressing deficiencies from the micro to the macro scale. This thesis presents a series of rigorous studies that bring valuable insights into the structural behavior of 3DPC components, each of which is detailed in its own chapter and includes relevant literature reviews.

Driven by this gap in knowledge, the research culminates in an in-depth investigation of real-scale and large-scale elements. This comprehensive exploration delves into the physical, mechanical, and thermal properties of 3DPC structures at real scale, meticulously examining variations along the height. The research scrutinizes the reasons behind these variations, providing detailed explanations for the anisotropic behavior observed in 3DPC. Ultimately, the primary focus is on the performance of 3DPC walls under lateral loads, such as seismic forces, which propels and shapes the entirety of this study.

To sum up, this thesis aims to bridge the knowledge gap in 3DPC performance by:

- Characterizing the physical, mechanical and thermophysical properties of 3DPC at real-scale.
- Unraveling the role of interlayer porosities in inducing anisotropy and incorporating it into numerical models.
- Providing comprehensive insights into the structural response and failure mechanisms of unreinforced large-scale 3DPC walls under lateral loads.

1.4 Limitations

This research is limited to the characterization and evaluation of a single fiber-reinforced printable concrete mixture, as broader investigations were not feasible within the constraints of the research design.

1.5 Organization of Thesis

Chapter 1 provides a comprehensive introduction to the research journey. This chapter delves into the motivations and context driving the investigation, defines the central question or challenge, and meticulously maps out the specific aims and goals to be explored in the following chapters.

Chapter 2 establishes the foundation for understanding the mechanical behavior of concrete through a review of existing literature. Additionally, it introduces the continuum damage plasticity model for concrete structures under cyclic loading. This chapter formulates the constitutive theory and develops the numerical implementation of the material model, providing a crucial basis for further analysis in subsequent chapters. **Appendix A** and **Appendix B** provide additional details on implementing the model in Abaqus and FEAPpv software, respectively, highlighting the development of custom user-defined material (UMAT) routines for advanced simulations.

Chapter 3 shifts focus to the experimental realm, conducting comprehensive tests on real-scale 3DPC walls to characterize the physical, mechanical and thermophysical properties throughout the entire height. The study unveils a compelling self-weight-induced densification in early layers, resulting in pronounced increase in compressive, elastic, and tensile strength in the lower wall sections. These insights advocate for the meticulous consideration of 3D printing processes in concrete construction, shaping industry practices and emphasizing the pivotal role of large-scale experiments in refining material understanding. On the other hand, these experimental data also serve as crucial validation points for the numerical models developed later.

Chapter 4 delves into the micro and meso scale, leveraging the detailed pore data from CT scans of Chapter 3's samples. It focuses on the crucial interlayer and interstrip porosities formed between printed layers, comparing their characteristics and distribution throughout the wall with those of cast concrete. By meticulously

analyzing the volume fraction and spatial distribution of these porosities, the chapter sheds light on their dominant influence on 3DPC's mechanical behavior. Using this newfound understanding, Chapter 4 employs finite element method to model the impact of these porosities on 3DPC walls. This analysis utilizes material models like the CDPM (developed in Chapter 2) and traction-separation laws to capture the complex interplay between the concrete and the interlayer/interstrip porosities. The findings reveal that these porosities significantly shape 3DPC's mechanical response, even explaining certain failure mechanisms. This crucial understanding forms the foundation for accurately modeling large-scale 3DPC walls in subsequent chapter.

Chapter 5 investigates a comprehensive macro-scale study, focusing on the structural response and failure mechanisms of unreinforced 3DPC walls under lateral loads. This chapter transcends traditional testing by synergistically employing cutting-edge Digital Image Correlation (DIC) techniques, offering high precision in capturing displacement and failure patterns across the entire wall surface. Building on insights from Chapter 4, the anisotropic walls are effectively modeled using the CDPM model. Through rigorous experimentation and detailed finite element simulations, this chapter offers valuable insights into the performance and limitations of 3DPC walls under lateral loading for design and construction practices in the field of 3DPC structures. By unlocking the secrets of lateral load resistance, Chapter 5 paves the way for a brighter future for this revolutionary building material.

Chapter 6 summarizes the key findings, contributions, and implications of the research. It serves as a synthesis of the entire thesis, providing a comprehensive understanding of the mechanical, physical, and structural aspects of 3DPC structures.

CHAPTER 2

CONTINUUM DAMAGE PLASTICITY MODEL FOR CONCRETE UNDER CYCLIC LOADING

2.1 Mechanical Behavior of Concrete

Concrete is the modern construction's primary material that demonstrates complicated mechanical behavior that is influenced by several variables such as composition, environmental exposure, and loading condition etc. Having a deep understanding of how concrete behaves mechanically is essential for designing structures that can withstand the demands of real-world applications.

Concrete is a composite material consisting of cement, aggregates, water, and admixtures. Its mechanical behavior encompasses a variety of properties, such as strength, stiffness, ductility, and durability. These properties are crucial in ensuring the structural integrity and safety of the built environment.

The mechanical behavior of concrete can be divided into three main phases: elastic, plastic, and damage. In the elastic phase, the material deforms reversibly, obeying Hooke's law when subjected to stress. As stress levels increase, concrete enters the plastic phase, where deformation becomes permanent. This phase involves yielding, strain hardening, and softening behavior.

Concrete is also susceptible to damage under different loading conditions, including micro-cracking, tensile stress-induced cracking, and failure due to factors like stress concentrations, defects, and material heterogeneity. Understanding and modeling these damage mechanisms are essential for accurately predicting the material's behavior under different conditions.

To elucidate concrete's intricate mechanical response, it is referred to a typical stress-strain curve (Figure 2.1) under monotonic and cyclic compression loading, which clearly illustrates its behavior.

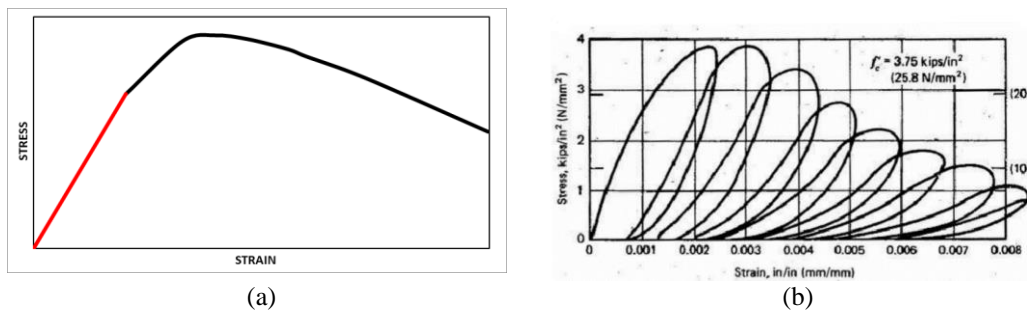


Figure 2.1. The Stress-Strain Curves Describing the Behavior of a Concrete Under (a) Monotonic and (b) Cyclic Compressive Loading [35]

Figure 2.1-a portrays concrete's initial linear elastic phase represented by red line, followed by nonlinearity represented by black line, indicative of plastic deformation. This phase starts with yielding, followed by strain hardening, where the material can carry additional load with increasing strain. Beyond a certain point, the peak stress, the material starts to soften, indicating a decline in its load-carrying capacity.

Under cyclic loading (Figure 2.1-b), concrete often exhibits a notable phenomenon known as stiffness degradation. This phenomenon is a consequence of the progressive damage that concrete undergoes as it is subjected to repeated loading cycles. Stiffness degradation represents a reduction in the material's ability to deform elastically in response to applied stress over time. Stiffness degradation manifests as a decrease in the slope of the stress-strain curve during subsequent loading cycles. In other words, as concrete is subjected to more cycles of loading and unloading, it gradually becomes less stiff and more compliant. This effect is particularly pronounced in concrete structures subjected to dynamic or cyclic forces, such as those experienced during earthquakes or repeated traffic loads.

2.2 Literature Review

Modeling crack initiation and propagation is crucial in analyzing concrete structure failures. Unlike metals or glass, concrete cracking involves a continuous development of microcracks, leading to material softening, hardening, and stiffness

degradation [36]. In cracked concrete, various stress and strain states coexist, necessitating a model capable of representing this complexity.

The literature is replete with various studies exploring constitutive theories relevant to concrete. These studies have been meticulously reviewed in the literature [37–39]. In this section, it will be discussed that how concrete modeling has evolved over time, leading up to the Lee and Fenves & Barcelona model [40,41]. Furthermore, other significant advancements in the field will also be discussed.

A range of approaches will be examined in understanding concrete behavior, progressing from linear elastic models to more sophisticated frameworks. In linear elastic models [42,43], concrete is considered to behave in a linearly elastic manner until it reaches its ultimate strength, at which point it experiences brittle failure. When dealing with concrete subjected to tension, where the failure strength is relatively low, the linear elastic model is accurate and satisfactory for predicting concrete behavior until the point of failure. However, the straightforward linear elastic constitutive law is frequently unsuitable for concrete because it belongs to the category of pressure-sensitive materials, exhibiting a nonlinear and inelastic overall response when subjected to external loads. Additionally, when loading conditions are reversed, these models are inadequate for predicting concrete behavior. By considering hyperelastic and hypoelastic models [44], the laws of thermodynamics can be violated due to the generation of energy during specific load cycles.

Additionally, Fracture Mechanics of concrete [45] and linear elastic fracture mechanics have become a valuable tool for understanding how cracks initiate and propagate in concrete structures. By examining factors like stress intensity and critical crack tip displacement, fracture mechanics helps characterize concrete's fracture behavior, particularly in brittle failure scenarios.

Plasticity-based models offer a significant advancement beyond linear elastic models in understanding concrete behavior. These models consider the material's ability to undergo plastic deformation before reaching failure. In concrete, plasticity arises due to complex interactions at the microstructural level, micro-cracking and slip. This

behavior can be modeled by classical plasticity approach [46,47]. However, it is difficult to represent the stiffness degradation and softening behaviors of concrete by using classical plasticity theory. In the classical plasticity theory, the fundamental principles encompass an elastic stress-strain relationship, hardening laws, a flow rule, a yield surface, loading-unloading conditions, and a consistency condition. The more details related to these conditions can be found in many books [48,49]. The use of a non-associative flow rule is essential for controlling dilatancy when modeling frictional granular materials like concrete [50], which means plastic potential function needs to be defined to the problem. The plastic potential function governs the flow direction independent of the yield criterion function. A classical model of non-associative plasticity is the Drucker-Prager model where the yield threshold depends on the pressure. In the Drucker-Prager model, the originally cylindrical yield surface of the von Mises model transforms into a conical shape. This conical yield surface expands in diameter, or hardens, as pressure increases. This adjustment accounts for the influence of pressure-induced confinement on the movement of particles within a frictional granular material. In the literature, various forms of plastic potential functions have been explored and used, including those in the Drucker-Prager type [51,52] and Mohr-Coulomb type [53,54]. In concrete plasticity, the yield surfaces are mostly expressed in terms of stress invariants due to isotropic behavior of concrete. The yield surfaces of concrete plasticity are categorized based on the number of material parameters, a classification introduced by Chen and Han [50]. It's crucial to consider the impact of hydrostatic pressure on the yield surface because concrete behaves uniquely when compared to materials like metals or glass. Unlike pure hydrostatic loading, concrete's ability to withstand shear stress increases under the influence of hydrostatic pressure. Initially, early finite element analysis used one-parameter models like the von Mises model for concrete. However, they had limitations in adequately representing tensile behavior. To address this, two-parameter models such as Drucker-Prager and Mohr-Coulomb were introduced to better capture concrete's nonlinear stress-strain relationship. Ottosen [55] proposed a four-parameter failure surface, allowing for a closer match to experimental data.

This model included an initial closed yield surface and a transition to a failure surface using a hardening rule. While increasing the number of model parameters provides more flexibility, it also complicates the calibration process, often necessitating extensive material response data that may not be readily available. For practical applications, Lubliner's plastic-damage model (also known as Barcelona model) [41], as modified by Lee and Fenves [40,56], aligns well with experimental data when excluding the high-pressure region from the yield surface definition.

On the other hand, stiffness degradation behavior of concrete can be modeled with plastic-damage based approaches. Stiffness degradation as a consequence of the microcracking process, becomes noticeable in cyclic loading cases. One approach by Ju, as presented in Ju's work in [57], relies on the principles of continuum damage mechanics and plasticity. This model incorporates two types of damage: one related to stiffness degradation and the other connected to plastic strain associated with the effective stress, both aimed at simulating the behavior of a cracked material. While this model can be implemented using a straightforward decoupled numerical algorithm, calibrating it with experimental data can be challenging due to the definition of the plastic component within the effective stress space rather than directly within the stress space itself. In contrast, the Barcelona model, as detailed in works by [41,58], provides an effective approach for modeling general concrete behavior. This model incorporates a well-defined damage variable, particularly suitable for capturing the failure process of brittle materials, and it allows for relatively straightforward calibration using experimental data. Additionally, the yield function within this model can accurately represent concrete's actual failure surfaces. However, it's worth noting that the coupled relation between the degradation variables and plastic strain can introduce complexity and numerical instability in the simulation process, as discussed by [40]. Lee and Fenves [40] introduced a plastic damage model featuring two damage variables, one for representing tensile damage and the other for compressive damage states. They made adjustments to the yield function of the Barcelona model to incorporate these two damage variables. Importantly, this model decouples the degradation due to damage

and the elastoplastic response in its constitutive relations. In this model, the reduced elastic stiffness remains isotropic. Still, the plastic damage aspect allows for the independent evolution of tensile and compressive strengths, and it takes into account the directionality of damage caused by plastic strains. Also, this model uses the stiffness recovery approach as well. The reason is that if cyclic loading occurs within the range spanning from tensile to compressive conditions, there is also a noticeable recovery of reduced stiffness observed when unloading from the tensile region back to the compressive region [59].

In addition to the concrete modeling methods mentioned earlier, it's important to recognize the significance of the microplane model [60–65]. This model provides a comprehensive framework for capturing the intricate behavior of concrete by considering multiple planes of failure. It's highly regarded for its ability to account for the complex interaction between concrete's microstructure and its macroscopic behavior. In contrast to other constitutive models that describe material behavior using second-order tensors, the microplane model represents it in stress and strain vectors. The overall stress and strain tensors at a macroscopic level are derived by summing up these vectors on multiple planes of different orientations (microplanes). This calculation is based on the assumption of static or kinematic constraint. To prevent unstable strain localization (spurious mesh sensitivity in finite element calculations), it is essential to couple this model with a nonlocal continuum formulation, such as the crack band model. Earlier, these benefits were outweighed by the higher computational requirements of the material subroutine because it requires significant computational effort and storage capacity. However, with the substantial increase in computing power, the microplane model is now commonly integrated into computer programs.

Furthermore, the field of concrete modeling encompasses several other noteworthy approaches. One such method is Plastic-Fracturing Modeling, which combines plasticity with fracture mechanics to depict how concrete behaves under both compressive and tensile loading conditions. This approach is especially valuable for predicting how concrete responds to different stress states.

Furthermore, the Endochronic Theory of Plasticity [66–68], an advanced concept in material modeling, provides a systematic framework for simulating time-dependent behaviors like creep and relaxation in concrete structures. The endochronic model effectively captures inelastic behaviors like volume dilatancy, unloading, strain softening, hydrostatic pressure sensitivity, and cyclic loading effects. Despite its superior performance, its complexity has limited its popularity. It requires numerous numerical coefficients estimated through curve fitting to experimental data, which makes it cumbersome to apply.

In the pursuit of a comprehensive analysis of concrete behavior, the Concrete Damage Plasticity Model, as formulated by Lee and Fenves [40], stands as a pivotal component of this study. This model, readily available in the Abaqus software, forms the bedrock of analysis in this thesis, albeit with a slight modification is observed to prevent encountering a singular point at the highest point of the potential surface [69].

In order to ensure the accuracy and reliability of the analysis, a critical step involved the development of a User Material (UMAT) subroutine. This UMAT, provided in APPENDICES-A and B, was meticulously crafted to adapt the CDPM model for use in both Abaqus and FEAP (Finite Element Analysis Program). The aim was twofold: to validate the Concrete Damage Plasticity Model implementation in Abaqus and to ensure consistency across both software platforms.

2.3 Constitutive Theory for Continuum Damage Plasticity Model

In this section, the foundational principles of the CDPM will be explored. Developed by Lee and Fenves, this model plays a pivotal role in capturing the intricate mechanical behavior of concrete structures. The model is restricted to the small deformation theory of plasticity, because the utilization of small strains is deemed appropriate, aligning with the mechanical behavior of concrete.

In the theory, total strain tensor, ε , is decomposed into two strain tensors: elastic strain, ε^e , and plastic strain, ε^p . The total strain tensor represents the external variable, while the elastic strain tensor is the recoverable part of the total strain that obeys the Hooke's law, and the plastic strain tensor, which is a symmetric internal variable, remains constant during unloading. The relation is given as follows:

$$\varepsilon = \varepsilon^e + \varepsilon^p \quad (2.1)$$

The stress-strain relationship is given as follows:

$$\sigma = \mathbb{C} : \varepsilon^e = \mathbb{C} : (\varepsilon - \varepsilon^p) \quad (2.2)$$

Also, the strain tensors can be divided into the deviatoric and the volumetric part:

$$\varepsilon = \varepsilon' + \frac{tr(\varepsilon)}{3} \mathbf{1} \quad (2.3)$$

where \mathbb{C} is the fourth order elastic stiffness tensor, ε' is deviatoric strain and $\mathbf{1}$ denotes the second order identity tensor. I can be written as $\varepsilon' = \varepsilon'^e + \varepsilon'^p$ and $tr(\varepsilon) = tr(\varepsilon^e) + tr(\varepsilon^p)$.

For the isotropic homogeneous material, the stress tensor is obtained the following representation:

$$\sigma = 2G_0(\varepsilon' - \varepsilon'^p) + K_0(tr(\varepsilon) - tr(\varepsilon^p)) \quad (2.4)$$

where G_0 and K_0 are called the shear modulus and the bulk modulus respectively.

2.3.1 Plastic-Damage Model

In the plastic damage model, the effective stress concept is used to define damage. In this model, the effective stress, and the elastic stiffness can be written as:

$$\sigma = (1 - d)\bar{\sigma} \quad (2.5a)$$

$$\mathbb{C} = (1 - d)\mathbb{C}_0 \quad (2.5b)$$

$$\bar{\sigma} = \mathbb{C}_0 : (\varepsilon - \varepsilon^p) \quad (2.5c)$$

In equation (2.5), $\bar{\sigma}$ represents the effective stress, d represents stiffness degradation variable, and \mathbb{C}_0 represents the initial elastic stiffness tensor. In this model, stiffness degradation variable, d , is only dependent on a vector κ , damage variable:

$$d = d(\kappa) \quad (2.6)$$

the damage variable should satisfy the damage evolution rule, and it can be in the form of principle states donated by (\wedge):

$$\dot{\kappa} = h(\bar{\sigma}, \kappa): \varepsilon^p \quad (2.7a)$$

$$\dot{\kappa} = h(\widehat{\bar{\sigma}}, \kappa): \widehat{\varepsilon}^p \quad (2.7b)$$

and the flow rule should satisfy the Karush-Kuhn-Tucker (KKT) optimality conditions as follows:

$$\varepsilon^p = \lambda \frac{\partial G}{\partial \bar{\sigma}} = \lambda g \quad (2.8a)$$

$$\widehat{\varepsilon}^p = \lambda \frac{\partial G}{\partial \widehat{\bar{\sigma}}} = \lambda \widehat{g} \quad (2.8b)$$

where $\lambda \geq 0$, G is the scalar plastic potential function, and g is the directional vector which is derivative of G with respect to effective stress.

2.3.2 Evolution of Damage and Stiffness Degradation

Lubliner et al. [41] employ a single damage variable, representing a combination of both tensile and compressive damage, which is suitable for monotonic loading scenarios. However, to accommodate the varying behavior of concrete in tension and compression during cyclic loading, Lee and Fenves [40] introduced a two-variable approach, where one variable accounts for tension and the other for compression in the damage state.

$$\kappa = \begin{bmatrix} \kappa_t \\ \kappa_c \end{bmatrix} \quad (2.9)$$

Therefore, a state variable, \aleph , to consider a uniaxial tensile (t) or compressive (c) stress state is defined:

$$\aleph \in \{t, c\} \quad (2.10)$$

An analytically useful function, denoted as $f_{\aleph}(\kappa_{\aleph})$, can act as either tension state $f_t(\kappa_t)$ or compressive state $f_c(\kappa_c)$. It should align with the experimental observation that stress-strain curves tend to approach the zero-stress level asymptotically, rather than at a specific "ultimate strain". This function, $f_{\aleph}(\kappa_{\aleph})$, can be obtained from the $\sigma - \varepsilon^p$ relationship provided by [41]:

$$\sigma_{\aleph} = f_{\aleph}(\kappa_{\aleph}) \quad (2.11a)$$

$$\sigma_{\aleph} = f_{\aleph 0} [(1 + a_{\aleph})e^{-b_{\aleph}\varepsilon^p} - a_{\aleph}e^{-2b_{\aleph}\varepsilon^p}] \quad (2.11b)$$

where $f_{\aleph 0}$ is initial yield stress at the related state and, a_{\aleph} and b_{\aleph} are dimensionless constants. If a_{\aleph} is less than 1, it indicates a softening effect right after yielding (Figure 2.2-a), whereas if a_{\aleph} is greater than 1, it suggests an initial phase of hardening (Figure 2.2-b).

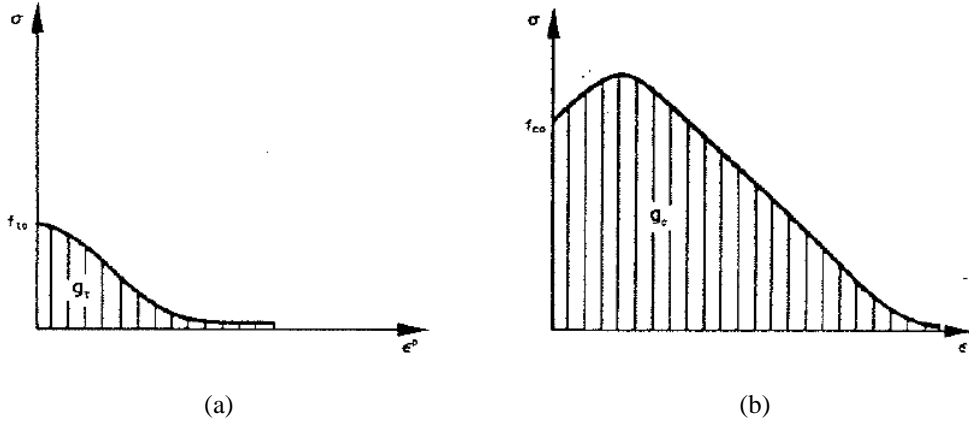


Figure 2.2. $\sigma - \varepsilon^p$ Relationship in (a) Tension, (b) Compression [41]

On the other hand, the degradation is assumed to be exponential as follow:

$$(1 - d_{\aleph}) = e^{-c_{\aleph}\varepsilon^p} \quad (2.12)$$

where c_{\aleph} is another dimensionless constant. As a result, the effective stress is obtained as follows:

$$\bar{\sigma}_N = \bar{f}_N(\kappa_N) \quad (2.13a)$$

$$\bar{\sigma}_N = f_{N0} \left[(1 + a_N)(e^{-b_N \varepsilon^p})^{1 - \frac{c_N}{b_N}} - a_N(e^{-b_N \varepsilon^p})^{2 - \frac{c_N}{b_N}} \right] \quad (2.13b)$$

Uniaxial version of damage variable, κ_N , is the area under $\sigma - \varepsilon^p$ curve in Figure 2.2. It is important to express stress and defined as:

$$\kappa_N = \frac{1}{g_N} \int_0^{\varepsilon^p} \sigma_N(\varepsilon^p) d\varepsilon^p \quad (2.14a)$$

$$g_N = \int_0^{\infty} \sigma_N(\varepsilon^p) d\varepsilon^p = \frac{f_{N0}}{b_N} \left(1 - \frac{a_N}{2} \right) \quad (2.14b, c)$$

where g_N is the dissipated strain energy density. By using equations (2.11) and (2.14a), the relationship between κ_N and ε^p is found as:

$$e^{-b\varepsilon^p} = \frac{1}{a_N} \left[(1 + a_N) - \sqrt{\phi_N(\kappa_N)} \right] \quad (2.15a)$$

$$\phi_N(\kappa_N) = 1 + a_N(2 + a_N)\kappa_N \quad (2.15b)$$

Substituting the equation (2.15) into equation (2.11), (2.13), and (2.12), the following representations for stress, effective stress and degradation variable is obtained:

$$\sigma_N = \frac{f_{N0}}{a_N} \left[(1 + a_N) \sqrt{\phi_N(\kappa_N)} - \phi_N(\kappa_N) \right] \quad (2.16a)$$

$$\bar{\sigma}_N = f_{N0} \left[\left(\frac{1}{a_N} \right) \left(1 + a_N - \sqrt{\phi_N(\kappa_N)} \right) \right]^{1 - \frac{c_N}{b_N}} \sqrt{\phi_N(\kappa_N)} \quad (2.16b)$$

$$d_N = 1 - \left[\left(\frac{1}{a_N} \right) \left(1 + a_N - \sqrt{\phi_N(\kappa_N)} \right) \right]^{\frac{c_N}{b_N}} \quad (2.16c)$$

A single degradation variable is defined by using equation (2.16c) in both tension and compression state as follows:

$$d = 1 - (1 - d_c(\kappa_c))(1 - d_t(\kappa_t)) \quad (2.17)$$

Microcracking is a recognized cause of this degradation. In cyclic loading conditions, the process of stiffness degradation becomes more intricate due to the opening and closing of microcracks. In the case of most quasi-brittle materials, like concrete, experimental findings indicate that the compressive stiffness is recovered when cracks closure during the transition from tension to compression loading. Conversely, the tensile stiffness does not recover as the load shifts from compression to tension, especially once crushing micro-cracks have formed. Therefore, stiffness recovery function, $s(\bar{\sigma})$, is defined to tension degradation variable of equation (2.17) as:

$$d = 1 - (1 - d_c(\kappa_c))(1 - s(\bar{\sigma})d_t(\kappa_t)) \quad (2.17a)$$

$$s(\bar{\sigma}) = s_0 + (1 - s_0)r(\hat{\sigma}) \quad (2.17b)$$

$$r(\hat{\sigma}) = \frac{1}{2} + \frac{I_1}{2(|\hat{\sigma}_1| + |\hat{\sigma}_2| + |\hat{\sigma}_3|)} \quad (2.17c)$$

Where, $\hat{\sigma}$ is the effective principal stress, $0 \leq s_0 \leq 1$ is a constant, $0 \leq r(\hat{\sigma}) \leq 1$ is a scalar weight factor, and I_1 is the first invariant of effective principal stress such that $I_1 = (\hat{\sigma})$. When s_0 equals to 1, no stiffness recovery is defined to the material; on the contrary, when s_0 equals to 0, stiffness will be fully recovered during the change in load from tension to compression as presented in Figure 2.3.

As a result, the stress can be computed as follows:

$$\sigma = (1 - d_c(\kappa_c))(1 - s(\bar{\sigma})d_t(\kappa_t)) \bar{\sigma} \quad (2.18)$$

How to find the constants, a_{κ} , b_{κ} and c_{κ} , is detailed in [40,56].

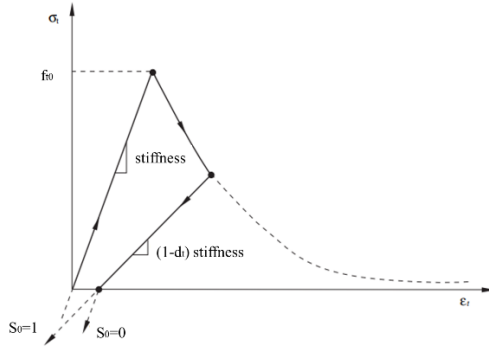


Figure 2.3. Stiffness Recovery Effect

It is known from equation (2.6) that d is a function of κ , damage evolution equation in its uniaxial state is written by using equations (2.14) and (2.16a) as:

$$\dot{\kappa}_{\kappa} = \frac{1}{g_{\kappa}} f_{\kappa}(\kappa_{\kappa}) \widehat{\varepsilon}_{1,3}^{\dot{p}} \quad (2.19a)$$

$$\widehat{\varepsilon}_{1,3}^{\dot{p}} = \begin{bmatrix} \widehat{\varepsilon}_1^{\dot{p}} \\ \widehat{\varepsilon}_3^{\dot{p}} \end{bmatrix} \quad (2.19b)$$

where $\widehat{\varepsilon}_1^{\dot{p}}$ and $\widehat{\varepsilon}_3^{\dot{p}}$ are maximum and minimum eigenvalues of plastic strain rate, respectively. Using equations (2.7), (2.8), and (2.19), following equations, essential to find damage evolution, are obtained:

$$\dot{\kappa} = H(\widehat{\sigma}, \kappa): \lambda \quad (2.20a)$$

$$H = h: \widehat{g} \quad (2.20b)$$

Where h is defined as:

$$h = \begin{bmatrix} \frac{r(\widehat{\sigma})}{g_t} f_t(\kappa_t) & 0 & 0 \\ 0 & 0 & -\frac{(1-r(\widehat{\sigma}))}{g_c} f_c(\kappa_c) \end{bmatrix} \quad (2.21)$$

2.3.3 Flow Rule and Yield Function

To model frictional granular materials like concrete, non-associative flow rule is used. For this reason, Drucker-Prager type plastic potential function, G , is adopted and g is found by using the relation in the equation (2.8) as follows:

$$G = \sqrt{2J_2} + \alpha_p I_1 = \|\sigma'\| + \alpha_p I_1 \quad (2.22a)$$

$$g = \frac{\sigma'}{\|\sigma'\|} + \alpha_p \mathbf{1} \quad (2.22b)$$

where σ' is the deviatoric part of the stress, $\|\sigma'\|$ is norm of the deviatoric stress, α_p is the dilatancy, $J_2 = \frac{1}{2}\sigma':\sigma'$, $I_1 = tr(\sigma)$, and $\mathbf{1}$ is the second order identity tensor. As a result, the plastic strain rate is found as follows by using equations (2.8) and (2.22):

$$\dot{\varepsilon}^p = \lambda \left(\frac{\bar{\sigma}'}{\|\bar{\sigma}'\|} + \alpha_p \mathbf{1} \right) \quad (2.23)$$

The yield function, $F(\sigma, \kappa)$, used in Lee and Fenves model [40] is modified version of the Barcelona model [41] as provided below:

$$F(\sigma, \kappa) = \frac{1}{1-\alpha} [\alpha I_1 + \sqrt{3J_2} + \beta(\kappa)\langle \hat{\sigma}_{max} \rangle] - c_c(\kappa) \quad (2.24a)$$

$$\alpha = \frac{f_{b0} - f_{c0}}{2f_{b0} - f_{c0}} \quad (2.24b)$$

$$\beta(\kappa) = \frac{c_c(\kappa_c)}{c_t(\kappa_t)} (1 - \alpha) - (1 + \alpha) \quad (2.24c)$$

where α is a dimensionless constant, the parameter β is and a function of κ , f_{b0} is the biaxial initial yielding compressive strength, $\hat{\sigma}_{max}$ is the maximum principle stress, and $\langle \hat{\sigma}_{max} \rangle = (|\hat{\sigma}_{max}| + \hat{\sigma}_{max})/2$ is the Macaulay bracket. On the other hand, $c_{\kappa}(\kappa_{\kappa})$ is the cohesion defined as follow:

$$c_c(\kappa_c) = \bar{f}_c(\kappa_c) \quad (2.25a)$$

$$c_t(\kappa_t) = \bar{f}_t(\kappa_t) \quad (2.25b)$$

The yield surface in plane stress space, octahedral plane, and meridian plane used in this model are shown in Figure 2.4.

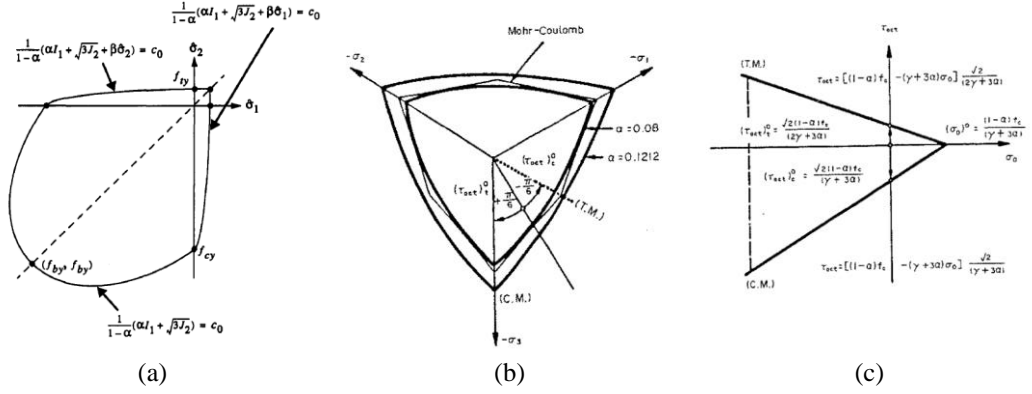


Figure 2.4. Lubliner Yield Function [41] in (a) Plane Stress Space, (b) Octahedral Plane, and (c) Meridian Plane

Derivative of the yield surface $F(\bar{\sigma}, \kappa)$ with respect to $\bar{\sigma}$ and κ are found by using the equations (2.24) and (2.25)

$$\frac{\partial}{\partial \bar{\sigma}} F(\bar{\sigma}, \kappa) = \frac{1}{1-\alpha} \left[\sqrt{\frac{3}{2}} \frac{\bar{\sigma}'}{\|\bar{\sigma}'\|} + \alpha \mathbf{1} + \beta H(\hat{\sigma}_{max}) \frac{\partial}{\partial \bar{\sigma}} \hat{\sigma}_{max} \right] \quad (2.26a)$$

$$\frac{\partial}{\partial \kappa} F(\bar{\sigma}, \kappa) = \begin{bmatrix} -\frac{c_c \langle \hat{\sigma}_{max} \rangle}{c_t^2} \frac{d\bar{f}_t}{d\kappa_t} \\ \left(\frac{\langle \hat{\sigma}_{max} \rangle}{c_t} - 1 \right) \frac{d\bar{f}_c}{d\kappa_c} \end{bmatrix} \quad (2.26b)$$

Where H is the Heaviside step function, and $\bar{\sigma}'$ is the deviatoric part of the effective stress.

In classical plasticity, the stress is required to be either within or on the yield function. Moreover, plastic loading is considered only when the stress lies on the yield function, while unloading is exclusively carried out elastically. These constraints are referred to as the loading/unloading conditions, and they are expressed through Karush-Kuhn-Tucker (KKT) optimality conditions as follows:

$$\lambda \geq 0 \quad (2.27a)$$

$$F(\bar{\sigma}, \kappa) \leq 0 \quad (2.27b)$$

$$\lambda F(\bar{\sigma}, \kappa) = 0 \quad (2.27c)$$

2.4 Numerical Implementation

This section provides a detailed examination of the numerical implementation of the CDPM, employing the Backward-Euler method. The Backward-Euler method, a renowned implicit numerical technique, stands out for its unconditional stability, making it a robust choice for simulating the complex mechanical behavior of concrete subjected to diverse loading conditions [49].

The Backward-Euler method's implicit nature offers distinct advantages, especially in handling nonlinear material behaviors. It ensures numerical stability throughout the simulation process, even when dealing with highly nonlinear responses. This section delves into the intricacies of the Backward-Euler scheme. Through the elucidation of the implicit and unconditionally stable characteristics of the Backward-Euler method, the pivotal role it plays in enhancing the understanding of concrete behavior and its capacity to deliver reliable results for the analysis is underscored.

In the context of this chapter, the notation, $\Delta x = x_{n+1} - x_n$, is commonly used. Also, the eigenvalue matrix notation represented by \hat{x} will be assumed to be employed to represent a column vector, with each element being arranged in magnitude order to correspond to the eigenvalues of x such as $\hat{\epsilon}_1 = \hat{\epsilon}_{max}$. Furthermore, owing to the column representation of the eigenvalues, a vector, $1^v = [1 \ 1 \ 1]^T$, is frequently employed in this chapter.

2.4.1 Stress Update Algorithm for Continuum Damage Plasticity

The extension of the radial return mapping scheme of elastoplasticity to include hardening/softening and damage effects is achieved by spectral decomposition of the

effective stress and incremental plastic strain tensors through the use of the implicit (backward) Euler scheme.

Utilizing equation (2.4), the effective stress at time step (n+1) is expressed as:

$$\bar{\sigma}_{n+1} = 2G_0(\varepsilon'_{n+1} - \varepsilon^{p'}_{n+1}) + K_0 tr(\varepsilon_{n+1} - \varepsilon^p_{n+1})\mathbf{1} \quad (2.28a)$$

$$\bar{\sigma}_{n+1} = \sigma_{n+1}^{tr} - (2G_0(\Delta\varepsilon^{p'}) + K_0 tr(\Delta\varepsilon^p)\mathbf{1}) \quad (2.28b)$$

$$\sigma_{n+1}^{tr} = 2G_0(\varepsilon'_{n+1} - \varepsilon^{p'}_n) + K_0 tr(\varepsilon_{n+1} - \varepsilon^p_n)\mathbf{1} \quad (2.28c)$$

where trial stress, σ_{n+1}^{tr} , is used for elastic predictor and the other terms in equation (2.28b) are used for plastic corrector.

On the other hand, the plastic strain at time step n+1 is given by using equations (2.8) and (2.23) as:

$$\Delta\varepsilon^p = \Delta\varepsilon^{p'} + \frac{1}{3} tr(\Delta\varepsilon^p)\mathbf{1} \quad (2.29a)$$

$$\Delta\varepsilon^{p'} = \Delta\lambda \frac{\bar{\sigma}'_{n+1}}{\|\bar{\sigma}'_{n+1}\|} \quad (2.29b)$$

$$tr(\Delta\varepsilon^p) = 3\Delta\lambda\alpha_p \quad (2.29c)$$

Insertion of equation (2.29) into equation (2.28) leads to

$$\frac{\bar{\sigma}'_{n+1}}{\|\bar{\sigma}'_{n+1}\|} = \frac{\sigma_{n+1}^{tr}}{\|\sigma_{n+1}^{tr}\|} \quad (2.30a)$$

$$\|\bar{\sigma}'_{n+1}\| = \|\sigma_{n+1}^{tr}\| - 2G_0\Delta\lambda \quad (2.30b)$$

$$\bar{I}_{1n+1} = I_{1n+1}^{tr} - 9K_0\Delta\lambda\alpha_p \quad (2.30c)$$

where \bar{I}_{1n+1} , and I_{1n+1}^{tr} are first invariants of the effective and trial stresses.

Considering the equations (2.28), (2.29), and (2.30), the effective stress can be rewritten as follows:

$$\bar{\sigma}_{n+1} = \sigma_{n+1}^{tr} - \Delta\lambda \left(2G_0 \frac{\sigma_{n+1}^{tr}}{\|\sigma_{n+1}^{tr}\|} + 3K_0\alpha_p\mathbf{1} \right) \quad (2.31)$$

2.4.2 Return-Mapping Algorithm and Spectral Decomposition

The proof and details of the following chapter is found in [56]. Through Karush-Kuhn-Tucker (KKT) optimality conditions, type of incremental loading based on trial condition is decided. The yield function serves as an indicator for the incremental loading as follow:

$$F(\sigma_{n+1}^{tr}, \kappa_n) = \begin{cases} \leq 0 & : \text{Elastic Loading/Unloading} \\ > 0 & : \text{Plastic Loading State} \end{cases} \quad (2.32)$$

where $F(\sigma_{n+1}^{tr}, \kappa_n)$ and $F(\bar{\sigma}_{n+1}, \kappa_{n+1})$ is redefined as:

$$F(\sigma_{n+1}^{tr}, \kappa_n) = \alpha I_{1n+1}^{tr} + \sqrt{\frac{3}{2}} \|\sigma'_{n+1}{}^{tr}\| + \beta(\kappa_n) \langle \hat{\sigma}_{n+1}^{tr} \rangle - (1 - \alpha)c_c(\kappa_n) \quad (2.33a)$$

$$F(\bar{\sigma}_{n+1}, \kappa_{n+1}) = \alpha \bar{I}_{1n+1} + \sqrt{\frac{3}{2}} \|\bar{\sigma}'_{n+1}\| + \beta(\kappa_{n+1}) \langle \hat{\bar{\sigma}}_{n+1} \rangle - (1 - \alpha)c_c(\kappa_{n+1}) \quad (2.33b)$$

If the elastic loading/unloading state is the current state in equation (2.32), the trial stress is considered admissible and accepted as the current effective stress for the given strain. This leads to the following results:

$$\lambda = 0 \quad (2.34a)$$

$$\bar{\sigma}_{n+1} = \sigma_{n+1}^{tr} \quad (2.34b)$$

$$\kappa_{n+1} = \kappa_n \quad (2.34c)$$

$$\varepsilon_{n+1}^p = \varepsilon_n^p \quad (2.34d)$$

It is important to note that, the degradation variable may not belong to the previous time step, because the degradation variable depends on stiffness recovery function, $s(\bar{\sigma})$. As it is shown in the Figure 2.3, the elastic stiffness can change even in the elastic step. Therefore, the degradation variable is calculated by using equation (2.17) even in the elastic step.

On the other hand, if the plastic loading state is the current state in equation (2.32), plastic corrector calculation is required. Therefore, iterations are performed for both the stress and the damage variable, at the plastic corrector step. Throughout these iterations, the plastic consistency condition is applied as a constraint,

$F(\bar{\sigma}_{n+1}, \kappa_{n+1}) = 0$. The additional constraint arises from the damage evolution equation, represented by equation (2.20), for which a discrete version is obtained using the backward-Euler method:

$$\Delta\kappa = H(\hat{\sigma}_{n+1}, \kappa_{n+1})\Delta\lambda \quad (2.35)$$

The details in spectral decomposition of decoupled version of the return-mapping algorithm is stated in [56]. It is worth noting that the non-singular orthonormal eigenvector matrix, Q , is applicable to both $\bar{\sigma}_{n+1}$ and σ_{n+1}^{tr} , as demonstrated by the following:

$$\bar{\sigma}_{n+1} = Q_{n+1}\hat{\sigma}_{n+1}Q_{n+1}^T \quad (2.36a)$$

$$\sigma_{n+1}^{tr} = Q_{n+1}\hat{\sigma}_{n+1}^{tr}Q_{n+1}^T \quad (2.36b)$$

where $\hat{\sigma}_{n+1}$ and $\hat{\sigma}_{n+1}^{tr}$ are the diagonal eigenvalue matrixes of $\bar{\sigma}_{n+1}$ and σ_{n+1}^{tr} , respectively. By taking equations (2.31) and (2.36) into consideration, it can be written that:

$$\hat{\sigma}_{n+1} = \hat{\sigma}_{n+1}^{tr} - \Delta\lambda \left(2G_0 \frac{\hat{\sigma}'_{n+1}{}^{tr}}{\|\hat{\sigma}'_{n+1}{}^{tr}\|} + 3K_0\alpha_p 1^\nu \right) \quad (2.37)$$

By using equation (2.29), eigenvalues of incremental plastic strain are found as:

$$\Delta\hat{\varepsilon}^p = \Delta\lambda \left(\frac{\hat{\sigma}'_{n+1}{}^{tr}}{\|\hat{\sigma}'_{n+1}{}^{tr}\|} + \alpha_p 1^\nu \right) \quad (2.38)$$

2.4.3 Linearizing the Equations Governing Damage Evolution

The evaluation of the damage variable κ is performed through the nonlinear function provided in the evolution law, equation (2.35), which is dependent on $\hat{\sigma}$, κ , and λ . The discrete form of the damage evolution equation, equation (2.35), is then expressed as follows:

$$\kappa_{n+1} = \Delta\lambda H(\hat{\sigma}_{n+1}, \kappa_{n+1}) + \kappa_n \quad (2.39)$$

Due to the non-linear dependence of κ_{n+1} on itself, an iterative approach is necessary to determine κ_{n+1} . The Newton-Raphson method is utilized for this purpose. The residual, R , is defined as follows:

$$R(\kappa_{n+1}, \hat{\sigma}_{n+1}, \Delta\lambda) = \Delta\lambda H(\hat{\sigma}_{n+1}, \kappa_{n+1}) + \kappa_n - \kappa_{n+1} \quad (2.40)$$

In the iterative process, the newly updated κ_{n+1} is denoted as κ_{n+1}^{new} , while the other from previous step is referred to as κ_{n+1}^{old} . The updating procedure is outlined as follows:

$$\kappa_{n+1}^{new} = \kappa_{n+1}^{old} - \left(\left. \frac{dR}{d\kappa_{n+1}} \right|_{\kappa_{n+1}^{old}} \right)^{-1} R(\kappa_{n+1}^{old}, \hat{\sigma}_{n+1}, \Delta\lambda) \quad (2.41)$$

In the initial stage, κ_{n+1}^{old} is set equal to κ_n , $\hat{\sigma}_{n+1}$ initialized as $\hat{\sigma}_{n+1}^{tr}$. Subsequently, κ_{n+1}^{old} is updated to κ_{n+1}^{new} at the outset of next iteration. The iteration process for κ_{n+1}^{new} continues until $R \leq TOLERANCE$ is met. Ultimately, κ_{n+1} is determined as κ_{n+1}^{new} .

Total differential of the residual, $\frac{dR}{d\kappa_{n+1}}$:

$$\frac{dR}{d\kappa_{n+1}} = \frac{\partial R}{\partial \kappa_{n+1}} + \frac{\partial R}{\partial \hat{\sigma}_{n+1}} \frac{d\hat{\sigma}_{n+1}}{d\Delta\lambda} \frac{d\Delta\lambda}{d\kappa_{n+1}} + \frac{\partial R}{\partial \Delta\lambda} \frac{d\Delta\lambda}{d\kappa_{n+1}} \quad (2.42a)$$

$$\frac{\partial R}{\partial \kappa_{n+1}} = \Delta\lambda \frac{\partial H}{\partial \kappa_{n+1}} - \mathbf{1} \quad (2.42b)$$

$$\frac{\partial R}{\partial \hat{\sigma}_{n+1}} = \Delta\lambda \frac{\partial H}{\partial \hat{\sigma}_{n+1}} \quad (2.42c)$$

$$\frac{\partial R}{\partial \Delta\lambda} = H \quad (2.42d)$$

The equation (2.42) is rewritten in indicial notation as:

$$\frac{dR_i}{d\kappa_j} = -\delta_{ij} + \Delta\lambda \frac{\partial H_i}{\partial \kappa_j} + \Delta\lambda \frac{\partial H_i}{\partial \hat{\sigma}_k} \frac{d\hat{\sigma}_k}{d\Delta\lambda} \frac{d\Delta\lambda}{d\kappa_j} + H_i \frac{d\Delta\lambda}{d\kappa_j} \quad (2.43)$$

where $i=2, j=2$ and $k=3$, with δ_{ij} representing the Kronecker's Delta. From this point onward until the end of this section, the terms within Equation (2.43) will be defined.

In the plastic step, equation (2.33b), the yield function, $F(\bar{\sigma}_{n+1}, \kappa_{n+1})$, is set equal to zero. In that case, $\Delta\lambda$ is calculated by inserting equations (2.30) and (2.37) into (2.33b):

$$\Delta\lambda = \frac{\alpha I_{1n+1}^{tr} + \sqrt{\frac{3}{2}} \|\sigma'_{n+1}^{tr}\| + \bar{\beta}(\hat{\sigma}_{n+1}^{tr}) - (1 - \alpha)c_c(\kappa_{n+1})}{9K_0\alpha_p\alpha + \sqrt{6}G_0 + \bar{\beta} \left[\frac{2G_0}{\|\sigma'_{n+1}^{tr}\|} \hat{\sigma}_{n+1}^{tr} - \frac{2G_0 I_{1n+1}^{tr}}{3\|\sigma'_{n+1}^{tr}\|} + 3K_0\alpha_p \right]} \quad (2.44a)$$

$$\bar{\beta} = \begin{cases} \beta(\kappa_{n+1}) & \text{if } \hat{\sigma}_{n+1}^{tr} < 0 \\ 0 & \text{if otherwise} \end{cases} \quad (2.44b)$$

$$\hat{\sigma}_{n+1}^{tr} = \hat{\sigma}_{n+1}^{tr} - \Delta\lambda \left[\frac{2G_0}{\|\sigma'_{n+1}^{tr}\|} \hat{\sigma}_{n+1}^{tr} - \frac{2G_0 I_{1n+1}^{tr}}{3\|\sigma'_{n+1}^{tr}\|} + 3K_0\alpha_p \right] \quad (2.44c)$$

The expression for $\frac{\partial H_i}{\partial \kappa_j}$ in the equation (2.43) can be determined by utilizing the equations (2.9), (2.20b), (2.21), and (2.22b) in the following manner:

$$\hat{g} = \frac{\hat{\sigma}_{n+1}}{\|\hat{\sigma}_{n+1}\|} + \alpha_p 1^v \quad (2.45a)$$

$$H = \begin{bmatrix} \frac{r(\hat{\sigma}_{n+1})}{g_t} f_t(\kappa_{n+1_t}) \hat{g}_1 \\ -\frac{1 - r(\hat{\sigma}_{n+1})}{g_c} f_c(\kappa_{n+1_c}) \hat{g}_3 \end{bmatrix} \quad (2.45b)$$

$$\frac{\partial H}{\partial \kappa_{n+1}} = \begin{bmatrix} \frac{r(\hat{\sigma}_{n+1})}{g_t} \hat{g}_1 \left(\frac{\partial f_t(\kappa_{n+1_t})}{\partial \kappa_{n+1_t}} \right) & 0 \\ 0 & -\frac{1 - r(\hat{\sigma}_{n+1})}{g_c} \hat{g}_3 \left(\frac{\partial f_c(\kappa_{n+1_c})}{\partial \kappa_{n+1_c}} \right) \end{bmatrix} \quad (2.45c)$$

The derivatives $\frac{\partial f_{\mathbb{N}}(\kappa_{n+1_{\mathbb{N}}})}{\partial \kappa_{n+1_{\mathbb{N}}}}$ are computed using the equation (2.13). When considering the expression $\frac{\partial H_i}{\partial \hat{\sigma}_k}$, it can be expanded utilizing equation (2.20b) and expressed in indicial notation as follows:

$$\frac{\partial H_i}{\partial \hat{\sigma}_k} = \frac{\partial h_{ij} \hat{g}_j}{\partial \hat{\sigma}_k} = \frac{\partial h_{ij}}{\partial \hat{\sigma}_k} \hat{g}_j + h_{ij} \frac{\partial \hat{g}_j}{\partial \hat{\sigma}_k} \quad (2.46a)$$

$$= h'_{ijk} \hat{g}_j + h_{ij} \hat{g}'_{jk} \quad (2.46b)$$

The calculation of $\frac{\partial H_i}{\partial \hat{\sigma}_k}$ in the equation (2.46) can be determined by applying the equations (2.17c), (2.21) and (2.45a) as follows:

$$\frac{\partial h_{ij}}{\partial \hat{\sigma}_k} = h'_{ijk} = \left[\begin{array}{ccc} \left[\begin{array}{c} \frac{f_t}{g_t} \frac{\partial r(\hat{\sigma})}{\partial \hat{\sigma}} \end{array} \right]_k & \begin{bmatrix} 0 \\ 0 \\ 0 \end{bmatrix}_k & \begin{bmatrix} 0 \\ 0 \\ 0 \end{bmatrix}_k \\ \begin{bmatrix} 0 \\ 0 \\ 0 \end{bmatrix}_k & \begin{bmatrix} 0 \\ 0 \\ 0 \end{bmatrix}_k & \left[\begin{array}{c} \frac{f_c}{g_c} \frac{\partial r(\hat{\sigma})}{\partial \hat{\sigma}} \end{array} \right]_k \end{array} \right]_{ij} \quad (2.47a)$$

$$\frac{\partial r(\hat{\sigma})}{\partial \hat{\sigma}_k} = \frac{|\hat{\sigma}_k|(\sum_{\alpha}^3 |\hat{\sigma}_{\alpha}| - |\hat{\sigma}_k|) - \hat{\sigma}_k(\hat{I}_1 - \hat{\sigma}_k)}{2|\hat{\sigma}_k|(\sum_{\alpha}^3 |\hat{\sigma}_{\alpha}|)^2} \quad (2.47b)$$

$$\frac{\partial \hat{g}_j}{\partial \hat{\sigma}_k} = \|\hat{\sigma}'\|^{-1} \left(\mathbf{1} - \frac{\hat{\sigma}'}{\|\hat{\sigma}'\|} \otimes \frac{\hat{\sigma}'}{\|\hat{\sigma}'\|} \right)_{jm} \left(\mathbf{1} - \frac{1}{3} \mathbf{1}^{\nu} \otimes \mathbf{1}^{\nu} \right)_{mk} \quad (2.47c)$$

The calculation of $\frac{d\hat{\sigma}_k}{d\Delta\lambda}$ in the equation (2.46) can be achieved by utilizing the equation (2.38) as follows:

$$\frac{d\hat{\sigma}_k}{d\Delta\lambda} = -2G_0 \frac{\hat{\sigma}'^{tr}_k}{\|\hat{\sigma}'\|} - 3K_0 \alpha_p \mathbf{1}_k^{\nu} \quad (2.48)$$

$\frac{d\Delta\lambda}{d\kappa_j}$ is obtained from the plastic consistency condition, $F(\bar{\sigma}_{n+1}, \kappa_{n+1}) = 0$. Given that only the principal values of the effective stress are required, equation (2.33b) for the yield function can be reformulated into another form as $F(\bar{\sigma}, \kappa) = \hat{F}(\hat{\sigma}, \kappa)$. Applying chain rule to $\hat{F}(\hat{\sigma}, \kappa)$ results in:

$$\frac{\partial \hat{F}}{\partial \hat{\sigma}_k} \frac{d\hat{\sigma}_k}{d\Delta\lambda} d\Delta\lambda + \frac{\partial \hat{F}}{\partial \kappa_j} d\kappa_j = 0 \quad (2.49a)$$

$$\frac{d\Delta\lambda}{d\kappa_j} = - \frac{\frac{\partial \hat{F}}{\partial \kappa_j}}{\frac{\partial \hat{F}}{\partial \hat{\sigma}_k} \frac{\partial \hat{\sigma}_k}{\partial \Delta\lambda}} \quad (2.49b)$$

The equation (2.49b) is computed by employing equations (2.26a) and (2.26b). In the final step, degradation variables and stress are calculated. The degradation variables are determined using the equations (2.16c), (2.17) as follows:

$$d_{n+1_t} = 1 - \left[\left(\frac{1}{a_t} \right) \left(1 + a_t - \sqrt{\phi_t(\kappa_{n+1_t})} \right) \right]^{\frac{c_t}{b_t}} \quad (2.50a)$$

$$d_{n+1_c} = 1 - \left[\left(\frac{1}{a_c} \right) \left(1 + a_c - \sqrt{\phi_c(\kappa_{n+1_c})} \right) \right]^{\frac{c_c}{b_c}} \quad (2.50b)$$

$$d_{n+1} = 1 - (1 - d_{n+1_c})(1 - s(\bar{\sigma})d_{n+1_t}) \quad (2.50c)$$

The stress and plastic strain are computed using the equations (2.5a), (2.23), (2.36a), and (2.51c) as follows:

$$\varepsilon_{n+1}^p = \varepsilon_n^p + \Delta\varepsilon^p \quad (2.51a)$$

$$\Delta\varepsilon^p = \Delta\lambda \left(\frac{\sigma'_{n+1}{}^{tr}}{\|\sigma'_{n+1}{}^{tr}\|} + \alpha_p \mathbf{1} \right) \quad (2.51b)$$

$$\sigma_{n+1} = (1 - d_{n+1})Q_{n+1}\hat{\sigma}_{n+1}Q_{n+1}^T \quad (2.51c)$$

2.4.4 Summary of Update Algorithm for CDPM

In this section, a concise summary of the update algorithm utilized for the CDPM. This summary is intended to provide a structured overview of the key components and steps of the algorithm previously discussed, with the aim of enhancing clarity and facilitating a deeper understanding of its intricate workings.

Step 1 (Initialization of Given Parameters and Historical Variables):

- Given Parameters: ε_{n+1}
- History variable: $\varepsilon_n^p, \kappa_n, d_{n_t}, d_{n_c}$

Step 2 (Find the trial stresses and trial yield surface):

- $\sigma_{n+1}^{tr} = 2G_0(\varepsilon'_{n+1} - \varepsilon^{p'}_n) + K_0 tr(\varepsilon_{n+1} - \varepsilon_n^p) \mathbf{1}$
- $\hat{\sigma}_{n+1}^{tr} = Q_{n+1}^T \sigma_{n+1}^{tr} Q_{n+1}$ (store in vector format)
- $F(\sigma_{n+1}^{tr}, \kappa_n) = \alpha I_{1_{n+1}}^{tr} + \sqrt{\frac{3}{2}} \|\sigma'_{n+1}{}^{tr}\| + \beta(\kappa_n) \langle \hat{\sigma}_{n+1}^{tr} \rangle_{max} - (1 - \alpha)c_c(\kappa_n)$

Step 3 (Elastic step):

- If $F(\sigma_{n+1}^{tr}, \kappa_n) \leq 0$,

Step 3.1 (Calculate degradation, stress, and update history):

- $d_{n+1} = 1 - (1 - d_{n+1c})(1 - s(\bar{\sigma})d_{n+1t})$
- $\sigma_{n+1} = (1 - d_{n+1})\sigma_{n+1}^{tr}$
- $\varepsilon_{n+1}^p = \varepsilon_n^p; \kappa_{n+1} = \kappa_n; d_{n+1c} = d_{nc}; d_{n+1t} = d_{nt}$

Step 4 (Plastic step, $F(\sigma_{n+1}^{tr}, \kappa_n) > 0$):

- Else

Step 4.1 (Initializing Values):

- $\bar{\sigma}_{n+1} = \sigma_{n+1}^{tr}; \hat{\sigma}_{n+1} = \hat{\sigma}_{n+1}^{tr}; \kappa_{n+1} = \kappa_n; \varepsilon_{n+1}^p = \varepsilon_n^p$

Step 4.2 (find $\Delta\lambda$ and $\hat{\sigma}_{n+1}$):

- $$\Delta\lambda = \frac{\alpha I_{1n+1}^{tr} + \sqrt{\frac{3}{2}} \|\sigma'_{n+1}^{tr}\| + \bar{\beta}(\hat{\sigma}_{n+1max}^{tr}) - (1-\alpha)c_c(\kappa_{n+1})}{9K_0\alpha_p\alpha + \sqrt{6}G_0 + \bar{\beta} \left[\frac{2G_0}{\|\sigma'_{n+1}^{tr}\|} \hat{\sigma}_{n+1max}^{tr} - \frac{2G_0 I_{1n+1}^{tr}}{3\|\sigma'_{n+1}^{tr}\|} + 3K_0\alpha_p \right]}$$
- $$\hat{\sigma}_{n+1} = \hat{\sigma}_{n+1}^{tr} - \Delta\lambda \left(2G_0 \frac{\hat{\sigma}_{n+1}^{tr}}{\|\hat{\sigma}_{n+1}^{tr}\|} + 3K_0\alpha_p 1^v \right)$$

Step 4.3 (Compute the residual, $R(\kappa_{n+1}, \hat{\sigma}_{n+1}, \Delta\lambda)$, and $\left. \frac{dR}{d\kappa_{n+1}} \right|_{\kappa_{n+1}}$):

- $R(\kappa_{n+1}, \hat{\sigma}_{n+1}, \Delta\lambda) = \Delta\lambda H(\hat{\sigma}_{n+1}, \kappa_{n+1}) + \kappa_n - \kappa_{n+1}$
- $\frac{dR}{d\kappa_{n+1}} = \frac{\partial R}{\partial \kappa_{n+1}} + \frac{\partial R}{\partial \hat{\sigma}_{n+1}} \frac{d\hat{\sigma}_{n+1}}{d\Delta\lambda} \frac{d\Delta\lambda}{d\kappa_{n+1}} + \frac{\partial R}{\partial \Delta\lambda} \frac{d\Delta\lambda}{d\kappa_{n+1}}$

Step 4.4 (check the convergence):

Step 4.4.1 (if $R > TOLERANCE$):

- if $R > TOLERANCE$
- $$\kappa_{n+1} = \kappa_{n+1} - \left(\left. \frac{dR}{d\kappa_{n+1}} \right|_{\kappa_{n+1}} \right)^{-1} R(\kappa_{n+1}, \hat{\sigma}_{n+1}, \Delta\lambda)$$

- Go to step 4.2

Step 4.4.2

- End If

Step 4.5 (update history variables and compute stresses):

- $d_{n+1_t} = 1 - \left[\left(\frac{1}{a_t} \right) \left(1 + a_t - \sqrt{\phi_t(\kappa_{n+1_t})} \right) \right]^{\frac{c_t}{b_t}}$
- $d_{n+1_c} = 1 - \left[\left(\frac{1}{a_c} \right) \left(1 + a_c - \sqrt{\phi_c(\kappa_{n+1_c})} \right) \right]^{\frac{c_c}{b_c}}$
- $d_{n+1} = 1 - (1 - d_{n+1_c})(1 - s(\bar{\sigma})d_{n+1_t})$
- $\varepsilon_{n+1}^p = \varepsilon_n^p + \Delta\lambda \left(\frac{\sigma'_{n+1}{}^{tr}}{\|\sigma'_{n+1}{}^{tr}\|} + \alpha_p \mathbf{1} \right)$
- $\sigma_{n+1} = (1 - d_{n+1})Q_{n+1}\hat{\sigma}_{n+1}Q_{n+1}^T$

2.5 Validation of CDPM Available in ABAQUS

The significance of computational models in simulating the behavior of complex materials and structures, such as 3D printed concrete, is well understood. The CDPM, which constitutes a fundamental element of the analytical framework for the study of 3D printed concrete structures, has been explored in detail in the preceding sections.

However, the effectiveness of any modeling tool is assessed by its capacity to faithfully replicate real-world phenomena. To ascertain the suitability of the Concrete Damage Plasticity Model available in ABAQUS for our research objectives, validation becomes an imperative process. In this section, dedication is given to the critical process of validation, where the predictions generated by the model are rigorously compared against experimental data.

Table 2.1. Material Parameters for the Numerical Tests

Parameters	Tensile	Compressive	Compressive
	Monotonic &Cyclic	Monotonic	Cyclic
K_0	16145.83	16145.83	15625
G_0	13135.59	13135.59	12711.86
S_0	0	0	0
α_p	0.2	0.2	0.2
α	0.12	0.12	0.12
a_t	0.5	0.5	0.5
a_c	3.8	3.8	3.88
b_t	25000	25000	25000
b_c	675	675	1100
c_t	15000	15000	15000
c_c	525.447	525.447	850
f_{t0}	3.5	3.5	3.5
f_{c0}	18	18	18
g_t	0.00066	0.00066	0.00066
g_c	0.07733	0.07733	0.07

In the analysis presented here, the User Material Subroutine (UMAT) developed for the CDPM will be employed in the simulations. Both monotonic and cyclic loading scenarios for both uniaxial tensile and compressive tests have been meticulously executed and thoroughly compared with experimental data [70,71]. The UMAT code, an essential component of the analysis, is provided in the APPENDICES-A for ABAQUS and APPENDICES-B for FEAP, and the specific parameters used are comprehensively detailed in the Table 2.1.

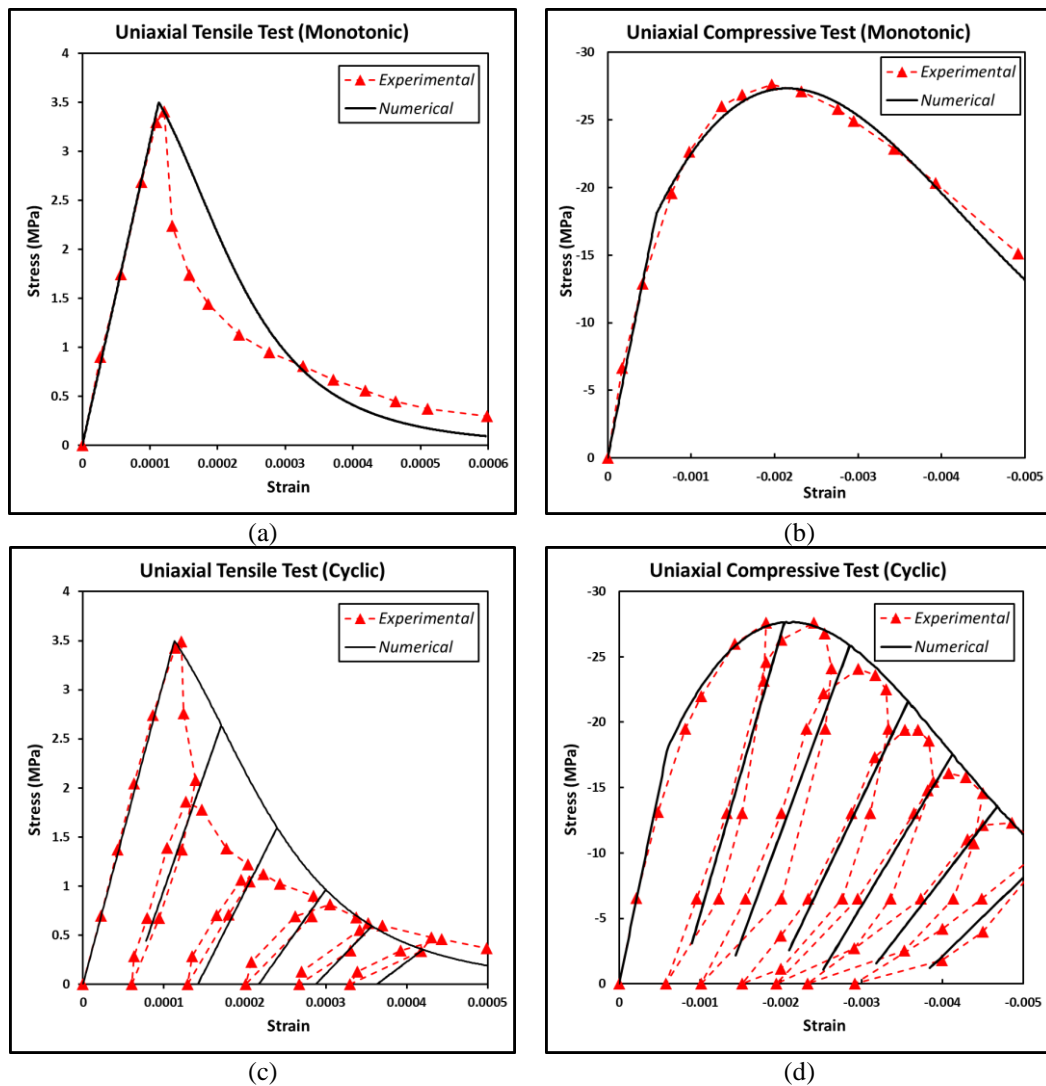


Figure 2.5. Comparison of Numerical Results and Experimental Data for (a) Uniaxial Monotonic Tensile Behavior, (b) Uniaxial Monotonic Compressive Behavior, (c) Cyclic Tensile Behavior, and (d) Cyclic Compressive Behavior

Analyses were conducted in ABAQUS, employing the C3D8 element. It was observed that the numerical simulation results closely matched the experimental data as shown in the Figure 2.5.

As a result of this strong alignment between numerical simulations and empirical observations, the model has been deemed suitable for utilization in the subsequent chapters of the study.

CHAPTER 3

MECHANICAL AND THERMOPHYSICAL PROPERTIES OF 3-D PRINTED CONCRETE THROUGHOUT A FULL-SCALE WALL

3.1 Introduction

Additive manufacturing, also known as three-dimensional printing, is a technique used to construct 3D objects via the layer-by-layer addition of a raw or composite material, creating freeform structures through a rapid prototyping system. Although AM has been widely applied in different fields such as prototyping, biomedical materials, aerospace and automotive industries, the progress of AM in the construction industry has been very slow. In the construction industry, 3D printed concrete (3DPC), which can be deposited through a 3D printer by using large nozzles and high pressure, is one of the main methods used in additive manufacturing of large buildings. 3D printing of cementitious materials requires a variety of properties such as pumpability, extrudability and buildability at the fresh stage, with high layer-interface strength and adequate compressive/flexural strength at the hardened stage, while demonstrating low or no shrinkage [72].

Reductions in labor, material usage, waste production, construction time and CO₂ emissions, as well as increased construction safety (i.e., injury and fatal accidents) are potential benefits of 3DPC [2,3]. Another important advantage of 3DPC is the elimination or reduction of formworks, thereby decreasing waste production. This amounts to significant savings, considering that the cost of the formwork is generally estimated at around 60% of the total concrete work of construction, and the formwork installation time takes up 50-70% of the total construction time [4–7,73].

Batikha et al. [8] showed that 3DPC is the most economical construction method compared to other construction methods, such as prefabricated modular construction, cold-formed steel-based construction, hot rolled steel-based construction and reinforced concrete construction. Furthermore, 3DPC is considered as one of the most sustainable and rapid construction methods. Another study by Mohammad et al. [74] compared the environmental impacts of conventional construction and 3DPC in the construction of an external load-bearing wall. This study showed that 3DPC decreased the environmental impact following the life cycle analysis conducted in the study. However, 3DPC construction with reinforced concrete columns and beams did not present a positive environmental impact compared to conventional construction, highlighting the need for feasible reinforcement strategies for 3DPC.

On the other hand, 3DPC poses several challenges, including the lack of standards, high cost of printing, excessive drying shrinkage, low bond strength between two successive layers (i.e., cold joint), plastic deformation of printed layers during printing, hydration control and anisotropic behavior [75]. The main challenge of printable concrete at an early age is the balance between stability and flow. Concrete is expected to behave like a fluid during extrusion, while being solid enough to sustain both its and the subsequent layers' weight just after extrusion, which is associated with its rheologic property and yield stress [76]. Cold joints between two successive layers should also be eliminated during the built-up process. The bond strength between successive layers depends on the time gap between printed layers [30,77–79]. An excessive time gap between layer deposition can cause cold joints, reducing the bond strength, whereas an insufficient time gap leads to the plastic collapse of the structure during the built-up process. Therefore, meeting these conflicting requirements is a challenge in optimizing printable concrete's early age behavior [80].

Buckling behavior is also commonly observed during the printing process of 3DPC due to the geometric properties of the printed objects and the mechanical properties of the printed concrete at early ages [25]. In the hardened state of the printed concrete, anisotropic/orthotropic behavior was examined by many researchers

[4,28,31,72,78]. Anisotropic behavior is exacerbated by layer-atop-layer printing process that causes voids to form between the filaments to weaken the structural resistance. Le et al. [78] examined the anisotropic behavior by performing compressive and flexural experiments on molded and printed specimens. The compressive strength of molded specimens was found to be higher than their printed counterparts which also exhibited directional dependency. Flexural strength of molded specimens was reported to be lower than the printed ones for the cases when the tensile stresses were aligned with the direction of printing, and vice versa when the interlayer was subjected to tension. These observations demonstrated the directional dependency of printed specimens. Feng et al. [28] examined the orthotropic behavior of 3D printed cementitious powders. In this study, directional dependency of the elastic modulus and Poisson's ratio was also studied. The results showed that 3D printed cementitious powders might have different elasticity and Poisson's ratio for each of the three directions. Apart from the anisotropic behavior of 3DPC, low or no directional dependency of the compressive stress was also observed in some studies [81–83]. By considering the tensile strength of printed concrete, Ingaglio et al. [82] (3D printed hydrated CSA cement was used in the study and compared with the molded specimens) observed lower tensile strength in the directions both parallel and normal to printing compared to the molded specimens. Conversely, Le et al. [78] and Rahul et al. [83] observed a higher tensile strength in the printing direction compared to the molded specimens. A possible reason for tensile strength contradiction is the porosity and density differences of the printed and molded specimens. Greater porosity and lower density of the printed specimens compared to the cast specimens in the study of Ingaglio et al. [82] resulted in lower tensile strength of printed specimens; on the contrary, lower porosity and higher density of the printed specimens compared to the cast counterparts in the studies of Le et al. [78] and Rahul et al. [83] resulted in higher tensile strength in the direction parallel to printing.

As aggregates make up a significant portion of the total volume of concrete, the aggregate-to-binder (a/b) ratio highly affects rheological properties. To satisfy

pumpability and buildability, 3D printable concrete mixtures often have low a/b ratios, with around 800 kg/m³ of binder, much more than the conventional mold-cast concrete [84]. Mohan et al. [84] researched the effect of different a/b ratios on the concrete yield stress using the flow table test and MCR 102 rheometer. With the three a/b ratios (1, 1.4 and 1.8) chosen, the yield stress and viscosity declined by decreasing the ratio, resulting in lower required pumping pressure. Suitable additives and/or admixtures also play a key role in designing mixes with desirable yield stress and thixotropic behavior at the fresh stage, while improving the strength and durability at the hardened stage [85,86].

Pozzolans such as silica fume, fly ash and ground granulated slag could be used to develop 3D printing mixes. Silica fume increases buildability and viscosity recovery, making it an ideal thixotropic material for 3D printing [86,87]. Kazemian et al. [88] showed that replacing cement with 10% silica fume improved the shape stability of fresh printing mixtures used in construction-scale 3DPC. Development of a 3D printing mix could be challenging without superplasticizers. The study of Klyuev et al. [89] on the effect of different superplasticizers on the fresh properties of cement paste proved the addition of 0.7% of polyfunctional air-entraining additive-superplasticizer (PFM-NLK) to be most effective in developing 3D printing mixes. Due to their high binder contents, concrete mixes used in 3D printing could experience drying and plastic shrinkage at early hours after printing. The addition of polypropylene fibers proved to be effective in decreasing shrinkage [90].

Other than the experiments performed in a lab-scale in the studies mentioned above, limited number of studies report comprehensive large-scale experiments to investigate the material properties of 3DPC at 1:1 scale, which is a critical issue for the analysis and design of these structures. The lack of regulatory framework and thorough understanding of 3DPC currently restrains its advancement in the construction industry [10]. In this regard, the work presented in this paper aims to reveal the properties of 3DPC walls at 1:1 scale by making use of the first 3DPC structure in Turkey, as shown in Figure 3.1. The load-bearing system of this structure

relies essentially on reinforced concrete columns, which were constructed without any formwork due to the extrusion-based 3DPC walls.

Analyzing and comparing results from previous research, it can be concluded that the properties and behavior of 3DPC is highly sensitive to printing parameters, mix constituents, environmental conditions, scale effect, and eventually their combination for the specific case determines the final performance. Therefore, in comparing results, this set of parameters should be clearly monitored, and conclusions can be generalized after proper normalization. This is essential for holistic understanding of the behavior and development of standardization procedures.

The printing process and the mix design used in this chapter were adopted from the first 3DPC structure constructed by IŞTON (İstanbul Concrete Elements and Ready Mixed Concrete Factories Corporation). Excessive pressure utilized to pump the concrete may cause more compact concrete during the printing process. This pressure may densify the concrete and dispose of the voids. As a result, the printed concrete may behave stiffer and denser than the cast one. On the other hand, in a study by Ranjbar et al. [91], strength differences along the wall height for cast-in-place concrete were investigated, revealing only minor strength variations in traditional casted concrete walls. In contrast, with printed concrete, the dead loads from subsequent layers, particularly on layers just initiating the hydration process, may lead to the formation of stiffer and denser layers at the lower sections of the wall height. Although this phenomenon was newly stated by Mechtcherine et al. [92], there is no work in the literature that comprehensively studies this. Considering the changes in stiffness and density across the wall height due to the pressure applied by the subsequent layers on earlier layers, it was necessary to investigate the whole wall without any scaling done on its height. To this end, 88 cylindrical core samples were taken from the upper and lower parts of the full-scale wall to investigate the physical, mechanical and thermophysical properties throughout the wall. Furthermore, 15 beam samples were extracted from separately printed walls to measure the flexural

and shear strength, and the effect of interface bonding on these properties. Finally, all results were compared to each other and those obtained from cast specimens.

Additionally, it's worth considering that the lengthy printing process, approximately 6 hours in duration, can potentially influence the mechanical properties. In other words, within the context of this extensive 6-hour timeframe, it's crucial to emphasize that the printer's pump heating process may lead to water loss, which has the potential to influence the material's mechanical properties. Therefore, this study involves a comparison between the compressive strength of the cylindrical samples extracted from the beams (the first printed samples) and those taken from the uppermost part of the wall (representing the latest segment of the last printed sample).



Figure 3.1. The First 3D Printed Structure in Turkey, ISTON

3.2 Materials and Sample Preparation

3.2.1 Raw Materials and Mix Design

A cubic meter of the utilized mix incorporated 820 kg CEM II/A-M (S-L) 42.5R (from OYAK Cement Factory), 1230 kg silica sand (with 1.5 mm maximum particle size), 26.5 kg calcium formate-based additive, 16.5 kg superplasticizer, and 0.65 kg monofilament micro polypropylene fibers. The water-to-cement (w/c) ratio of the mix was 0.32. The properties of the fibers, which were used to prevent shrinkage cracks, are provided in Table 3.1. The particle size distribution of the fine aggregates

was determined by sieve analysis and provided in Figure 3.2. The initial setting time of the mix was determined as 45min and 28-day compressive strength of cast \varnothing 10cm cylinders was 37.0 ± 2.1 MPa.

Table 3.1. Properties of Used Monofilament Polypropylene Fibers

Shape	Length (mm)	Diameter (μ m)	Tensile strength (MPa)	Elastic modulus (GPa)	Elongation at rupture (%)	Specific gravity
Circular	12	30-32	467 - 548	4.048 – 5.674	20 - 25	0.91

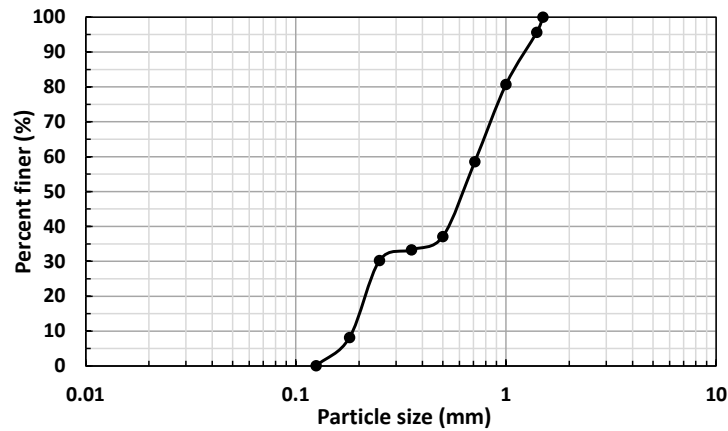


Figure 3.2. Particle Size Distribution of Fine Aggregates

3.2.2 Printing Process and Sample Preparation

Test walls with varying width \times length \times height dimensions (Wall-1: 26 \times 200 \times 235.5 cm, Wall-2: 19.5 \times 95 \times 60 cm, and 2 \times Wall-3: 19.5 \times 310 \times 15 cm) were printed with ISTON's 6-axis printer (Figure 3.3-a). The printer's nozzle had a down-flow of 5 cm round opening and extruded a concrete layer 6.5 cm wide and 1.5 cm thick. The hose length from the concrete pump to the printer was 15 m. The applied pressure to pump the concrete was around 25-30 bar. The average extrusion speed was 100 mm/sec resulting in interlayer printing times of approximately 80s, 28.5s and 93s for Wall-1, Wall-2 and Wall-3 respectively. The printing paths are illustrated in Figure 3.3-b. The printing start points were marked with a red star. The printing path and the endpoint of the first layer were shown with red arrows and a green star, respectively.

As the nozzle reached the endpoint, it rose 1.5 cm (thickness of a single layer) and started to extrude in the opposite direction, following the green arrows back to the red star, rising another 1.5 cm at the end. This process was repeated until the required wall height was reached (Wall-1: 4 horizontal and 157 vertical layers in 280 minutes, Wall-2: 3 horizontal and 40 vertical layers in 25 minutes, Wall-3: 3 horizontal and 10 vertical layers in 21 minutes). The concrete mix was prepared in 600kg-batches, and continuously fed to the pump so that extrusion was completed without interruption.

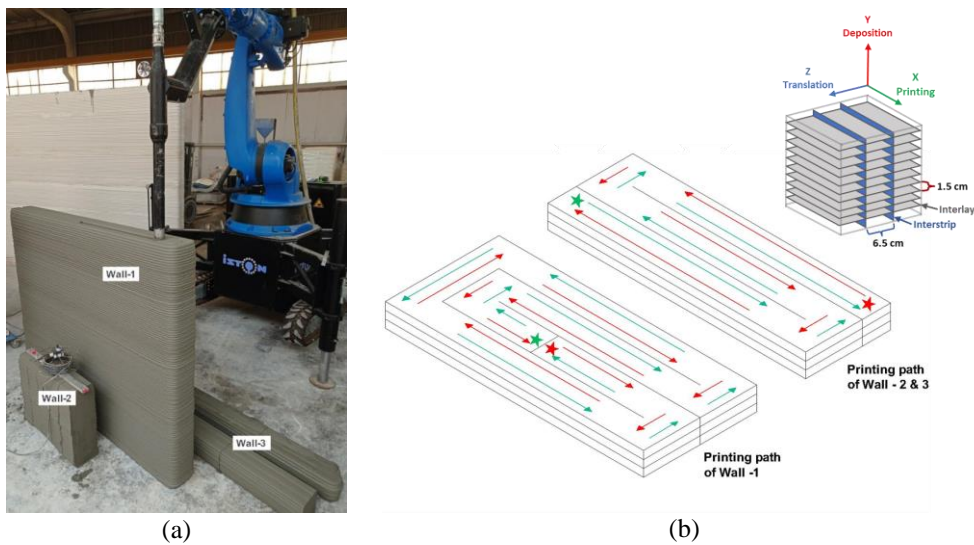


Figure 3.3. (a) Printing Process and (b) Printing Paths of the Walls (Not to Scale. Red Arrows: First Path; Green Arrows: Reverse Path; Stars: Start and End Points.)

Two types of samples were obtained from the printed walls: cylindrical cores and beams. The 10 cm-diameter cylindrical cores were taken with a water-cooled diamond driller from the upper (U) and lower (L) halves of Wall-1 in three different directions (Figure 3.4): (i) X (printing direction), (ii) Y (deposition direction), and (iii) Z (translation direction). In total, there were 28 X, 32 Y, and 28 Z cores. The X cores were centered on interstrip interfaces, while the Z cores were centered on interlayer interfaces. Half of the Y cores were centered on the interstrip interfaces (S), whereas the other half were centered on a filament, and therefore has two interstrip interfaces (D). The core lengths were about 35 cm, 35 cm, and 26 cm for

the X, Y, and Z directions, respectively. The exact core extraction locations are illustrated in Figure 3.5. $\varnothing 10 \times 20$ cm cylindrical samples were obtained from the mid-sections of these cores by sawing the core ends. Furthermore, three types of $150 \times 150 \times 600$ mm beams were obtained from Wall-2 (B1) and Wall-3 (B2 and B3) using a water-cooled diamond saw (Figure 3.6). The 3DPC results were then compared $\varnothing 10 \times 20$ cm cylinders and $150 \times 150 \times 600$ mm beams, cast and compacted according to ASTM C39/C39M-16 [93], and ASTM C78/C78M-22 [94], respectively.

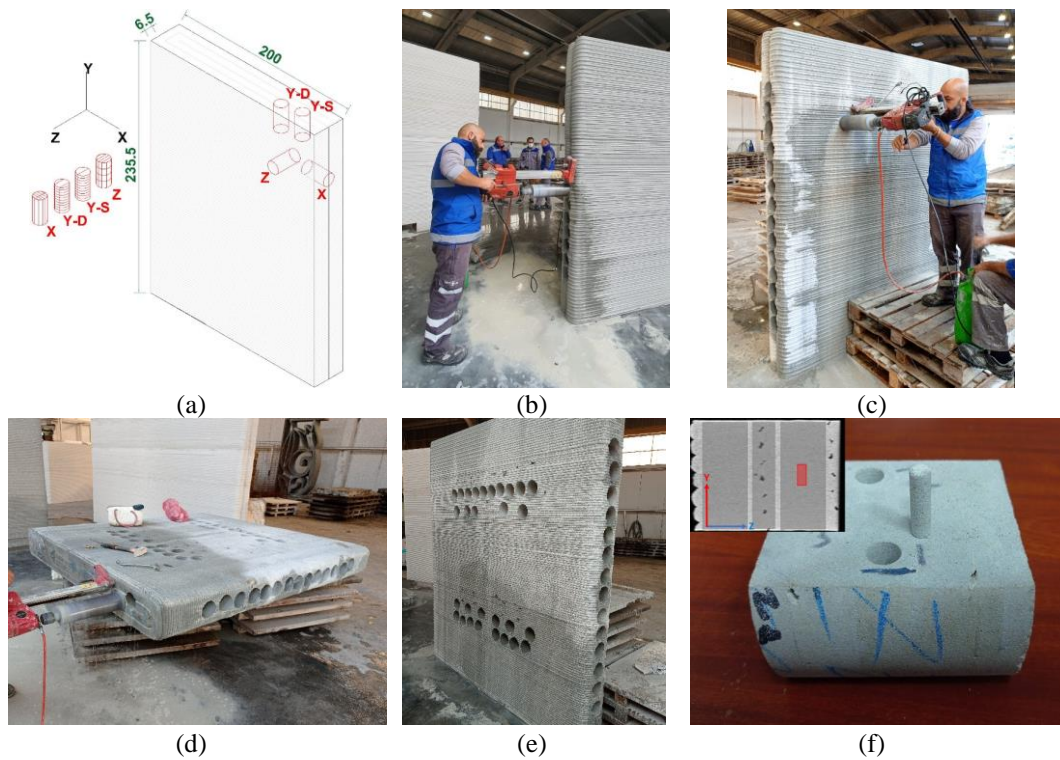


Figure 3.4. Images Showing (a) Coring Directions (Dimensions in cm), (b-d) Coring of Wall-1 in X (Printing), Y (Deposition) and Z (Translation) Directions, (e) Cored Wall, and (f) Cored Micro-CT Sample

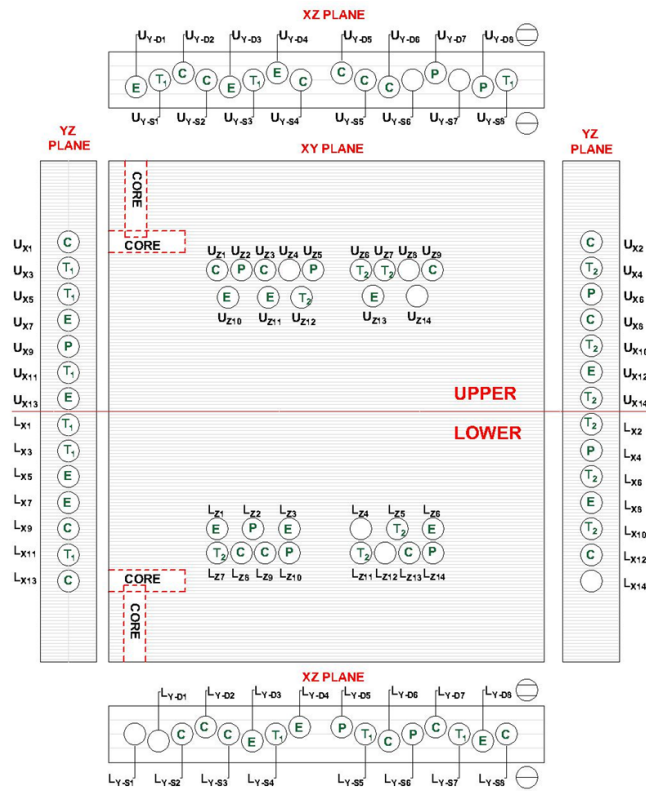


Figure 3.5. Tests Conducted on Wall-1 Cores (The Center of the UZ1-9, UZ10-14, LZ1-6, and LZ7-14 Cores were Located at 49.5 cm, 64.5 cm, 171 cm, and 186 cm from the Top of Wall-1, Respectively.)

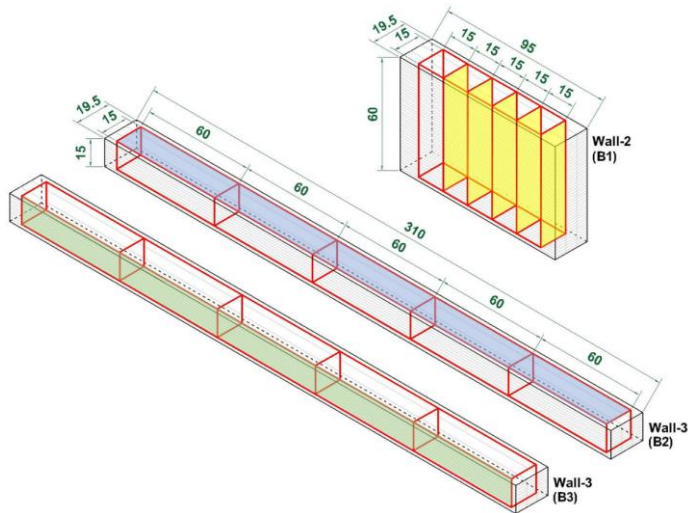


Figure 3.6. Beams from Wall-2 and -3 (Beam Top Surfaces were Marked with Yellow, Blue, and Green for B1, B2, and B3, Respectively. Dimensions in cm.)

For micro-CT measurements, an U_Z, a L_Z and a cast cylinder were sawn into two symmetric parts from the interstrip interlayer, and $\varnothing 0.75\text{cm} \times 1.5\text{cm}$ cylindrical specimens were prepared by drilling in the Y direction through the flattened surface of the core halves with a water-cooled diamond driller as shown in Figure 3.4-f. with a focus on the center of the filaments as illustrated by red area in Figure 3.4-f, and the details of CT measurements will be detailed in Chapter 4.

3.3 Experimental Program

Tests conducted on hardened concrete samples are summarized in Table 3.2 and discussed in detail in this section.

Table 3.2. Tests on Hardened Concrete ^(†)

Test	Method	Specimen (cm)	Age (day)
<i>Physical properties</i>			
Density, absorption, and voids in hardened concrete ⁽⁻⁾	ASTM C642 [95]	Volume > 350 cm ³ (~0.7 kg)	90
Rate of water absorption ⁽⁻⁾	ASTM C1585 [96]	$\varnothing 10 \times 5$	90
Water permeability ⁽⁻⁾	EN 12390-8 [97]	$\varnothing 10 \times 20$	90
<i>Mechanical properties</i> ⁽⁻⁾			
Compressive strength	ASTM C39/C39M-21 [93]	$\varnothing 10 \times 20$	90
Elastic modulus and Poisson's ratio	ASTM C469/C469M-17 [98]	$\varnothing 10 \times 20$ ^(*)	48
Splitting tensile	ASTM C496/C496M [99]	$\varnothing 10 \times 20$ ^(‡)	35
Four-point bending	ASTM C78/C78M-22 [94]	15 × 15 × 60	35
Direct shear	TS-EN 1052-3 [100]	15 × 15 × 60 ⁽⁺⁾	150
<i>Thermophysical properties</i> ⁽⁻⁾			
Thermal conductivity, thermal diffusivity and volumetric heat capacity	ISO 22007-2:2015 [101]	2 $\varnothing 10 \times 5$ ^(*)	60

^(†) $\varnothing 10$ core locations used in each experiment are summarized in Figure 3.5. ⁽⁻⁾ Reported values are average of three specimens. ⁽⁻⁾ Three measurements were taken for each specimen. ^(*) on cast, X, Y-D and Z samples; ^(‡) on cast, X, Y-S and Z samples; ⁽⁺⁾ on cast and B1.

3.3.1 Physical Properties

3.3.1.1 Density, Absorption, and Permeable Void Ratio

Specimens weighing around 0.7 kg were cut off from cylindrical samples, oven-dried for 24 hours at 120°C), immersed in water for 72 hours, boiled for 5 hours, and then, suspended in water. Measured weights at each step were used to calculate the density, absorption, and permeable voids in hardened concrete according to ASTM C642 [95].

3.3.1.2 Rate of Water Absorption

50 mm thick discs from the cylindrical samples were cut. All sides of the discs, except the one in contact with water, were sealed with a waterproof band. Each disc was immersed in tap water up to 3 mm above the bottom surface. Discs were weighed at specified time intervals. Initial and secondary rate of water absorption were determined from the slope of the absorption (change in mass divided by the exposed area and density of water) versus root of time curves during the first 6h and from 1 to 7 days, respectively, according to ASTM C1585 [96].

3.3.1.3 Water Permeability

A pressure of 5 bars was applied to the bottom of the cylindrical samples for 72 hours. Then samples were split in half, and water penetration was identified following EN 12390-8 [97]. Average water penetration depth less than 30mm, and 30 to 60mm were considered as low and medium permeability, respectively.

3.3.2 Mechanical Properties

$\varnothing 10 \times 20$ cm cylinders were used for the compressive strength (ASTM C39/C39M-21 [93]), elastic modulus (E) and Poisson's ratio (ν) (ASTM C469/C469M-17 [98]), and splitting tensile (ASTM C496/C496M [99]) tests (Figure 3.7-a). The Poisson's ratio measurements were conducted on two orthogonal transverse directions (ν_{xy} and ν_{xz} for X specimens, ν_{yx} and ν_{yz} for Y-D specimens, and ν_{zx} and ν_{zy} for Z specimens, respectively). In the splitting tensile tests, samples were placed such that the loading plane was aligned with the interlayers. The tests with a loading plane in global XY are labeled as T1, and those in global XZ are labeled as T2. The four-point bending (ASTM C78/C78M-22 [94]) and direct shear (TS-EN 1052-3 [100]) tests were conducted on $15 \times 15 \times 60$ cm beams, as shown in Figure 3.7-b and c, respectively.

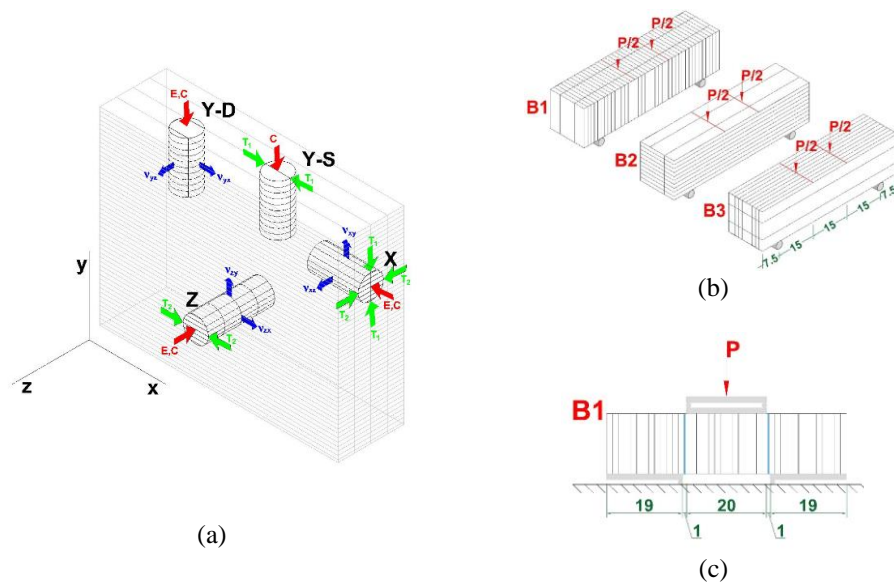


Figure 3.7. Schematic Representation of (a) Cylindrical, (b) Four-Point Bending and (c) Direct Shear Samples (Dimensions are in cm. in (c), Shear Failure Expected Interlayers are Marked with Blue.)

3.3.3 Thermophysical Properties

The transient plane source (TPS) method [102] was used to determine the thermal conductivity (λ), thermal diffusivity (α), and volumetric heat capacity (c_{vol}) of the

samples. The measurements were conducted according to ISO 22007-2:2015 [101] at room temperature using a Hot Disc TPS 2500 S Thermal Constants Analyzer [103] equipped with a Kapton sensor with radius of 9.868 mm. For the measurements, the sensor was placed between two 50 mm discs cut from the cylinders (Figure 3.8). The standard module of the TPS analyzer was used at a power-time combination of 250 mW-80 seconds. The standard module assumes isotropic thermal conductivity to evaluate the thermophysical properties by default. Although this assumption is not valid for 3DPC, which is expected to have anisotropic behavior, the results of the standard module TPS measurements still provide valuable information [104] by approximating an isotropic thermophysical response.

Measured in-plane thermal conductivity ($\lambda_{XY,TPS}$, $\lambda_{XZ,TPS}$, $\lambda_{YZ,TPS}$) and diffusivity ($\alpha_{XY,TPS}$, $\alpha_{XZ,TPS}$, $\alpha_{YZ,TPS}$) values are used to calculate the triaxial thermal conductivities through equation (3.1) [105].

$$\lambda_x = \frac{\lambda_{YZ,TPS}^2}{\alpha_{YZ,TPS} \times c_{vol}} \quad (3.1a)$$

$$\lambda_y = \frac{\lambda_{XZ,TPS}^2}{\alpha_{XZ,TPS} \times c_{vol}} \quad (3.1b)$$

$$\lambda_z = \frac{\lambda_{XY,TPS}^2}{\alpha_{XY,TPS} \times c_{vol}} \quad (3.1c)$$

During the calculation process, the heat capacity of the corresponding materials was assumed to be equal to the cast specimen volumetric heat capacity, as the capability to measure c_{vol} for anisotropic materials is not present in the standard TPS method. By using the measurement and the assumption mentioned above, directional thermal conductivities of printed specimens were evaluated using the same approach presented in [105].

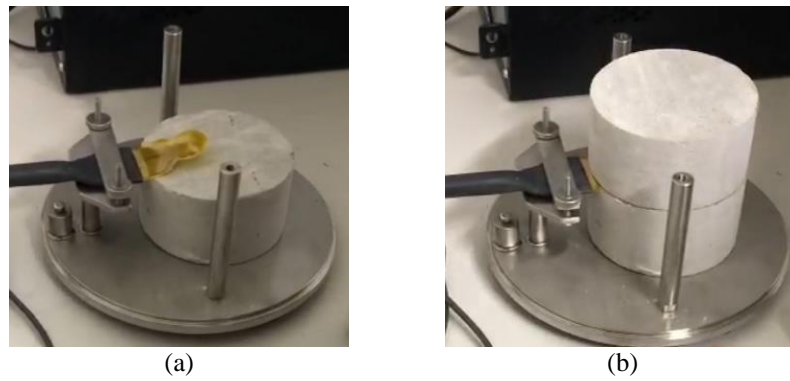


Figure 3.8. The Standard Module TPS Setup with a Kapton 8563 Sensor

3.4 Results and Discussions

3.4.1 Physical Properties

Water absorption, density, and permeable void of the tested specimens are presented in Table 3.3.

Table 3.3. Water Absorption, Density, and Permeable Voids per ASTM C642

Specimen	Water absorption (%)	Density (kg/m ³)		Permeable Voids (%)
		Bulk dry	Apparent	
<i>Cast</i>	9.25	1653.8	1952.4	15.3
<i>Upper</i>				
U _{x6}	13.40	1604.5	2043.8	21.5
U _{Y-D7}	17.17	1663.0	2327.7	28.6
U _{Z5}	18.62	1591.7	2262.3	29.6
<i>Average</i>	<i>16.40</i>	<i>1619.7</i>	<i>2211.3</i>	<i>26.6</i>
<i>Lower</i>				
L _{X4}	9.44	1705.6	2033.0	16.1
L _{Y-D5}	8.29	1785.4	2095.7	14.8
L _{Z14}	10.5	1779.5	2188.2	18.7
<i>Average</i>	<i>9.41</i>	<i>1756.8</i>	<i>2105.6</i>	<i>16.5</i>

Analysis of the data presented in Table 3.3, it can be inferred that the pressure due to the subsequent layers caused lower (L) specimens to be denser than upper (U) specimens in terms of dry bulk density (corresponding to the ratio of the mass without water to the volume of the solid, permeable and impermeable pores). In order to explain this physical phenomenon further, the transition of permeable voids to

impermeable voids and/or solid parts is depicted in Figure 3.9. This figure is instrumental in describing the variations in density and void ratio values for the lower and upper specimens, as indicated in Table 3.3.

By examining the dry bulk density values listed in Table 3.3 and comparing them with the calculated values using equations (3.2) and (3.3) from Table 3.4, it becomes apparent that the dry bulk density for U and cast specimens is expected to be lower than that of the L specimens. This suggests that additional mass per unit volume was introduced during the compaction of the lower sections of the wall due to the pressure exerted by subsequently printed layers.

With regard to the fact that the apparent density of U specimens being greater than L specimens in Table 3.3, the relative increase of impermeable pore spaces must be more than that of solid volume as evident from the comparison of apparent density from equation (3.5) being smaller than what would be obtained from equation (3.4). This could be possible if impermeable voids and/or solid parts are formed in L specimens as a result of the pressure exerted by the self-weight of the subsequently printed layers along the height of the wall.

By considering these facts, it is concluded that the lower parts of the wall were compacted to such a degree that a percentage of the permeable pores were filled up to become impermeable pores or solid parts as depicted in Figure 3.9, and this compaction process also increases density since the amount of solid parts increases in the rearranged compacted state. Moreover, the pressure exerted on the lower parts of the wall from subsequently printed layers enabled the lower specimens to be denser than the cast specimen in terms of dry bulk density, as well as apparent density. According to the density measurements in Table 3.3, it is concluded that the cast specimen and the U specimens had the highest and lowest impermeable pore spaces, respectively.

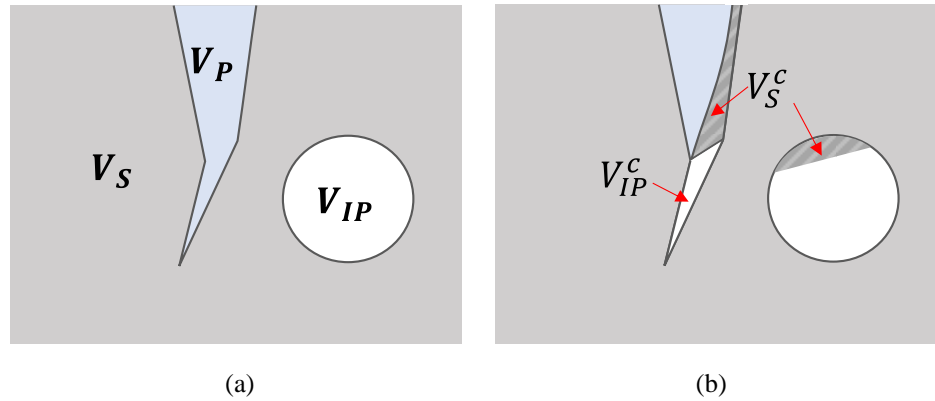


Figure 3.9. Representative Figure Illustrating Permeable and Impermeable Voids in: (a) Upper Layers and (b) Lower Layers (Blue: Permeable Voids, White: Impermeable Voids, and Grey: Solid Volume)

Table 3.4. Definition of the Densities and Voids Ratio Related to Figure 3.9

	U or Cast		L	
Dry bulk density	$\frac{M}{V_S+V_{IP}+V_P}$ (3.2)		$\frac{M+M^c}{V_S+V_{IP}+V_P}$ (3.3)	
Apparent density	$\frac{M}{V_S+V_{IP}}$ (3.4)		$\frac{M+M^c}{V_S+V_S^c+V_{IP}+V_{IP}^c}$ (3.5)	
Permeable voids ratio	$\frac{V_P}{V_S+V_{IP}+V_P}$ (3.6)		$\frac{V_P^c}{V_S+V_{IP}+V_P}$ (3.7)	

When comparing U specimens to the cast specimen, dry bulk densities are quite similar. However, the apparent density of U specimens was much greater than cast specimen, which points out that the printing process caused the pores to protrude from the bulk part of the concrete and formed more compacted and denser layers. The dry bulk density of U specimens was almost the same as the cast specimen, which points out that the impermeable voids ratio of U specimens was much less than cast specimen. The permeable voids ratio of U specimens, mostly in the interlayers, was much higher than cast specimens. Although the bulk part and interlayer part were not directly investigated in this chapter (will be detailed in Chapter 4), this inference makes sense because the studies [83,106] also show that pores concentrate in the interlayers of 3DPC, and by considering the upcoming water penetration and absorption results, most of these pores are considered to be permeable pores; therefore, the comparison made on the apparent and bulk density

gives the relevant idea about the effect of the printing process on the variation of density and voids ratios throughout a full-scale 3DPC wall. After taking into account all the preceding discussion, the volumes V_S , V_P , V_{IP} can be sorted in the following manner for cast, U, and L samples:

$$V_S^L > V_S^{cast} \approx V_S^U$$

$$V_P^U > V_P^L \approx V_P^{cast}$$

$$V_{IP}^{cast} > V_{IP}^L > V_{IP}^U$$

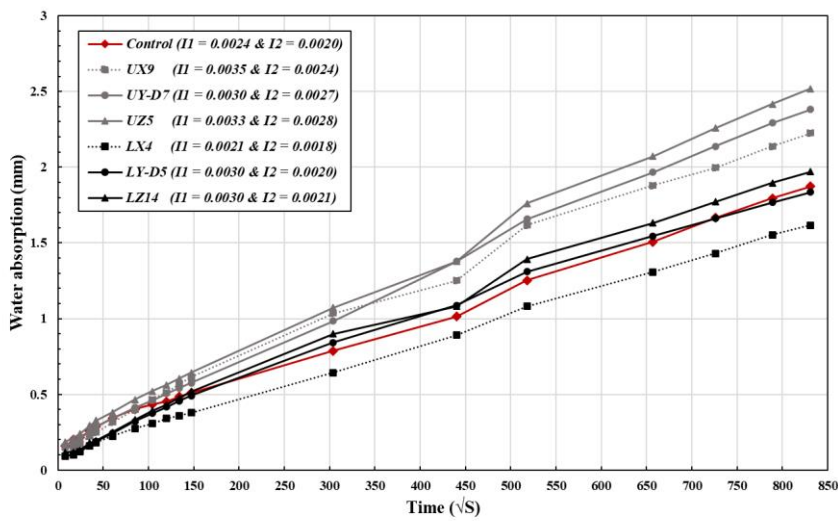









Figure 3.10. Capillary Rise Results of Cast and Printed Specimens

Capillary rise and water penetration experiments give significant information on the durability of concrete. The results from capillary rise experiments of cast and printed specimens are presented in Figure 3.10. In ASTM C1585 [96] standard, the water absorption is estimated in terms of two rates: initial rate - from first minute to sixth hour, and secondary rate - from first day to seventh day, whose results are represented as I1 and I2 in Figure 3.10, respectively. The rates were determined as the slope of the absorption curves versus the square root of time, so the unit of I1 and I2 is $\text{mm/s}^{1/2}$. If each of the U and L samples were to be considered collectively, the average initial rates of U and L were 0.0033 and 0.0027 $\text{mm/s}^{1/2}$, respectively. The water absorption rate of the U specimens was higher than both the L and cast

specimens, the lowest one being the cast specimen with $0.0024 \text{ mm/s}^{1/2}$. Regarding U and cast specimens, the same trend of results was previously presented in [107], which also states that the voids at the interlayer zone led to a faster water transport along the printed concrete interlayer zone than that of cast concrete. Additionally, the average initial rate of L specimens was close to the cast one. As for the secondary rate, the average values for U, L and cast specimens were 0.0026 , 0.0020 and $0.0020 \text{ mm/s}^{1/2}$, respectively. The results for the cast and L specimens were very similar, and at the same time lower than the U specimen. As a result, concrete printing negatively affects the capillary rise in general but the compaction due to self-weight of subsequently printed layers in 3DPC positively affects the capillary rise of the earlier printed layers.

Table 3.5. Water Penetration Depths of the Cast and Printed Specimens

<i>Sample</i>	Cast	U _{X9}	U _{Y-D8}	U _{Z2}	L _{X4}	L _{Y-S6}	L _{Z10}
<i>Photo</i>							
<i>Water penetration depth (mm) (*)</i>							
Maximum	52.1	81.7	46.3	19.5	11.8	10.9	9.0
Minimum	33.2	3.7	4.6	12.9	0.0	0.0	0.2
Average	41.3	39.9	13.8	16.1	8.0	9.0	8.3
St. Deviation	3.0	27.7	10.5	1.6	4.6	4.8	3.9

(*) For each sample, measurements were taken at 0.5 cm intervals over the sample width to calculate the average water penetration depth and its standard deviation. For U_{Y-D8} and U_{Z2}, the close-ups of circled regions are provided in the Figure 3.11.

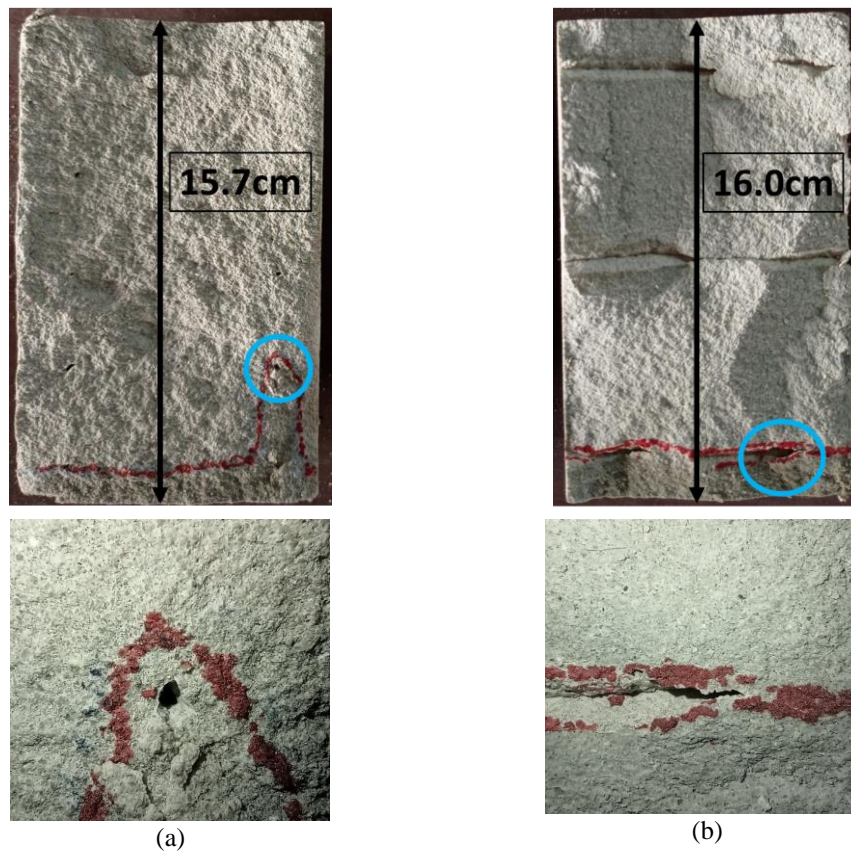


Figure 3.11. Cross-Sections of the Specimens Subjected to Water Penetration Tests: (a) U_{Y-D8} and (b) U_{Z2}

The average water penetration results are presented in Table 3.5. For the specimen U_{Z2} , water penetrated 16.1 mm equally to the first interlayer belonging to the XY plane and flowed out through the void channel formed due to the nature of 3DPC. The same result was observed for U_{Y-D8} specimen. These void channels were emphasized by blue circles in related figures in Table 3.5. However, although U_{Y-D} had two interlayers belonging to XY plane, water penetrated 46.3 mm to only the weakest bonded layer, unable to reach the other layer that had stronger interlayer bond. For U_{X9} specimen, water penetrated more through the same interlayer belonging to XY plane, but no void channel or water flow outside the sample was observed. The maximum penetration depth of U_{X9} was 81.7 mm. By considering U specimens results, it can be said that the bond between interlayer belonging to XZ plane was better than XY plane in terms of the water penetration for this printing strategy. For L specimens, the water penetrated with lower standard deviation

compared to the cast and U specimens. No void channel or water flow outside of the sample and no interlayer effect were observed, as shown in Table 3.5. The water penetration depth of L_{X4} , L_{Z10} and L_{Y-S6} are 8.0, 8.3 and 9.0 mm from lowest to highest, respectively and the average was found as 8.4 mm. According to the location of the sample illustrated in Figure 3.4-a, as pressure on the sample got higher due to the printing of the subsequent layers, this resulted into the water penetration depth to be lower in the test. The penetration depth of the cast specimen, 41.3 mm, was 4.9 times the average penetration depth of the L specimens. A possible explanation is that the pressure induced by the self-weight of the subsequently printed layers compacted the lower part of the wall as previously realized in water absorption, densities and voids measurements presented in Table 3.3.

3.4.2 Mechanical Properties

3.4.2.1 Uniaxial Compression Tests

The compressive strength results are presented in Figure 3.12 for the core samples extracted from the full-scale 3DPC wall (Wall-1), as well as the cast specimens. The 90-day compressive strength of the cast specimens averaged 37.8 ± 3.2 MPa. For the X, Y-D, Y-S and Z directions, U/L compressive strengths were 101%/134%, 81%/141%, 91%/156% and 60%/125% of the cast specimen, respectively. The difference between U and L specimens is attributed to the compaction of the lower layers due to self-weight of the subsequently printed layers in Wall-1, reducing the void ratio at the lower specimens, as presented in Table 3.3.

The strength reduction details are explored in Chapter 4. The reduction in U specimens compared to the cast one was attributed to low interlayer bond strength and porosities. For the U specimens, the cracks were extended through interlayers as shown in Figure 3.13, showing that failure under compression was due to the low interlayer bond strength (discussed further in Section 3.4.2.3) [108]. On the other hand, the failure types of the L specimens were similar to the cast specimens, which

were commonly type 1, 2, 3 and 4 failure modes according to ASTM C39/C39M [93]. The cracks were observed to only slightly extend through the interlayer of the failed L specimen, which is related to the increased interlayer bond strength of these specimens. Therefore, failure mode of the L specimens was a combination of both interlayer and the filament bulk failure, where the failure of the matrix seems to be the dominant mode as shown in Figure 3.13. The higher strength exhibited by the L specimens compared to the upper and cast ones is correlated with their greater dry bulk density and lower total void ratio, as summarized in Table 3.3. On the other hand, it can be ascribed to compaction due to the extrusion process [78,83] and pressure exerted by the subsequent layers.

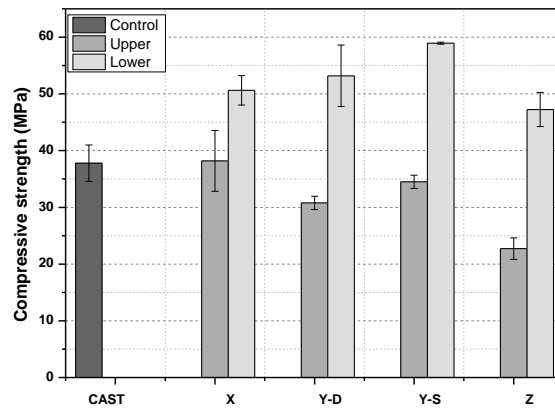


Figure 3.12. Compressive Strength of the Cast and Printed Specimens

Furthermore, Y-S specimens had greater strength than Y-D specimens, possibly due to the larger interstrip interface (in the vertical XY plane) area of the Y-D specimens (293.2 cm^2) compared to that of Y-S specimens (196 cm^2). Therefore, the place of specimen extraction is important for the measurements and should be carefully selected and investigated in detail.

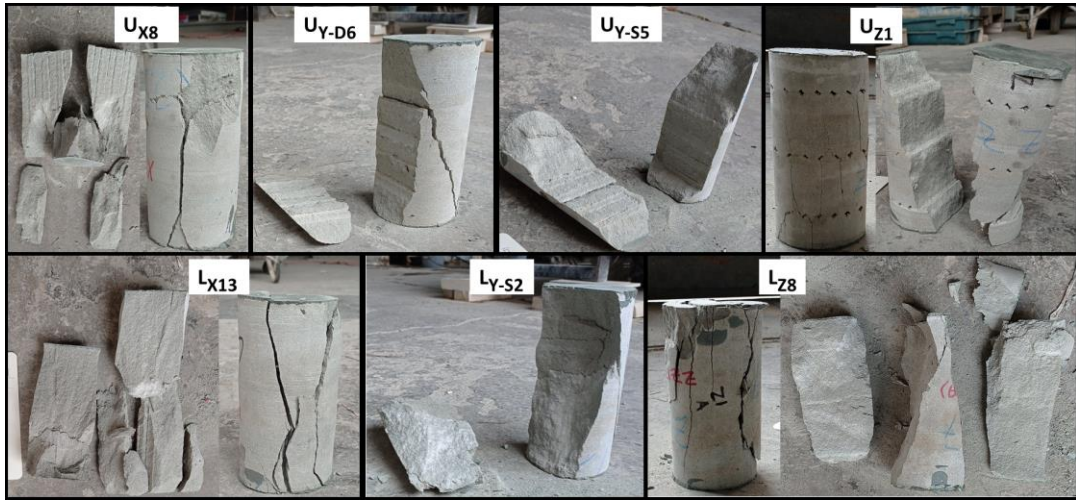


Figure 3.13. Failure Modes (Fracture Patterns) of Upper and Lower Specimens Under Compression

3.4.2.2 Elastic Modulus and Poisson's Ratio

E and ν are two important material parameters to understand the overall behavior of the material and are commonly used for constitutive modeling of materials and analysis and design of structures. Unlike an isotropic material, behavior of an anisotropic material changes with the loading and deformation directions in the body.

The results from elastic modulus and Poisson's ratio experiments are presented in Figure 3.14, where the specimens' locations were shown in Figure 3.5 and the undertaken experiments on the core specimens were previously depicted in Figure 3.7. The elastic modulus of lower specimens, L_X , L_{Y-D} and L_Z were greater by 9.7%, 53.1% and 21.2% than that of U_X , U_{Y-D} and U_Z , respectively. This again is correlated with their pore volumes and consequently dry bulk density. The elastic modulus of the cast specimen is in between L_X and U_X , while the difference in elastic modulus between L_X and U_X is not as pronounced as observed in type Z and Y-D specimens. A possible reason for this can be the smaller distance between the upper and lower X specimens used for elastic modulus measurements, due to limitation on the number of cores that can be extracted from the same 3DPC wall, as shown in Figure 3.5. It is seen from the figure that the very bottom and top specimens on X face were used

for the compression strength measurements, while specimens closer to the mid-height of the wall were used for elastic modulus tests. This choice resulted in a smaller variation of the elastic modulus values between L_X and U_X specimens, while in reality a more significant variation similar to Y-D specimens in Figure 3.14-a should have been measured.

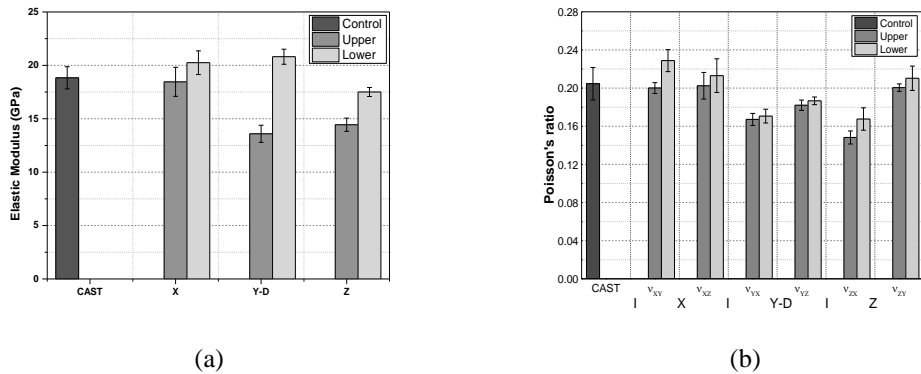


Figure 3.14. Results of (a) Elastic Modulus and (b) Poisson's Ratio in Cast and Printed Specimens

The same dissimilarity but to a lesser extent was observed for the Poisson's ratio results. The L specimens exhibited greater lateral strain under axial loading, but the percentage change in Poisson's ratio values was not as significant as for the elastic modulus. An interesting behavior was observed in the U_Z specimens. Lateral strain versus axial strain graphs of U_Z specimens under the third loading cycle are presented in Figure 3.15, where non-linear increases were observed in U_Z specimens. The possible reason for this non-linearity might be the loading having no remarkable effect on the lateral strain until a certain point due to the large voids present in the interstrip interfaces (in the XY plane). As mentioned in Section 3.4.1, the interstrip interface (in XY plane) located in the upper part of the full-scale 3DPC wall (Wall-1) had large voids in which water could flow, where these voids were previously shown in Table 3.5 and Figure 3.11. Facing non-linearities in 3DPC for Poisson's ratio results is inevitable because 3DPC is not an isotropic material like the cast-in-place concrete, but it also incorporates physical deficiencies such as interlayers. The Poisson's ratio values were recalculated from the linear part in between the bracket

shown in Figure 3.15, and presented aligned with the related curves. The calculated average Poisson's ratios, ν_{zx} and ν_{zy} , increased from 0.148 and 0.201 to 0.171 and 0.227 with standard deviations of 0.005 and 0.012, respectively.

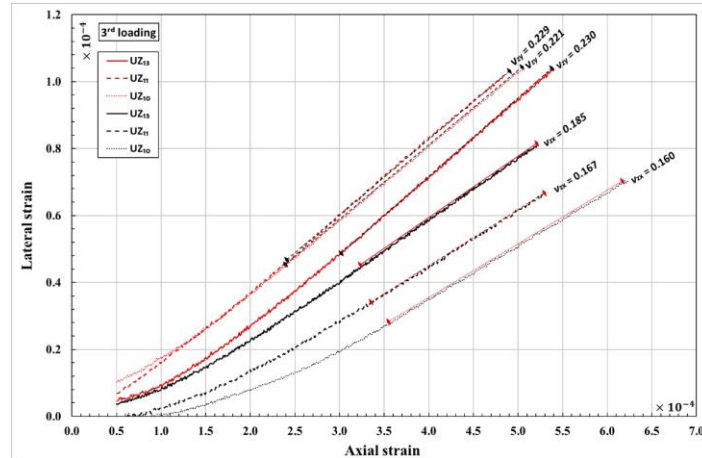


Figure 3.15. Lateral Strain Versus Axial Strain Graph for Type U_Z Specimens

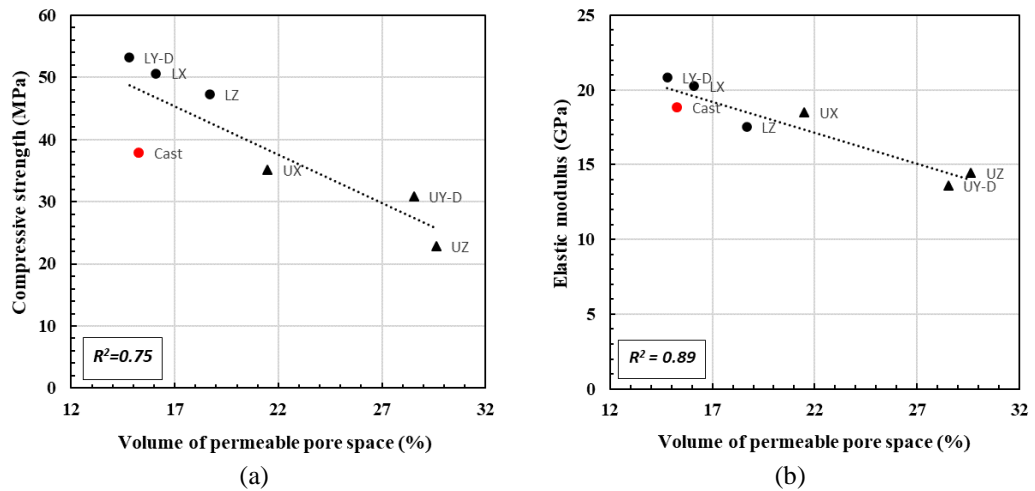


Figure 3.16. Correlation Between Volume of Permeable Pore Space (%) and (a) Compressive Strength (MPa) and (b) Elastic Modulus (GPa)

Finally, the compressive strength and elastic modulus are observed to be inversely correlated with the permeable pore space of the samples with a correlation coefficient of -0.866 and -0.941, respectively, as shown in Figure 3.16. As the volume of permeable pore space decreases from the upper to the lower half of the wall,

compressive strength and elastic modulus increase in the earlier printed layers due to the reduction in permeable pore space and increase in the density.

3.4.2.3 Splitting Tensile Tests

The results from the splitting tensile experiment are presented in Figure 3.17. On average, it is observed that the interlayer bond strength in L specimens, which are extracted from the lower half of the full-scale 3DPC wall (Wall-1), is much higher than U specimens extracted from the upper part of the wall, while the coefficient of variation is relatively high in these tests. The splitting tensile strength values of lower specimens, L_{XT1} , L_{XT2} , L_{Y-ST1} , and L_{ZT2} , were greater by 32.0%, 99.8%, 55.2%, and 83.4% than those of U_{XT1} , U_{XT2} , U_{Y-ST1} , and U_{ZT2} , respectively, where definition of T1 and T2 is available in Section 3.2.2. Also, the strength of mold cast specimens taken for control purposes was almost the same with U specimens except for specimens extracted from X face of the wall, namely type X specimens. Once again, the reason for the results of X specimens is due to the locations of type X specimens as shown in Figure 3.5-a. The increase of bond strength of X_{T2} and Z_{T2} specimens was higher than X_{T1} and $Y-S_{T1}$ specimens because the subsequent layers directly affected interlayers belonging to the XZ plane but indirectly affected the interlayers belonging to the XY plane. This result shows us that the interlayer bond strength is significantly affected by the self-weight of the wall along its height due to printing process; i.e., the interlayer bond strength increases as a result of the pressure exerted by self-weight of subsequently printed layers on it. The void ratio experiments previously presented in Table 3.3 clearly demonstrate that the interlayer voids are also reduced in the lower parts of the wall due to exerted pressure, and this results into the bond strength of lower layers to get closer to the cast specimens. On the other hand, the increased pressure can also trigger fiber breaching between filaments, which further improves the bond. The T2 score for specimen Z at the lower half of Wall-1 was even higher than the splitting tensile strength for the cast specimen, i.e., as expected the compaction and fiber breaching were more significant here, and

substantially enhanced the response. Moreover, for Z_{T2} the variation in results was smaller than for the cast specimen, i.e., a more stable and predictable behavior was achieved at the lower part of the 3DPC Wall-1 in terms of interlayer strength. This conclusion is also supported by the split surfaces being perfectly visible in U specimens in Figure 3.18, while they are more hardly distinguishable in L specimens.

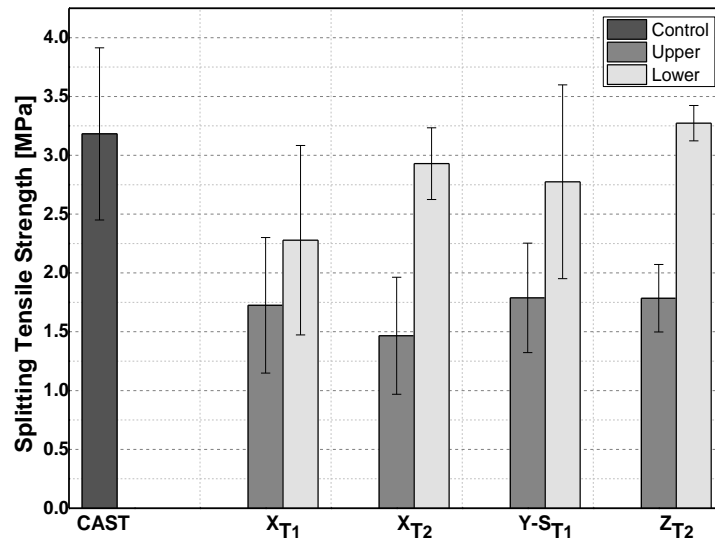


Figure 3.17. Splitting Tensile Strength Results of Cast and Printed Specimens

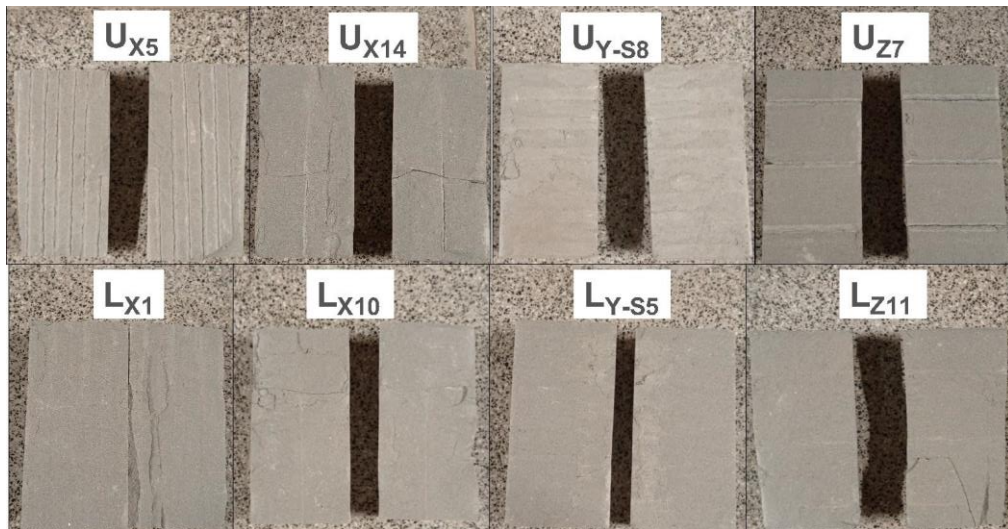


Figure 3.18. The Split Specimens Located at Upper and Lower Part of Wall-1

3.4.2.4 Four-Point Bending Tests

The aim of this experiment is to measure the interface (interlayer and interstrip) bond strength and the flexural tensile strength of the filament's bulk for the printed specimens and compare these results with the flexural strength of cast specimens. Furthermore, the results from the four-point bending tests will be compared with the splitting tensile strength of the cored and cast specimens presented in the previous section.

Description of the printing process for the beam specimens was provided in Figure 3.3-b, and the type of printed beam specimens and loading directions were given in Figure 3.5-b. For all tested specimens, a sudden brittle failure was observed as expected, and the flexural strength results are shown in Figure 3.19. The flexural strength of the cast beam was 3 MPa, and being so it was greater than all printed beams, and very close to the splitting tensile strength value observed for the mold-cast specimens in previous section. The lowest flexural strength for printed beams was observed in B1 type beam, in which the interlayer surfaces were parallel to the loading direction and subjected to tensile stresses. In between printed beams, B2 type beams had the highest flexural strength, since there were no interlayers in the direction of loading (no interlayer surfaces subjected to tension), and furthermore the number of interlayer interfaces was lower than in B1 type beam specimens as shown in Figure 3.5-b. In order for a beam to carry a bending moment and shearing force, it must be able to carry shear stresses on its horizontal surfaces (perpendicular to the direction of loading), as well. In the four-point bending test, there is pure bending region in the middle of the beam, while the rest of the beam is under combined bending and shearing. In B3 the horizontal surfaces to carry the shearing stresses are the interstrip interfaces, while in B2 - the interlayer interfaces. The latter exhibit a higher bond strength, as also observed from splitting tensile tests, and consequently B2 type beam is expected to exhibit a higher flexural strength compared to B3. In general, it is observed that undertaking a beam test on 3DPC does not perfectly provide a definitive assessment of measuring a material property for 3DPC.

However, it actually replicates the nature of a more complex stress distribution that would be present in a 3DPC beam under pure bending or combined bending and shearing. It is in conclusion suggested that the measurement of interlayer tensile bond strength through splitting cylindrical core specimens provides a much more practical testing strategy, especially for the measurement of the interlayer bond strength present in full-scale 3DPC walls. Furthermore, while there are difficulties in extracting core samples, it is still more feasible to extract cylindrical core samples from different parts of a full-scale wall compared to cutting and sawing beam specimens for four-point bending tests.

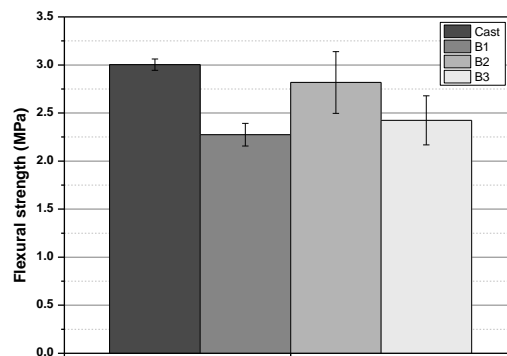


Figure 3.19. Flexural Strength for the Cast and Printed Beams Estimated from Four-Point Bending Tests

3.4.2.5 Direct Shear Tests

Direct shear test was applied to the cast and B1 type beams with interlayers parallel to the loading direction (perpendicular to the beam axis). The experimental procedure provided in TS-EN 1052-3 [100] is followed for this purpose, and the experimental setup is represented in Figure 3.5-c. Shear strength of the cast and B1 type specimens were determined as 3.88 and 3.72 MPa, respectively, and the result of this method shows that the presence of interlayers did not have a significant effect on the shear strength property. This is also supported by the fact that the failure surface of B1 type specimens did not demonstrate a perfectly slid interlayer surface,

but a slightly more irregular slid surface, which was also observed in for the cast specimen.

3.4.3 Thermophysical Properties

The thermophysical properties, conductivity and diffusivity, were measured using the TPS method. The ratio of the conductivity to the diffusivity is known as the volumetric heat capacity. The results are tabulated in Table 3.6.

Table 3.6. Thermophysical Properties of the Printed and Cast Specimens

Specimen	Plane	λ (W/mK)	α (mm²/s)	c_{vol} (MJ/m³K)
<i>Cast</i>	-	1.194	0.662	1.806
<i>Upper</i>				
U _{X6}	YZ	1.017	0.587	1.735
U _{Y-D7}	XZ	1.097	0.634	1.731
U _{Z5}	XY	0.965	0.595	1.622
Average		1.026	0.605	1.696
<i>Lower</i>				
L _{X4}	YZ	1.172	0.638	1.837
L _{Y-D5}	XZ	1.296	0.700	1.850
L _{Z2}	XY	1.123	0.647	1.735
Average		1.197	0.662	1.807

(λ : Thermal conductivity; α : Thermal diffusivity; c_{vol} : Volumetric heat capacity)

Compared to the cast specimens, the thermal conductivity of L_{Y-D5} increased by 8.5%, and L_{X4}, L_{Z2}, U_{X6}, U_{Y-D7} and U_{Z5} decreased by 1.8%, 5.9%, 14.8%, 8.1% and 19.2%, respectively. When the results of the printed specimens were compared among each other, the ratio of the highest to the lowest in U and L specimens were 1.14 for U and 1.15 for L specimens, which is considered to be due to anisotropy in physical properties.

Anisotropic behavior should be investigated in more detail, because the isotropic behavior assumption will lead to underestimation or overestimation of measured values [104]. For this reason, directional thermal conductivities were evaluated next, as suggested by [104,105]. To calculate the directional thermal conductivities, the volumetric heat capacity must be known; however, the standard TPS method does

not give reliable volumetric heat capacity for an anisotropic material. Therefore, the cast specimen's result was assumed as the volumetric heat capacity for the printed specimens in order to evaluate the directional thermal conductivity.

This assumption will not alter the ratio of the highest to the lowest thermal conductivity values. By using this volumetric heat capacity, measured thermal conductivities and diffusivities, the triaxial anisotropic thermal conductivities were calculated by using equations (3.1) according to the studies [104,105]. In these equations, λ_X , λ_Y and λ_Z are thermal conductivities in the direction of X, Y and Z, respectively. c_{vol} is the volume-specific heat capacity of the cast specimen. $\lambda_{X,TPS}$, $\lambda_{Y-D,TPS}$, $\lambda_{Z,TPS}$ and $\alpha_{X,TPS}$, $\alpha_{Y-D,TPS}$, $\alpha_{Z,TPS}$ are measured thermal properties of the specimen type X, Y-D and Z, respectively.

The calculated thermal conductivity results are presented in Figure 3.20. Among these results, the ratio of λ_Y to λ_Z , i.e., the highest to the lowest, were 1.21 and 1.23 for U and L specimens, respectively. It is important to point out that the relative variation of these ratios among each other are independent from the assumption on c_{vol} as evident from this value being in the denominator of equations (3.1). This result shows the clear anisotropic thermal behavior for 3DPC. On the other hand, comparing the U and L specimens with each other, the thermal conductivity of U specimens was measured to be smaller than L specimens which is an expected result because L specimens were denser than U specimens as shown in Table 3.3. It is known that the thermal conductivity increases with increasing density for the same material due to the low thermal conductivity of the air enclosed by the pores [104,105]. However, the triaxial thermal conductivity differences between upper and lower part of the full-scale 3DPC wall might be lesser than the result in Figure 3.20 because of the volumetric heat capacity assumption. The reason is that higher porosity may cause lower volumetric heat capacity for the same material. The volumetric heat capacity of the wall was observed to change along its height because density and porosity also change with the wall height, as discussed in Section 3.4.1. For future studies, the volumetric heat capacities of the printed specimens extracted from a full-scale 3DPC wall may be investigated for a reevaluation of the effect of

printing parameters and the self-weight of subsequently printed layers, thus, resulting in a variation of the volumetric heat capacities along the height of the wall as compared to the cast specimens.

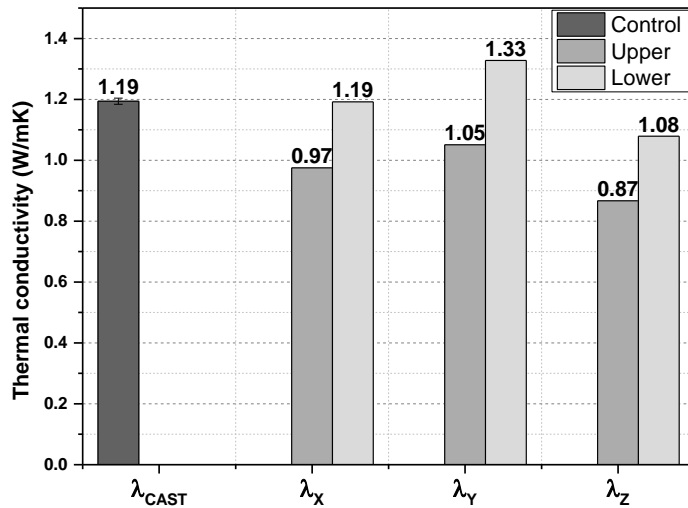


Figure 3.20. The Triaxial Anisotropic Thermal Conductivities

3.5 Further Discussions

In this section, a deeper exploration is undertaken regarding the factors that influence the mechanical properties of 3D printed concrete, and additional experimental results are introduced.

3.5.1 Factors Beyond Self-Weight

While the self-weight of subsequent layers has been identified as a significant factor affecting concrete properties, it's important to acknowledge that other dynamics are at play. While self-weight undeniably plays a pivotal role in shaping the physical properties, including density, porosity, and void distribution, it's worth noting that other factors, such as the temperature of the pump outlet, may also influence these physical properties. Therefore, this prompts us to explore an additional discussion.

Researchers have examined the influence of moisture content on interlayers [109–111]. Sanjayan et al. [110] conducted a study focused on the impact of surface moisture on the interlayer strength of 3D printed concrete. The findings indicated an initial decrease in interlayer bond strength due to surface evaporation, followed by an increase attributed to bleeding of the concrete, wherein the surface gained moisture, as the rest time increased. This underscores the significant role of moisture content in affecting bond strength. On another note, Keita et al. [109] highlighted that the pumping and extrusion processes induce elevated levels of friction, leading to temperature escalation. Using a sample in a 50% relative humidity environment as a baseline at 20 °C, a temperature rise of 5 °C is expected to enhance the drying rate by 15%, while a 10 °C increase is projected to amplify it by 80%. This acceleration in drying rate prompts a transition to the second drying regime, characterized by surface-localized water loss for lower water-to-cement ratios or shorter resting times. This localized water loss hinders cement hydration, resulting in a reduction in interface strength. These insights lay the foundation for a more comprehensive exploration of potential temperature-related effects, as discussed in the subsequent section 3.5.2.

Approximately 3 hours into the extrusion process, the pump outlet temperature elevates, likely due to friction. This temperature shift may result in increased viscosity, which has a notable impact on adhesion and intermixing between freshly printed layers and the underlying ones. This phenomenon introduces a unique layering effect that manifests along the height of the concrete wall.

3.5.2 Additional Experimental Insights

To further investigate potential temperature-related effects, compressive strength tests were conducted on samples extracted from undamaged sections of the firstly printed samples, the beams used in bending tests (representing the early stage of printing with presumably normal temperature) and named as control sample in Figure 3.21. Valuable insights into the material's response to such variations are

provided by these tests. The results contribute to understanding the influence of temperature, if any, on the mechanical properties and behavior of the printed concrete.

Unfortunately, only one sample was available for both the Z and Y-S groups taken from the beam. This limitation in sample size may lead to implications for the robustness and generalizability of the results. The smaller sample size can introduce increased variability and may affect the statistical significance of the findings. This constraint should be acknowledged, and its potential impact on the validity and generalizability of the conclusions drawn from these specific groups should be considered.

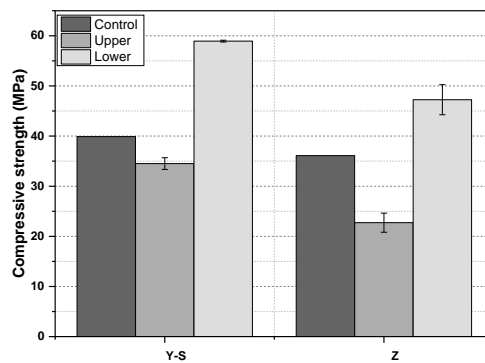


Figure 3.21. A Comparison of the Initially Printed Concrete with U and L Samples

Based on the results presented in Figure 3.21, it can be concluded that the printing process also impacts the mechanical properties of the 3DPC, because the compressive strength results of the control samples fall beyond the standard deviation range of the U and L samples for the Y-S and Z groups. Therefore, attributing the variations solely to the self-weight effect is not entirely accurate. Nevertheless, it is crucial to emphasize that while the self-weight effect may not be the sole contributing factor, the explanation provided in the physical properties section (Section 3.4.1) and summarized by Figure 3.9 remains valid and may be

associated with the increase in pump outlet temperature. In other words, the observations and comparisons regarding total porosity, impermeable and permeable porosity, and densities can be attributed to a combination of self-weight and the elevation in pump temperature rather than self-weight alone.

3.6 Conclusion

This chapter presents a comprehensive study of variation in material properties throughout a large-scale 3DPC wall. Samples from different locations along the real scale 3DPC wall were extracted and tested for physical, thermophysical and mechanical properties to further study the directionality in material properties, the effect of the scale, and analyze the relationships between different properties and the impact of printing parameters and self-weight. The samples were categorized in terms of the extraction location along the wall height (upper (U) and lower (L)), and the alignment of the longitudinal axis with respect to the printing space (X – printing, Y-translation, and Z – deposition direction). The contribution of the chapter is that properties are scale-dependent, and especially for a layered anisotropic material the scale effect is more pronounced, and extracting specimens from real-scale structures is essential for including the production parameters in the analysis. The behavior was also compared against a control specimen which was mold-cast from the same concrete mix. The results indicated a pronounced anisotropy and significant variation of all properties along the 3DPC wall height. The main parameters expected to contribute to the height-dependence and directionality for the analyzed wall are the pressure due to self-weight of subsequent layers, due to extrusion, and the temperature of the printing equipment which can affect the mix viscosity. The major conclusions from the experimental study are as follows:

1. The lower part of the wall was compacted due to the self-weight of the subsequently printed layers exerting pressure on the earlier printed layers. This reduced the amount of permeable voids in the compacted layers, resulting in a denser 3DPC in the lower parts as compared to the upper parts of the wall. This difference

in density and voids can also be attributed to the increase in mix viscosity due to pump heating for increased printing time. This was also validated by the water penetration and capillary rise measurements, where it was observed that water hardly penetrated the lower specimens, whereas it easily penetrated and rose in the specimens extracted from the upper parts of the wall. The penetration depth of the cast specimen was measured to be 4.5 times of the average penetration depth of the L specimens. Regarding the capillary rise, the water absorption rate of U specimens was higher than the L and cast specimens, and the rates of the L and cast specimens were comparable.

2. Since the upper part of the wall was more permeable, it was more prone to durability problems. Further durability tests can be conducted to evaluate the possible long term durability issues.

3. The lower parts of the wall exhibited significantly stronger and stiffer behavior compared to the upper parts. Compressive strength, elastic modulus and splitting tensile strength of the lower parts increased by up to 108%, 52.9%, 99.8% when compared to the upper parts, respectively. The presence of single or double interlayers and/or interstrip interfaces in the direction of loading had a significant effect on the compressive strength results. Anisotropic behavior was generally observed depending on the location, printed layer orientation and loading direction of the specimens. However, variations in material response were always dominated by the elevation of the printed specimen in the wall.

4. Failure modes under compression of the L specimens were similar to the cast specimens, while for the U specimens the cracks dominantly passed through the interlayer interfaces. In splitting tensile tests, the printing-generated interfaces of the split U specimens were visually distinguishable. However, the layers in the L specimens were interlaced with the adjacent layers, albeit being hardly distinguishable in the split specimens.

5. Poisson's ratio values of the lower parts of the specimens were larger than the upper parts, though this variation was not as significant as those observed in

compressive strength, tensile strength or elastic modulus values. Depending on layer orientation and the presence of higher permeable voids, nonlinear Poisson's ratio response was observed in some of the U specimens in the elastic range.

6. Regarding the four-point bending tests on 3DPC beam specimens, the response of beams with vertically oriented layers (i.e. layers oriented parallel to the loading direction) demonstrated the lowest load-carrying capacity due to the weakness in the interlayer bond. Alternatively, when the printed layers were oriented perpendicular to the loading direction, the load-carrying capacity of the beams approached the cast beam's response.

7. With respect to the direct shear tests on beam specimens with layers oriented parallel to the loading direction, it was observed that the shear strength of the cast and 3DPC beams were very similar, demonstrating a nearly perfect bond in shear between the printed interlayers.

8. Anisotropic thermal conductivity was observed, where the thermal conductivity ratios of λ_Y to λ_Z and λ_Y to λ_X were calculated as 1.23 and 1.12 for the lower part and 1.21 and 1.08 for the upper part of the wall, respectively. In general, the upper part of the wall revealed lower thermal conductivity than the lower part, which was caused by the presence of more permeable voids in the upper parts of the wall.

While the extruded material was the same, the 3D printing process of concrete opposing gravity direction caused significant variations in material properties during the hydration process, which was associated with the pressure exerted by the self-weight of the subsequently printed layers on the earlier ones and the increase in mix viscosity due to pump heating for increased printing time. The presence of voids between the interlayers and the resulting interlayer bond strength, especially in tension, resulted in significant variations in material properties. Therefore, conducting large-scale and real-size experiments on 3DPC structures plays a critical role in understanding the true response of cementitious materials, which will ease the standardization process of 3DPC in the construction industry.

CHAPTER 4

EXPLORING THE FABRIC: MICRO AND MESO SCALE INVESTIGATION OF POROSITY AND INTERLAYER EFFECTS IN 3D PRINTED CONCRETE

4.1 Introduction

The intricate mechanical behavior of 3D printed concrete (3DPC) is influenced by a myriad of factors, encompassing raw material composition, mix design, printing process intricacies, and printer components such as nozzle type. Various researchers have conducted extensive reviews on the mechanical performance and key parameters affecting the mechanical behavior of 3DPC [2,3,75,77,80], as elaborated in Chapter 1 and Chapter 3. In contrast to the discussions Chapter 1 and Chapter 3, this chapter delves into specific aspects, namely the impact of porosity, the influence of interlayer strength. These aspects can significantly shape the hardened properties of 3DPC, providing critical insights into its overall performance.

The interlayer effect and capacities are numerically investigated by [108,112], incorporating a traction-separation law. Among these, Xiao et al. [108] studied the strength differences observed by researchers numerically. The findings demonstrate that horizontal shear deformation between printed layers reduces compressive strength, while tensile strength at the mid-span primarily influences flexural strength. The study reveals that variations in anisotropy under compression and flexure are influenced by the number of interfaces and the tensile and shear properties of the interface between printed filaments.

Numerous investigations have indicated a decrease in tensile bond strength with prolonged rest time. The term "rest time" refers to the duration in which the freshly mixed concrete undergoes a loss of its initial properties within the printer before the printing process [28,30,78,79,111,113,114]. Panda et al. [113] investigated the impact of different printing parameters, including printing time gap, printing speed,

and nozzle standoff distance, on the bond strength of interlayers in geopolymer. The key findings of this study are succinctly presented in Figure 4.1. The experimental results emphasize that, for the same material batch, a larger time gap between layers leads to reduced strength, while the effects of printing speed and nozzle standoff distance are more significant at lower values. Moreover, the mean tensile bond strength diminishes as the nozzle speed rises. This is attributed to the fact that higher speeds make it easier to generate voids.

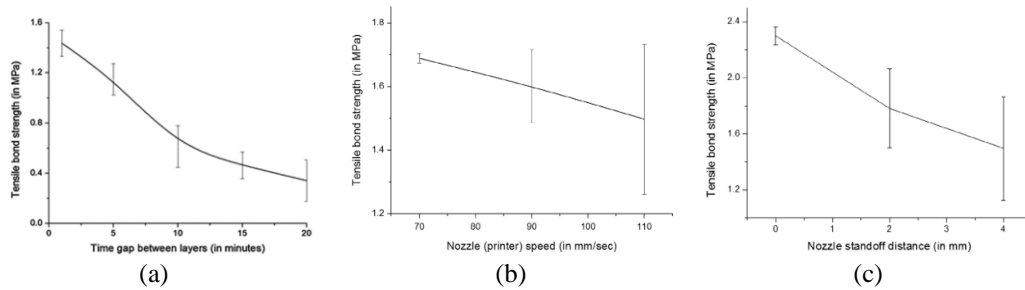


Figure 4.1. Impact of Printing Parameters on Bond Strength: (a) Varying Time Gap, (b) Printing Speed, and (c) Nozzle Standoff Distance [113]

Beyond this aspect, other researchers have explored the impact of moisture content on interlayers [109–111,115]. Sanjayan et al. [110] investigated the effect of surface moisture on the interlayer strength of 3D printed concrete. Their study revealed that the interlayer bond strength initially decreased due to surface evaporation, followed by an increase in bond strength due to bleeding of the concrete, where the surface gained moisture, with an increasing rest time. Consequently, these studies concludes that moisture content significantly influences bond strength.

Furthermore, researchers have examined various nozzle types, comparing their advantages and disadvantages. They have also investigated the impact of nozzle types on the mechanical properties of 3DPC [116–121]. The advantages of using a circular nozzle compared to a rectangular nozzle are that the circular nozzle is suited for complex shapes, providing more freedom of movement. The disadvantages include low compactness and contact area, a lack of adhesion between layers, resulting in more voids, and low surface quality with wavy edges. Paul et al. [4]

compared the issues arising from using circular and square nozzles in Figure 4.2-a and Figure 4.2-b. The study briefly highlights the strength variation between circular and rectangular nozzles, noting that circular nozzles tend to create voids in the printed object, potentially negatively impacting compressive strength. In contrast, rectangular or square nozzles exhibit fewer issues in this regard.

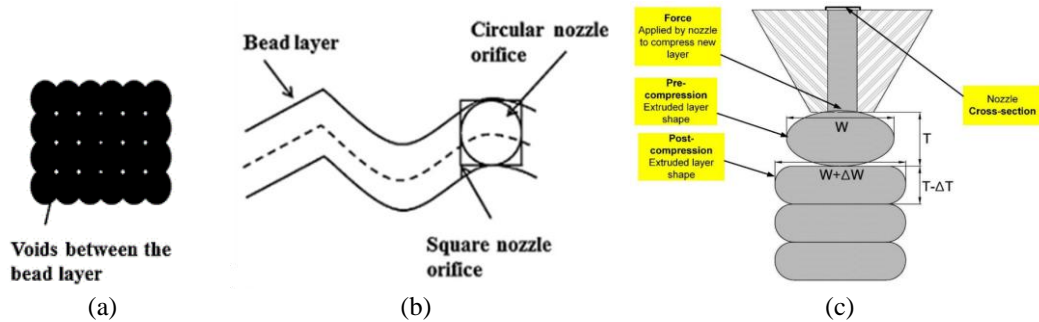


Figure 4.2. Challenges Arising from Using Circular and Square Nozzles: (a) Voids Between the Circular Bead Layers [4], (b) Misalignment of Bead Layers due to the Nozzle [4], and (c) Schematic Illustration Depicting the Flow of Printed Mortar Through the Circular Nozzle Problems [118]

In another study [118], the results for flexural strength indicate that a rectangular or square shape consistently outperforms a circular nozzle print. This observation aligns with another study that investigated the compressive strength of 3DPC using circular and rectangular nozzles [122].

Figure 4.2-c [118] illustrates the evolution of shape, width ($W + \Delta W$), and thickness ($T - \Delta T$) during printing using a circular nozzle. The extruded layers revert to their original shapes, with the first layer undergoing continuous changes until stability is achieved. The final layer maintains its shape. Area variations during pre-compression and post-compression stages are affected by rheology, mix proportions, and subsequent layer impact. Detailed cross-sectional area changes based on printing parameters are provided in Figure 4.2-c [118]. As a result of these cross-sectional area changes, voids between the layers are formed. Examples of these voids were encountered by many researchers, and the figures from some of these researchers' studies are incorporated into Figure 4.3. In Figure 4.3-a, the comparisons between rectangular and circular nozzle is highlighted. Voids are emphasized in Figure 4.3-

b, Figure 4.3-c, and Figure 4.3-d. While Figure 4.3-c and Figure 4.3-d showcase good printing examples, it's noteworthy that the detailed printing parameters for achieving these positive outcomes are not provided in these studies. Other than these studies, Zhang et al. [123] highlighted those continuous voids by using Computed Tomography (CT) images.

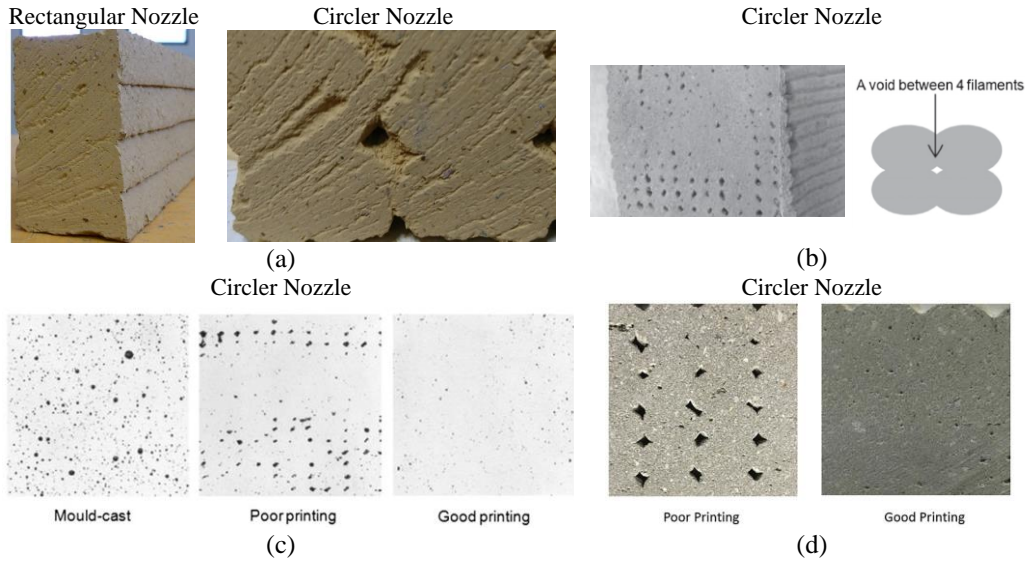


Figure 4.3. Example Figures of Void Formation Between Layers due to the Use of Circular Nozzle (Taken from (a) [122], (b)-(c) [78], and (d) [31])

Tay et al. [79] indicated that an increasing time-gap leads to more voids in the interlayers. Examination of the bond cross-section reveals minimal voids in the interlayers for the 1-minute specimen (Figure 4.4-a). With increasing time-gap, voids become more evident (Figure 4.4-b to Figure 4.4-d). Short time-gaps promote interaction and bonding at the interface, while longer time-gaps result in deformities and voids due to insufficient interaction between layers and disturbances during the printing process. In the study by Tay et al. [79], a rectangular nozzle was used, indicating that void formation between layers is independent of the nozzle type in this case.

In a study conducted by He et al. [121], it was observed that the rectangular nozzle has a slightly smaller notch angle, as depicted in Figure 4.5, compared to the circular nozzle. Contrary to expectations, the study found that the circular nozzle generates

stronger interlayer connections compared to the rectangular nozzle. Additionally, He et al. [30] analyzed the impact of interlayer notch and shear stress on interlayer strength using experimental and numerical simulation methods. The findings indicated that reducing the interlayer notch and increasing the interlayer shear stress contribute to improving the strength between layers.

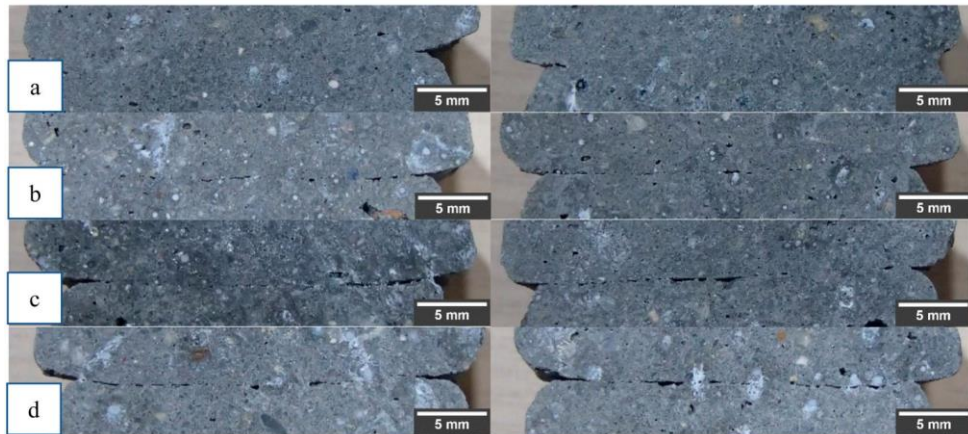


Figure 4.4. Sample Printed by Rectangular Nozzle at (a) 1-Min Time-Gap, (b) 5-Min Time-Gap, (c) 10-Min Time-Gap, and (d) 20-Min Time-Gap, Illustrating the Impact of Time-Gap on Printed Samples [79]

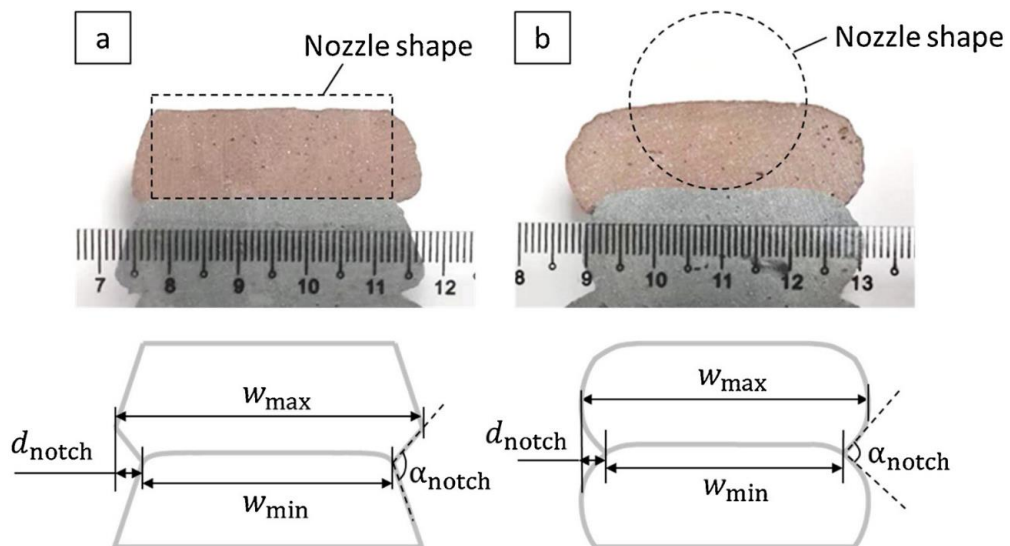


Figure 4.5. The Cross-Sectional Geometries Achieved by the (a) Rectangular and (b) Circular Nozzles [121]

Considering the aforementioned observations, the impact of pore characteristics on the mechanical behavior of 3DPC is explored by [124–128] using computed tomography. Studies [125–128] indicate that irregular-shaped pores are more prevalent in 3DPC than in cast concrete. Chen et al. [126] stated that irregular-shaped pores are predominantly found between layers, possibly due to the merging and overlapping of layers inherent in the printing process. The study showed that pores tend to be more irregular with increasing size, while smaller pores exhibit a more circular shape. In the studies of by Heever et al. [127] and by Liu et al. [128], the theoretical and analytical aspects of these porosities are investigated by simplifying their irregular shape to an ellipsoidal form. However, these approaches do not explain the effects of localized pores between layers in 3DPC, commonly observed in the field due to the nature of concrete printing, especially with circular nozzles as summarized in Figure 4.2 and Figure 4.3. Therefore, this study aims to investigate these localized pores between layers. To delve into these localized porosities, CT scans are utilized. These CT scans are derived from cylindrical samples extracted from both the upper and lower parts of a 2.35 m wall shown in Figure 3.4, in addition to cast cylindrical samples. The selection of these specific locations ensures a representative exploration of the structural variations along the height of the wall, offering valuable insights into the observed anisotropic behavior of 3DPC structures. Porosity analyses are meticulously conducted on the CT images, offering a detailed exploration of the nature and distribution of these pores. The CT images are further reconstructed into 3D images, facilitating thickness analysis to highlight the spatial characteristics of the observed porosities. Smoothened porosity distributions are then presented, informing the creation of a simplified geometry that encapsulates these porosities.

Finite element analyses are subsequently conducted to elucidate the impact of these simplified geometries, and the results are meticulously compared with the experimental findings presented in Chapter 3, considering both the lower and upper parts of the wall. The findings unequivocally reveal that these localized porosities act as triggers for tensile damage, consequently diminishing the overall strength of

3DPC structures in most cases. To supplement these findings, additional analyses are carried out through finite element simulations, adopting the traction-separation law. This comprehensive approach sheds light on both localized porosities and interlayer effects, providing a nuanced understanding of their influence on the structural behavior of 3DPC.

4.2 Mix Design and Sample Preparation

The foundation of the study lies in the thoughtful mix design and meticulous sample preparation, building upon the parameters detailed in Chapter 3. This section provides a succinct overview of the mix design process and the steps taken for sample preparation, ensuring a seamless continuity with the earlier experimentation.

4.2.1 Mix Design

The same mixture in Chapter 3 was used for the current study to print the walls. The mixture consisted of 820 kg CEM II/A-M (S-L) 42.5R (obtained from OYAK Cement Factory), 1230 kg silica sand with a maximum particle size of 1.5 mm, 26.5 kg of a calcium formate-based additive, 16.5 kg of a superplasticizer, and 0.65 kg of monofilament micro polypropylene fibers. The water-to-cement (w/c) ratio of the mix was 0.32, and the mixture was designed to prevent shrinkage cracks by incorporating fibers with specific properties (Table 3.1). The particle size distribution of the fine aggregates was determined by sieve analysis and shown Figure 3.2. The compressive strength of the mixture was determined by casting \varnothing 10cm cylinders and testing them at 28 days, resulting in an average strength of 37.0 \pm 2.1 MPa.

4.2.2 Sample Preparation

The focus of this chapter revolves around Wall-1, and the sample preparation process adhered to the dimensions outlined below:

4.2.2.1 Printing Process

Wall-1, with dimensions of 26×200×235.5 cm, was fabricated utilizing ISTON's 6-axis printer, as depicted in Figure 3.3-a. The printer's nozzle, featuring a 5 cm round opening, extruded a 6.5 cm wide and 1.5 cm thick concrete layer. The concrete pump applied pressure in the range of 25-30 bar, with an extrusion speed of 100 mm/sec. The printing paths for Wall-1 are illustrated in Figure 3.3-b, showcasing the intricate layering process. The wall was constructed with 4 horizontal and 157 vertical layers, completed in 280 minutes.

4.2.2.2 Sample Types

Table 4.1. Mechanical Properties of Printed and Cast Concrete

Material Properties	Compressive Strength (MPa)	Elastic Modulus (GPa) and Poisson's Ratio			Tensile Strength (MPa)
	ASTM C39 [93]	ASTM C469 [98]			ASTM C496 [99]
Printed Concrete Wall (Upper Part)	$\sigma_x = 38.2 \pm 5.4$ $\sigma_y = 30.8 \pm 1.2$ $\sigma_z = 22.7 \pm 1.9$	$E_x = 18.5$ $E_y = 13.6$ $E_z = 14.4$	$\nu_{xy} = 0.20$ $\nu_{yx} = 0.17$ $\nu_{zx} = 0.17$	$\nu_{xz} = 0.20$ $\nu_{yz} = 0.18$ $\nu_{zy} = 0.23$	$\sigma_{T1} = 1.8$ $\sigma_{T2} = 1.6$
Printed Concrete Wall (Lower Part)	$\sigma_x = 50.6 \pm 2.6$ $\sigma_{y,D} = 53.2 \pm 5.4$ $\sigma_z = 47.3 \pm 3.0$	$E_x = 20.2$ $E_y = 20.8$ $E_z = 17.5$	$\nu_{xy} = 0.23$ $\nu_{yx} = 0.17$ $\nu_{zx} = 0.17$	$\nu_{xz} = 0.21$ $\nu_{yz} = 0.19$ $\nu_{zy} = 0.21$	$\sigma_{T1} = 2.5$ $\sigma_{T2} = 3.1$
Cast Concrete	$\sigma = 37.8 \pm 3.2$	$E_x = 18.8$	$\nu = 0.21$		$\sigma_T = 3.2$

From Wall-1, cylindrical cores with a diameter of 10 cm were meticulously extracted for comprehensive analysis. These cores were obtained from both the upper (U) and lower (L) halves of Wall-1, focusing on two distinct directions: X (printing direction)

and Z (translation direction), as illustrated in Figure 4.6-a. The core extraction points were strategically chosen, aligning with interstrip and interlayer interfaces, as detailed in Figure 3.4. The mechanical properties of these samples investigated in Chapter 3 are summarized in Table 4.1.

To investigate the concrete structure at two different scales, scans were performed using both macro-CT (X-CT) and micro-CT (μ -CT) techniques. The cores used for macro-CT analysis were subjected to X-ray scans. This macro-CT analysis aimed to offer insights into larger-scale features, enhancing the understanding of the concrete's internal structure.

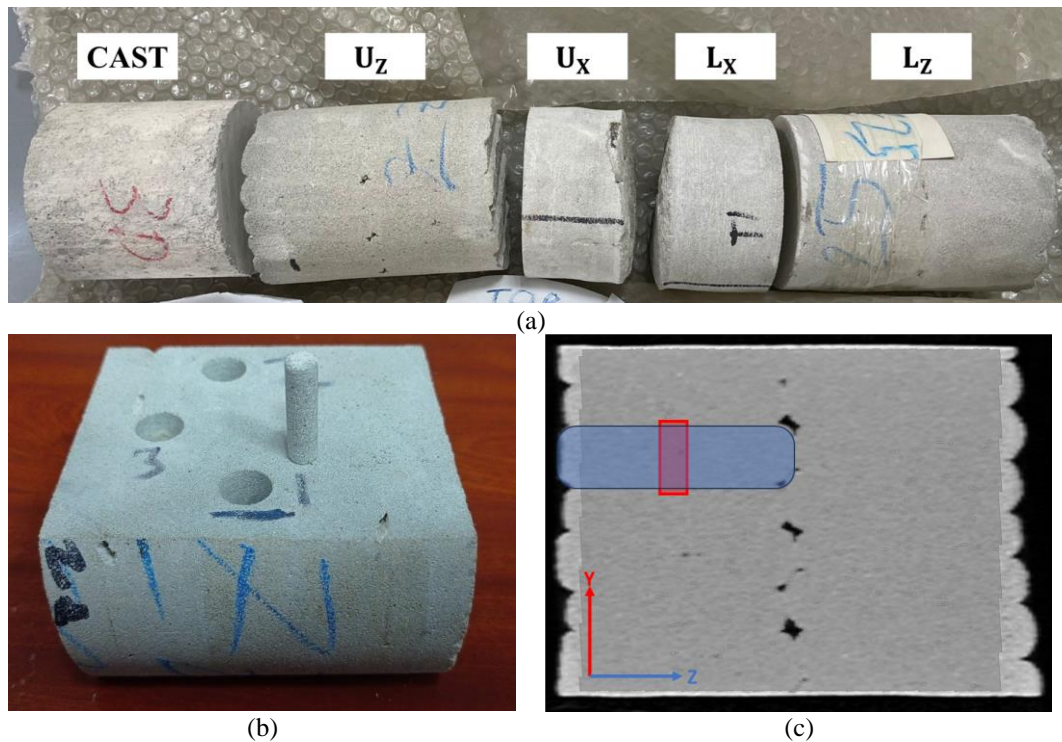


Figure 4.6. (a) Cored CT-Samples, (b) Micro CT Sample, and (c) the Location of Micro CT sample Highlighted by Red (Blue is a Concrete Filament)

In parallel, for micro-CT investigations, cylindrical specimens with a reduced diameter of $\varnothing 0.75$ cm and a height of approximately 1.5 cm were meticulously prepared. This involved drilling through the flattened surface of the core halves in the Y (Deposition) direction, as depicted in Figure 4.6-b. The drilling process specifically targeted the center of the filaments, denoted by the blue area in Figure

4.6-c. The resulting μ -CT samples, crucial for capturing finer details, are indicated by the red area in Figure 4.6-c.

For the purpose of comparative analysis, control samples, both $\varnothing 10$ cm and $\varnothing 0.75$ cm in diameter, were included in the study. These control samples provide a baseline for evaluating the results obtained through macro-CT and micro-CT techniques.

4.3 Computed Tomography (CT) Analysis

4.3.1 CT Analysis Procedures

In this study, CT scans at two different scales were conducted, as summarized in Table 4.2. Scans of $\varnothing 0.75$ cm cores were conducted using a micro-CT scanner, SkyScan 1272, at Hunitek Laboratory. The micro-CT scans were performed at a voltage of 80 kV and a current of 125 μ A, with a finer voxel size ranging between 9-10.5 μ m. The analysis of these micro-CT scans was carried out using Bruker Micro-CT Software CT-Analyzer (CTAn) Version 1.20.3.0, providing a detailed understanding of overall porosity. Additionally, scans of $\varnothing 10$ cm cores were acquired with a Siemens Somatom Definition AS at the National Cheng Kung University Hospital. The scans consisted of slices at 1 mm intervals, conducted at a voltage of 120 kV and a current of 200mA, with a voxel size of 460.5 μ m. The processing of these scans was performed using 3D Slicer 5.2.1 software [129], enhancing the ability to comprehend larger pores within the concrete structure.

Table 4.2. CT Scans on Hardened Concrete

Test	Specimen (cm)	Voxel Size (μ m)	Age (day)	Software
μ -CT	$\varnothing 0.75 \times \sim 1.5$	9-10.5	360	CTAn
X-CT	$\varnothing 10 \times 15$	460.5	360	3D-Slicer & Rhino

Porosity analysis using the μ -CT images was performed with CTAn. The analysis involved carefully selecting a region of interest and the outer layer is trimmed all around the surface to eliminate any potential errors at the edges. Custom processing

was applied over the volume of interest (VOI) of each specimen. First, median filtering with a round kernel radius of 1 was applied in 3D space. This filtering technique helps in reducing noise and preserving the edges of the structures. To convert the image to binary, lower grey threshold was set to around 24, and upper grey threshold was set to 255, providing a clear distinction between the pore spaces and the solid structure. De-speckling in 3D space was applied to remove small erroneous speckles, and a sweep was performed to identify seemingly disconnected pores by removing all except the largest pore. 3D analysis was performed to obtain the number of closed pores and porosity information, including structure separation (i.e., pore size distribution).

In the Macro-CT analysis, the scans of $\varnothing 10$ cm cores were processed using 3D-Slicer. The analysis involved carefully selecting a region of interest and the outer layer is trimmed all around the surface to eliminate any potential errors at the edges. A defined threshold range (735 - 2815 for concrete and -1023.26 to 735 for pores) aided in distinguishing between concrete and pore spaces. The 3D images were then exported to Rhino for further evaluation. In Rhino, a thickness analysis was conducted on the reconstructed 3D pore structure through meshing. The thickness analysis in Rhino [130] employed a false-color display to assess the thickness of the solid. This process calculated the distance from each vertex to the 'other side' of the mesh and assigned colors accordingly. The analysis provided a detailed understanding of thickness distribution within the pore structure. This thorough analysis offered valuable insights into the internal characteristics and distribution of thickness within the concrete sample.

4.3.2 CT Analysis Results

The μ -CT scans of $\varnothing 0.75$ cm specimens allowed better understanding of the matrix porosity (Figure 4.7). The obtained porosity distributions for each of the three samples is shown in Figure 4.8. Here, the pore size is expressed as an equivalent diameter obtained from a circumscribed sphere of equal volume to that of the pore.

All of the obtained porosity distributions from the μ -CT scans (Figure 4.8) were right-skewed, with pore diameters in the range 0.02 – 0.5mm for the cast and 0.02 – 0.4mm for the printed samples. The cast specimen contained large pores not observed in the printed counterparts and was characterized with a broader spectrum of pore dimensions. Although the upper specimen had a larger total porosity than the cast one, it did not contain large pores, possibly due to the pressure during extrusion which can break larger voids into smaller ones (Table 4.3). The lower specimen had the lowest total porosity and showed significantly higher closed and lower open porosity compared to other samples. It is important to note that these results are limited to a small section of the specimen and may not represent the overall porosity in full scale. Additionally, the voxel size of the μ -CT analysis, which was around 10 microns, may not be small enough to accurately determine whether these closed pores are truly impermeable or if they could become open pores at a smaller voxel size. This mechanism was extensively discussed in Chapter 3, where the experimental results from ASTM C642 were utilized for a detailed analysis.

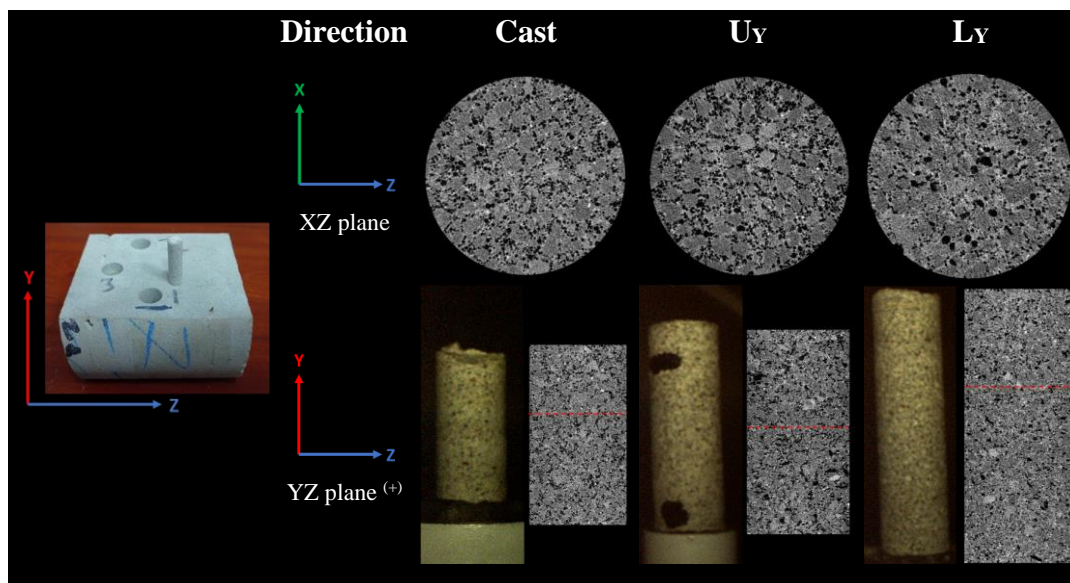


Figure 4.7. (Top) μ -CT Slices and (Bottom) Reconstructed Cross Sections of Cast, U_Y, L_Y \varnothing 0.75cm Samples - ⁽⁺⁾ Dashed Red Lines Mark the Location of the Selected Slice

Additionally, Figure 4.9 presents the distribution of porosity along the height of the printed specimens, based on an extensive analysis comprising approximately 1600 tomograms. Each data point represents the average porosity over a segment of around 0.29 mm in height, calculated from a subset of 30 tomograms. The absence of a significant trend in porosity along the height of the specimens suggests a lack of pronounced interlayer effects within the observed range. It's important to note that the analysis focused on smaller pores, and while no substantial interlayer-related porosity was observed in this context, the potential influence of larger pores will be explored in the forthcoming macro-CT analysis, as discussed later in this chapter.

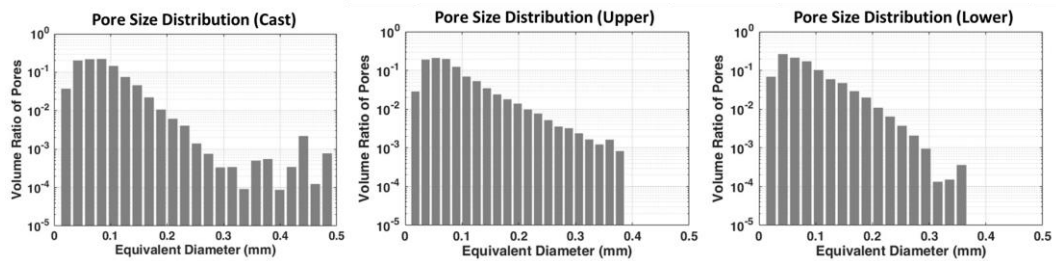


Figure 4.8. Pore Size Distribution Estimated on μ -CT Samples (*) The Pore Size is Expressed as an Equivalent Diameter Obtained from a Circumscribed Sphere of Equal Volume to That of the Pore

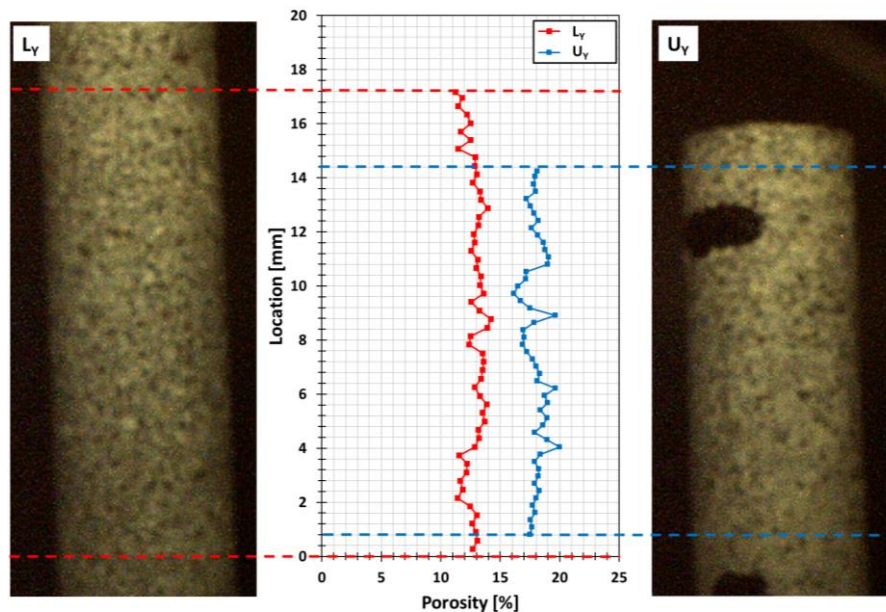


Figure 4.9. Porosity Distribution Along Printed Specimens' Height

Figure 4.10 presents the 3D reconstructed μ -CT analysis results for both cast and printed concrete samples. Clearly, the cast sample exhibits more circular porosities compared to the printed concretes. Additionally, the porosities in the upper samples are larger and wider than those in the lower samples, indicating that the self-weight caused larger voids to break into smaller ones. Conversely, the circularity of the porosities in the cast samples may be attributed to the application of vibration, which was not applied to the printed samples. As a result, the porosities in the printed samples are more irregularly shaped compared to those in the cast samples.

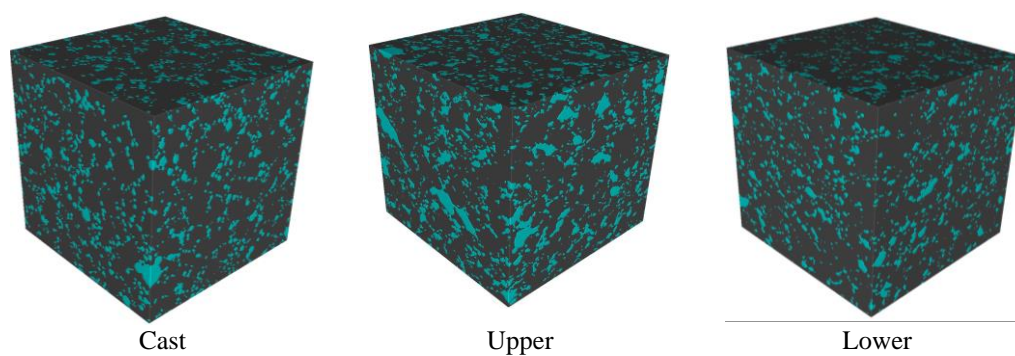


Figure 4.10. 3D Reconstructed μ -CT Analysis Results for Cast and Printed Concrete Samples (Each Edge of the Cubes is 4.5 mm – Pores are Highlighted by Cyan Color)

The macro-CT scans of $\varnothing 10$ cm specimens, which were utilized to understand larger pores, revealed distinct differences in pore characteristics of cast and printed concretes (Figure 4.11). The cast matrix exhibited larger and more irregularly distributed pores in contrast to the printed matrix in which the pores were smaller and sparser. This discrepancy can be attributed to the matrix compaction due to the extrusion process. Furthermore, the pores in the printed samples were predominantly concentrated at the interlayers and interstrips. Notably, the interstrip porosities were very dominant, as evidenced in regions of interest (ROI-1 and ROI-2) in Figure 4.11. These ROIs encompass areas including and excluding interstrips, respectively. The preeminence of porosity within the interstrips can be attributed to the selected printing path, extrusion speed, and nozzle type. The difference in the porosities of U and L samples was also significant (Table 4.3). The porosity of the L sample was significantly smaller than in the upper one, in both ROI1 and ROI2. The

difference was much more notable for ROI1, suggesting higher interlayer porosity for the U sample. This variation in porosity was mainly attributed to the limited compaction at the upper layers due to lower self-weight and progressively increasing concrete viscosity caused by heating of the pumping system over time.

Table 4.3. %Porosity from CT Scans: (Left) μ -CT and (Right) Macro-CT

Specimen Type	μ -CT on $\varnothing 0.75$ cm samples			Specimen Type	Macro-CT on $\varnothing 10$ cm samples		
	Open	Closed	Total		ROI - 1	ROI - 2	Overall
Cast	13.5	1.2	14.6	Cast	-	0.7	0.7
U _Y	16.7	1.2	17.6	U _Z	4.6	0.3	1.2
L _Y	7.9	4.9	12.3	L _Z	3.3	<0.1	0.7

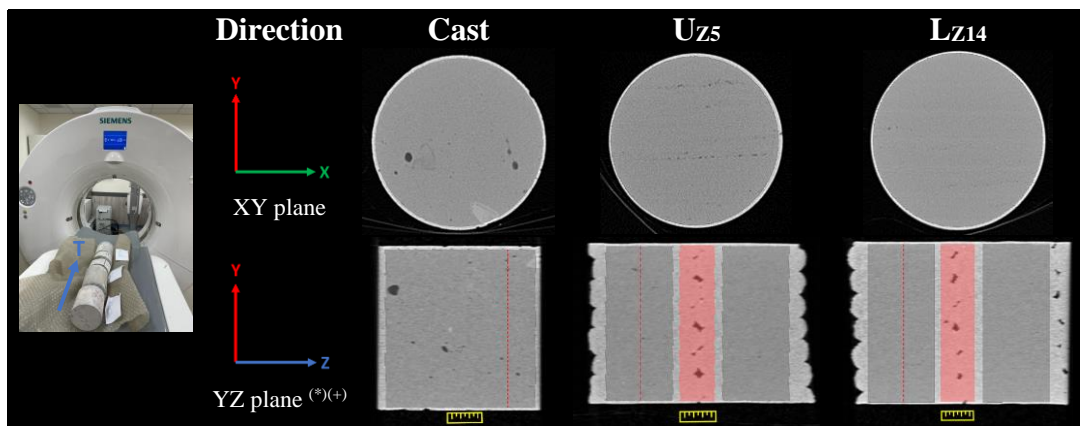


Figure 4.11. (Top) Macro-CT Slices and (Bottom) Reconstructed Cross Sections of Cast, U_Z, L_Z $\varnothing 10$ cm Specimens: (*) The Transparent Red and Black Areas Indicate the ROI-1 (Including Interstrip) and ROI-2 (Excluding Interstrip), Respectively. (+) Dashed Red Lines Mark the Location of the Selected Slice.

In Figure 4.12, the thickness analysis results reveal distinctive characteristics of the cast and printed concrete samples. The analysis highlights the distribution and shape of interlayer and interstrip pores, providing insights into the structural characteristics of the concrete specimens.

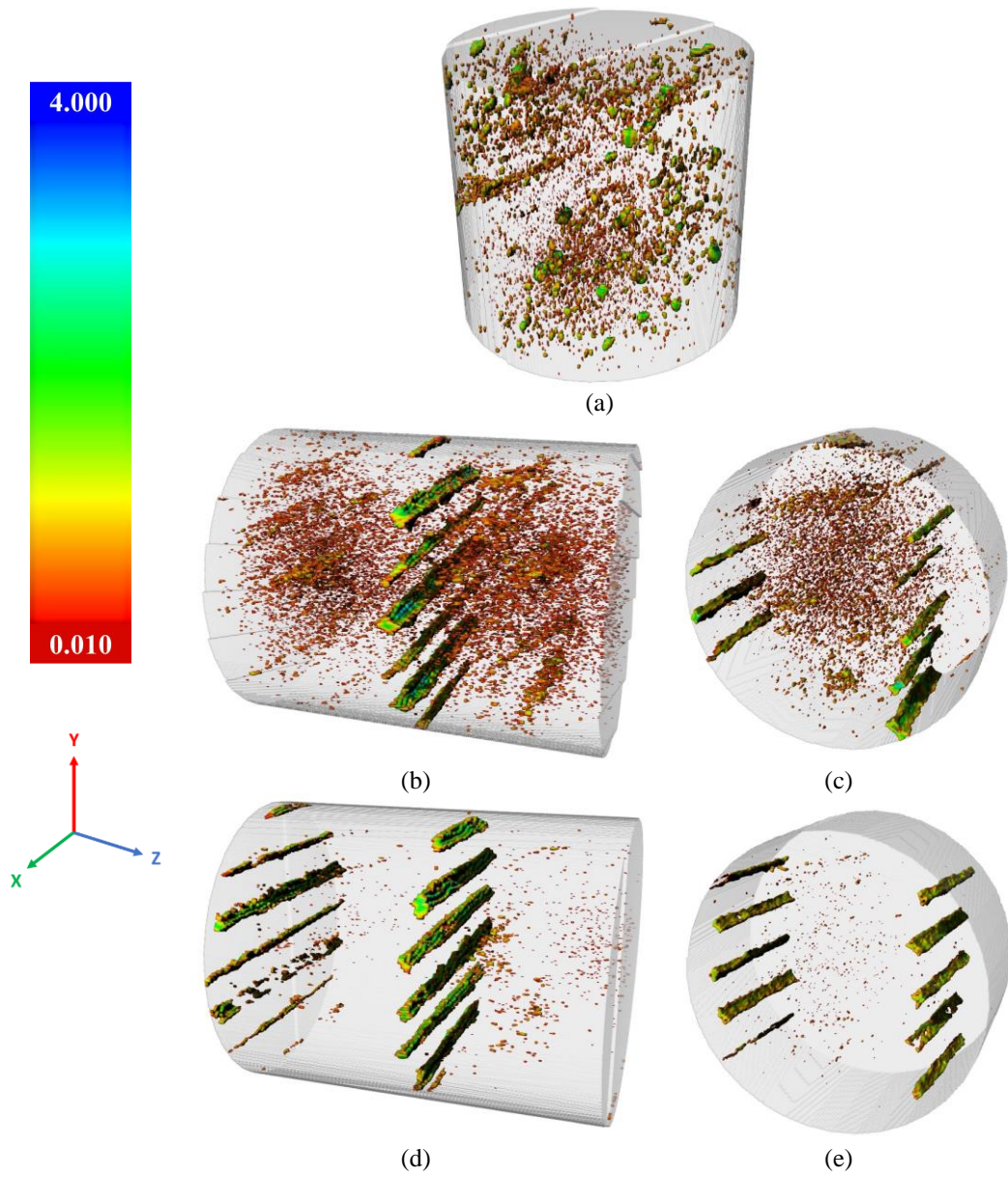
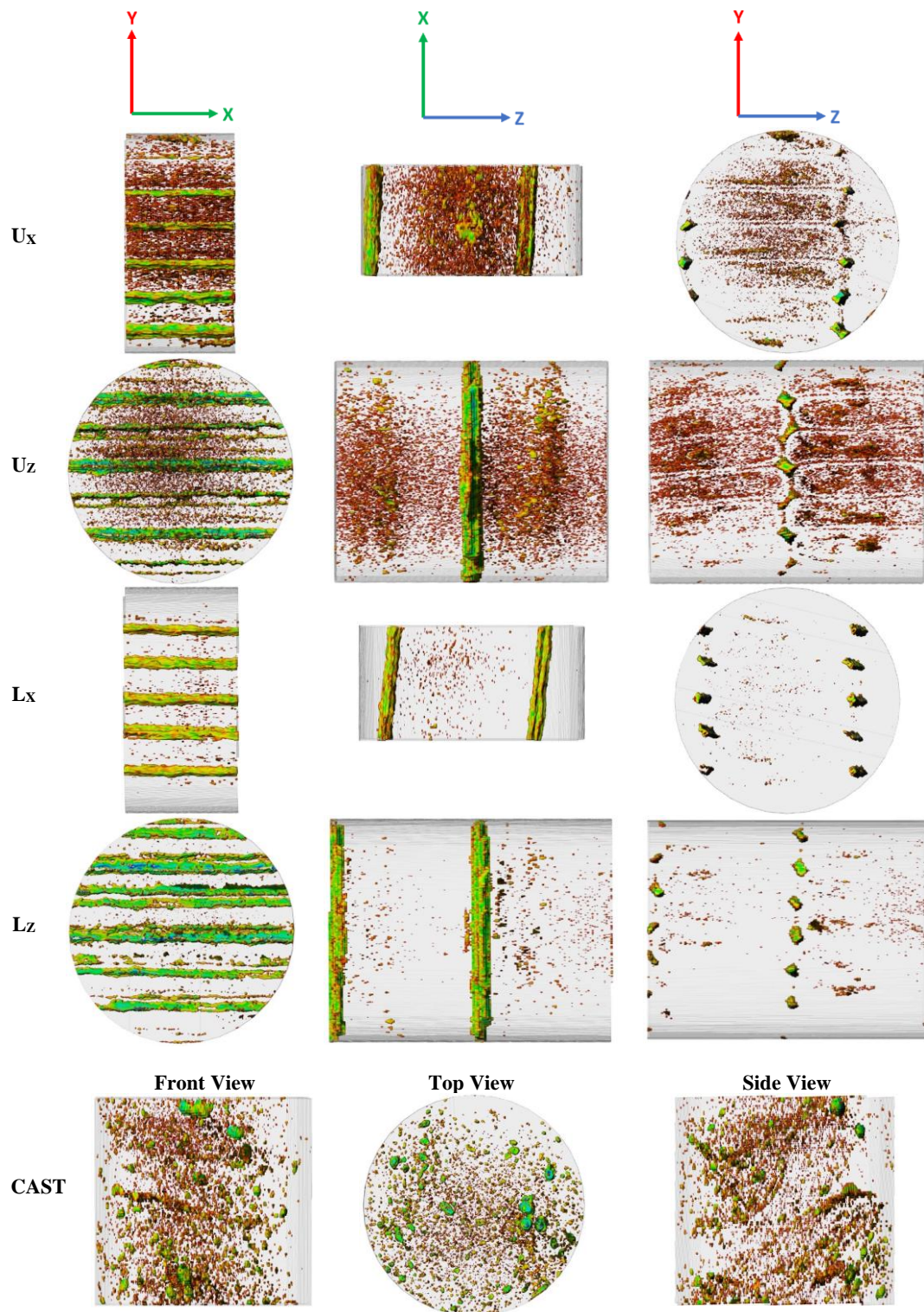


Figure 4.12. Thickness Analysis Results of Macro-CT Scans. (a) Cast and Printed Concrete, (b) U_z , (c) U_x , (d) L_z , (e) L_x Macro-CT Scans

Table 4.4. Cross-Sectional Views (XY, YZ, and XZ planes) of Porosities in 3D Reconstructed Macro-CT Analysis Results for Printed and Cast Concrete Samples



The cast sample exhibits randomly distributed pores with larger diameters, contrasting with the printed samples where prominent void channels are observed between interlayers and interstrips. These void channels may significantly influence the mechanical properties of the printed concrete. Furthermore, a comparison between upper (U) and lower (L) samples shows a notable reduction in the occurrence of small pores in the lower samples, highlighting the impact of factors such as self-weight or prolonged printing time, leading to an elevated temperature during the printing process.

The supplementary figures presented in Table 4.4 further illuminate noteworthy observations in the 3D reconstructed CT analysis results for printed and cast concrete samples. Beyond the evident void channels, a distinctive pattern in U samples emerges in the YZ plane, where the interlayer regions exhibit the smallest pores in their line. In contrast, irregularly shaped and larger pores predominantly manifest between the interlayers. This spatial distribution of pores, particularly in the interlayer context, adds a nuanced dimension to the understanding of porosity variations within the printed concrete matrix. Such insights contribute to a comprehensive appraisal of the intricate pore network, guiding implications for the material's mechanical characteristics and structural integrity.

4.4 Numerical Analysis Strategies

In order to gain deeper insights into the structural behavior of the printed concrete specimens, two distinct numerical analysis approaches were employed. These approaches were strategically designed to capture the complex interplay between material composition, printing processes, and resulting porosity characteristics. The first approach, detailed in Section 4.4.1, involves the simplification of porosities as imperfections. This method seeks to represent the inherent irregularities introduced by the porosity distribution within the printed concrete matrix as imperfections, allowing for a comprehensive structural assessment. Subsequently, in Section 4.4.2, the focus shifts to the second approach, where interfaces are defined using traction

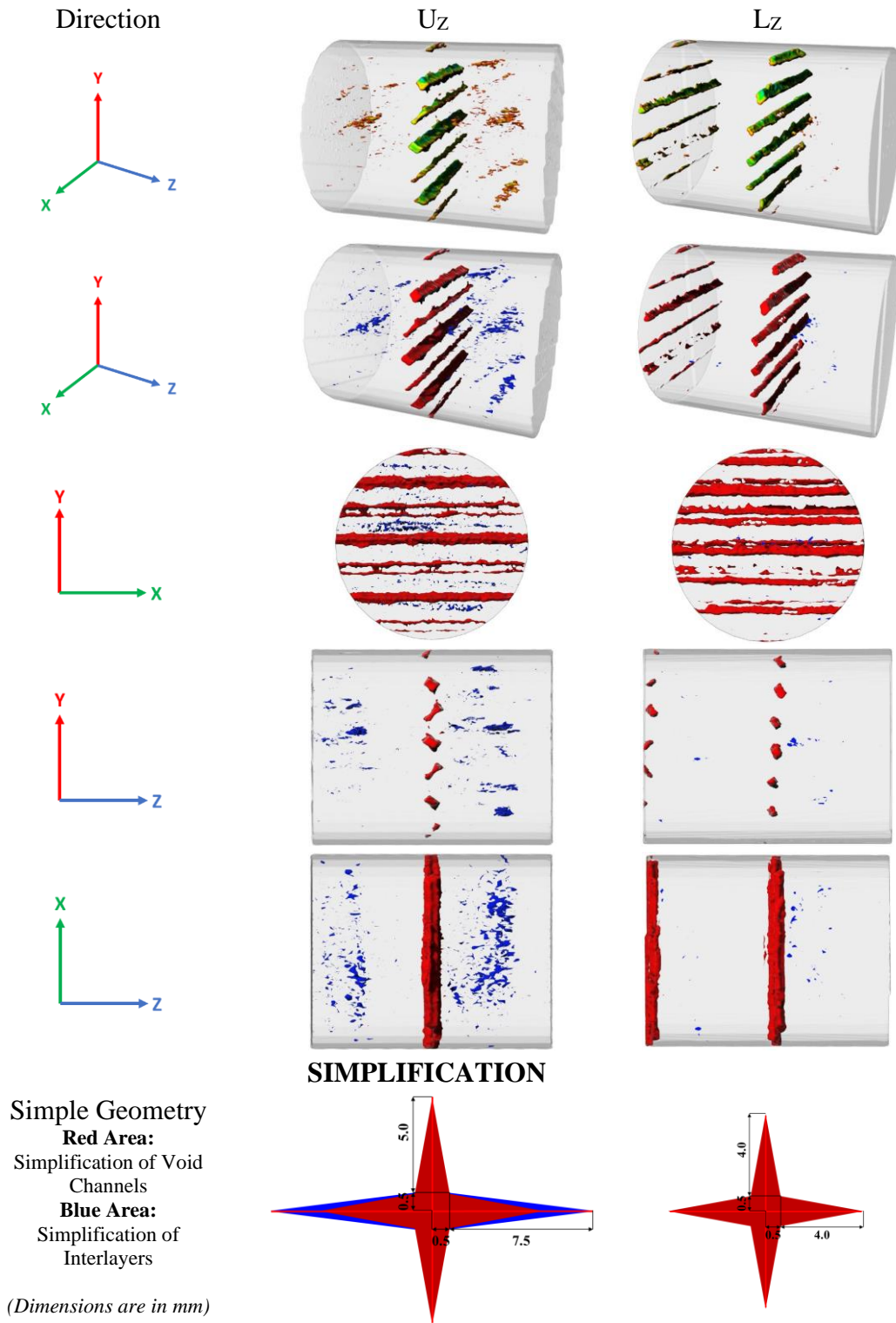
and separation laws. This approach delves into the intricacies of interface interactions, providing a more detailed representation of the unique properties and effects associated with the layered nature of the printed concrete structure. Together, these numerical analysis strategies contribute to a holistic understanding of the structural performance and resilience of the printed concrete under various loading conditions.

4.4.1 Approach 1: Simplification of Porosities as Imperfections

4.4.1.1 Porosity Simplification Procedure and Sampling

To accentuate and emphasize the dominant pores within the concrete matrix, a surface smoothing technique was employed using the 3D Slicer software [131,132]. This preprocessing step in numerical analysis enhances the visual clarity of irregularly shaped pores and void channels, isolating and highlighting the features of interest. The application of surface smoothing was instrumental in revealing the structural nuances of these dominant pores, laying the foundation for subsequent numerical analyses. Specifically, surface smoothing was applied to the CT scans of U_z and L_z samples' porosities to effectively mesh and reduce computational time. Given the three-dimensional nature of the circular-shaped samples and the highly non-linear material model used in the analysis, computational efficiency is crucial, necessitating a judicious simplification.

Table 4.5. Visualization of Smoothened Porosity in U_Z and L_Z Samples and Simplified Geometries



Based on the findings of Montero-Chacón et al. [133], the decision to use hexahedral elements in finite element analysis is grounded in the advantage of significantly reducing computational costs. The study suggests that modeling the material with a continuum damage plastic approach can be effectively implemented with hexahedral elements. This choice is motivated by the notable speed-up observed compared to other approaches, such as a tetrahedralized version, while still maintaining good agreement and obtaining similar results, particularly in the elastic and hardening regimes for quasi-brittle materials. Thus, the selection of hexahedral elements aligns with the goal of achieving computational efficiency without compromising the accuracy of results, as demonstrated in Montero-Chacón et al.'s research [133].

Table 4.5 provides a comprehensive visualization of the smoothed porosity and the resulting simplified geometries in U_z and L_z samples. The top section of the table showcases the thickness analysis results for the perspective views of U_z and L_z samples, providing insights into the overall porosity distribution. Subsequently, the perspectives, as well as the cross-sectional (XY, YZ, and XZ) views, are presented for both U_z and L_z samples.

To enhance clarity, areas of interest, including void channels and irregularly shaped coarse interlayer porosities, are highlighted in red and blue, respectively. These visual cues aid in discerning the dominant features within the concrete matrix, emphasizing the effectiveness of the smoothing and simplification process.

In the last row of the table, the simplified geometries of these highlighted areas are presented. The simplified geometries, symmetrically prepared in both axes highlighted by light red lines and the dimensions (in mm) of the quarter part of these simplified geometries are provided. The red and blue areas represent the simplified forms of void channels and irregularly shaped coarse interlayer porosities, contributing to a clearer representation of the key structural elements. This visualization is crucial for the subsequent numerical analyses, where these simplified geometries play a pivotal role in reducing computational complexity while preserving the essential characteristics of the concrete matrix.

Figure 4.13 provides a comprehensive depiction of the sampling procedure and pore simplification employed in the printed wall, all within a CAD environment. In Figure 4.13-a, a schematic representation showcases the wall with simplified pores strategically located at the corners of the filaments deposited by the printing nozzle. The illustration extends to include a representative filament and nozzle, offering a visual insight into the printing process. The samples' locations and coring directions are clearly delineated, providing a precise overview of the extraction process. Furthermore, Figure 4.13-b details the cored samples, emphasizing the spatial relationship between the extracted specimens and the intricate pore structures. These figures collectively serve as crucial references for understanding the origins of the samples, their correlation with the printed wall, and the rationale behind the simplification of pore geometries for subsequent numerical analyses.

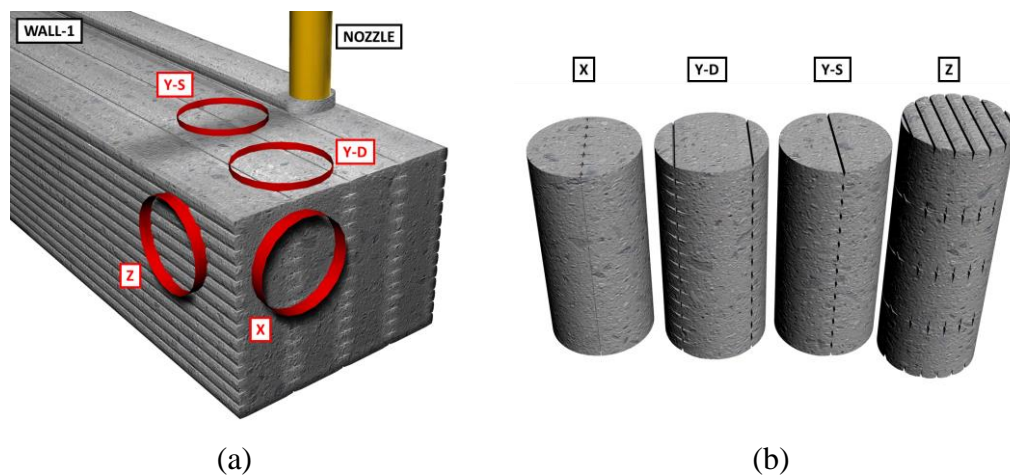


Figure 4.13. (a) Schematic Representation of Sampling Procedure and Pore Simplification in the Printed Wall and (b) Cored Samples in a CAD Environment

4.4.1.2 Numerical Analysis Details

To comprehensively explore the effect of these porosities on printed concrete samples, advanced numerical analyses were conducted using ABAQUS software. The Concrete Damage Plasticity model, specifically the Seanz stress-strain

relationship [134], was employed to capture the intricate behavior of the printed concrete matrix under various loading conditions.

In this numerical analysis, the material properties for the upper samples are modeled using the parameters obtained from the cast material, as extensively discussed in Chapter 3 and summarized in Table 4.1. For the lower samples, the material modeling strategy adopts the most favorable properties, leveraging the compressive strength of L_{Y-S} , and the elastic modulus of L_{Y-D} , all meticulously discussed in Chapter 3 and tabulated in Table 4.1. To simulate tensile behavior, a 6MPa tensile strength is applied exclusively to the lower samples. Additionally, special parameters, including dilation angle, eccentricity, biaxial loading ratio, coefficient K, and viscosity parameter, are defined in ABAQUS (for detailed information, refer to [135]). These parameters can be set to their widely accepted values as found in literature. A low viscosity parameter is beneficial for enhancing convergence speed within the concrete stress-strain curve's softening regime. The comprehensive material parameters for these models and plasticity parameters for concrete damage plasticity model are neatly compiled in Table 4.6.

Table 4.6. Used Material Properties

Material Model	Compressive Strength σ_{cu} - (MPa)	Tensile Strength σ_{tu} - (MPa)	Elastic Modulus E - (MPa)	Poisson's Ratio
Upper Sample	38	3.2	18800	0.21
Lower Sample	60	6	21000	0.21
Dilation Angle	Eccentricity	f_{b0}/f_{c0}	K	Viscosity Parameter
40	0.1	1.16	0.6667	0.0005

$$\sigma_c = \frac{E \times \varepsilon_c}{1 + \left[\left(\frac{E \times \varepsilon_{cu}}{\sigma_{cu}} \right) - 2 \right] \times \left(\frac{\varepsilon_c}{\varepsilon_{cu}} \right) + \left(\frac{\varepsilon_c}{\varepsilon_{cu}} \right)^2} \quad (4.1a)$$

$$\sigma_t = \sigma_{tu} \left(\frac{\varepsilon_{tu}}{\varepsilon_t} \right)^{0.7+1000 \times \varepsilon_t} \quad (4.1b)$$

$$\varepsilon_{tu} = \frac{\sigma_{tu}}{E} \quad (4.1c)$$

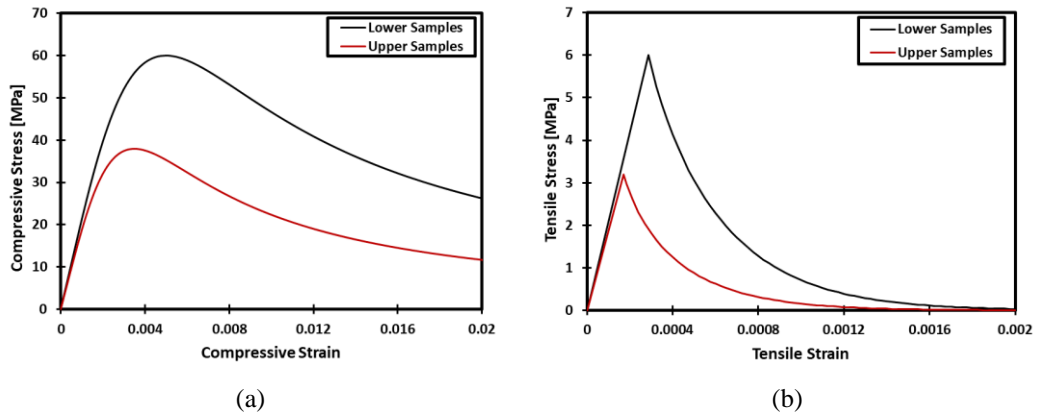


Figure 4.14. Generated Stress-Strain Curves in (a) Compression and (b) Tension

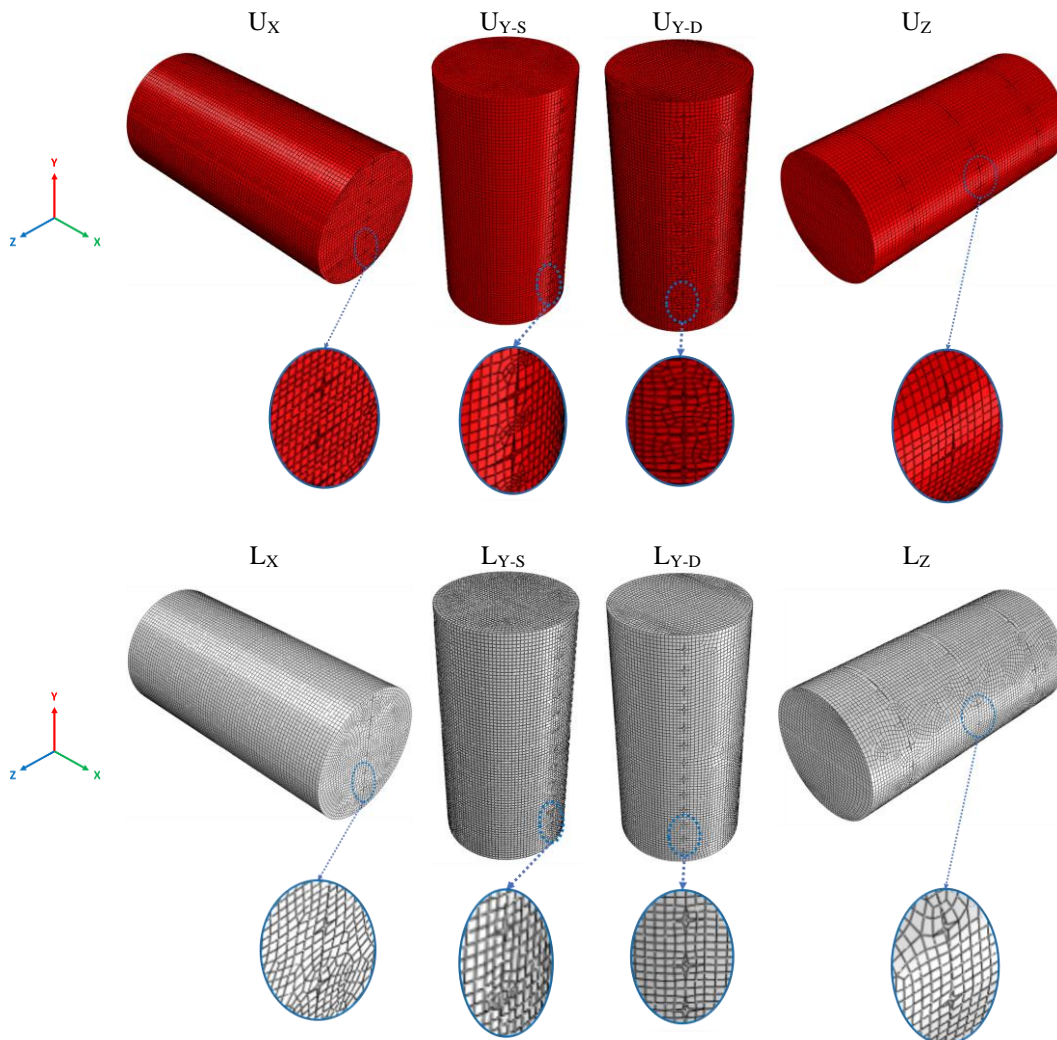


Figure 4.15. Generated Meshes for the Samples

The stress-strain characteristics, crucial for understanding the material response, are systematically portrayed in Figure 4.14. The accompanying formulas, encapsulated in Equations 4.1a, 4.1b, and 4.1c, detail the mathematical underpinnings used to generate the stress-strain curves under both compression and tension. Utilizing the parameters available in Table 4.6, a constitutive law for compression, as proposed by Seanz [134], is employed for material modeling in compression. The relationship between uniaxial unconfined compressive stress (σ_c) and strain (ε_c) according to this model is given in Equation 4.1a, where σ_c represents compressive stress, σ_{cu} is compressive strength, ε_c stands for compressive strain, ε_{cu} denotes compressive strain at peak stress, σ_{cu} , and E is the elastic modulus of the material.

The tensile stress (σ_t) and strain (ε_t) relationship was assumed to exhibit linearity up to the point of reaching the uniaxial tensile strength, σ_{tu} . Beyond this strength limit, the relationship was determined using the exponential function specified in Equation 4.1b provided in [136].

Employing the Abaqus static solver, the numerical simulations deploy C3D8R elements with an approximate mesh size of 2.5 mm. The generated meshes for each sample (Figure 4.13-b) are visually represented in Figure 4.15. To mimic real-world conditions, the boundary conditions dictate that both the bottom and top of the samples remain fixed, while displacement is strategically applied to the top during the analysis. These meticulous details form the cornerstone of the numerical analysis, providing a robust framework for evaluating the mechanical responses of the printed concrete samples under diverse loading scenarios.

4.4.2 Approach 2: Interface Model Using Traction and Separation Law

While Approach 1 simplifies the porosities as imperfections using the CDPM model for the bulk material, Approach 2 employs a detailed model for the interlayer and interstrip regions. To model interlayers and interstrips, the traction-separation law is employed.

Traction-Separation model available in Abaqus [137] for cohesive elements captures interface behavior by modeling an initial linear elastic stage followed by damage progression. This model is defined through an elastic constitutive matrix in Equation (4.2) that relates nominal stresses and nominal strains. The default initial thickness is set to 1, aligning nominal strain with separation. However, this constitutive thickness may differ from the actual geometric thickness, typically close to zero. The model considers normal, τ_n , and shear components, τ_s and τ_t , in the nominal traction vector, τ , and corresponding separations, δ , represent relative displacements at the interface δ_n , δ_s , and δ_t , respectively. Together with the initial thickness, these values define the initial elastic stage until damage initiation and evolution occur. Elasticity matrix in Equation (4.2) is the fully coupled elasticity matrix providing coupled behavior between all the traction and separation vectors. Setting off-diagonal part in the elasticity matrix to zero will provide uncoupled behavior between normal and shear components, which will be used in this study.

$$\tau = \begin{bmatrix} \tau_n \\ \tau_s \\ \tau_t \end{bmatrix} = \begin{bmatrix} K_{nn} & K_{ns} & K_{nt} \\ K_{ns} & K_{ss} & K_{st} \\ K_{nt} & K_{st} & K_{tt} \end{bmatrix} \begin{bmatrix} \delta_n \\ \delta_s \\ \delta_t \end{bmatrix} \quad (4.2)$$

Quadratic nominal stress criterion in Equation (4.3) is used as damage initiation criterion which refers to the beginning of degradation. In Figure 4.16-a, the peak tractions and separations in the pure loading cases for a cohesive layer's damage initiation are denoted by τ_n^0 , τ_s^0 , τ_t^0 and δ_n^0 , δ_s^0 , δ_t^0 , depending on the direction of deformation. Initially, the layer's thickness is set to 1, making strains simply the displacements between its top and bottom. Importantly, " $\langle \cdot \rangle$ " symbols called Macaulay brackets highlight that only tension or shear stresses, not compression, trigger damage. These terms lay the groundwork for understanding how damage begins in this model.

$$\left(\frac{\langle \tau_n \rangle}{\tau_n^0} \right)^2 + \left(\frac{\tau_s}{\tau_s^0} \right)^2 + \left(\frac{\tau_t}{\tau_t^0} \right)^2 = 1 \quad (4.3)$$

Once damage starts in a cohesive layer, its "stiffness" (resistance to deformation) gradually weakens. This process follows a specific law, different from bulk materials discussed in Chapter 2 but sharing similar concepts. A single "damage variable in traction-separation law" (D^{T-S}) tracks the overall effect, increasing from 0 (undamaged) to 1 (completely damaged) as stresses accumulate. Damage primarily affects tensile and shear stresses. These decrease proportionally with D^{T-S} , while compressive stress remains unaffected (no damage in compression). To understand how damage progresses under combined normal and shear forces, an "effective displacement" (δ_m) [138] in Equation (4.4a) is introduced that combines their individual contributions, which acts as the main driver for damage evolution.

$$\delta_m = \sqrt{\langle \delta_n \rangle^2 + \delta_s^2 + \delta_t^2} \quad (4.4a)$$

$$D^{T-S} = \frac{\delta_m^f (\delta_m - \delta_m^0)}{\delta_m (\delta_m^f - \delta_m^0)} \quad (4.4b)$$

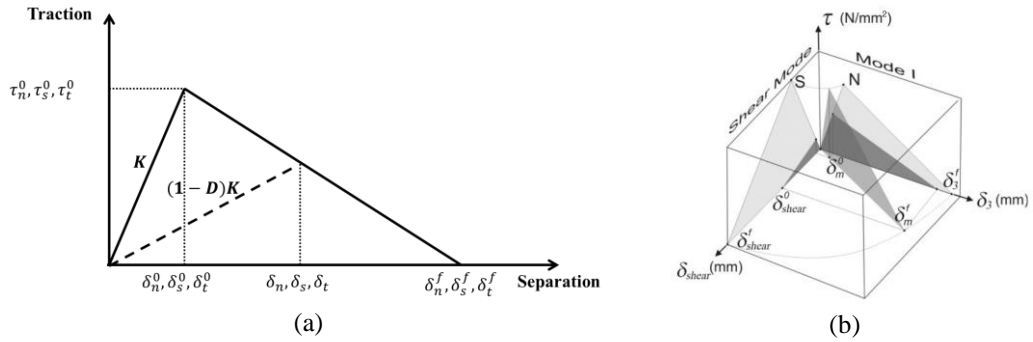


Figure 4.16. (a) Typical Traction-Separation Model, and (b) Illustration of Mixed-Mode Softening [138]

For bilinear cohesive model as shown in Figure 4.16-a, evolution of damage variable, D^{T-S} , beyond the initiation phase is modeled through the expression based on the work of Camanho et al. [138] in Equation (4.4b). Here, δ_m^0 and δ_m^f represent the effective displacements at the initiation of damage and complete failure, respectively. The term δ_m signifies the maximum effective displacement attained during the loading history. It's noteworthy that assuming a constant mode mix

between damage initiation and final failure is a customary approach for scenarios involving monotonic damage or fracture.

In Figure 4.16-b, a conceptual depiction illustrates the initiation and progression of damage concerning mode mix in a traction-separation response. The figure employs a three-part coordinate system, with traction represented along the vertical axis and magnitudes of normal and shear separations, indicative of deformation, plotted along the two horizontal axes. Unfilled triangles within the individual vertical planes illustrate the response to pure normal and pure shear deformation. Intermediate vertical planes, spanning the vertical axis, portray the damage response under mixed-mode conditions, reflecting different degrees of mode mix.

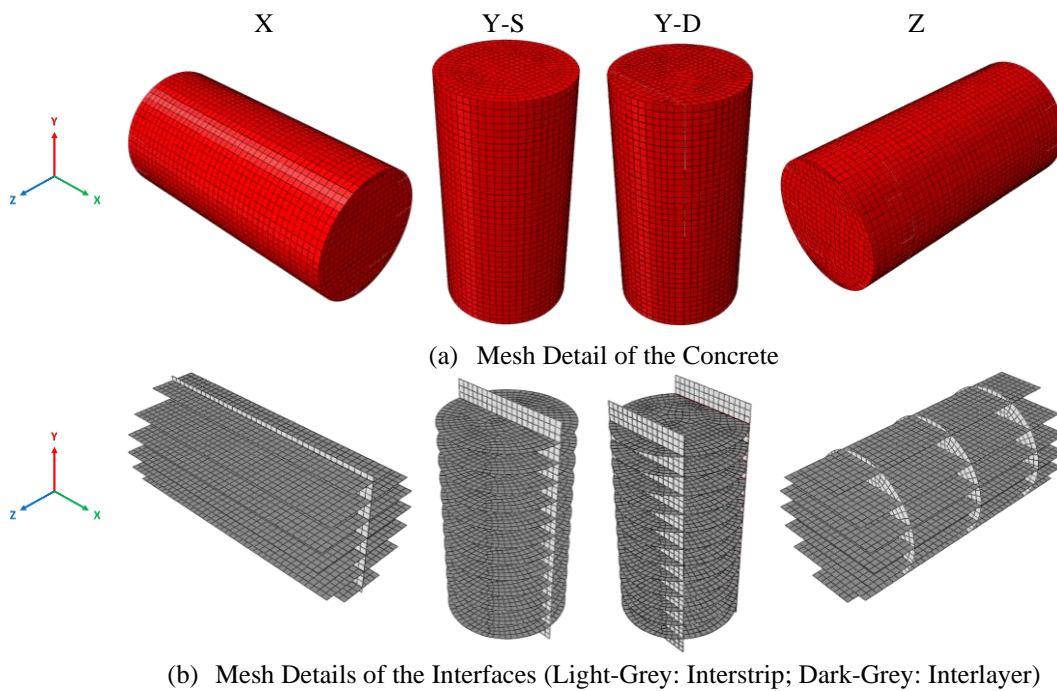


Figure 4.17. Generated Meshes for the Samples

In this approach, the numerical model utilizes C3D8R elements to represent the concrete material, while Zero-Thickness Cohesive elements (COH3D8) are introduced to model interlayer and interstrips employing the traction-separation law. Element deletion option for the cohesive element is active in all analysis. The

detailed mesh employed in this approach is presented in Figure 4.17, ensuring accurate representation of the geometry and facilitating convergence analysis. The Abaqus/Explicit solver is chosen for its suitability. The boundary conditions mirror those established in Approach 1 explained in the section 4.4.1.2, maintaining consistency in the simulation setup. To enhance the reliability of the results, a thorough mesh convergence analysis is conducted before the actual calculations, ensuring that the outcomes are not contingent on the mesh density.

Table 4.7. Traction-Separation Law Parameters for Interlayer and Interstrip Modeling

Location	Surfaces	τ_n^0	τ_s^0	τ_t^0	δ^f	K_{nn}	K_{ss}	K_{tt}	Viscosity Parameter
Upper (U)	Interlayer	2.00	1.10	1.10	0.007	5000	3750	3750	0.0001
	Interstrip	1.50	0.85	0.85	0.005	1600	1200	1200	0.0001
Lower (L)	Interlayer	3.10	3.50	3.50	0.020	12000	10500	10500	0.0001
	Interstrip	2.50	2.40	2.40	0.011	2100	1500	1500	0.0001

Table 4.7 encapsulates the specific parameters employed in the traction-separation law for this approach, delineating the numerical inputs that govern the damage initiation and progression in the cohesive elements. These parameters are systematically selected by numerical tests to best represent the response of 3DPC to various loading conditions.

4.5 Results & Discussion

This section presents the results of two numerical approaches aimed at quantifying the impact of dominant pores on the mechanical behavior of printed concrete samples. Approach 1 involves the simplification of porosities as imperfections, while Approach 2 focuses on defining interfaces using traction and separation laws.

In numerical analyses strategies, the compressive strength was determined by calculating the ultimate reaction forces at the top of the specimens and dividing by

the total circular area ($50 \times 50 \times \pi \text{ mm}^2$). For elastic modulus, the top displacement was divided by the height of the numerical samples (200 mm). As for Poisson's ratio, the standard measurement technique suggested by ASTM C469/C469M-17 [98] as not employed due to the localized displacements caused by simplifications of pores in the numerical model. Instead, the average of a local area on the nodes in the desired location was used to accurately determine Poisson's ratio for each sample.

4.5.1 Approach 1: Simplification of Porosities as Imperfections

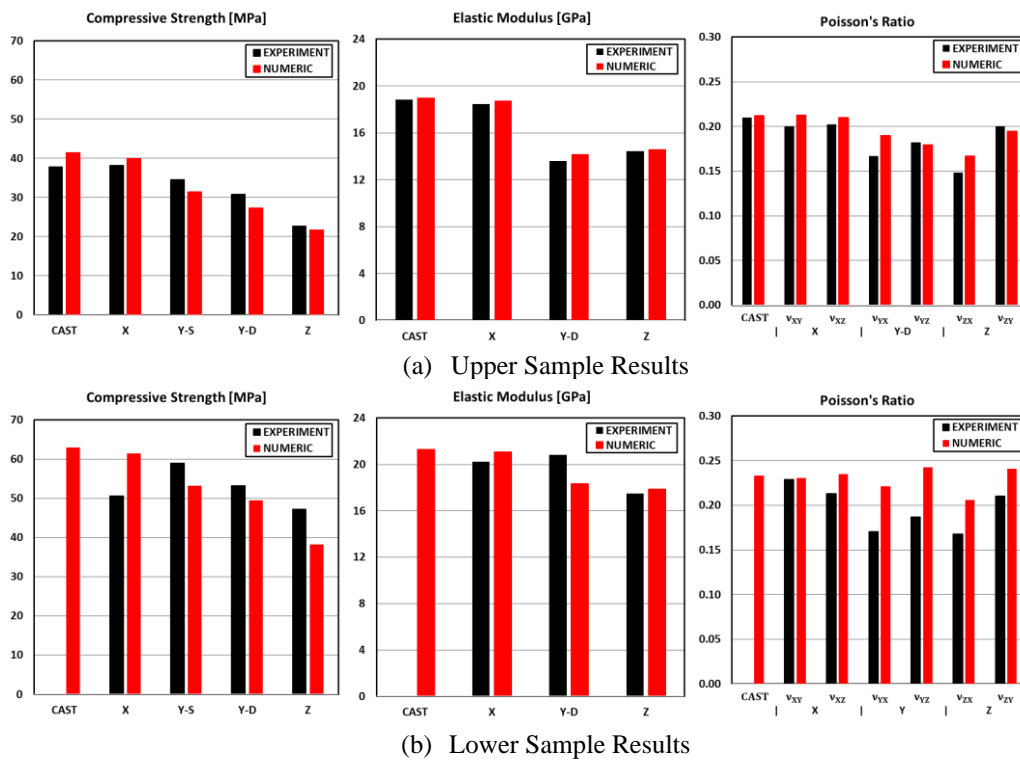


Figure 4.18. Comparison Between Experimental and Numerical Results of Compressive Strength, Elastic Modulus, and Poisson's Ratio for the Upper and Lower Samples in the First Approach

The comparison between experimental and numerical results, as depicted in Figure 4.18, reveals a remarkable agreement in the upper sample outcomes for Compressive Strength, Elastic Modulus, and Poisson's Ratio. Minor discrepancies, notably observed in the measurement of Poisson's Ratio for the Y-D sample, can be attributed

to localized differences resulting from the simplification of pores in the numerical model.

For the lower samples, the trends align well with experimental results for Compressive Strength, with the exception of the X sample. This deviation is likely due to the drilling misalignment observed in several L_X samples, introducing an angle of approximately 7 degrees as shown in Table 4.4. These misalignments, unfortunately prevalent in many L_X samples. Additionally, it's worth noting that the L_X sample, deviating from the overall trend, might be influenced by its higher placement shown in Figure 3.5 compared to L_{Y-D} , L_{Y-S} , and L_Z samples.

While overall trends are noticeable in the lower sample results, they do not exhibit the same precision observed in the upper sample outcomes. This discrepancy may stem from using material parameters derived from cast samples for the upper sample, a good estimation considering the bulk concrete's expected similarity between cast and upper samples. However, for the lower sample, more refined prediction methods may be necessary, as the chosen material parameters may not fully capture its material behavior.

The variations in elastic modulus among printed concrete samples—lower in U_{Y-D} compared to U_Z and higher in L_{Y-D} compared to L_Z —stem from distinct simplified geometries detailed in Table 4.5. Dominant interlayer porosity in U samples, contrasting with non-dominance in L samples, significantly shapes their geometries. For L samples, subtraction of the blue area related to dominant interlayer porosity and reduced the red area distance, contributing to the greater elasticity in L_{Y-D} compared to L_Z . Conversely, in U samples, the dominant interlayer porosity, coupled with a slightly greater red area distance, results in lower elasticity for U_{Y-D} compared to U_Z . Therefore, the intricacies of the simplified geometries, influenced by the presence or absence of dominant interlayer porosities, play a pivotal role in shaping the elastic properties of the printed concrete samples in the Y-D direction relative to the Z direction.

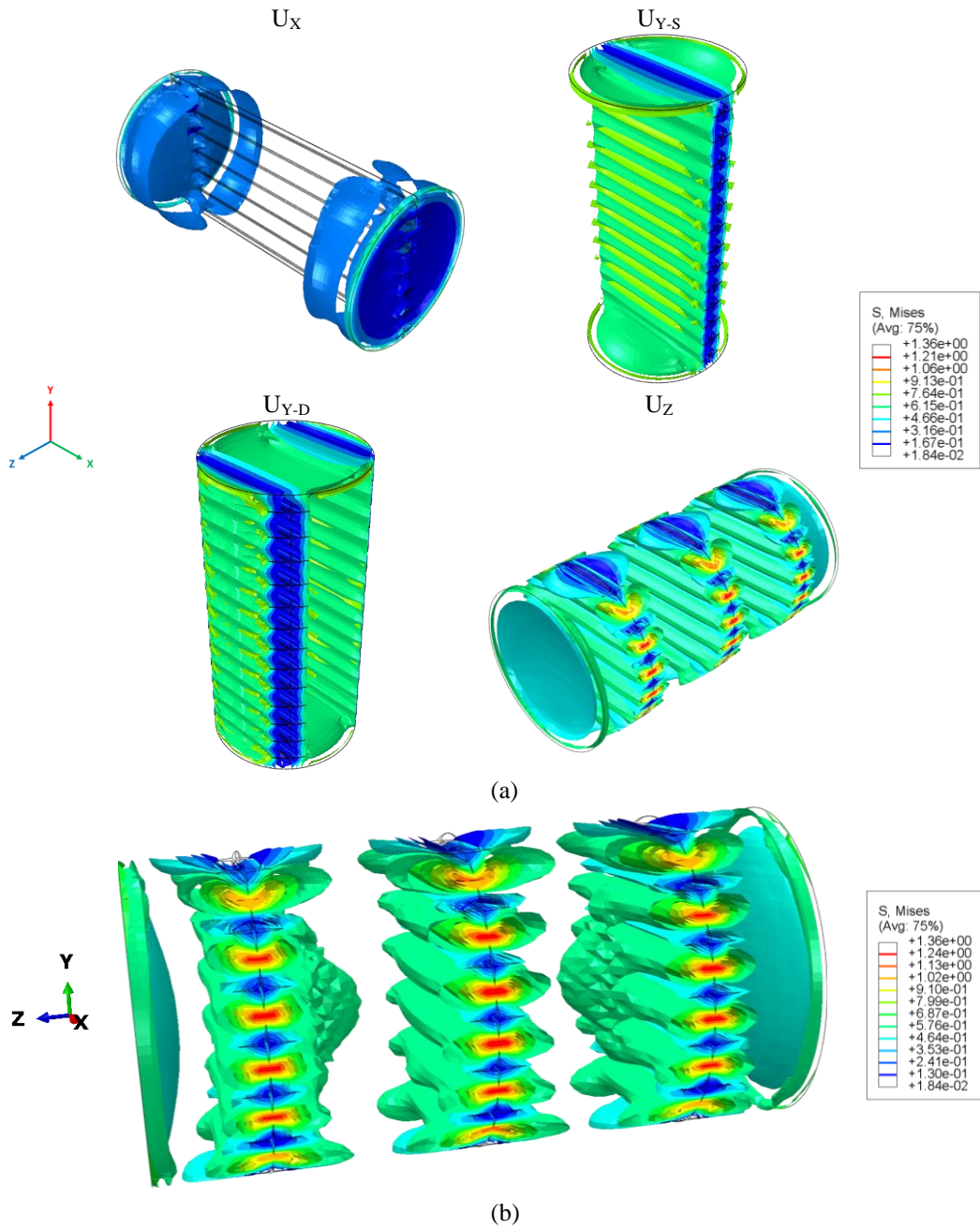


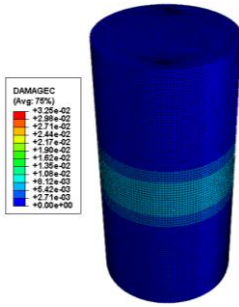
Figure 4.19 Isosurface Illustrations of Mises Stress Distribution in Fully Elastic State for (a) Upper Samples, and (b) details of U_Z sample

Figure 4.19 presents isosurface illustrations depicting the distribution of Mises stress in a fully elastic state (0.0075 mm top displacement) for distinct sample types, specifically (a) Upper Samples and (b) detailed representation focusing on the U_Z sample. The stress patterns elucidated in these visualizations are instrumental in discerning the mechanical response of the numerical samples under investigation. Notably, the stress distribution in the U_X sample closely mirrors that of the cast sample, indicating a similarity in the response to applied loads. Conversely, discernible variations emerge in the stress distributions of the other samples, wherein higher stress intensity is observed around localized porosities. In particular, for the U_Z sample type, the stress concentrations around porosities surpass those observed in the U_{Y-S} and U_{Y-D} sample types. These localized regions of heightened stress correspond spatially to areas where plastic strain initiation occurs earlier in the loading history. The disparities in stress distribution among the various sample types underscore the influence of localized porosities on the mechanical behavior of the 3D printed concrete.

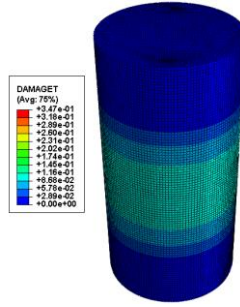
To delve more into the intricacies of the observed anisotropic behavior in printed concrete, Figure 4.20 and Figure 4.21 meticulously illustrate the compressive and tensile damage, along with plastic strain evolution, for the cast, upper, and lower samples at their respective ultimate loads. A detailed examination reveals that the simplified porosities, when comparing cast samples with X samples, exert minimal impact on both damage and plastic strain evolutions. This negligible effect is attributed to the slight reduction in the area, resulting in no discernible differences between cast and X samples, as indicated in Figure 4.18.

However, a more nuanced scenario unfolds for Y-S, Y-D, and Z samples. These simplified porosities play a pivotal role in triggering tension damage evolution, with subsequent effects on compression damage evolution at earlier stages. Consequently, noticeable reductions in strength are observed for these samples. Notably, the Y-S samples, characterized by a lower number of pores compared to Y-D samples, exhibit higher strength and elasticity. At ultimate loads, the Y-D and Y-S samples demonstrate tension damage crossing between layers in the thickness direction.

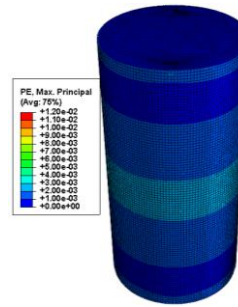
COMPRESSIVE DAMAGE



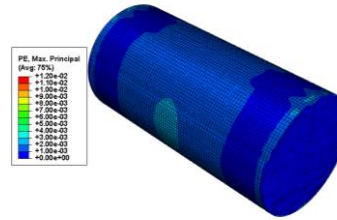
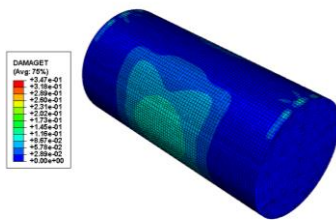
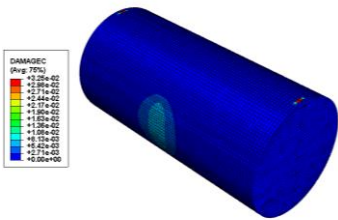
TENSILE DAMAGE



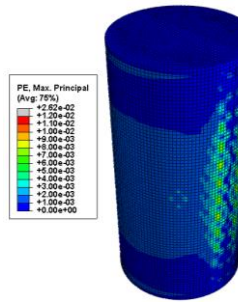
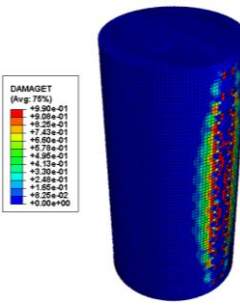
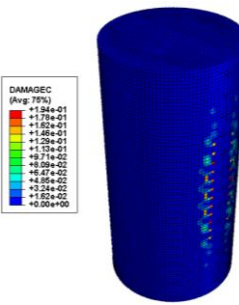
PLASTIC STRAIN



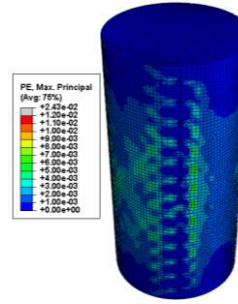
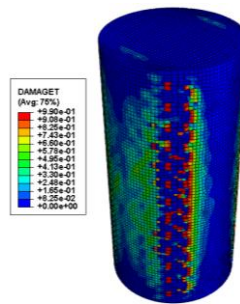
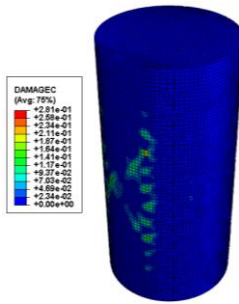
(a) CAST



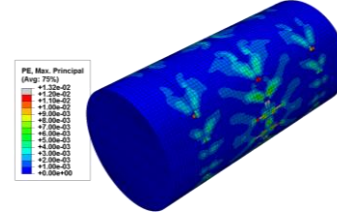
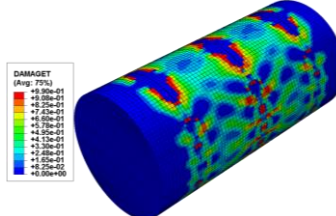
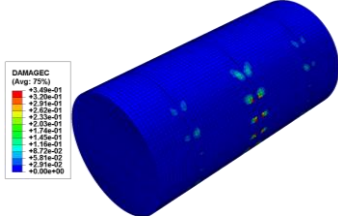
(b) U_x



(c) U_{y-s}



(d) U_{y-D}



(e) U_z

Figure 4.20. Compressive and Tensile Damage, and Plastic Strain Evolution on Cast and Upper Samples at Their Respective Ultimate Loads

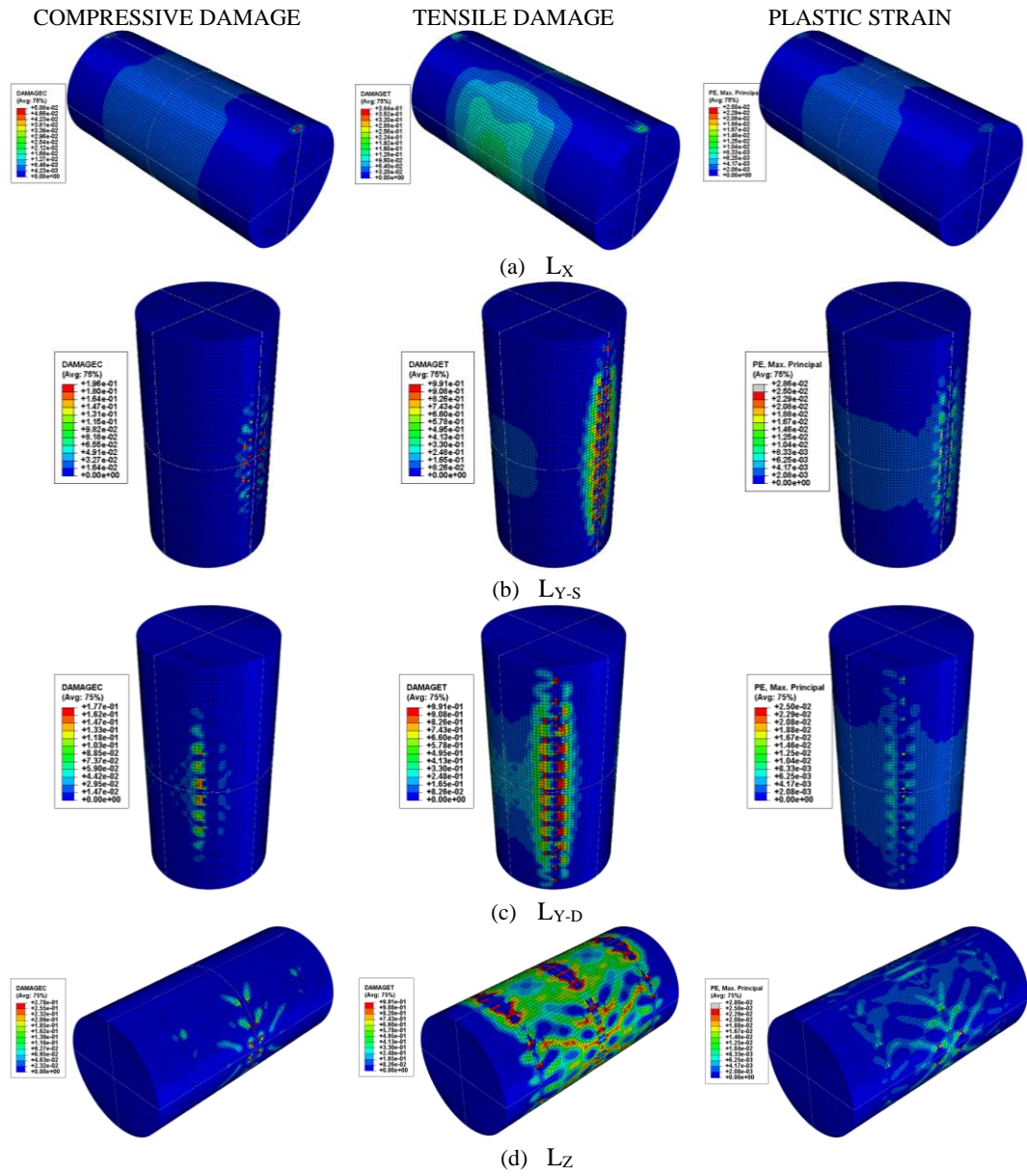


Figure 4.21. Compressive and Tensile Damage, and Plastic Strain Evolution on Lower Samples at Their Respective Ultimate Loads

For Z samples, a distinctive pattern emerges, with the simplified porosities prominently influencing tension damage. This tension damage traverses through layers in the width direction, covering a more extensive distance than thickness direction. Consequently, Z samples exhibit the least strength among the samples studied. In summary, the analyses presented in Figure 4.20 and Figure 4.21 provide valuable insights into how these simplified porosities contribute to the damage and strength variations observed in printed concrete samples, emphasizing the nuanced interplay between porosity, material behavior, and mechanical performance.

In Figure 4.22, a detailed examination of isosurface illustrations reveals distinct patterns in the distribution of damage and plastic strain among various printed concrete samples at equivalent levels corresponding to their ultimate loads. Notably, the U_X sample displays a lesser susceptibility to the influence of dominant pores compared to U_{Y-S} , U_{Y-D} , and U_Z samples. Specifically, U_X exhibits lower levels of compressive damage, with localized damage concentrated around interstrips, in contrast to the more pronounced damage observed in U_{Y-S} , U_{Y-D} , and U_Z samples. The spatial distribution of tensile damage further accentuates the impact of dominant pores, with U_X showcasing no damage around both interlayers and interstrips. In contrast, U_{Y-D} , U_{Y-S} , and U_Z samples exhibit dominant damage, particularly around interstrips, and for U_Z , this damage extends through layers in the width direction. The consistent correlation between damage distribution and plastic strain evolution across samples underscores the significance of dominant pores in influencing the mechanical behavior of printed concrete.

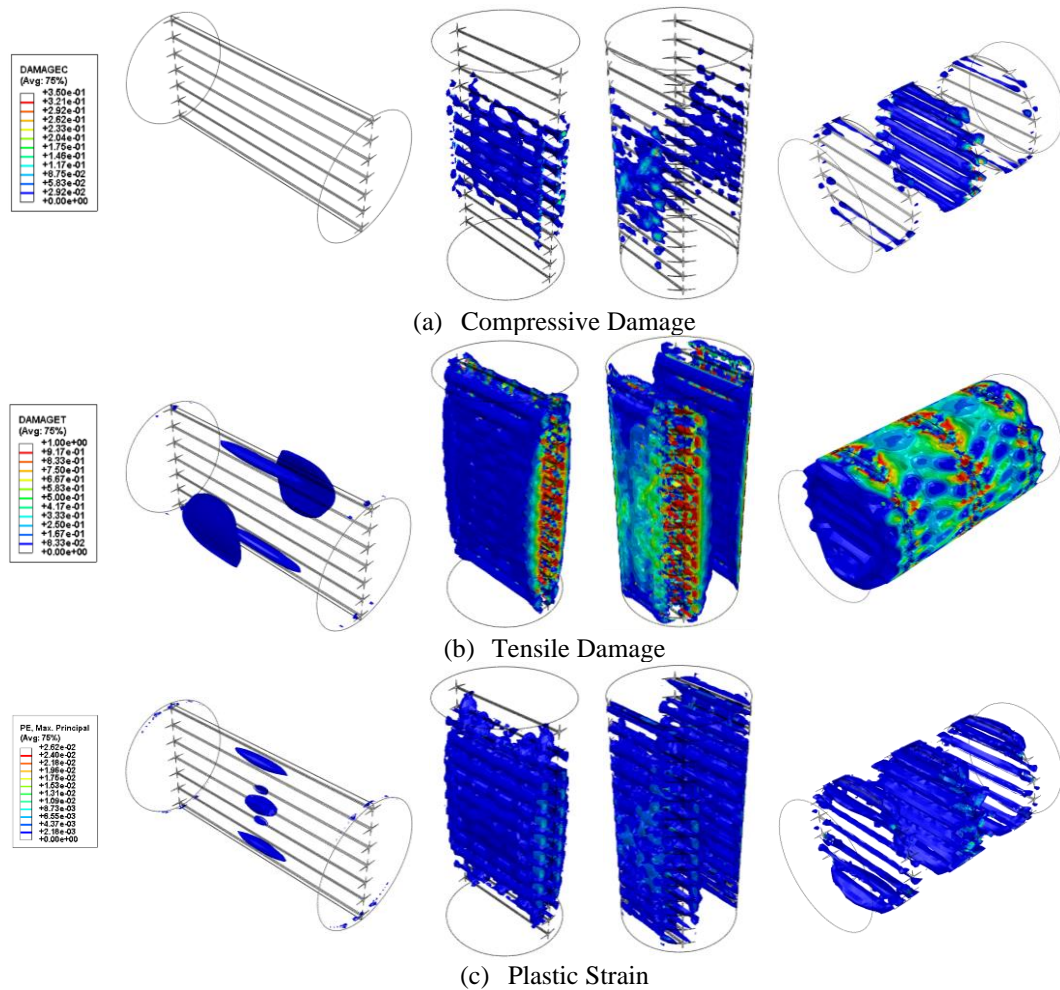


Figure 4.22. Isosurface Illustrations of Damage and Plastic Strain Distribution in Upper Samples at Equivalent Damage and Plastic Strain Levels

4.5.2 Approach 2: Interface Model Using Traction and Separation Law

The comparison between experimental and numerical results, as depicted in Figure 4.23, reveals a good agreement in the upper sample outcomes for Compressive Strength, Elastic Modulus, and Poisson's Ratio. Minor discrepancies, notably observed in the measurement of Poisson's Ratio for the Z sample. For the lower samples, the trends align well with experimental results for Compressive Strength, with the exception of the X and Y-S sample. The possible reasons are explained in the part 4.5.1.

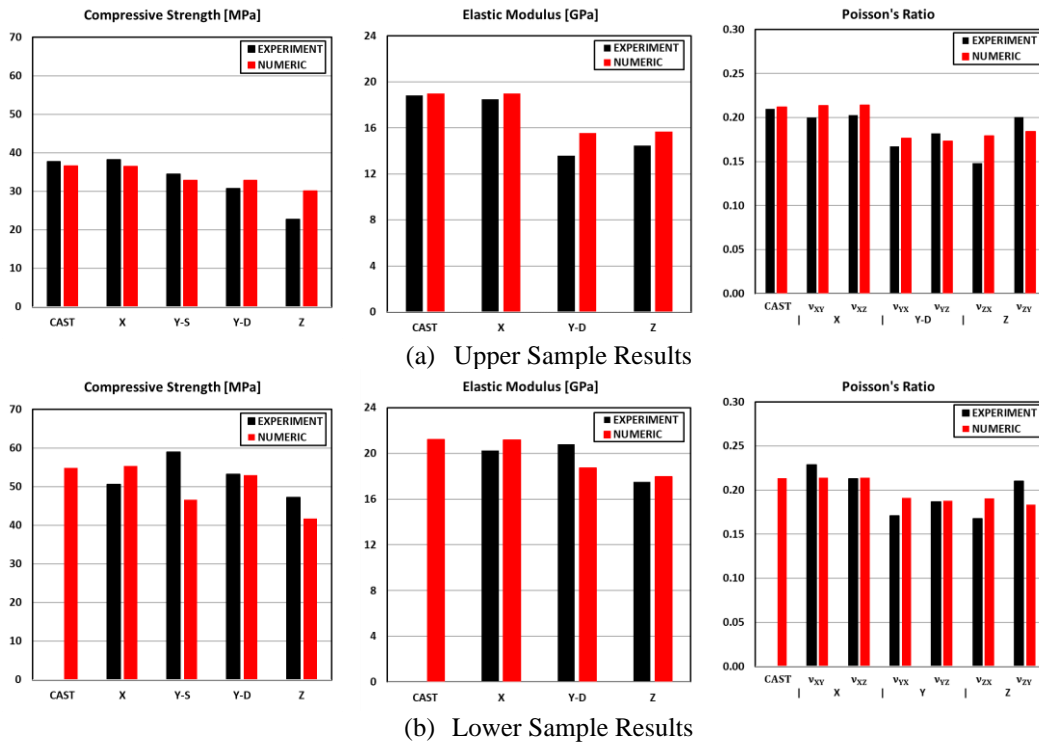


Figure 4.23. Comparison Between Experimental and Numerical Results of Compressive Strength, Elastic Modulus, and Poisson's Ratio in the Second Approach

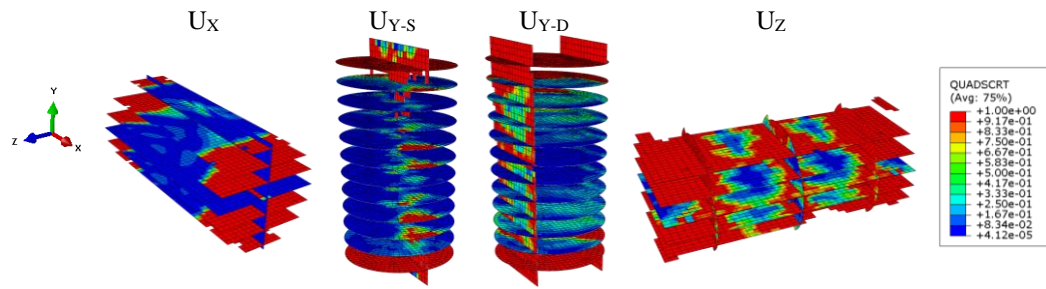
The variations in elastic modulus among printed concrete samples stem from number of interfaces and mode-I stiffness value of the interlayer for Y-D sample and interstrip for Z sample. A heightened mode-I stiffness results in higher elastic modulus, while a greater number of interlayers for Y-D sample and interstrips for Z samples result in lower elastic modulus. On the other hand, Poisson's ratio is influenced by the mode-II stiffness, number of concrete filament and the width/thickness of the filament. However, the detailed exploration of each parameter's contribution to Poisson's ratio is not within the scope of this study.

In this approach, the primary cause of failure in printed samples, except for the X samples, is attributed to the interface failure. The U_X and L_X samples exhibit both concrete failure and interface failure. Quantitative metrics associated with interface failures, quadratic stress criterion, MMIXDME, and stiffness degradation values, are presented in Figure 4.24 for upper samples and Figure 4.25 for lower samples. These quantitative metrics are taken at their respective ultimate load of the samples.

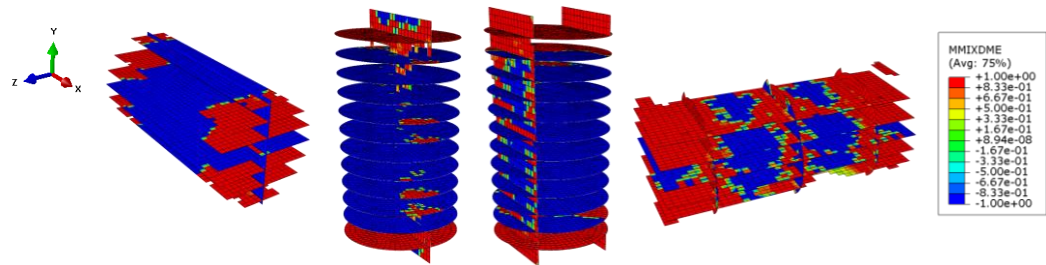
The Quadratic Stress Criterion (QUADSCRT), defined by Equation 4.3, plays a crucial role in identifying the initiation of damage. When QUADSCRT reaches a value of 1, it signifies the initiation of damage in the element. Stiffness degradation, represented by the value in Equation 4.4b, characterizes the gradual weakening of an element's resistance to deformation as damage evolves.

The mode mix ratio during damage evolution (MMIXDME) serves as an indicator of the predominant mode of damage in the elements. A value of -1 denotes an undamaged element, while values between 0 and 0.5 suggest predominant damage due to tensile stress. Conversely, values between 0.5 and 1 indicate predominant damage by shear stress. In Figure 4.24-a and Figure 4.25-a, the presented MMIXDME values clearly indicate that interface failures are predominantly attributed to shear stresses. The numerical analysis reveals that interface damages occurring in the loading direction (interlayer for Z, interstrip for Y-S and Y-D) trigger interface failure perpendicular to the loading direction (interstrip for Z, interlayer for Y-S and Y-D). This consequential failure mechanism leads to the loss of stability in the samples at their respective ultimate loads.

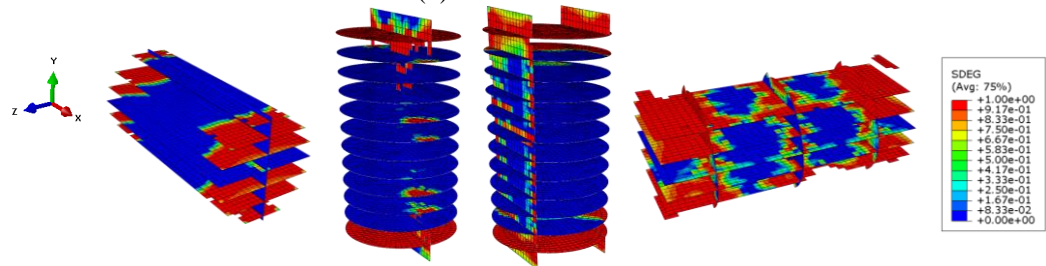
Moreover, the activated cohesive element deletion option during the analysis results in the removal of failed elements. In the case of U_{Y-S} , U_{Y-D} , and U_Z samples, a significant number of deleted elements are notably concentrated in the loading direction interfaces (interlayer for Z, interstrip for Y-S and Y-D), at the ultimate load. Conversely, for the L_{Y-S} , L_{Y-D} , and L_Z samples, although deleted elements are still observable, they are comparatively rarer. Consequently, while interfaces contribute to reducing the ultimate strength of the L samples, the dominant failure mechanism is not solely attributed to interface failure. Instead, the failure in L samples results from a combination of both concrete and interface failures. Specifically, the interface failure triggers the subsequent onset of concrete failure in these cases. In contrast, for the U samples, the failure is predominantly governed by interface failure.



(a) Quadratic Stress Criterion (QUADSCRT) Values



(b) MMIXDME Values



(c) Stiffness Degradation Values

Figure 4.24. QUADSCRT, MMIXDME, and Stiffness Degradation on Upper Samples at Their Respective Ultimate Loads

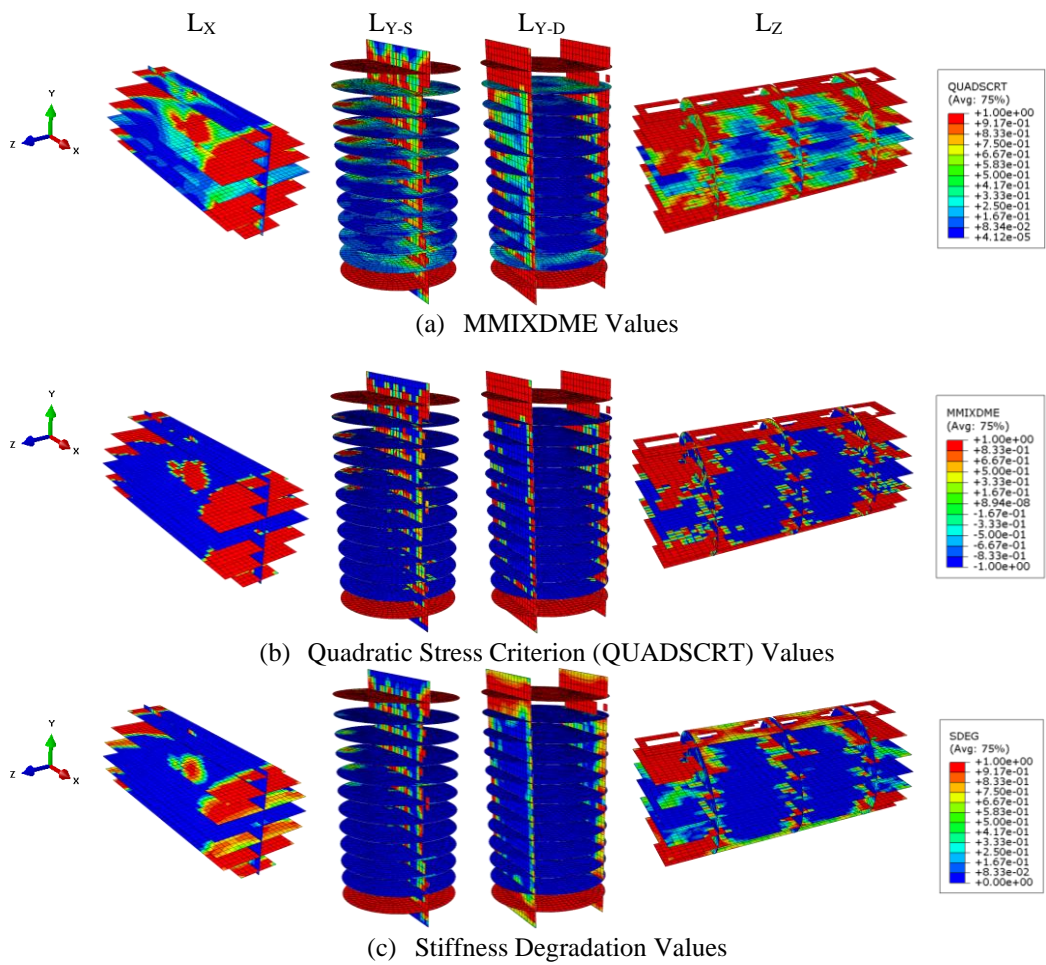


Figure 4.25. QUADSCRT, MMIXDME, and Stiffness Degradation on Lower Samples at Their Respective Ultimate Loads

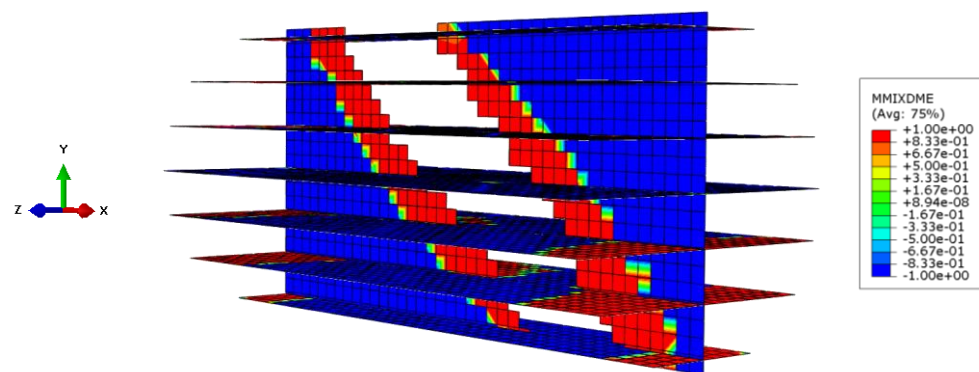


Figure 4.26. Diagonal Shear Failure in the Interstrip of L_x sample

In the case of X sample, minimal element deletion is observed in the U_X sample at the ultimate load, indicating that the failure in this case is primarily dominated by concrete failure. For the L_X sample, a distinct diagonal interstrip failure is observed (Figure 4.26), leading to the deletion of elements in the diagonal direction within the interstrip region.

4.6 Crack Propagation and Failure Mechanism: A Comparative Analysis

In this section, an intricate examination of fracture modes is conducted through a comprehensive analysis, combining experimental observations with numerical simulations. Visual insights into fractured samples are presented, accompanied by a meticulous comparison with numerical results, shedding light on the detailed mechanisms and causes of failure. The initial focus of the analysis involves a scrutiny of traction-separation analysis results, where numerical samples at ultimate loads are presented, with the exception of the X sample, which is depicted at its post-peak stress level. Additionally, in the simplified porosity as imperfection model, all numerical samples are showcased at a 1.5 mm top displacement level, corresponding to a sample strain of 0.0075.

Figure 4.27, Figure 4.28, Figure 4.29, and Figure 4.30 provide a comparative illustration of the failure modes observed in the U_X , U_{Y-S} , U_{Y-D} and U_Z samples, respectively, presenting both experimental findings and numerical results derived from the traction-separation law. The numerical analysis focuses on showcasing MMIXDME values for interfaces and plastic strain distributions in the concrete.

In these figures, it is noteworthy that all interface failures are most dominantly characterized by shear failure, and the resultant failure shapes accurately predict the experimental failure modes of the printed concrete. Remarkably, the plastic strain development in the concrete does not precisely estimate the fracture behavior. Consequently, it can be inferred that cracks propagate through interfaces, where they

are intentionally designed to be weaker, justifying the observed crack propagation through the interfaces in this model.

For sample type X, the failure mode closely resembles the cast concrete failure mode, with the exception that cracks propagate through the interface when the diagonally incoming fracture penetrates it.

In sample types Y-S and Y-D, the interface failure is clearly reflected in the numerical and experimental results, as evidenced by the deletion of cohesive elements due to failure in both sets of data.



(a) Failure Mode of U_{x8}

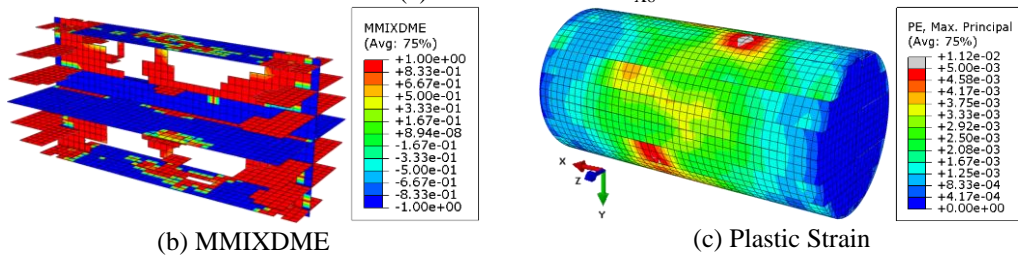


Figure 4.27. Comparative Analysis of U_x Sample Failure Modes

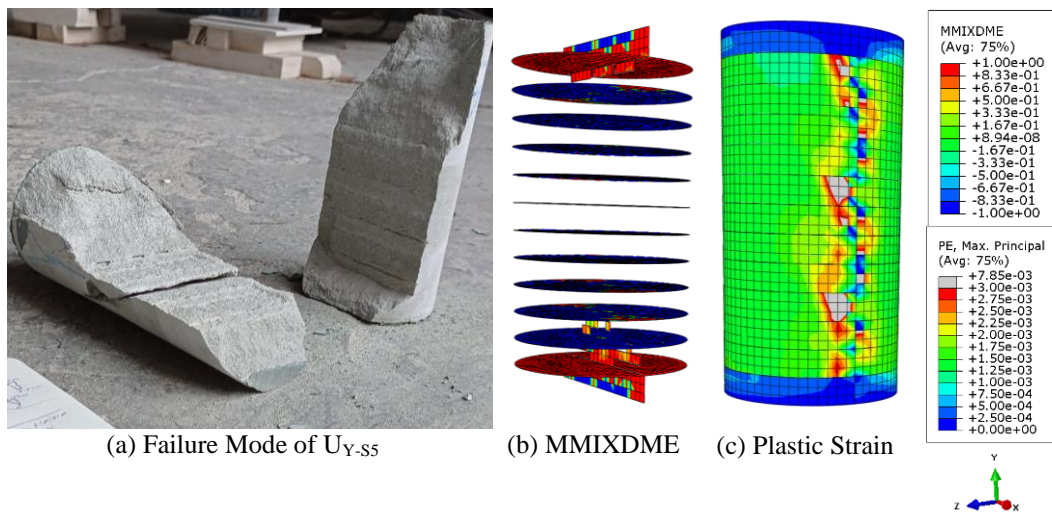


Figure 4.28. Comparative Analysis of U_{Y-S} Sample Failure Modes (Approach 2)

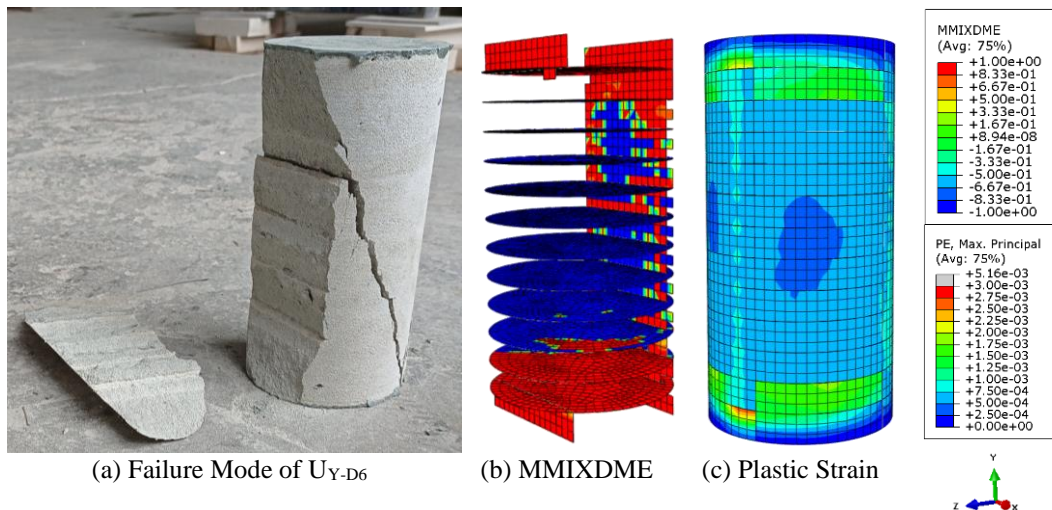
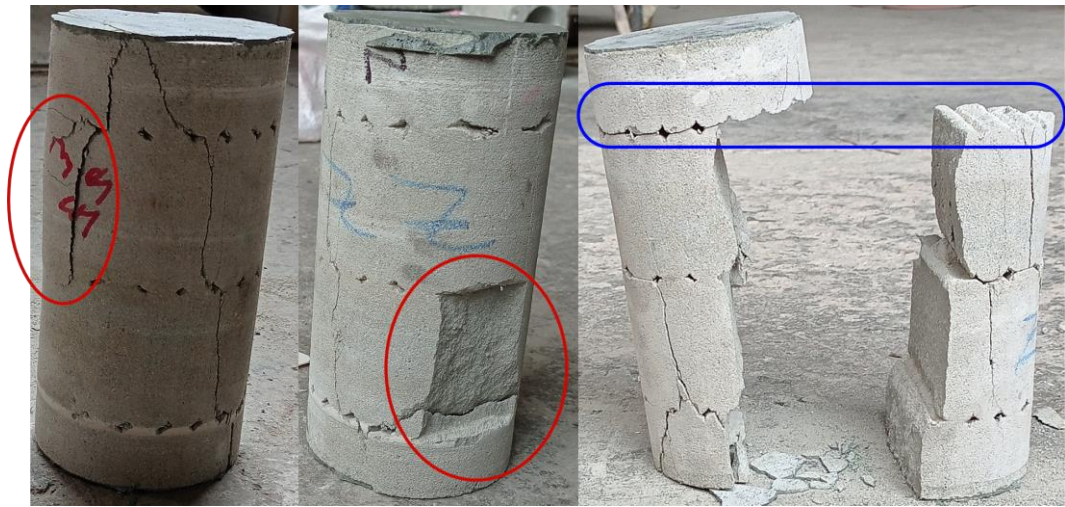


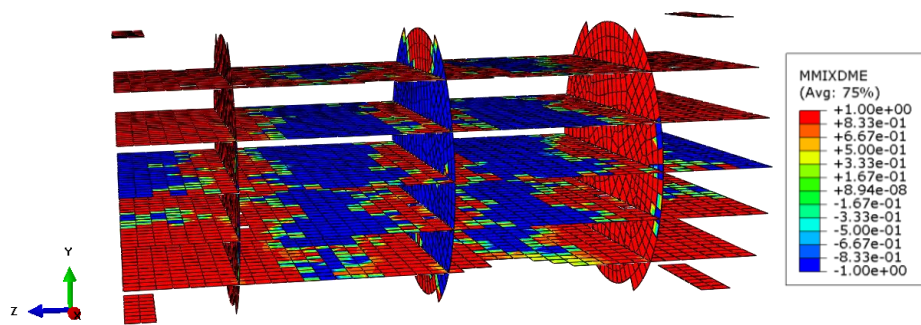
Figure 4.29. Comparative Analysis of U_{Y-D} Sample Failure Modes (Approach 2)

In sample type Z, experimental results reveal both outermost layer spalling and interstrip failure. These observations align with the interface shear failure depicted in the MMIXDME figure, illustrating the failed or deleted surface as a consequence of the failure process.

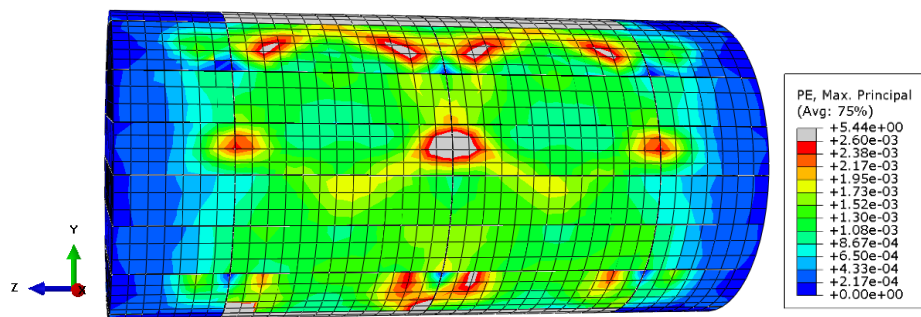
On the other hand, Figure 4.31, Figure 4.32, Figure 4.33, and Figure 4.34 provide a comparative illustration of the failure modes observed in the U_{Y-S} , U_{Y-D} and U_Z samples, respectively, presenting both experimental findings and numerical results derived from the FEA of simplification of the porosities as imperfections.



(a) Failure Mode of U_{z3} (Right Face), U_{z3} (Left Face), U_{z1} , Respectively (Red and Blue Circles Highlight Outermost Layer Spalling and Interstrip Failure, respectively.)



(b) MMIXDME



(c) Plastic Strain

Figure 4.30. Comparative Analysis of U_z Sample Failure Modes (Approach 2)

In U_{Y-S} samples (Figure 4.31), plastic strains and tension damage predominantly localize between the star-shaped imperfections rather than in the interstrip region. This aligns well with experimental results, offering a clearer understanding than the interface model. Intensified Mises stresses (Figure 4.19) contribute to earlier plastic strain development, emphasizing that localized porosities drive fracture propagation rather than weak interfaces.



(a) Failure mode of U_{Y-S2} and U_{Y-S5} , respectively

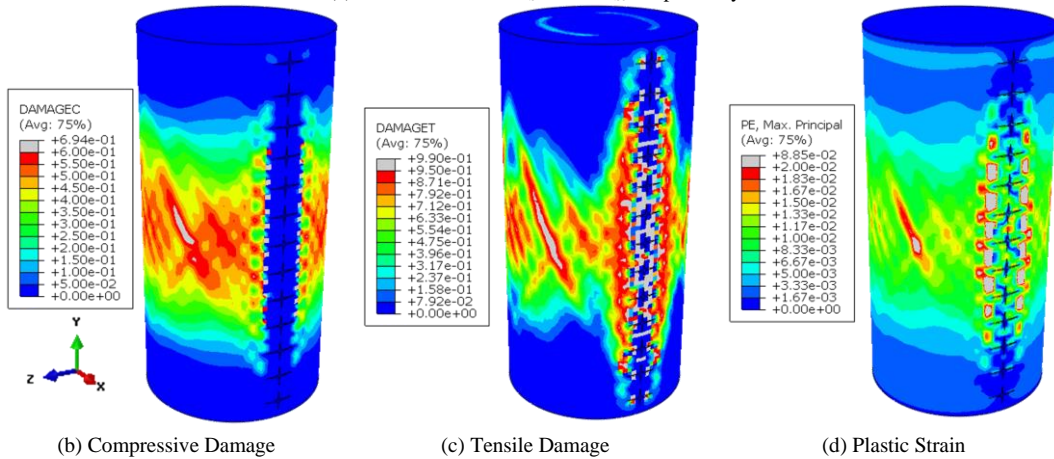


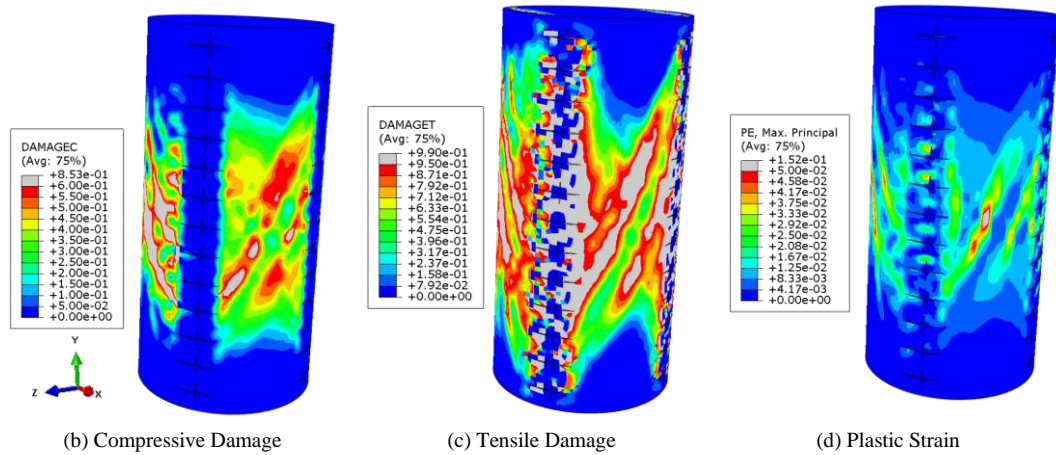
Figure 4.31. Comparative Analysis of U_{Y-S} Sample Failure Modes (Approach 1)

Similar to U_{Y-S} , U_{Y-D} samples (Figure 4.32) exhibit high plastic strains and tension damage between star-shaped imperfections, deviating from the interstrip region. The intensified Mises stresses (Figure 4.19) again correlate with early plastic strain development. Additionally, the diagonal failure mode and outer part spalling

observed in Figure 4.32 are better understood in light of the numerical results. The conclusion remains consistent: localized porosities play a more crucial role in fracture propagation than weak interfaces.



(a) Failure mode of U_{Y-D8}



(b) Compressive Damage

(c) Tensile Damage

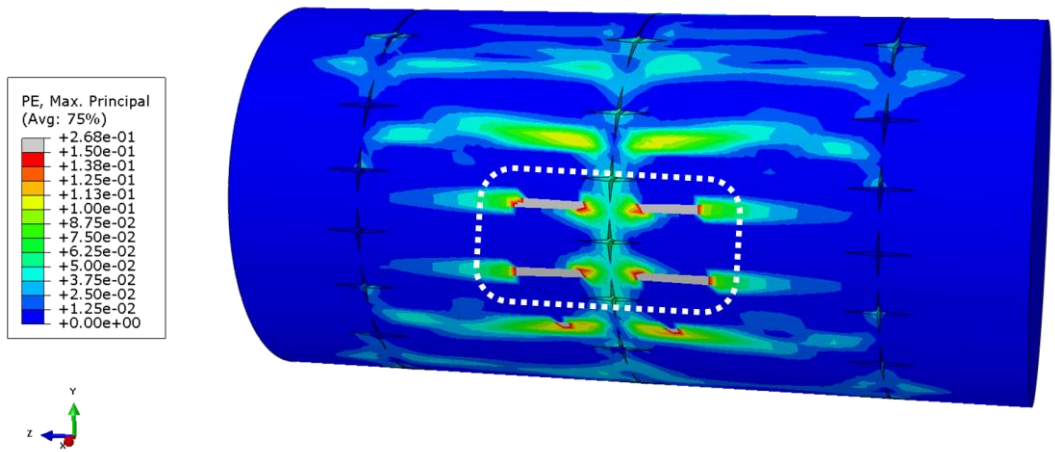
(d) Plastic Strain

Figure 4.32. Comparative Analysis of U_{Y-D} Sample Failure Modes (Approach 1)

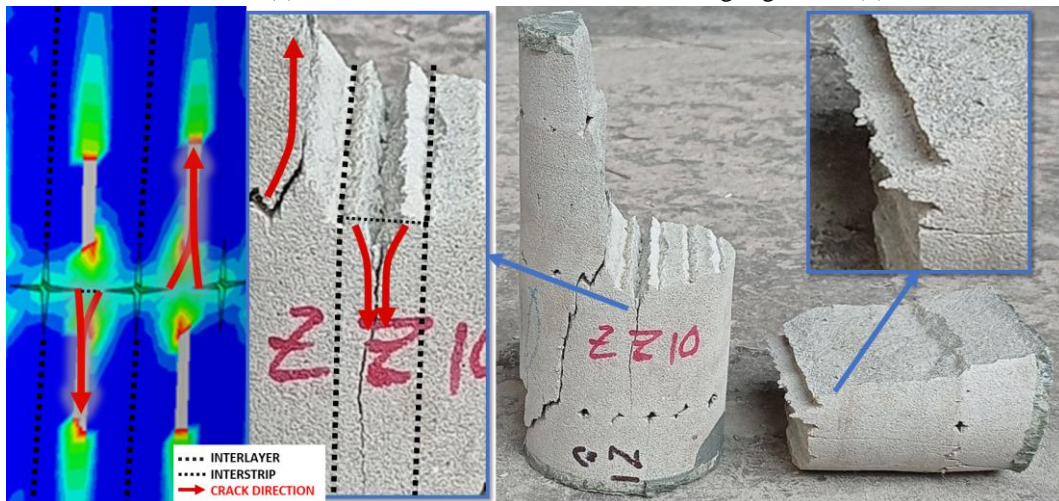
U_z samples (Figure 4.33) demonstrate crack propagation within concrete filaments, contrasting with interlayer or interstrip failure. Intensified Mises stresses, again shown in Figure 4.19, highlight higher stress concentrations around the contact area of interstrip faces, leading to plastic strain development within the concrete filament. This observation is confirmed in Figure 4.33-a, where the highest maximum plastic strains occur in the concrete filament, not the interlayer. In Figure 4.33-b, a detailed comparison with fractured sample U_{z9} further illustrates crack propagation (red arrows in Figure 4.33-b) through the center of the concrete filament.

To better understand failure modes, Figure 4.34 provides a comparative analysis of U_z sample failure modes. The interlayer crack adjacent to the crack in the concrete

filament is explored, demonstrating that the crack in the filament is wider. This figure also highlights that cracks in the interlayer are rarely observed.



(a) Plastic Strain - * White dotted area is highlighted in (b)



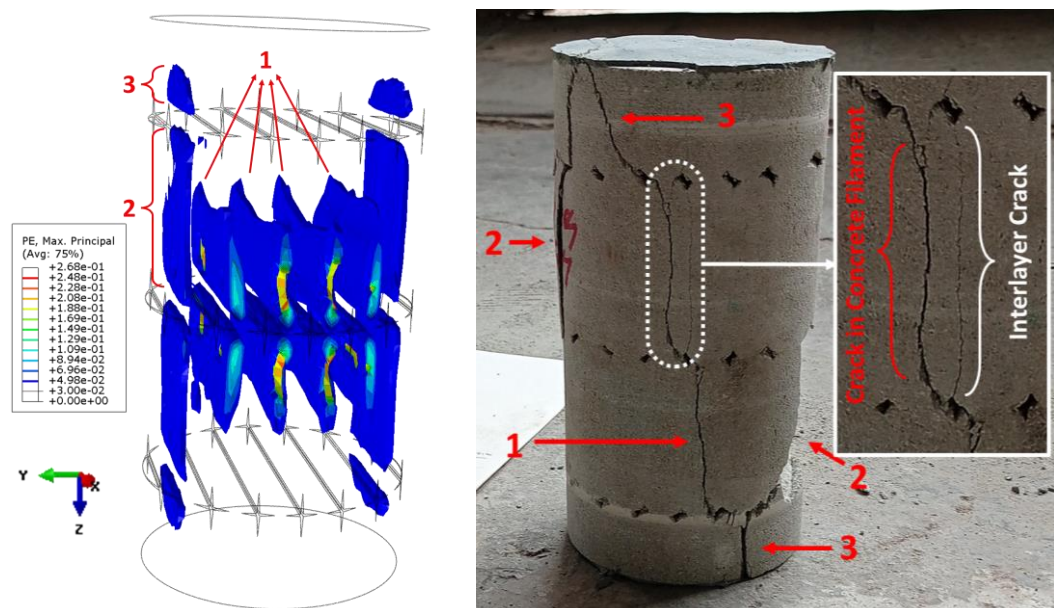
(b) Explanation of the Crack Propagation and Failure Mode of U_{Z9}

Figure 4.33. Crack Propagation within the Concrete Filament in U_Z Sample (Approach 1)

Considering both experimental and numerical results, it becomes evident that localized porosities, rather than weak interfaces resulting from the printing process, serve as the dominant factor influencing the failure of printed samples contrary to popular belief. Experimental and numerical analyses consistently support this conclusion.



(a) Failure Modes of U_{Z1} , U_{Z3} (Front View), U_{Z3} (Right Face), U_{Z3} (Left Face), U_{Z9} , respectively.



(b) Isosurface Illustrations of Plastic Strain Distribution in U_Z sample, and Crack Comparisons (#1, #2, and #3 Show Crack Propagated within Concrete Filament, #2 Leads to Spalling of the Outermost Layer, and #3 Propagates Through the Outermost Regions at the Top and Bottom of the Sample)

Figure 4.34. Comparative Analysis of U_Z Sample Failure Modes (Approach 1)

4.7 Conclusion

In conclusion, Chapter 4 aimed to shed light on the micro and meso scale aspects of 3DPC, focusing on the effects of localized pores between layers in 3DPC, a common occurrence in real-world concrete printing processes. The investigation incorporated Computed Tomography (CT) analysis, porosity analysis, and 3D image reconstructions, allowing for a nuanced understanding of these localized porosities.

The subsequent finite element analysis, based on the simplified geometry derived from CT scan data, provided insights into the impact of these pores on the structural performance of 3DPC. The key findings can be summarized as follows:

- μ -CT analysis results:
 - Porosity distributions exhibit a right-skewed pattern, with notable distinctions between the cast and printed samples. The cast sample displays a wider range of porosities compared to the printed counterparts.
 - Analysis of the lower samples reveals a significant reduction in porosity, indicating a denser structure compared to the upper samples. This may be attributed to factors such as self-weight, resulting in more effective compaction during the printing process.
 - Despite variations in total porosity, there is an absence of a pronounced trend in porosity along the height of the specimens. This suggests a lack of observable interlayer effects within the investigated range.
- Macro-CT analysis results:
 - Macro-CT results highlighted differences between cast and printed matrices, with larger, irregularly distributed pores in the former.
 - Printed samples exhibited concentrated pores at interlayers and interstrips, with interstrip porosities being particularly dominant.
 - Variations in porosity between upper and lower samples were attributed to factors such as self-weight and printing time, showcasing the impact of these parameters on material properties.
- Finite element analysis results:
 - A strong agreement between experimental and numerical results was observed for compressive strength, elastic modulus, and Poisson's ratio.
 - Stress distribution in the U_x sample closely mirrored that of the cast sample, indicating similar responses to applied loads.

- Variations in stress distributions among different sample types revealed higher stress intensity around localized porosities, influencing the mechanical behavior of 3DPC.
- Detailed examination demonstrated that simplified porosities had minimal impact on damage and plastic strain evolution in X samples but played a crucial role in triggering tension damage in Y-S, Y-D and Z samples.
- Printed samples demonstrate crack propagation within concrete filaments, contrasting with interlayer or interstrip failure under compressive load.
- Contrary to popular belief, the dominant reason for failure in these samples is localized porosities rather than weak interfaces resulting from the printing process. Experimental and numerical analyses consistently support this conclusion.

In conclusion, the findings from Chapter 4 provide valuable insights into the intricate interplay between porosity distribution and mechanical properties at the micro and meso scales. These insights set the stage for a deeper understanding of 3DPC behavior, laying the foundation for subsequent chapters' exploration into macrostructural and seismic aspects.

CHAPTER 5

MACRO/STRUCTURAL LEVEL STUDY: STRUCTURAL RESPONSE AND FAILURE MECHANISMS OF UNREINFORCED 3D PRINTED CONCRETE WALLS UNDER MONOTONIC LATERAL LOADS

5.1 Introduction

In recent years, 3D printed concrete (3DPC) technology has emerged as a groundbreaking approach in construction and structural engineering. Its potential for creating complex geometries and reducing material waste has garnered significant attention. However, its integration as a load-bearing element in structures remains a challenge. Unlike traditional concrete, 3DPC lacks standardized design and performance guidelines, particularly when it comes to its behavior under lateral loads. This gap in knowledge presents a critical need for extensive testing and analysis to determine its behavior under various loading conditions.

Unlike material-level investigations, there is a notable scarcity of research addressing the structural performance of large-scale 3D printed concrete structures when used as load-bearing components in buildings. These structures, which include load-bearing walls, beams, and columns, play a pivotal role in 3D printed construction. In 3DPC, there is a need for the preparation of documents containing recommendations for material selection, open or on-site production processes, and even standardization efforts. Additionally, it is observed that there is a lack of international regulations regarding the design and analysis of structural behavior, which is as important as these processes [139]. In other words, the existing body of literature in this domain remains relatively limited, as outlined below.

In a study conducted in 2021 by Daungwilailuk et al. [34], wall samples were determined with two different models, and unconfined uniaxial loading tests were

conducted. The behavior of the wall was observed throughout the experiment. In addition, analyses were also carried out using finite element methods. One of the models used in the experiments was a flat wall with an inner truss, and the other was a diamond-patterned wall (diamond wall/wavy design wall). It was observed that the wall pattern affected the wall's load-bearing capacity. High tensile strains were observed in the pits of the diamond pattern, which caused cracks and spalling in the concrete. A flat wall with internal support performed better than a diamond wall in terms of strain and deflection. In addition, a flat wall without internal truss was also evaluated with finite element analysis. As a result of these analyses, it was determined that a wall without internal support had a higher risk of buckling than a wall with internal support for walls of the same shape and size. Additionally, internal trusses acted as a support for the wall, reducing its lateral deflection and preventing buckling failure. Finally, strain-gauge readings showed both tensile and compressive deformation in the same location and direction, which was due to the wall's bending and the deformation of the compressed concrete. Han et al. [140] investigated the structural mechanical properties and failure modes of large-scale 3D printed concrete walls under axial compression loads. Eight large-scale 3D printed concrete wall samples with different height/thickness ratios (two samples without horizontal reinforcement and six samples with horizontal reinforcement) were tested under axial compression. The results show that the failure of 3D printed concrete walls under axial compression load is brittle. In addition, the use of horizontal reinforcement has been observed to reduce the ultimate load-carrying capacity of 3D printed concrete walls under axial compression. The horizontal reinforcement created weak zones in the layers where it was placed. Samples with horizontal reinforcement have been broken along this weak plane, exposing these reinforcements. Furthermore, when walls with 3, 5, 8, and 10 different height/thickness ratios were compared, the ultimate load-carrying capacity first increased, then decreased. In another study, Cai et al. [141] investigated the mechanical behavior of 3D printed fiber-reinforced cementitious composite (FRCC) beams. Four total 3D printed FRCC beams with different reinforcement methods and

one conventional steel reinforced FRCC beam were tested. Each beam was subjected to a four-point bending test to measure its load-carrying capacity, deflection, and crack propagation behavior. The test results showed that the 3D printed FRCC beams with steel fibers and carbon fiber reinforcement had higher load-carrying capacities and better crack resistance than the other two 3D printed beams with basalt fibers and polypropylene fibers. However, all 3D printed FRCC beams showed lower load-carrying capacities than the conventional steel reinforced FRCC beam, which is commonly used in construction. Overall, the study demonstrated that 3D printed FRCC beams with certain types of reinforcement can provide an alternative to traditional construction materials in certain applications.

While considerable progress has been made in understanding the mechanical properties of 3DPC, there is a notable gap in the exploration of its response to lateral loading conditions. In the existing literature, the behavior of unreinforced 3DPC walls under monotonic lateral load remains a relatively unexplored territory. This chapter addresses this gap by presenting a comprehensive investigation into the response of unreinforced 3DPC walls under monotonic lateral loads. Through a series of experimental tests and advanced numerical analysis using ABAQUS and Digital Image Correlation (DIC) techniques, the aim is to shed light on how unreinforced 3DPC structures respond to lateral loading conditions.

The experiments in this chapter involve subjecting unreinforced 3DPC walls with varying heights, lengths, and width to lateral loads. These walls include varying heights of 1m and 1.5m, lengths of 1m and 1.5m, and width of 20cm, 25cm, and 30cm for the 1.5m length, 1m height walls. The goal is not just to test these walls but to push them to their limits, aiming to investigate their failure modes under substantial lateral loads.

Integral to this investigation is the incorporation of numerical simulations using ABAQUS, enhancing the understanding of the complex responses of 3DPC walls. In the ABAQUS analysis, the contribution of the webs and inner trusses to shear force is investigated, along with a thorough examination of the failure mechanisms

of 3DPC walls under lateral loads. By combining experimental and numerical approaches, comprehensive insights are provided that can contribute to the development of standardized practices and guidelines for the application of unreinforced 3DPC in lateral load-bearing scenarios. This research not only advances the understanding of 3DPC technology but also aims to inform and influence its practical implementation in structural engineering, especially in the realm of lateral load capacity.

5.2 Experimental Program

5.2.1 Raw Materials and Mix Design

The same mixture in Chapter 3 was used for the current study to print the load-bearing walls. The mixture consisted of 820 kg CEM II/A-M (S-L) 42.5R (obtained from OYAK Cement Factory), 1230 kg silica sand with a maximum particle size of 1.5 mm, 26.5 kg of a calcium formate-based additive, 16.5 kg of a superplasticizer, and 0.65 kg of monofilament micro polypropylene fibers. The water-to-cement (w/c) ratio of the mix was 0.32, and the mixture was designed to prevent shrinkage cracks by incorporating fibers with specific properties (Table 3.1). The particle size distribution of the fine aggregates was determined by sieve analysis and shown Figure 3.2. The compressive strength of the mixture was determined by casting \varnothing 10cm cylinders and testing them at 28 days, resulting in an average strength of 37.0 ± 2.1 MPa.

5.2.2 Mechanical Properties of 3D Printed Concrete Walls

To provide a brief overview of the mechanical experiments conducted in the Chapter 3, Figure 5.1 illustrates the cored wall and cylindrical samples used for the tests. Figure 5.1-a displays the wall from which the cylindrical samples were extracted. Figure 5.1-b includes dimensions of the wall and the number of layers in each section

and shows the naming convention for each cylindrical sample based on the Cartesian coordinate system. Finally, Figure 5.1-c provides a schematic of the mechanical tests applied to the cylindrical samples, including compressive strength (C), elastic modulus (E) and Poisson's ratio (ν), and splitting tensile strength (T). The dimension of the wall is provided in centimeters in the Figure 5.1-b. The T1 and T2 values indicate the splitting tensile strength for the two interface planes where the split was applied.

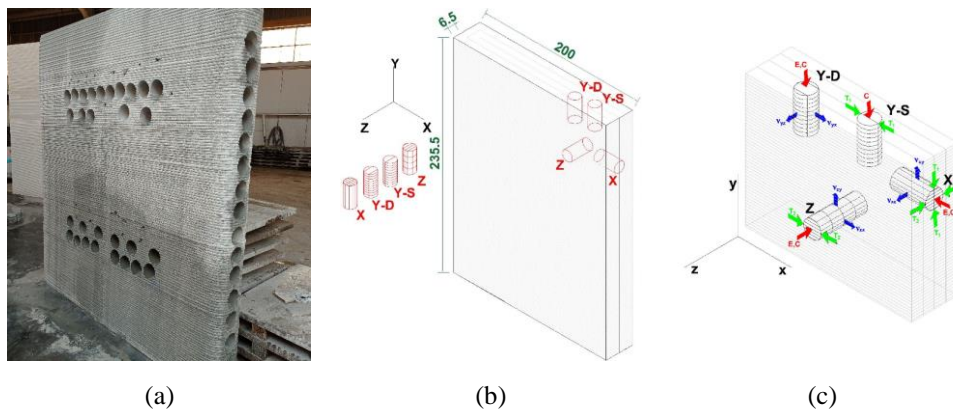


Figure 5.1. Images Showing (a) Cored Wall, (b) Coring Directions (Coring of Wall-1 in X, Y and Z), and (c) Schematic of Cylindrical Samples and the Experiments (Dimensions are in cm)

Table 5.1 provides a summary of the mechanical properties of the printed and cast concrete specimens investigated in the Chapter 3. The results for compressive strength, elastic modulus, and Poisson's ratio, as well as the splitting tensile strength, are presented for the upper, lower, and cast specimens. The Y-D specimens are used to determine the compressive strength and elastic modulus of the Y direction, while Y-S specimens are employed to measure the splitting tensile strength in between the Y specimens. The T1 splitting tensile strength results are obtained by averaging the Y-S and X_{T1} specimens, while the T2 results are generated by averaging the Z and X_{T2} specimens. Overall, the Table 5.1 provides a comprehensive overview of the mechanical properties of printed and cast concrete, highlighting the differences between the upper, lower, and cast specimens in terms of their performance under different loading conditions.

Table 5.1. Mechanical Properties of Printed and Cast Concrete

Material Properties	Compressive Strength (MPa)	Elastic Modulus (GPa) and Poisson's Ratio			Tensile Strength (MPa)
	ASTM C39 [93]	ASTM C469 [98]			ASTM C496 [99]
Printed Concrete Wall (Upper Part)	$\sigma_x = 38.2 \pm 5.4$ $\sigma_y = 30.8 \pm 1.2$ $\sigma_z = 22.7 \pm 1.9$	$E_x = 18.5$ $E_y = 13.6$ $E_z = 14.4$	$\nu_{xy} = 0.20$ $\nu_{yx} = 0.17$ $\nu_{zx} = 0.17$	$\nu_{xz} = 0.20$ $\nu_{yz} = 0.18$ $\nu_{zy} = 0.23$	$\sigma_{T1} = 1.8$ $\sigma_{T2} = 1.6$
Printed Concrete Wall (Lower Part)	$\sigma_x = 50.6 \pm 2.6$ $\sigma_y = 53.2 \pm 5.4$ $\sigma_z = 47.3 \pm 3.0$	$E_x = 20.2$ $E_y = 20.8$ $E_z = 17.5$	$\nu_{xy} = 0.23$ $\nu_{yx} = 0.17$ $\nu_{zx} = 0.17$	$\nu_{xz} = 0.21$ $\nu_{yz} = 0.19$ $\nu_{zy} = 0.21$	$\sigma_{T1} = 2.5$ $\sigma_{T2} = 3.1$
Cast Concrete	$\sigma = 37.8 \pm 3.2$	$E_x = 18.8$	$\nu = 0.20$		$\sigma_T = 3.2$

5.2.3 Specimen Design and Building Procedures

The walls were printed using a large-scale 3D printer provided by ISTON, a company specializing in 3D printing technology. Five different walls with varying width×length×height dimensions were designed as follows and they were named based on their dimensions:

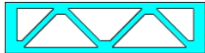




- Wall 25-100-100: 25×100×100 cm
- Wall 25-100-150: 25×100×150 cm
- Wall 30-150-100: 30×150×100 cm
- Wall 25-150-100: 25×150×100 cm
- Wall 20-150-100: 20×150×100 cm

The variation in width and length dimensions has an impact on the configuration of the inner truss. For all patterns, a consistent 45-degree inner truss angle was maintained, and details regarding the shape and angle can be found in Table 5.2.

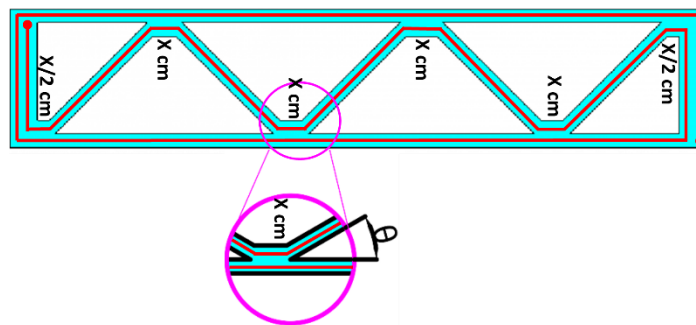
To produce the 3D printed concrete walls, a similar process to that described in Chapter 3 was followed. The layer height was 1 cm, and the layer width was approximately 3 cm for the interlayer and 3.5 cm for the bulk part of the layer. The variation in layer width is attributed to the circular shape of the printing nozzle used.

To ensure the reproducibility of the printed walls, meticulous records of the printing process were maintained. Table 5.2 provides an overview of the printing parameters and specimen cross-section shapes. The angle location is highlighted by a magenta circle, and the printing direction is represented by a red line. The nozzle rising location is indicated by a red dot, and the truss distances are shown as x cm and $x/2$ cm. By utilizing this information, along with the cross-section shapes, the wall can be easily reproduced. This allows for accurate comparisons between different specimens and enhances the reliability of the study.

Table 5.2. Printing Procedure and Printed Walls

Specimen cross-section shapes	Specimen name	Concrete area (cm ²)	Void area (cm ²)
	25-100-100	1171.5	1328.5
	25-100-150	1171.5	1328.5
	30-150-100	1732.5	2767.5
	25-150-100	1641.4	2108.6
	20-150-100	1529.8	1470.2

Printing details



5.2.4 Test Setup and Instrumentation

This section provides a detailed overview of the test setups and instrumentation employed in the earthquake experiments, focusing on unreinforced 3D printed concrete (3DPC) walls. The primary objective was to conduct a comprehensive evaluation of how these walls respond to lateral loads, particularly considering the impact of varying wall geometries.

For this study, two distinct test setups were utilized. The key distinguishing factor between these setups was the approach taken to prevent any uplift movement of the walls during the experiments. Notably, it is imperative to emphasize that the restraining bars employed in the initial test setup proved to be inadequate for inducing wall fracture in the last two experiments.

The first test setup was dedicated to testing the response of walls 25-100-100, 25-150-100, 20-150-100, and 30-150-100. However, due to the insufficiency of the restraining bars to achieve the primary objective of wall breakage, a necessary modification was carried out. The modified test setup aimed to address this issue and was specifically employed for testing walls 25-100-100, and 25-100-150. This strategic modification was essential in enabling the experiments to achieve the desired outcome of wall fracture.

5.2.4.1 Initial Test Setup

Figure 5.2 shows the experimental setup and measurement locations used in the study. The setup includes eight linear variable differential transformers - LVDTs (indicated as #2 to #9) placed at different positions along the height and width of the printed walls, as well as a load cell (indicated as #1) for measuring the applied load. These measurement devices were used to monitor the deformation and load-bearing capacity of the printed walls during the testing phase. In Figure 5.2-a, an IPE O 450 section is fixed to the frame system by 4 bolts, and the printed wall is sandwiched between the IPE O 450 section and another IPE O 450 section placed on top of the

wall, using Master Brace ADH 1420 (for the walls 20-150-100 and 30-150-100) and Sikadur 31 (for the walls 25-100-100 and 25-150-100) epoxies to distribute the lateral load to the entire wall section. Four steel bars (combination of shackle, tension screw, and eyebolt) were pinned to the flanges of the IPE sections to prevent uplift movement during the load application, as shown in the Figure 5.2-a. Additionally, four stoppers were bolted to the IPE section right after the wall edges to prevent lateral movement during the load application, as illustrated in Figure 5.2-c. As shown in the Figure 5.2-a, an actuator was pinned to the frame system to apply lateral load to the wall, and the LVDTs were positioned to measure different types of movement. #1 is the load cell location, and #8 and #9 are the LVDT locations that read the out-of-plane movement of the wall. LVDTs #2 to #6 were used to measure the lateral displacement of the wall, with their elevations based on the bottom of the wall shown in Figure 5.2-a. LVDT #2 reads from the top stopper, and the others read from the wall. LVDT #7 was used to monitor uplift displacement of the wall during load application. Figure 5.2-a also illustrates the elevations of the LVDTs. Finally, four strain gauges were employed for each axial steel bar to continuously track the evolution of axial load throughout the experiment. Data was collected once per second.

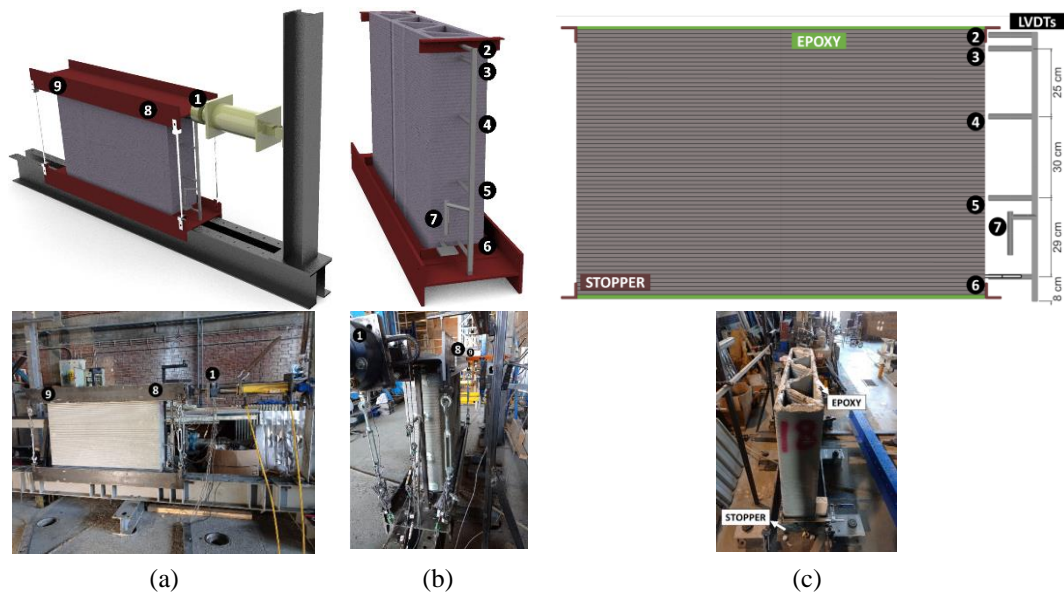


Figure 5.2. Experimental Setup Details

5.2.4.2 Modified Test Setup

Indeed, with the initial test setup, walls 25-150-100, 20-150-100, and 30-150-100 were successfully fractured. However, walls 25-100-100 and 25-100-150 proved to be inadequately broken by the initial test setup. Consequently, the decision was made to modify the initial test setup, and as a result, walls 25-100-100 and 25-100-150 were successfully broken. Therefore, the primary objective behind this modification was to enhance the test setup to the extent that all the walls could be effectively subjected to extreme lateral forces, with the ultimate goal of achieving wall fracture.

To achieve this, the original restraining bars used in the initial test setup were replaced with a more robust 60x60x7 L-section bars. These redesigned bars played a crucial role in preventing substantial uplift capable of causing a rocking effect during the experiments, thereby enhancing the ability to reach the walls' breaking points.

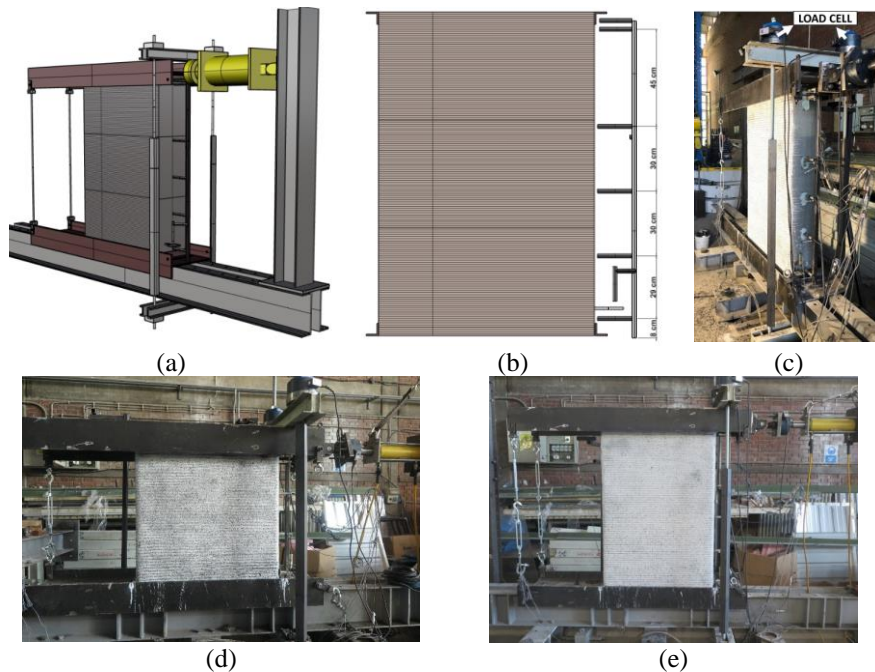


Figure 5.3. Modified Experimental Setup Details

In Figure 5.3-a, the representative figure of the modified experimental setup provides a visual overview of the key components and instrumentation. In Figure 5.3-d and

Figure 5.3-e, Wall 25-100-100, and Wall 25-100-150 are presented undergoing testing with the adapted configuration, respectively. The two test setups shared similar instrumentation and data collection methods, guaranteeing the accurate measurement of the walls' response to lateral loads throughout the experiments. However, for the wall 25-100-150, which had a height of 1.5m, an additional LVDT was employed, as illustrated in Figure 5.3-b. Furthermore, the monitoring system for the restraining bars was enhanced by integrating a load cell (Figure 5.3-c) to measure the axial loads experienced by the bars, providing a more comprehensive understanding of the structural response.

5.2.5 Loading Configurations

The testing procedure involved applying a lateral load to the printed walls using the actuator pinned to the frame system, as shown in Figure 5.2-a, and Figure 5.3-a. The load was applied incrementally, starting from zero and increasing gradually up to the point of failure. During the test, the out-of-plane and lateral displacements of the wall were monitored using the LVDTs placed at different positions along the height and width of the wall, as described in Figure 5.2-a. The load and displacement data were recorded using a data acquisition system.

To ensure the stability of the testing setup, a pre-test calibration was performed by applying a known lateral load to the system without the wall. The calibration was repeated before each test to ensure the accuracy of the measurement devices.

The failure mode of the printed walls was observed and recorded, and the corresponding load and displacement data were used to analyze the load-bearing capacity and deformation behavior of the printed walls. The failure mode was defined as the point at which the wall could no longer resist the applied lateral load and collapsed. The ultimate load-bearing capacity and displacement of the walls were calculated based on the load and displacement data obtained during the test.

5.2.6 Measurements and Digital Image Correlation (DIC)

DIC (Digital Image Correlation) was applied to 25-100-150, 25-100-100 and 25-150-100 wall samples. In preparation for the experiments, the walls were initially coated with white paint, a mixture of lime and plaster, providing a consistent base for optical measurements (Figure 5.4-a). Subsequently, a pattern of randomly distributed, small black dots was meticulously applied to the wall surfaces using spray paint (Figure 5.4-b). This pattern, characterized by its random shapes and sizes, served as the reference for the Digital Image Correlation (DIC) system. To ensure the accuracy of the pattern, quality checks were performed using GOM Correlate software (Figure 5.4-c). The process involved a series of steps, transitioning from an unpainted surface to a painted surface and, finally, to a GOM-verified pattern.

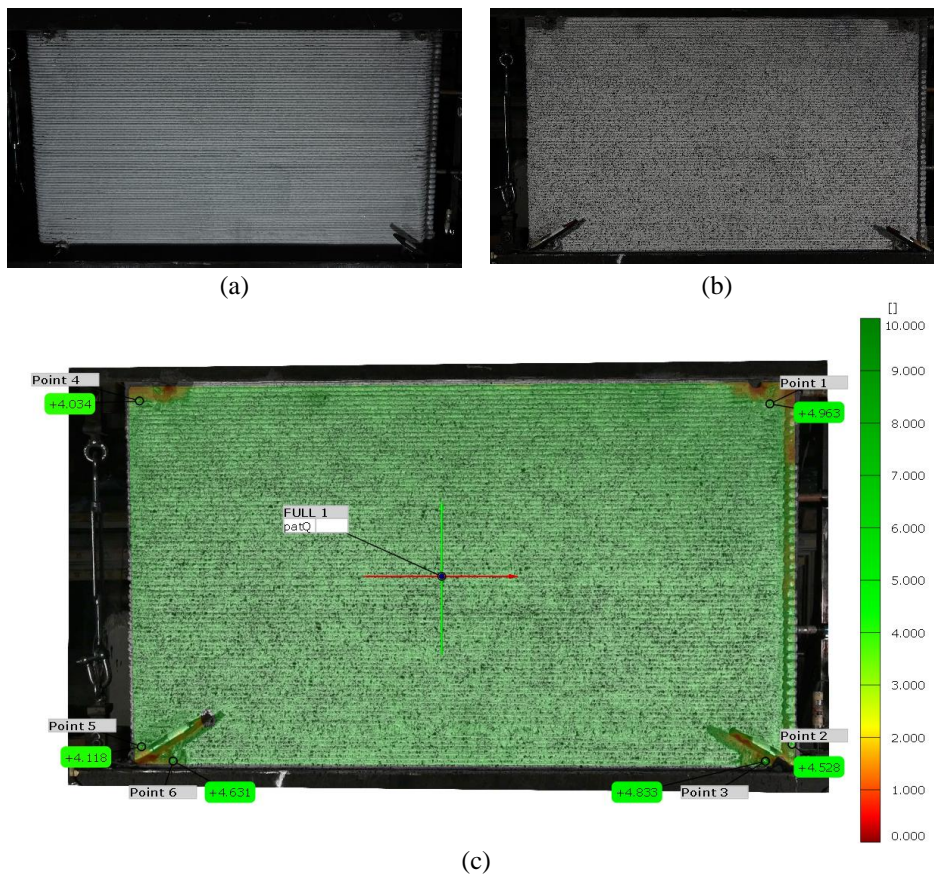


Figure 5.4. Wall Surface Preparation for Digital Image Correlation (DIC)

5.3 Experimental Results and Discussion

This section presents the results of the experimental program conducted to evaluate the mechanical behavior of large-scale 3D printed concrete walls under lateral loading. The results are organized into three subsections: load-displacement curves of the walls, failure modes of the walls, and discussion of the factors influencing the performance.

5.3.1 Load-Displacement Curves of the Walls

The load-displacement response of the 3D printed concrete walls was measured using the instrumentation described in the part 5.2.4. The walls were subjected to lateral loading at different levels of displacement, and the load and displacement data were recorded using the data acquisition system.

The subsequent subsections delve into specific aspects of the load-displacement response, offering insights into measurements obtained from LVDTs, DICs, and net lateral deformation, which collectively contribute to a comprehensive understanding of the walls' behavior under lateral loading.

5.3.1.1 Results from LVDTs Measurements

This section presents the results obtained from LVDT (Linear Variable Differential Transformer) measurements during the experiments. The data under investigation includes lateral load, displacements, and force measurements. The purpose of this presentation is to provide an overview of the collected data without an indicate analysis. In all the graphs featured in this section, the results from the initial test setup are represented by red lines, while those from the modified test setup are indicated by blue lines.

In Figure 5.5, the discernible relationships between lateral load and top displacement measured from LVDT #2 shown in Figure 5.2-b and Figure 5.2-c are illustrated for

various wall configurations, including 30-150-100, 25-150-100, 20-150-100, 25-100-100, and 25-100-150. The graph presents data depicting how top displacement corresponds to lateral load for these walls. The graphs within Figure 5.5 share a consistent scale for load (ranging from 0 to 120 kN) and displacement (spanning from 0 to 20 mm) to facilitate an accurate comparison of stiffness variations.

In Figure 5.6, a comprehensive view of the relationships between lateral load and uplift displacement measured from LVDT #7 shown in Figure 5.2-b and Figure 5.2-c is presented for various wall configurations: 30-150-100, 25-150-100, 20-150-100, 25-100-100, and 25-100-150. Each of these configurations is represented by a separate graph within the figure. Again, consistency in the scales of both lateral load (ranging from 0 to 120 kN) and displacement (spanning from 0 to 20 mm) across all sub-graphs allows for a clear visual comparison of uplift displacement patterns under uniform loading conditions.

In Figure 5.7, the presented graphs illustrate the relationship between lateral load and the response in the bars. The first and second graphs depict the variation of lateral load versus the induced strain in the bars. This strain measurement was obtained in the initial test setup using strain gauges. Conversely, the third and fourth graphs demonstrate how the lateral load relates to the induced force in the bars. These force measurements were collected using a load cell in the modified test setup as shown in Figure 5.3-c. The induced strain and force in the bars occur due to the conservation of momentum as a response to the applied lateral load, preventing uplift movement.

In Figure 5.8, an analysis of lateral displacement profiles is presented. The evolution of lateral (horizontal) displacement at different heights of the walls was measured using an array of LVDTs. For the 1-meter-high walls, as shown in Figure 5.2-b and Figure 5.2-c, five LVDTs were employed. In the case of the taller 1.5-meter-high wall, depicted in Figure 5.3-b and Figure 5.3-c, the setup was expanded to include six LVDTs.

The red line in the graphs represents the results from the initial test setup, while the blue in the graphs represents the results from the modified test setup.

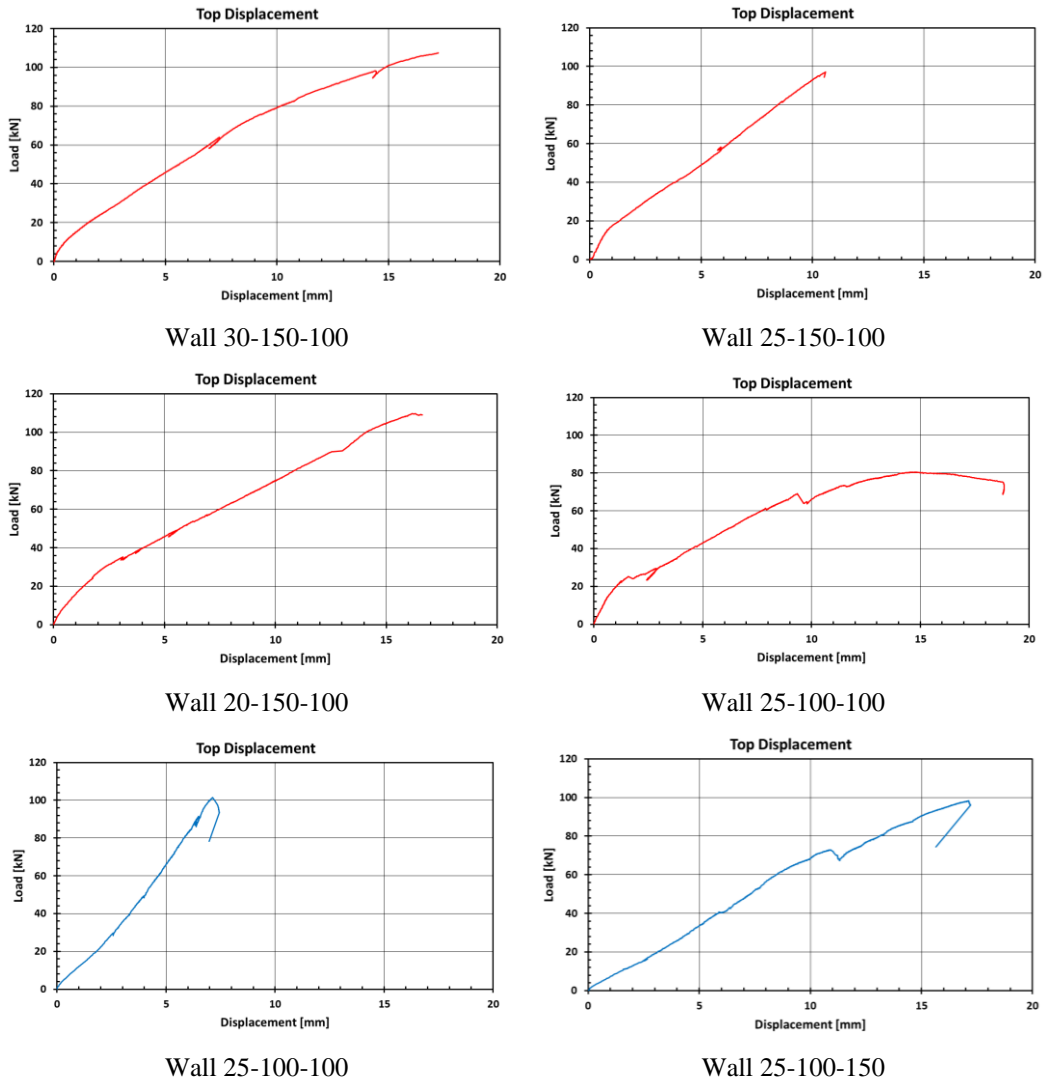
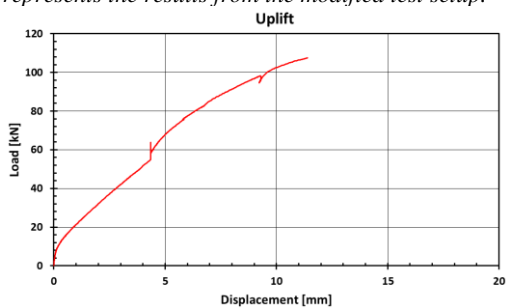
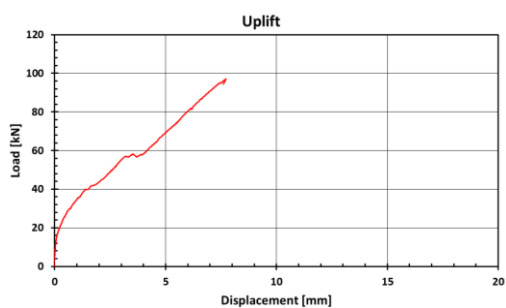


Figure 5.5. Lateral Load – Top Displacement Measured from Load-Cell and LVDT #2

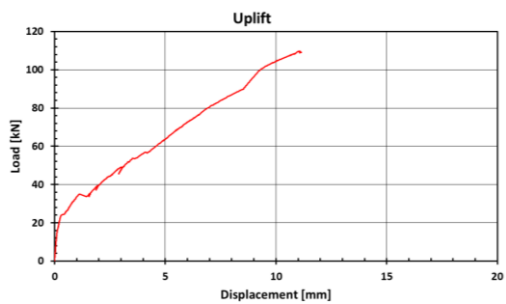
The red line in the graphs represents the results from the initial test setup, while the blue in the graphs represents the results from the modified test setup.



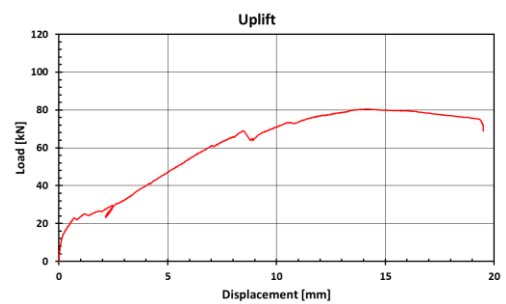
Wall 30-150-100



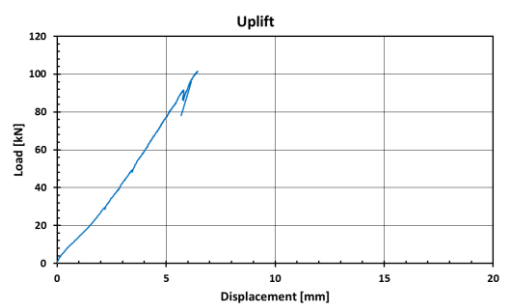
Wall 25-150-100



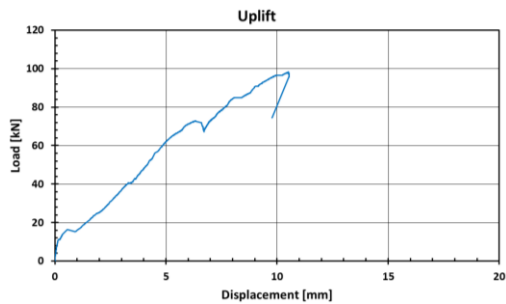
Wall 20-150-100



Wall 25-100-100



Wall 25-100-100



Wall 25-100-150

Figure 5.6. Lateral Load – Uplift Displacement Measured from Load-Cell and LVDT #7

The red line in the graphs represents the results from the initial test setup, while the blue in the graphs represents the results from the modified test setup.

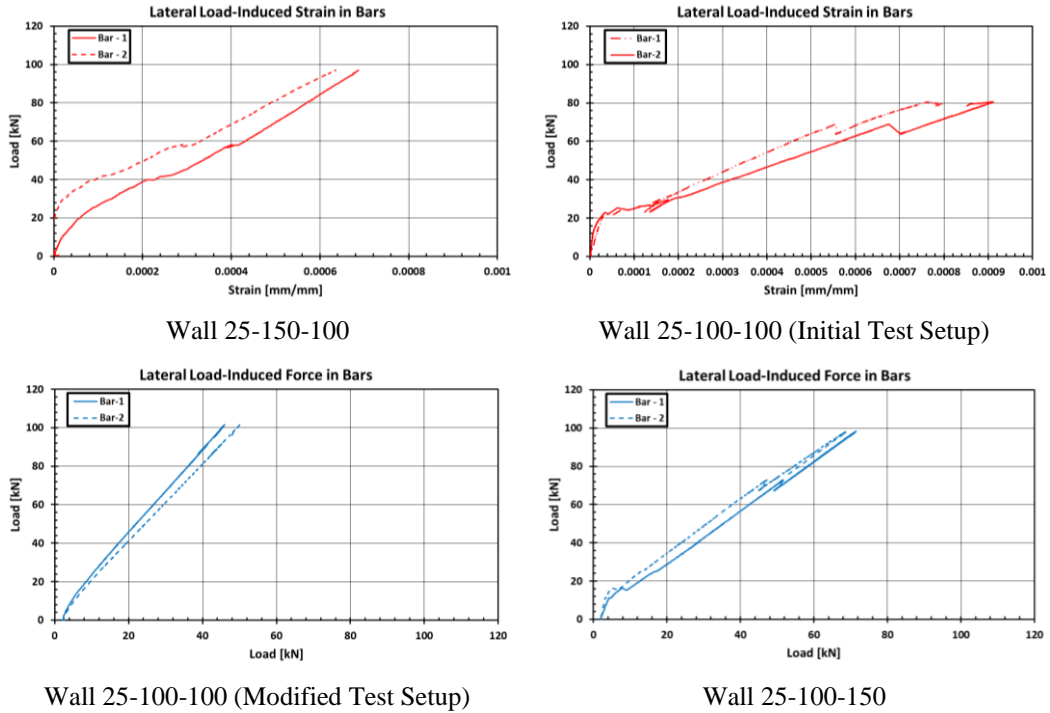
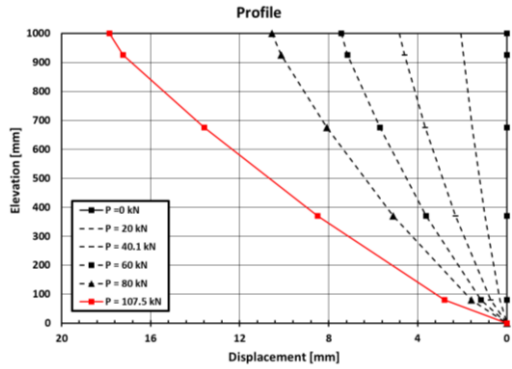


Figure 5.7. Lateral Load vs. Induced Strain/Force in the Bars

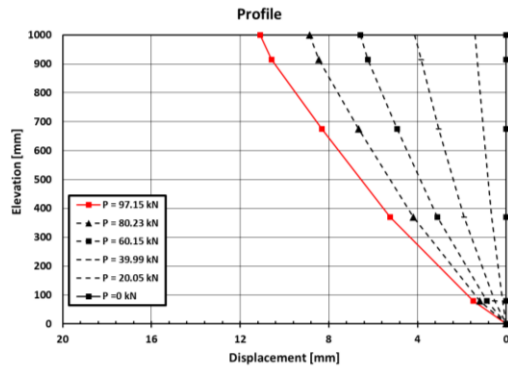
The profiles for each wall are displayed individually in Figure 5.8, providing a detailed view of how lateral displacement is influenced under various lateral load levels, including 0 kN (no load), 20 kN, 40 kN, 60 kN, 80 kN, and the maximum applied load.

Figure 5.9 is dedicated to comparisons of lateral displacement profiles at two crucial moments: (a) 80 kN lateral load and (b) the ultimate lateral load applied to the wall. These comparisons enable a direct assessment of the walls' response to these significant load levels and emphasize any disparities in displacement patterns.

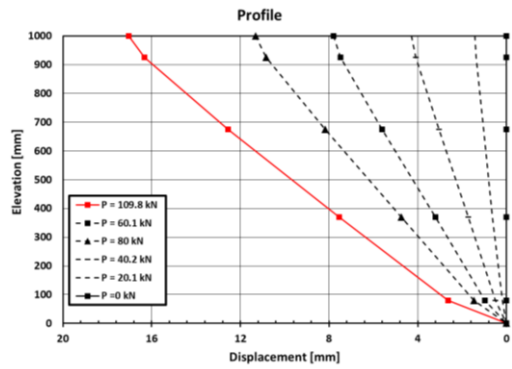
The red line in the graphs represents the results from the initial test setup, while the blue in the graphs represents the results from the modified test setup.



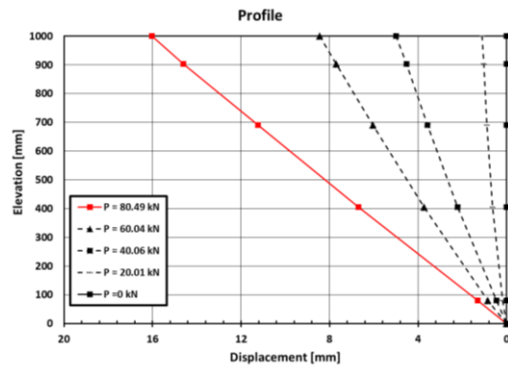
Wall 30-150-100



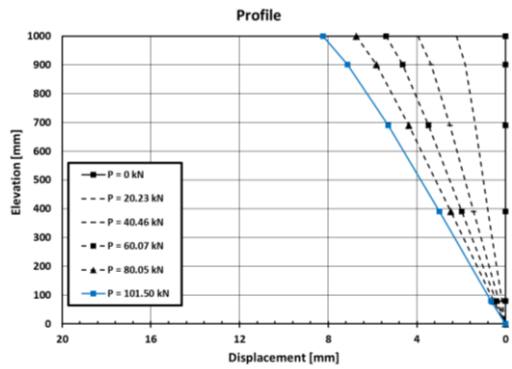
Wall 25-150-100



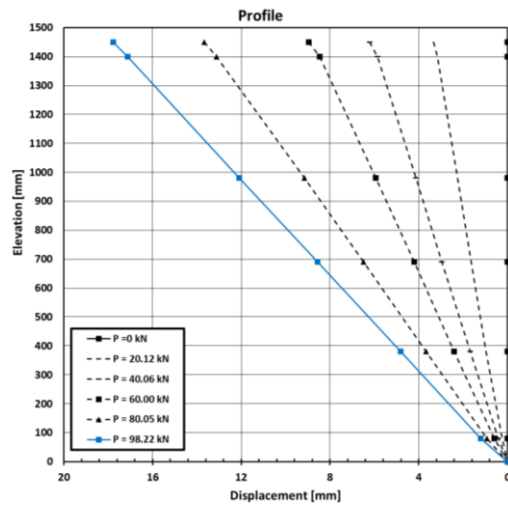
Wall 20-150-100



Wall 25-100-100



Wall 25-100-100



Wall 25-100-150

Figure 5.8. Lateral Displacement Profiles

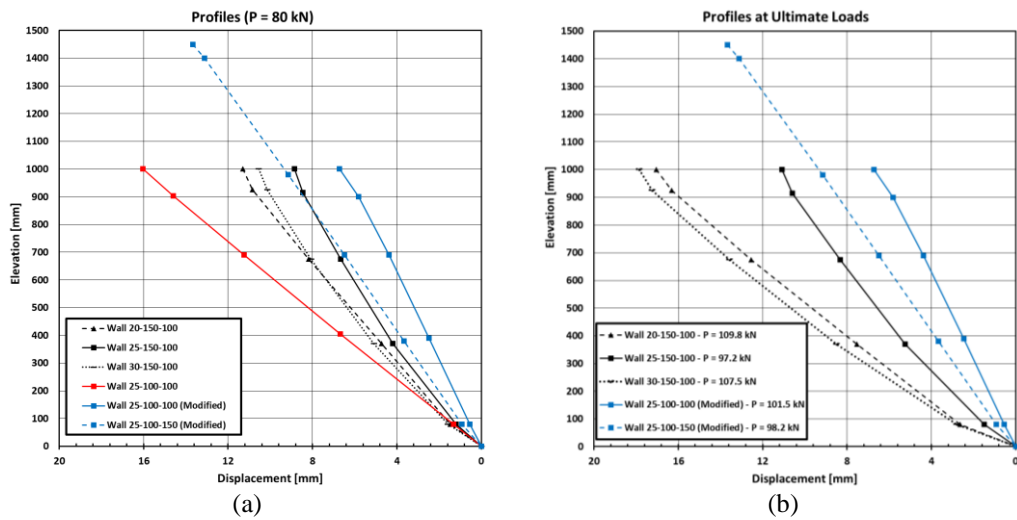


Figure 5.9. Comparisons of the Lateral Displacement Profiles of the Walls at (a) 80 kN Lateral Load, and (b) Ultimate Lateral Load Applied to the Wall

5.3.1.2 Results from DICs Measurements

Coupled with the LVDT measurements, DIC was employed to critically assess the lateral behavior of the large-scale 3D printed concrete walls. The DIC technique allowed surface deformation patterns to be thoroughly examined, offering invaluable insights into the response of these structures to varying lateral loads. The results obtained through DIC measurements are presented in this section, providing a detailed examination of wall surface displacements and deformations under the loading conditions. The analyses herein delve into how DIC technology enriches the understanding of wall behavior, serving as a pivotal component in the experimental framework.

The red line in the graphs represents the results from the initial test setup, while the blue in the graphs represents the results from the modified test setup

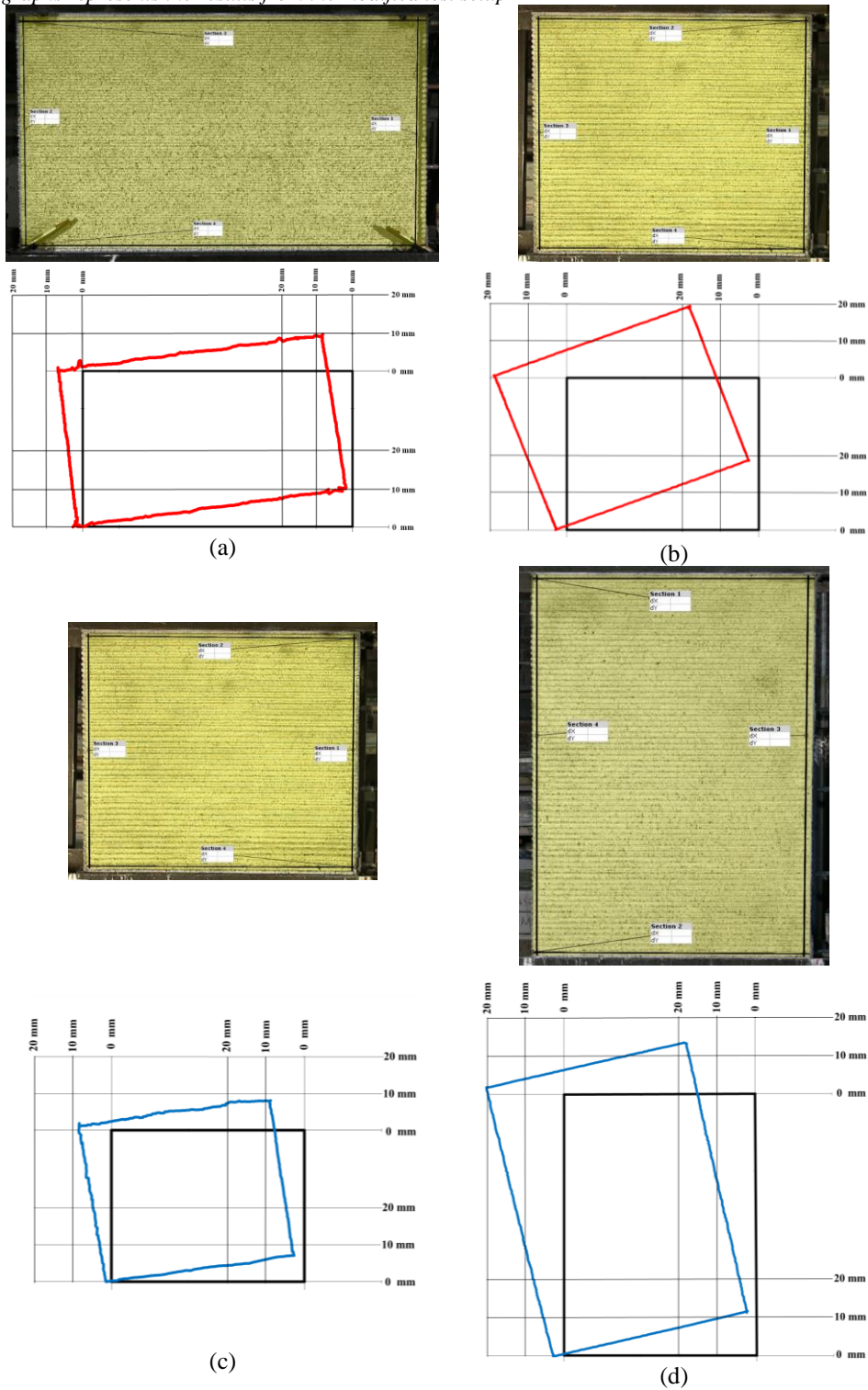


Figure 5.10. Comparison of Initial and Deformed Surface Patterns for the Walls (a) 25-150-100, (b) 25-100-100, (c) 25-100-100, and (d) 25-100-150

Figure 5.10 provides a visual comparison of the initial and deformed surface patterns for various wall configurations. In each subfigure (a, b, c, and d), the top section represents the respective wall and the sections of interest, demarcated by black lines, which are slightly set inwards to ensure precise results. The bottom section within each subfigure displays the initial wall configurations outlined by black lines, alongside the deformed shapes of the walls highlighted in red and blue lines, representing the highest lateral load levels. It's important to note that the red lines indicate results from the initial test setup, while the blue lines represent those from the modified test setup. The deformed shapes have been magnified for visual clarity, exaggerating them by 20 times.

At the bottom section of Figure 5.10, each subfigure includes a metric that indicates the magnitude of wall deformation, ranging from 0 to 20 mm. This metric is aligned with the top, left, right, and bottom sides of the initial wall configurations outlined by black lines.

As evident from the deformed surface patterns for the walls in Figure 5.10 and the uplift displacement data in Figure 5.6, the walls exhibit an expected behavior akin to rigid body rotation. Consequently, it becomes imperative to calculate the net lateral deformation of the walls. To achieve this, the deformed shape is adjusted by rotating it according to the uplift displacement. Subsequently, the top displacement is recalculated based on this rotation. This process enables a more accurate determination of the net lateral deformation.

5.3.1.3 Net Lateral Deformation of the Walls

The net lateral deformation of the walls is determined through a two-stage calculation process, as illustrated in Figure 5.11. In Figure 5.11-a, the parameters used for these calculations are provided, and the undeformed configuration of the wall is depicted by a grey rectangle, while the deformed configuration is represented by a black rectangle. The dimensions of the wall (length, L , and height, H) are

represented by blue, while the measurements, namely Δ_{BOTTOM} , Δ_{UPLIFT} , and Δ_{TOP} , are indicated by red data points. These measurements are taken at specific locations as demonstrated in Figure 5.2-c and Figure 5.3-b.

In the first step, the wall is rotated to account for the observed behavior, as shown in Figure 5.11-b. Here, the tangent of the angle, θ , for each recorded load displacement data is calculated using Equation 5.1-a. This angle is used to determine the rotated positions at the top and base of the wall, known as $\bar{\Delta}_{TOP}$ (calculated with Equation 5.1-b) and Δ_{BASE} (calculated using Equation 5.1-c), respectively. The parameter H_{BOTTOM} in Equation 5.1-c represents the measurement height, which is set at 80 mm, as displayed in Figure 5.2-c and Figure 5.3-b.

In the second stage, the wall's lateral position is adjusted by an amount equal to the wall's shear displacement for each recorded dataset, as depicted in Figure 5.11-c. The assumption is made that the wall's shear displacement corresponds to the rotated shear displacement, Δ_{BASE} . This assumption is made because the lowest measurement point is located at 80 mm rather than the base (0 mm). The displacement operation is carried out using Equation 5.1-d, ultimately resulting in the determination of the net lateral deformation of the wall, referred to as Δ_{NET} .

The Figure 5.11-d displays the anticipated net lateral deformation resulting from these corrections (Δ_{NET}).

$$\tan \theta = \frac{\Delta_{UPLIFT}}{L} \quad (5.1a)$$

$$\bar{\Delta}_{TOP} = \Delta_{TOP} - H \times \tan \theta \quad (5.1b)$$

$$\Delta_{BASE} = \Delta_{BOTTOM} - H_{BOTTOM} \times \tan \theta \quad (5.1c)$$

$$\Delta_{NET} = \bar{\Delta}_{TOP} - \Delta_{BASE} \quad (5.1d)$$

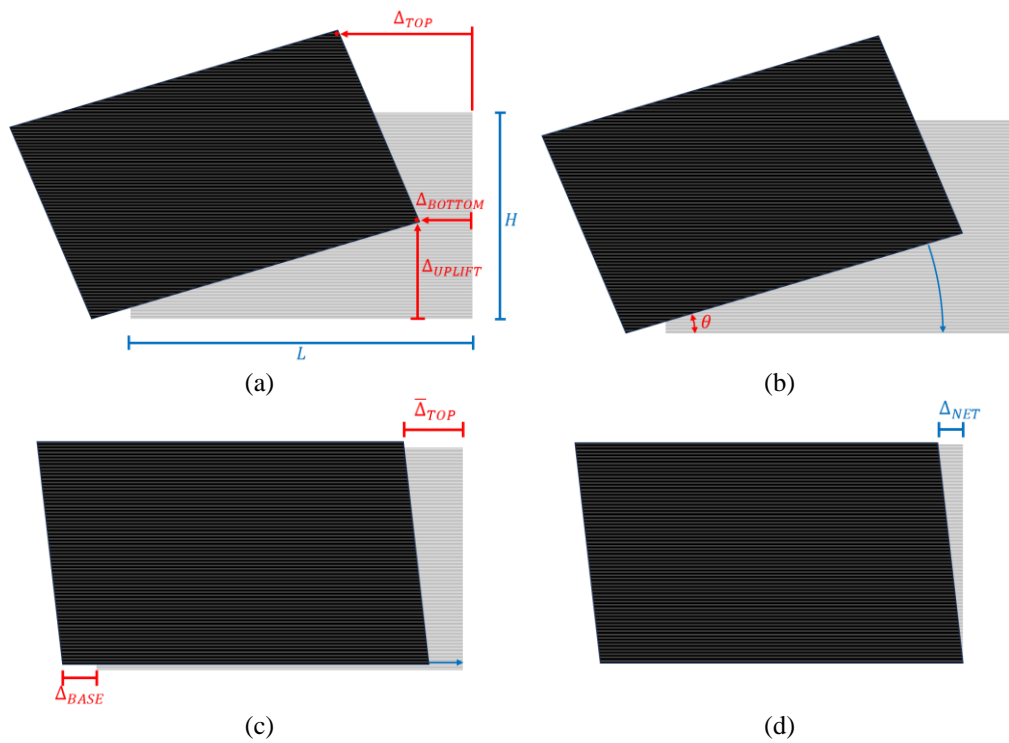
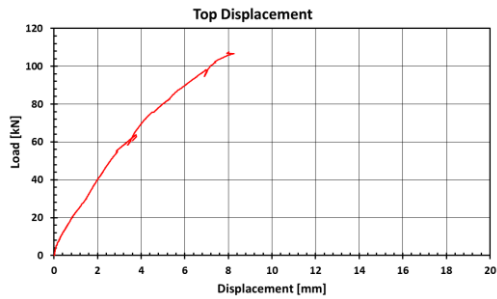


Figure 5.11. Calculation Procedure of Net Lateral Deformation

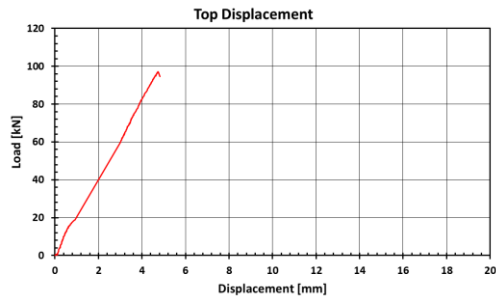
Figure 5.12 illustrates the relationship between the lateral load applied to the walls and the corresponding net lateral deformation, as determined from LVDT measurements. The results presented in Figure 5.12 reveal how the walls respond to increasing lateral loads, with the net lateral deformation values being crucial indicators of their mechanical behavior. These measurements, obtained through the described two-stage calculation process, provide valuable insights into the structural response of the walls under the applied loads.

Figure 5.13 demonstrates the correlation between the lateral load applied to the walls and the corresponding net lateral deformation, as determined through DIC measurements. Importantly, the discrepancies in stiffness between Figure 5.12 and Figure 5.13 can be attributed to the deformation of the IPE section. This IPE section is the structural element that supports the LVDTs. Consequently, the walls exhibit diverse deformations in response to varying lateral loads, offering a comprehensive view of their mechanical behavior. The net lateral deformation data, obtained using DIC technology, plays a pivotal role in understanding the structural performance of

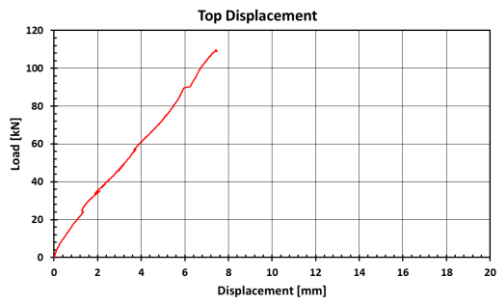
the walls under different loading conditions. It's worth noting that DIC measurements are considered more accurate due to this particular reason.



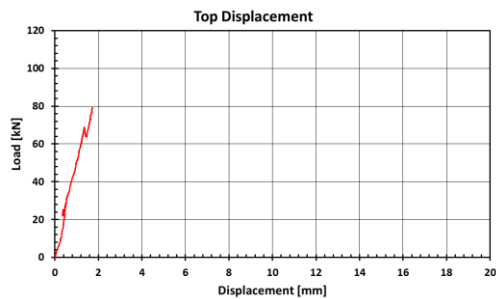
Wall 30-150-100



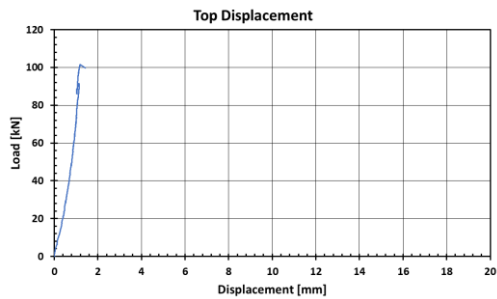
Wall 25-150-100



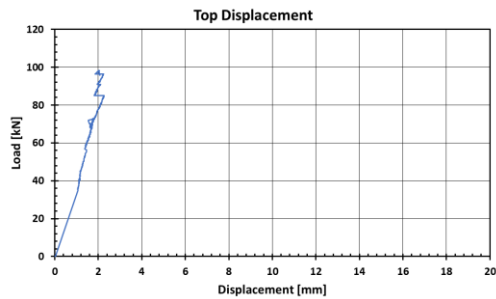
Wall 20-150-100



Wall 25-100-100



Wall 25-100-100



Wall 25-100-150

Figure 5.12. Lateral Load – Net Lateral Deformation Derived from LVDT Measurements

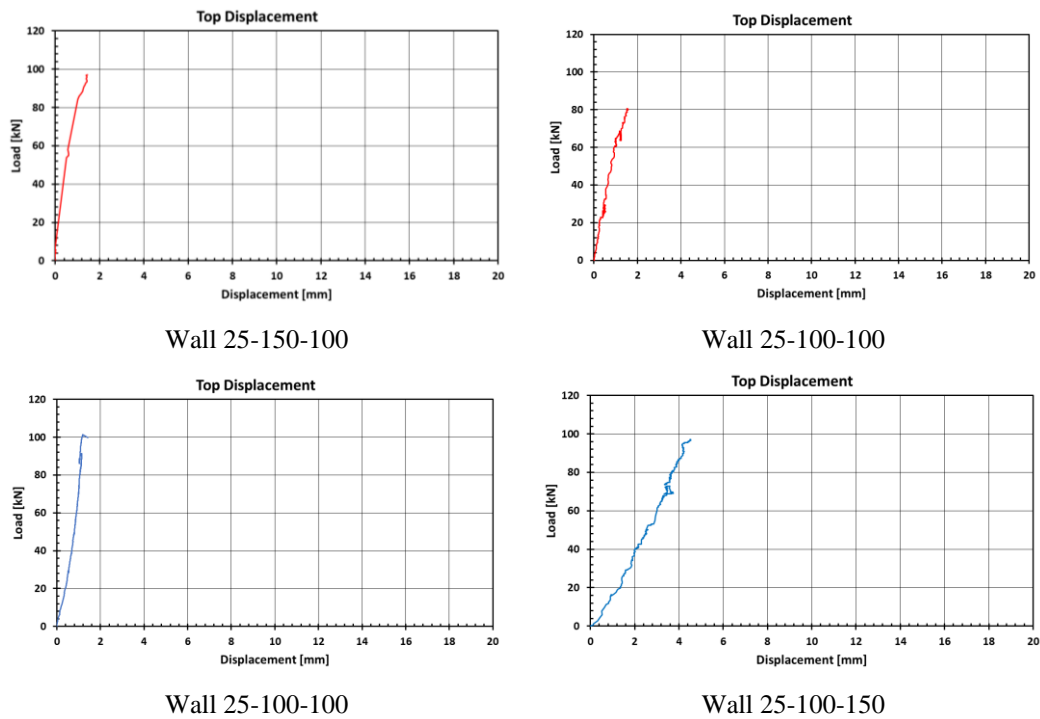


Figure 5.13. Lateral Load – Net Lateral Deformation Derived from DIC Measurements

5.3.2 Failure Modes of the Walls

In this section, a comprehensive examination is undertaken to explore the diverse failure modes exhibited by the walls under various test setups. The structural behavior of these constructions is unveiled through a detailed analysis of the failures. The importance of understanding these failure modes lies in the assessment of the walls' performance under different conditions. Furthermore, the disparities observed in the load-displacement curves will be addressed, and explanations for these variations will be provided. Each failure case will be meticulously examined to reveal the distinctive characteristics that influence the structural responses.

5.3.2.1 Failures of the Walls 30-150-100, 25-150-100, 20-150-100 (Initial Test Setup)

In this sub-section, the initial test setup serves as the focal point for an investigation into the failures experienced by the walls with configurations 30-150-100, 25-150-100, and 20-150-100. The reason for presenting these three walls together is that the fractures and cracks observed in all three share common characteristics. These cases are examined in detail, with a presentation of the failures, including their specific attributes, patterns of distress, and any deviations in the load-displacement curves from the anticipated outcomes.

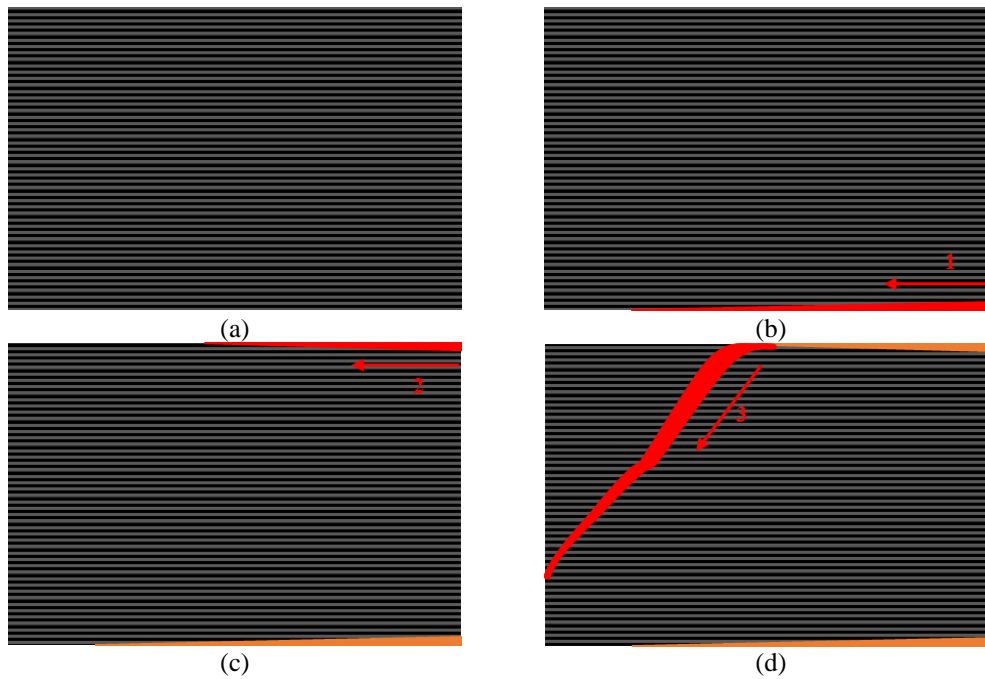


Figure 5.14. Crack Propagation Process: (a) Initial Undamaged Wall Configuration, (b) First Sudden Crack, (c) Second Continuous Crack, and (d) Brittle Diagonal Failure of the Front Face

In Figure 5.14, the progression of failures in walls with configurations 30-150-100, 25-150-100, and 20-150-100 (initial test setup) is visually depicted. The cracks and fractures observed in these walls exhibit common characteristics, which are closely related to the distinctive bilinear patterns observed in their load-displacement curves. This figure provides a step-by-step visualization of the failure process, starting with

the initial undamaged configuration (Figure 5.14-a), followed by the sudden crack formation in Figure 5.14-b.

The abrupt crack, as seen in Figure 5.14-b, appears quickly and corresponds to the initial linear and stiffer phase in the wall graphs (Figure 5.5, Figure 5.6, and Figure 5.7). In these graphs, it can be observed that the primary fractures began to appear at loads of approximately 5 kN, 17 kN, and 23 kN for wall specimens 30-150-100, 25-150-100, and 20-150-100, respectively. The discrepancy in the initial fracture load of wall specimen 30-150-100 is attributed to inadequate epoxy penetration between the wall and the IPE section. Consequently, due to the underperformance of the Master Brace ADH 1420 brand epoxy, the experiment transitioned to the usage of Sikadur 31 brand epoxy in subsequent tests. On the other hand, this bilinear behavior is not seen in the net lateral deformation graphs in Figure 5.12 and Figure 5.13 because the measurements before the first crack are very close to the net lateral deformation. After the first crack occurs, the wall performs rigid body rotation. With the corrections made in the part 5.3.1.3, the lateral load – net lateral deformation graphs were found as linear.

The second crack (Figure 5.14-c), following the initial fracture, develops more gradually and incrementally with increasing load, aligning with the second linear phase within the relevant wall graphs presented in Figure 5.5, Figure 5.6, and Figure 5.7. These parts are close to linear even if not completely linear due to continuous crack progression. Upon reaching the maximum load in the graphs, it marks the ongoing propagation of cracks, eventually leading to a brittle diagonal failure, depicted in Figure 5.14-d. This type of crack is brittle, making the wall non-load bearing beyond this point. The evolution of this crack is detailedly illustrated in the Figure 5.15.

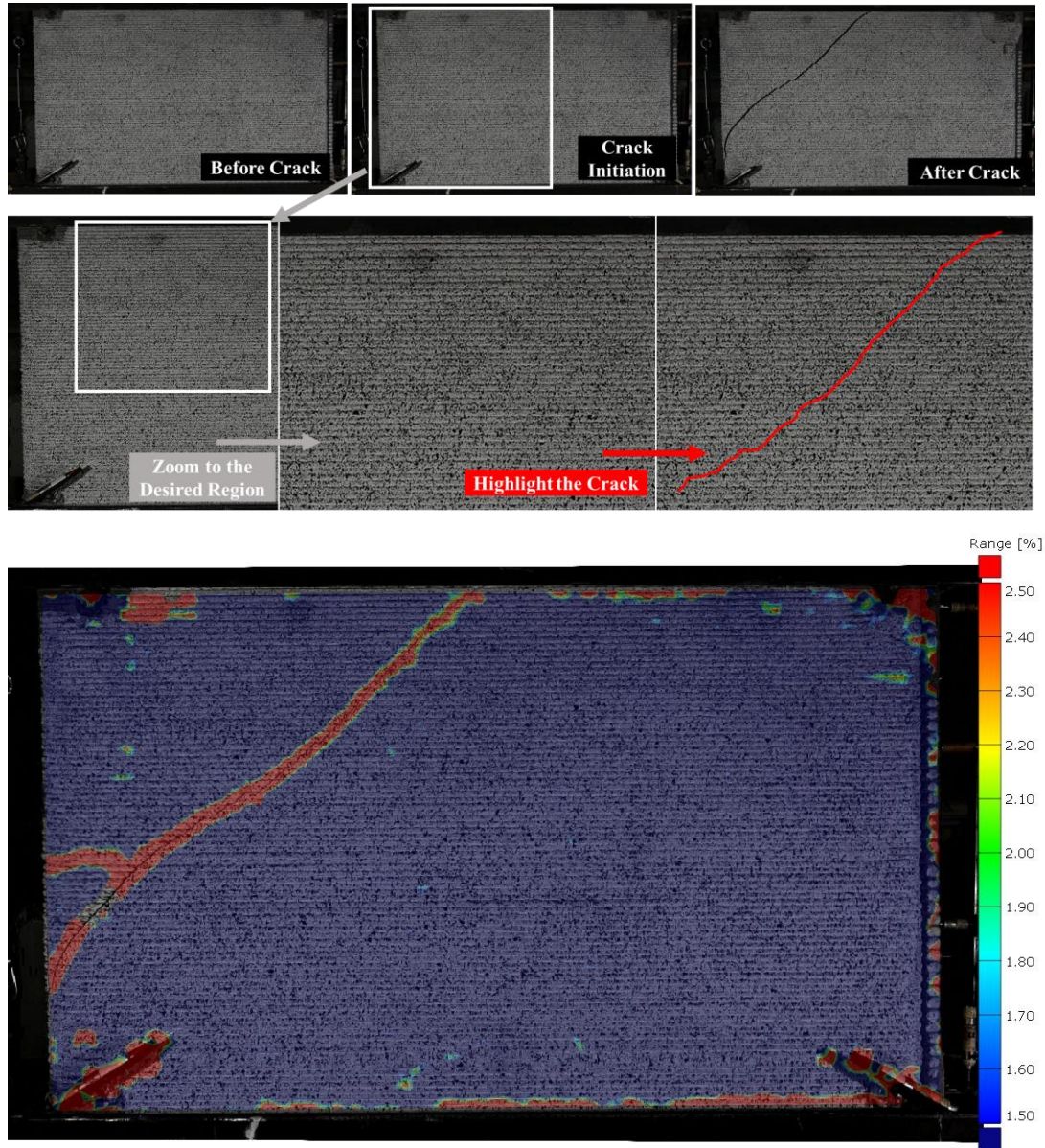
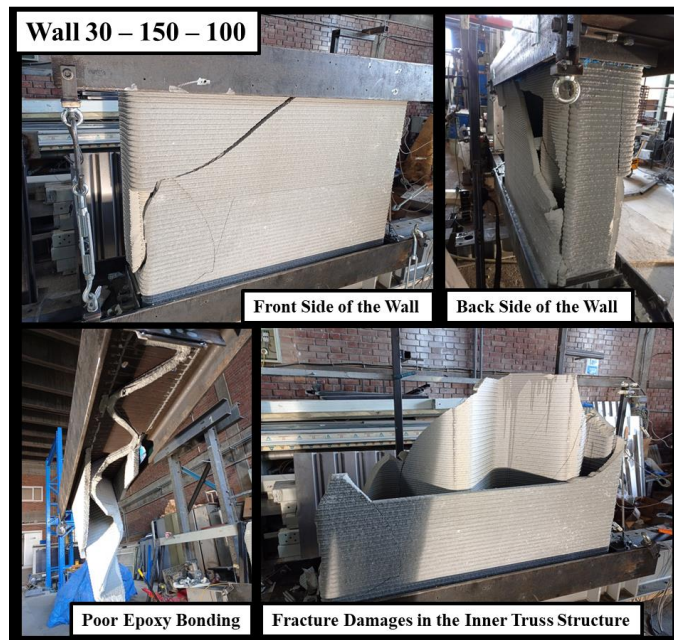
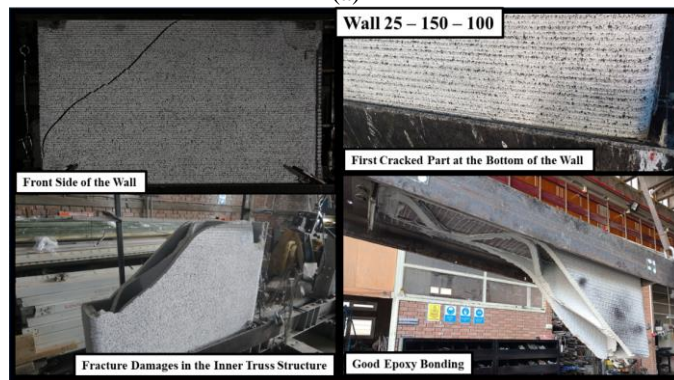


Figure 5.15. Sudden Diagonal Crack Propagation of the Wall 25-100-150 Captured by DIC



(a)



(b)



(c)

Figure 5.16. Key Images and Notes from Fractured Walls: Walls (a) 30-150-100, (b) 25-150-100, and (c) 20-150-100

Figure 5.16 provides a visual representation of critical images and corresponding notes captured from the fractured walls with configurations 30-150-100, 25-150-100, and 20-150-100. Each subfigure within this comprehensive illustration features a selection of essential images, each accompanied by concise notes highlighting the significance of the depicted features and conditions. These images offer valuable insights into the observed fractures, crack propagation, and specific aspects of distress, contributing to a deeper understanding of the structural performance of these walls under different loading conditions.

In Figure 5.16-a and Figure 5.16-c, prominent interlayer fractures are evident. It is worth noting that a portion of these fractures can be attributed to the ultimate wall failure. The greater portion of these interlayer fractures is primarily attributed to dynamic effects. These dynamic effects result from the abrupt wall failure, which, in turn, causes these interlayer fractures.

5.3.2.2 Failure of the Wall 25-100-100 (Initial Test Setup)

In this section, the specific failure behavior of the 25-100-100 wall configuration in the initial test setup is explored. The failure process is illuminated through two key figures: Figure 5.17 and Figure 5.19-a.

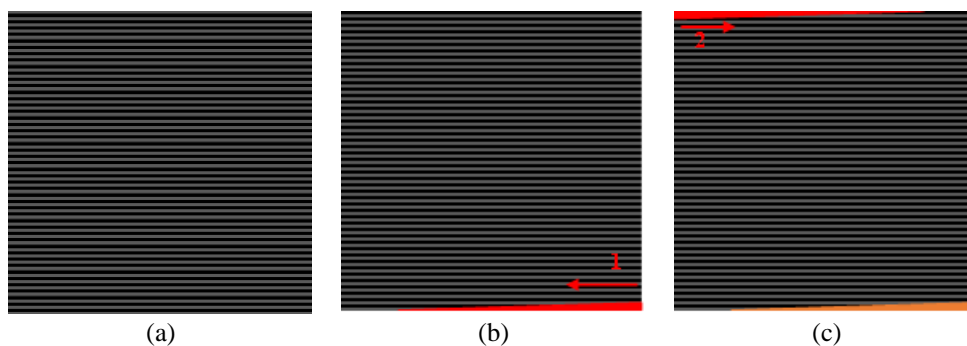


Figure 5.17. Crack Propagation Process: (a) Initial Undamaged Wall Configuration, (b) First Sudden Crack, and (c) Second Sudden Crack

Figure 5.17 provides a detailed visualization of the failure mechanism. The progression of cracks is portrayed in a step-by-step manner, beginning with the

presentation of the initial, undamaged configuration (Figure 5.17-a) and highlighting the emergence of the first sudden crack (Figure 5.17-b), which was observed at an approximate load of 15 kN. Subsequently, the sudden initiation of a second crack (Figure 5.17-c), which manifested around 70 kN, is depicted.

The investigation into the behavior of the wall with configuration 25-100-100 during the initial test setup reveals a distinctive bilinear pattern in the load-displacement graphs (related graphs in the Figure 5.5, Figure 5.6, and Figure 5.7) up to second crack formation which is around 70 kN. This bi-linearity is closely linked to the formation of the initial crack, which is observed at approximately 15 kN. Before the initial crack forms, the top displacement graph in Figure 5.5 exhibits a remarkable stiffness, closely matching the Net Lateral Deformation of the wall. However, after the initiation of the initial crack, the top displacement graph in Figure 5.5 becomes softer, indicating that the wall has started to rotate.

The second significant crack, occurring at around 70 kN, gives rise to a non-linear load-deformation behavior. This non-linearity is primarily a result of the yielding of the steel bars within the wall. A similar trend can be observed in the corresponding graphs in Figure 5.6 and Figure 5.7. However, this bi-linearity or non-linearity is not evident in the graphs presented in Figure 5.12 and Figure 5.13. This is because these graphs depict the calculated net lateral deformation, where a linear response is expected for the walls made of brittle concrete.

Figure 5.19-a offers visual insights into the key failure moments for this wall configuration. Figure 5.19-a showcases images from the initial test setup. These images, accompanied by notes, provide essential context and documentation of the wall's failure characteristics.

Additionally, it's worth noting that the experiment was halted due to the observation of steel bar yielding and the onset of plastic deformation after the load exceeded 80 kN. The plastic deformation of the bars rendered them incapable of sustaining additional load, resulting in a decrease in the reaction of the experimental system as

the actuator attempted to displace the wall. Consequently, a decision was made to modify the experimental setup to facilitate the desired wall failure.

5.3.2.3 Failure of the Wall 25-100-100 (Modified Test Setup)

In this section, the failure behavior of the 25-100-100 wall configuration within the modified test setup is explored. The examination of this wall in its cracked state is facilitated through the utilization of two figures: Figure 5.18 and Figure 5.19-b.

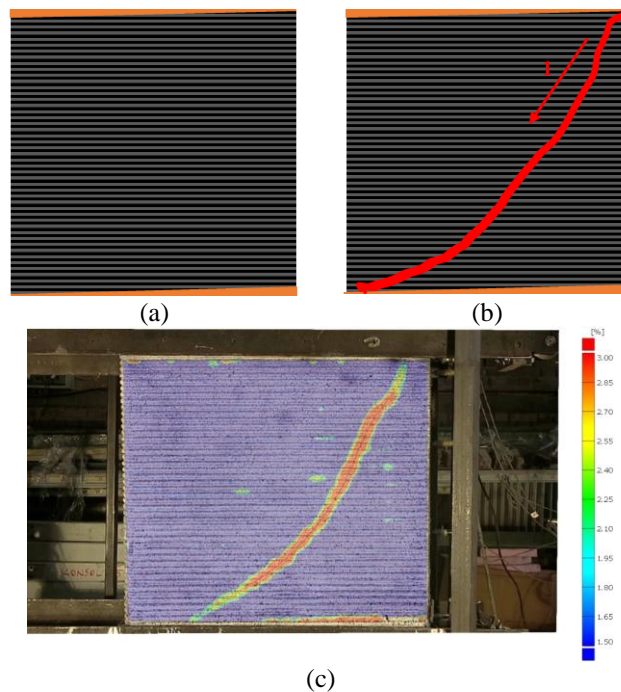


Figure 5.18. Crack Propagation Process: (a) Initial Damaged Wall from the First Test, (b) Brittle Diagonal Failure of the Front Face, and (c) Brittle Diagonal Failure of the Front Face Captured by DIC

Figure 5.18 provides an illustrative narrative of the wall's failure sequence. It commences with the depiction of the initial state of damage sustained during the first test (Figure 5.18-a). Notably, in this setup, the wall was not bonded to the IPE section using epoxy. Instead, the wall was tested in its cracked condition, as it demonstrated the capacity to sustain load even with cracks predominantly concentrated at the top

and bottom portions. This capability allows for an understanding of how the wall behaved despite the presence of cracks.

The related load-displacement curves in Figure 5.5, Figure 5.6, and Figure 5.7 reveal a distinct linear behavior in the modified test setup up to the point of failure. This linear behavior is attributed to the unbonded nature of the top and bottom portions of the wall. Due to usage of much stiffer axial bars in the modified test setup, stiffer load displacement behavior is observed in these graphs compared to the initial test setup. Nevertheless, it's worth noting that the observed stiffness in the net lateral displacement graphs in Figure 5.12 and Figure 5.13 remains consistent between the modified and initial test results of the wall 25-100-100.

Figure 5.18-b provides a more detailed insight into the final stages of the wall's behavior, specifically highlighting a brittle diagonal failure. This particular type of failure starts at the upper right corner of the wall and progresses diagonally to reach the lower left corner. This diagonal fracture sequence becomes apparent when the applied load reaches approximately 101.5 kN.

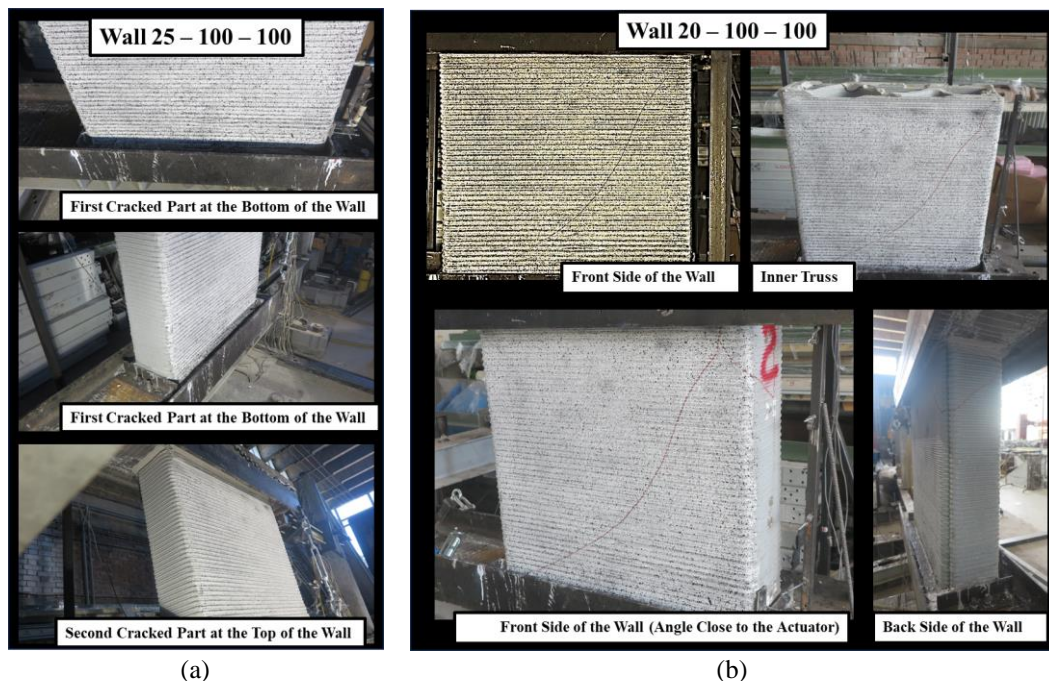


Figure 5.19. Key Images and Notes from Fractured Wall 25-100-100: (a) Initial Test Setup, and (b) Modified Test Setup

Figure 5.19-b provides essential visual documentation of the wall's critical moments. The presence of annotated notes and the demarcation of crack patterns using a red board marker in Figure 5.19-b enhances the comprehensibility of the wall's failure characteristics, offering valuable insights into the wall's performance throughout the testing process.

5.3.2.4 Failure of the Wall 25-100-150 (Modified Test Setup)

This section delves into the structural behavior and failure mechanisms observed in the modified test setup for the wall with a 25-100-150 configuration. The progression of cracks is portrayed in a step-by-step manner, beginning with the presentation of the initial, undamaged configuration (Figure 5.20-a) and highlighting the emergence of the first sudden crack (Figure 5.20-b), which was observed at an approximate load of 15 kN. Subsequently, the sudden initiation of a second crack (Figure 5.20-c), which manifested around 73 kN, is depicted.

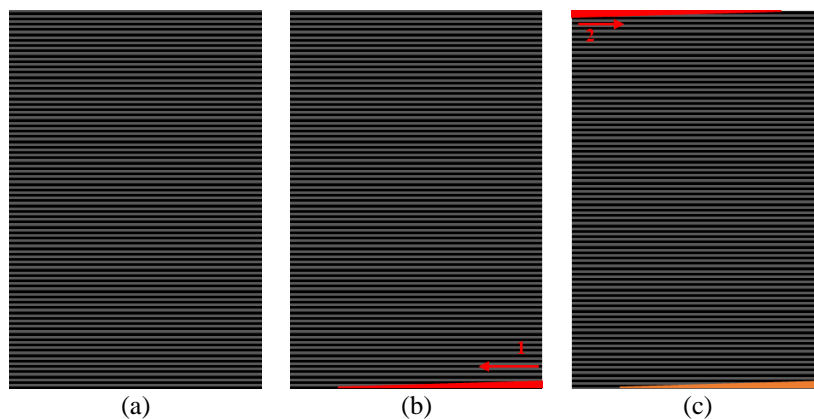


Figure 5.20. Crack Propagation Process: (a) Initial Undamaged Wall Configuration, (b) First Crack Propagation, and (c) Second Crack Propagation

In Figure 5.5, a nearly linear curve is observed. However, a sudden small drop is noted in the load-displacement curve, occurring between 73 kN and 67 kN, corresponding to the second crack formation. In contrast, the initial crack formation can be observed in the related graphs in Figure 5.5 and Figure 5.6.

The wall exhibited a certain resistance to further deformation despite these cracks. This is evident from the fact that the wall wasn't completely breached in the modified test setup. It is essential to highlight that the applied load was approaching the limits of safe loading capacity, and further testing could risk the structural integrity of the experimental system. As a result, a more rigid experimental setup to safely apply lateral loads to 3D printed concrete walls is recommended.

To provide visual insight into the wall's initial crack location, Figure 5.21 highlights the first crack's occurrence at the bottom of the wall. This presentation further enhances the understanding of the wall's structural performance during the testing process.

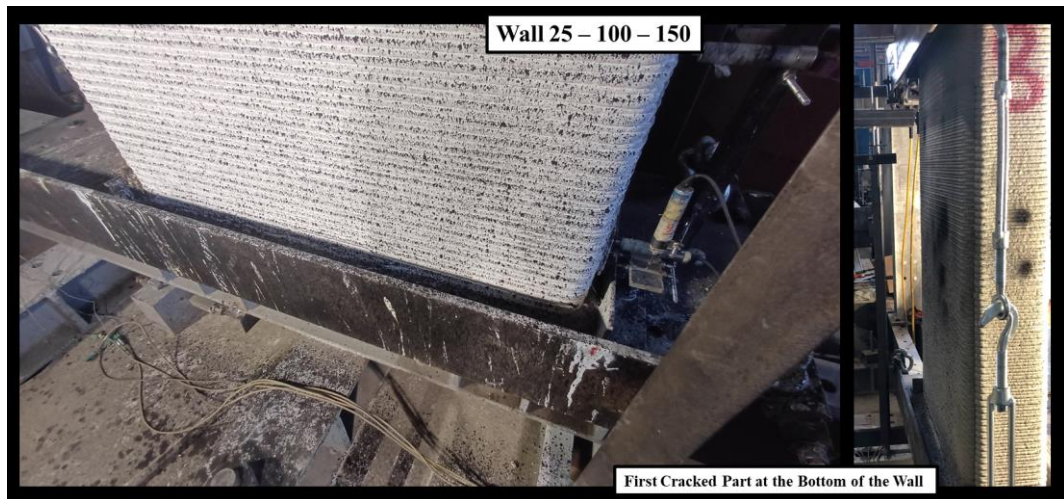


Figure 5.21. Key Images and Notes from Fractured Wall 25-100-150

5.3.3 Discussion of Factors Influencing Performance

In this section, a comprehensive discussion is initiated regarding the various factors that are significantly influenced by the performance and behavior of the tested concrete wall configurations. The analysis centers on key structural properties and performance metrics, shedding light on their interplay and impact on the walls' ability to withstand lateral loads. The presented data in Table 5.3 encompasses critical aspects such as concrete (A_{concrete}) and void areas (A_{void}), void ratio, major

inertia (I_x), maximum applied load (P_{MAX}), maximum net lateral deformation measured via LVDT ($\Delta_{NET\ MAX}^{LVDT}$) and DIC ($\Delta_{NET\ MAX}^{DIC}$), and the calculated stiffness (K^{LVDT} , and K^{DIC}) of the walls. By examining these factors, a deeper understanding is aimed to be gained concerning how variations in design, materials, and other parameters shape the structural performance of the walls, providing valuable insights for engineering and construction applications.

Table 5.3. Wall Properties and Performance Metrics

Property	Unit	Wall				
		25-100-100	25-100-150	30-150-100	25-150-100	20-150-100
$A_{concrete}$	cm ²	1171.5	1171.5	1732.5	1641.4	1529.8
A_{void}	cm ²	1328.5	1328.5	2767.5	2108.6	1470.2
Void Ratio	%	53.14	53.14	61.50	56.23	49.01
I_x	cm ⁴	1224493.7	1224493.7	4044452.6	3676846.0	3299324.4
P_{MAX}	kN	101.5	98.2	107.5	97.2	109.8
$\Delta_{NET\ MAX}^{LVDT}$	cm	0.12	0.23	0.83	0.47	0.75
$\Delta_{NET\ MAX}^{DIC}$	cm	0.20	0.45	–	0.15	–
K^{LVDT}	kN/cm	845.83	426.97	129.52	206.81	146.4
K^{DIC}	kN/cm	507.5	218.22	–	648.00	–

The disparities in deformation measurements, as evident from the table, primarily stem from the bending of the IPE section, which carries the LVDTs, during the application of lateral loads. This bending introduces variations and compromises the reliability of LVDT measurements. In light of these challenges, a more meaningful comparison can be achieved by categorizing the walls into two groups: those with a length of 150 cm and those with a width of 25 cm.

For walls with a 150 cm length, the IPE plate deformation behaves in a similar manner due to comparable boundary conditions created by these walls. These conditions foster a degree of consistency in deformation response, rendering them suitable for comparative analysis using LVDT data. However, it's essential to note that DIC measurements were not applied to walls 30-150-100 and 20-150-100, limiting the options for utilizing DIC in these cases.

Conversely, for walls with a width of 25 cm (25-150-100, 25-100-100, 25-100-150), DIC results are preferred for comparative purposes. This preference arises from the higher accuracy of DIC measurements and the varying boundary conditions imposed on the IPE section by these three distinct wall configurations. DIC, not being affected by the IPE section's deformation, offers a more precise evaluation of deformation behavior under differing boundary conditions.

In summary, the choice of measurement method depends on the specific wall configuration and its impact on the deformation measurements. These distinctions are vital for making accurate comparisons and inferences regarding the performance of the walls under different loading conditions.

1. **Concrete Area, Void Area, and Void Ratio:** The width of the wall significantly influences both the void area and the void ratio. A narrower width results in a more substantial reduction in the void area and contributes to a decrease in the void ratio, which is the ratio of void to total area. Conversely, the length of the wall remains the primary factor affecting the concrete area.
2. **Major Inertia (I_x):** The major inertia (I_x) is a measure of the wall's resistance to bending. Larger inertia values indicate greater stiffness. As expected, the larger walls (30-150-100 and 25-150-100) have significantly larger major inertia values, indicating their increased resistance to bending. The major inertia of the wall primarily depends on its length, with length being the dominant factor influencing I_x . As the width of the wall decreases, the impact of width on I_x diminishes.
3. **Maximum Applied Load (P_{MAX}):** The walls exhibit comparable maximum applied loads, with the primary influencing factor being the length of the wall, as well as concrete area and major inertia. Longer walls tend to show slightly higher strength than shorter ones. However, it is noteworthy that the wall 25-150-100 displayed the lowest strength despite its considerable length

of 150 cm. This observation may be attributed to factors such as potential printing imperfections, labor-related issues, or material inhomogeneities.

4. **Maximum Net Lateral Deformation (Δ_{NET}), and Stiffness (K):** When comparing the walls with a 150 cm length, there are no significant differences in both maximum displacement and stiffness for the walls 30-150-100 and 20-150-100. However, there is a notable difference for the wall 25-150-100, which experienced almost half the displacement and exhibited greater stiffness. The reason for this discrepancy could be attributed to several factors, such as variations in material properties, differences in the printing process, or potential issues related to the construction of this specific wall, with one key factor being variations in the epoxy used. The walls 20-150-100 and 30-150-100 initially used Master Brace ADH 1420 epoxy, which resulted in a poor bond between the epoxy and the IPE section, as shown in Figure 5.16-a. Recognizing this issue, the epoxy was switched to Sikadur 31 for the subsequent tests, which improved the bond as shown in Figure 5.16-b. Therefore, the observed differences between these two walls and the wall 25-150-100 may be due to the epoxy variations. Further investigation is required to pinpoint the exact cause of this behavior. In the group of walls with a 25 cm width, the observed differences are more aligned with expectations. As the height of the wall increases from 100 cm to 150 cm, its maximum displacement capacity also increases (from 20 to 45 mm), while the stiffness decreases (from 507.5 to 218.2 kN/cm). This behavior is logical, as taller walls can absorb more lateral deformation. Conversely, when the length of the wall increases from 100 cm to 150 cm, its stiffness increases (from 507.5 to 648.0 kN/cm), as anticipated, while the maximum displacement decreases (from 0.2 to 0.15 m). This change in stiffness is predominantly influenced by the height of the wall. The height of the wall plays a critical role in determining its structural stiffness, whereas the length primarily affects the wall's displacement capacity.

Overall, the table and its data provide valuable insights into the structural performance of the different wall configurations. These insights can be used to assess the walls' behavior under lateral loads and help optimize designs for future projects. The variations in properties and performance metrics highlight the importance of considering these factors when designing and constructing concrete walls for specific applications. Additionally, the differences observed in LVDT and DIC measurements emphasize the benefits of using advanced measurement techniques like DIC for more accurate and detailed data.

5.4 Numerical Simulation of 3DPC Wall 25-150-100

In this section, numerical simulations are employed to delve into the realm of structural behavior analysis for the 3D printed concrete wall with dimensions 25-150-100. These simulations aim to complement the experimental findings with computational analyses, providing insights into the wall's performance under various loading conditions. The unique mechanical and physical properties observed in Chapter 3, characterized by significant variations along the wall height, serve as the foundational basis for this numerical investigation. The simulations ensure that real-world conditions of the experimental setup are replicated, with careful consideration given to accurately representing boundary conditions and material properties. Additionally, a parametric study is conducted to explore the effects of different material parameters on the wall's strength and stiffness, particularly in relation to the variations found along its height. A comprehensive view of the wall's response to lateral loads is offered by these simulations, elucidating the influence of its unique material characteristics and height-dependent properties. The results obtained from this numerical exploration not only enhance the understanding of the wall's structural behavior but also provide valuable insights for the broader field of 3D printed concrete construction.

5.4.1 Model Details, Parameters and Boundary Conditions

The numerical simulation of the 3D printed concrete wall, specifically the 25-150-100 configuration, was conducted using the ABAQUS finite element analysis software. Both the ABAQUS static and explicit solvers were employed for different aspects of the simulation. The static solver was utilized for the primary analysis, while the explicit solver was used to determine the idealized stiffness of the axial bars responsible for preventing the uplift movement of the wall.

On the other hand, the walls possess a three-dimensional shape due to the inner truss structure. As a result, the analysis was conducted using a 3D modeling strategy, which demands greater computational time compared to 2D analysis. Additionally, the use of concrete damage plasticity models, known for their highly non-linear material behavior, further increases computational demands but is essential for accurately predicting the wall's behavior.

Due to the significant increase in computational time associated with modeling interlayers in the wall, which includes options like using cohesive elements or applying phase field modeling, the decision was made to omit the interlayers from the analysis. This was mainly due to the presence of 99 interlayers in the height direction, which would substantially extend computational time.

Instead of employing these time-intensive interlayer modeling strategies, this study presents an alternative approach.

Components Modeled: In the simulation model, various components were meticulously represented. These components included the 3D printed wall, the accompanying IPE sections, axial bars, and the frame system that supports the IPE sections situated at the bottom of the wall, as shown in Figure 5.22-a.

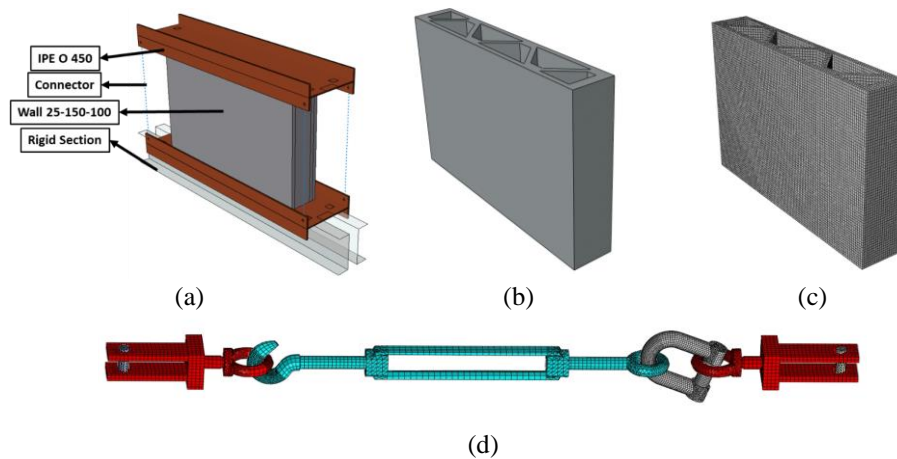


Figure 5.22. Numerical Simulation Model Details: (a) the Experimental Setup, (b) Wall Details, (c) Mesh Details of the Wall, and (d) Mesh Details of the Tension Bar System

IPE Section Modeling (IPE O 450): The IPE sections were modeled using S4 shell elements with a linear elastic material model. This model employed an elastic modulus (E) of 210,000 MPa and a Poisson's ratio of 0.3 to represent the linear elastic behavior of the IPE section. Furthermore, the areas associated with the bolts were restricted to prevent both translational and rotational movement, effectively simulating rigid bolts within the structure. Additionally, the IPE section was firmly connected to the wall using Tie contact, eliminating the need for modeling epoxy interactions. This approach was chosen because the tensile strength of Sikadur 31 [142] exceeds that of the concrete, rendering detailed epoxy modeling unnecessary and contributing to reduced computation time.

Frame System: The frame system, consisting of two C-sections, was meticulously integrated into the simulation. Discrete rigid R3D4 elements were utilized to ensure the structural integrity of this component. To account for the interactions between the C-section and the IPE section, frictionless hard contact constraints were applied, and separation after contact was allowed, thus mirroring real-world structural behavior.

Axial Bar Modeling: The axial bars, crucial for preventing the uplift movement of the wall, were meticulously modeled using axial connectors to ensure an accurate

representation of their behavior within the system. The connector stiffness was determined by employing the Abaqus Explicit solver, which simulated the precise geometry of the tension bar system, comprising shackles, tension screws, eyebolts, and bolts, as depicted in Figure 5.22-d. A general contact algorithm was implemented to account for the interactions between these components. The material properties employed for the axial connectors were an elastic modulus of 210,000 MPa and a Poisson's ratio of 0.3. To establish the idealized stiffness of the connectors, the middle of the bottom bolt was constrained from moving, while the middle of the top bolt was subjected to tension. This approach resulted in an idealized stiffness value of 4500 kN/mm. The idealized stiffness value was used as the stiffness of the axial connectors, which function exclusively under tension, as depicted in Figure 5.22-a.

Geometry Generation of the Wall: The geometry for the numerical simulation was generated by extruding the specimen's cross-section shape as presented in Table 5.2 within a CAD environment. The extruded geometry is illustrated in Figure 5.22-b. The layer width was set to 3 cm, with the expanded part due to the circular printer outlet not being taken into account. Subsequently, the generated shape was meshed with a 15 mm mesh length, as depicted in Figure 5.22-c. The mesh was generated with 69904 nodes and 49446 elements.

Material Model for the 3D Printed Wall: The material properties of the 3DPC wall were modeled using the Concrete Damage Plasticity Model (CDPM), an available material model in ABAQUS. A total of six different material models were employed to account for the mechanical property variations observed along the height of the wall. Five of these models, denoted as CDPM-1, CDPM-2, CDPM-3, CDPM-4, and CDPM-5, represent the changes in mechanical properties across the height of the wall, allowing to consider the compaction effects caused by the self-weight of subsequently printed layers and their impact on material properties. One of the main motivations for this modeling strategy is closely related to the observations made in Chapter 3. Additionally, during the demolition of the tested wall after the experiment, it was observed (Figure 5.23) that the interlayers in the lower portion of

the wall were interlaced and hardly distinguishable. This phenomenon is attributed to the increased pressure caused by self-weight, which can trigger fiber breaching between filaments and enhance the bond between them, thereby improving overall structural integrity. In contrast, the interlayer of the upper portion of the wall was perfectly visible.

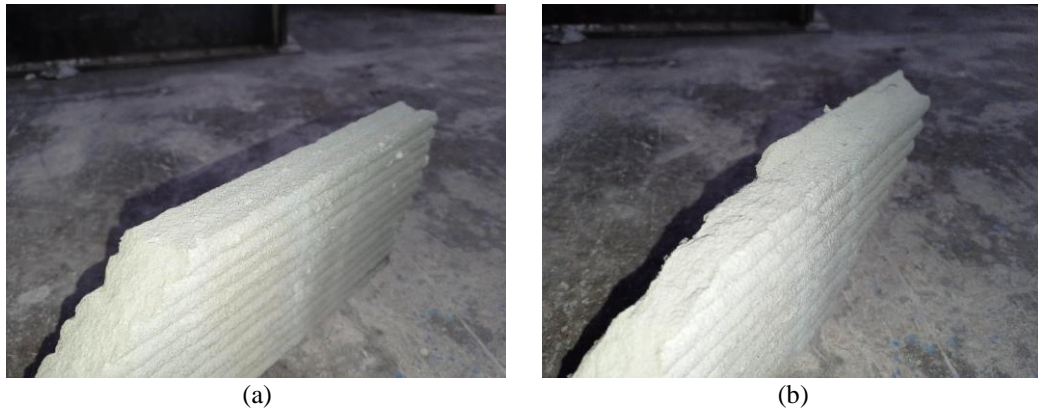


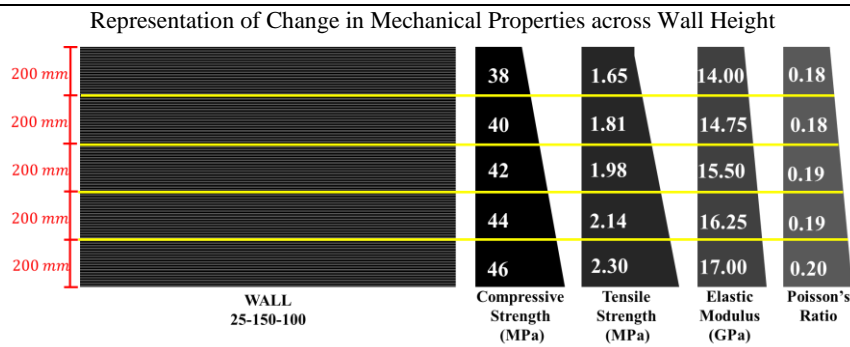
Figure 5.23. Interlayer Observations During Wall Demolition: (a) Upper Portion and (b) Lower Portion

On the other hand, the sixth material model, CDPM-CAST, utilizes the control/cast sample parameters to provide a baseline reference for the material. The key parameters defining the CDPM material model, such as concrete compressive strength, tensile strength, modulus of elasticity, and Poisson's ratio, are presented in Table 5.4. In Table 5.4, variations in material properties, including compressive strength, tensile strength, elastic modulus, and Poisson's ratio, are linearly adjusted to represent changes along the height of the wall. These adjustments were based on data from Table 5.1, which was developed using results obtained in Chapter 3. It's essential to note that Table 5.1 was originally generated for a wall with a height of 2.35 meters. As such, the maximum property values in the table were adjusted to align with the properties of a 1-meter-high wall. Specifically, the selected material parameters for this simulation include σ_x (for compressive strength), σ_{T2} (for splitting tensile strength), and E_Y (for elastic modulus). These parameters were chosen because they hold particular significance under the considered loading conditions. Additionally, special parameters, including dilation angle, eccentricity,

biaxial loading ratio, coefficient K, and viscosity parameter, are defined in ABAQUS (for detailed information, refer to [135]). These parameters can be set to their widely accepted values as found in the literature (refer to Table 5.4 for specific values). A low viscosity parameter is beneficial for enhancing convergence speed within the concrete stress-strain curve's softening regime.

Table 5.4. The Key Parameters Defining the CDPM Material Model and Its Logic

Material Model	Compressive Strength σ_{cu} - (MPa)	Tensile Strength σ_{tu} - (MPa)	Elastic Modulus E - (MPa)	Poisson's Ratio
CDPM-1	38	1.65	14400	0.180
CDPM-2	40	1.81	14750	0.185
CDPM-3	42	1.98	15500	0.190
CDPM-4	44	2.14	16250	0.195
CDPM-5	46	2.30	17000	0.200
CDPM-CAST	38	3.20	18800	0.200



Dilation Angle	Eccentricity	f_{b0}/f_{c0}	K	Viscosity Parameter
40	0.1	1.16	0.6667	0.0005

Utilizing the parameters available in Table 5.4, a constitutive law for compression, as proposed by Thorenfeldt et al. [143], is employed for material modeling in compression. The relationship between uniaxial unconfined compressive stress (σ_c) and strain (ϵ_c) according to this model is given as follows:

$$\sigma_c(\varepsilon_c) = \sigma_{cu} \times \frac{\varepsilon_c}{\varepsilon_{cu}} \left(\frac{n}{n-1 + \left(\frac{\varepsilon_c}{\varepsilon_{cu}}\right)^{n \times k}} \right) \quad (5.2a)$$

$$n = 0.8 + \frac{\sigma_{cu}}{17} \quad (5.2b)$$

$$k = \begin{cases} 1 & \text{if } 0 < \varepsilon_c < \varepsilon_{cu} \\ 0.67 + \frac{\sigma_{cu}}{62} & \text{if } \varepsilon_c \geq \varepsilon_{cu} \end{cases} \quad (5.3c)$$

Here, σ_c represents compressive stress, σ_{cu} is compressive strength, ε_c stands for compressive strain, and ε_{cu} denotes compressive strain at peak stress, σ_{cu} . Additionally, n and k are curve-fitting parameters.

The tensile stress (σ_t) and strain (ε_t) relationship was assumed to exhibit linearity up to the point of reaching the uniaxial tensile strength, σ_{tu} . Beyond this strength limit, the relationship was determined using the exponential function specified in Equation 5.4 provided in [136].

$$\sigma_t = \sigma_{tu} \left(\frac{\varepsilon_{tu}}{\varepsilon_t} \right)^{0.7+1000 \times \varepsilon_t} \quad (5.4a)$$

$$\varepsilon_{tu} = \frac{\sigma_{tu}}{E} \quad (5.4b)$$

Where E is the elastic modulus of the material. The generated stress-strain curves for both compression and tension are given in Figure 5.24-a and Figure 5.24-b, respectively.

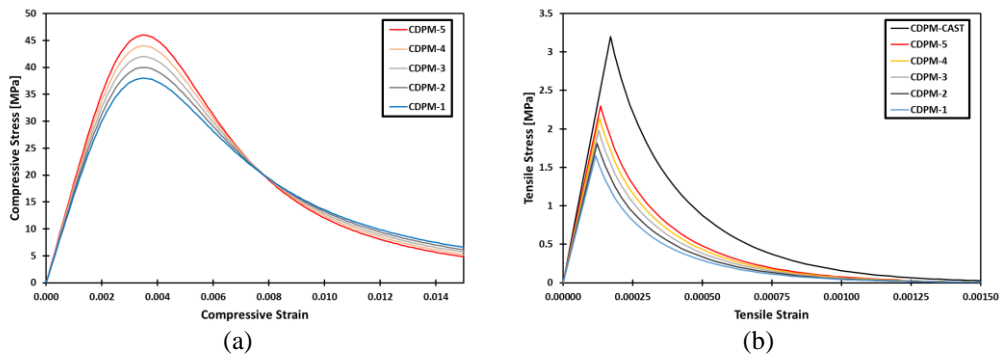


Figure 5.24. Stress-Strain Curves in (a) Compression and (b) Tension

For modeling the tensile behavior of concrete, the fracture energy cracking criterion in ABAQUS, described in the Abaqus materials guide [135], is employed, as recommended by Hillerborg [45]. In cases of a lack of reinforcement in significant model areas, using the tension stiffening method may introduce undesired mesh sensitivity into the results. However, Hillerborg's proposal regarding fracture energy is generally deemed suitable for numerous practical applications. Hillerborg's approach defines the energy required to initiate a crack per unit area as a material parameter, founded on principles of brittle fracture. This method characterizes the brittle behavior of concrete through a stress-displacement response, as opposed to a stress-strain response. When concrete is subjected to tension, it develops cracks in a specific section. As it is pulled apart significantly, reducing stress, the length is primarily determined by the crack opening, independent of the specimen's overall length.

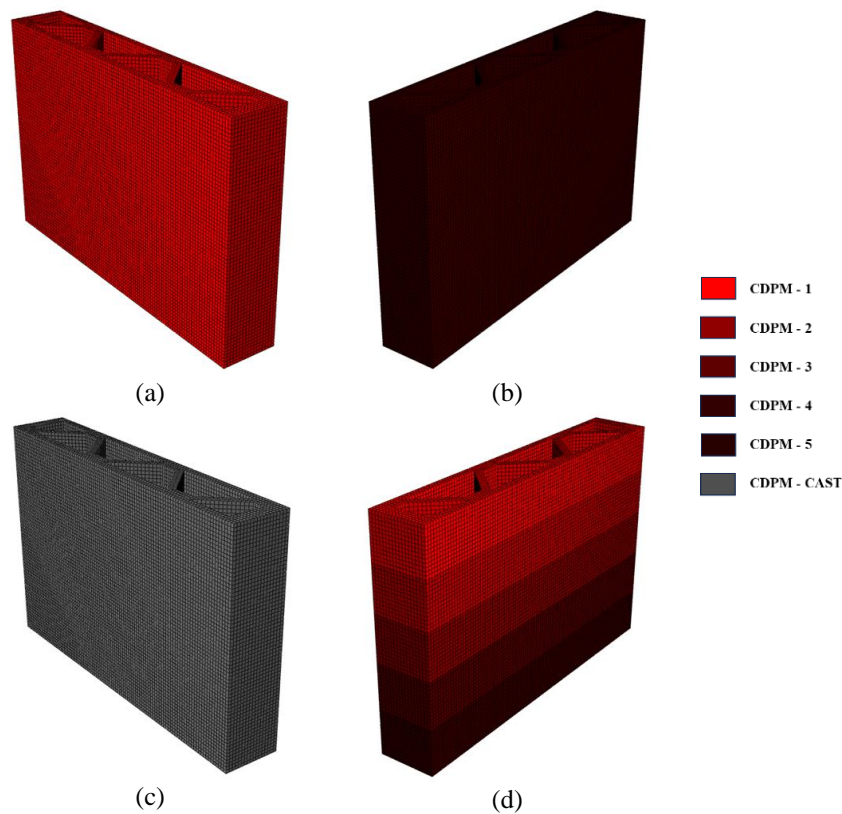


Figure 5.25. Material Model Assignments for Wall 25-150-100 - (a) Wall-CDPM-1, (b) Wall-CDPM-5, (c) Wall-CDPM-CAST, and (d) Wall-CDPM-Segmented

In this study, four different analyses were conducted using six distinct material models as detailed in Table 5.4. For these analyses, the wall shown in Figure 5.25-a was modeled with the mechanical properties corresponding to the top portion of the wall, CDPM-1, while the wall in Figure 5.25-b was modeled with properties associated with the bottom portion, CDPM-5. Additionally, the wall illustrated in Figure 5.25-c was modeled with CDPM-CAST. Finally, the wall in Figure 5.25-d was modeled with properties varying along the height of the wall.

5.4.2 Numerical Simulation Results and Discussions

In this section, the numerical simulation results are comprehensively examined and compared with the experimental data obtained from the Digital Image Correlation (DIC) measurements. The aim is to validate the accuracy and reliability of the numerical model, with a focus on various key aspects of the 3D printed concrete wall's behavior under lateral loading.

The top displacement of the wall and the observed fracture patterns are analyzed, particularly highlighting the Tensile Damage Distribution. Additionally, insights are sought into the material behavior throughout the wall's response to external forces through the exploration of logarithmic and plastic strain results.

To provide a more in-depth understanding, the investigation extends to the examination of shear force distribution along the length of the wall. Through this analysis, the intricate behavior of the wall's cross-section, especially the inner truss structure, is illuminated, given its significant role in the overall performance.

These results and discussions are a crucial step in the evaluation of the accuracy of the numerical simulation and the enhancement of the comprehension of the 3D printed concrete wall's response to lateral loads.

5.4.2.1 Lateral Load and Top Displacement Comparison: DIC vs. Numerical Analysis

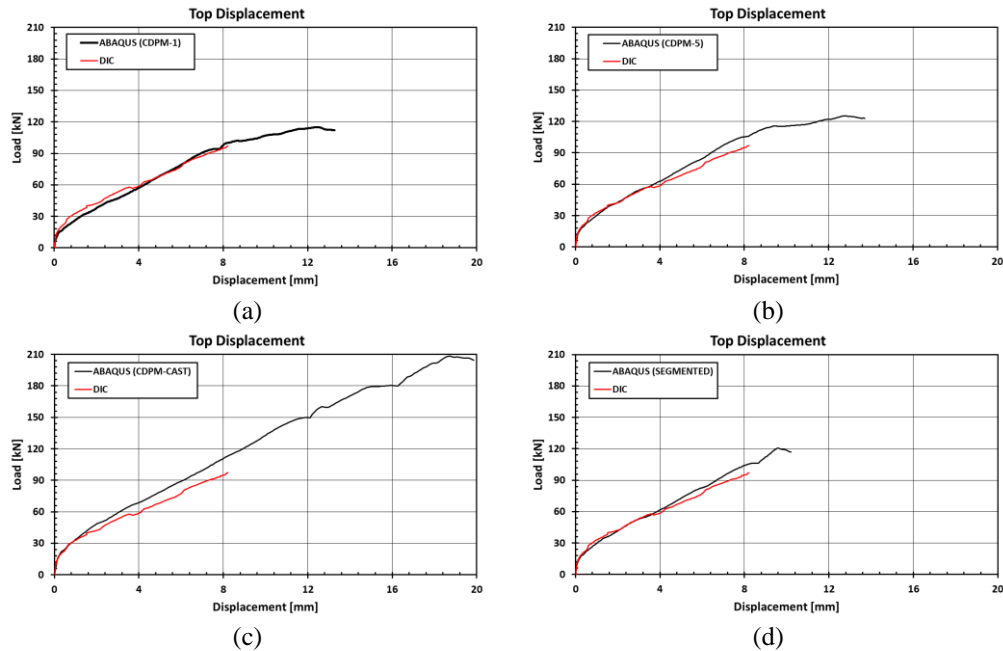


Figure 5.26. Comparison of DIC and Numerical Simulation Results for (a) Wall-CDPM-1, (b) Wall-CDPM-5, (c) Wall-CDPM-CAST, and (d) Wall-CDPM-Segmented

Figure 5.26 provides a comprehensive comparison between the results obtained through Digital Image Correlation (DIC) and those simulated using ABAQUS for different wall models, including Wall-CDPM-1, Wall-CDPM-5, Wall-CDPM-CAST, and Wall-CDPM-Segmented. The comparison of these results serves as a vital step in the assessment of the numerical model's accuracy in predicting the behavior of 3D printed concrete walls under lateral loading. Additionally, the experimental bearing capacity of Wall 25-150-100 was determined to be 97.2 kN. As discussed in Section 5.3, this capacity is lower than anticipated, and the results from the numerical analysis closely align with Wall 20-150-100 (109.8 kN) and Wall 30-150-100 (107.5 kN). Wall 25-150-100 was selected for analysis due to the application of the DIC method, which was not utilized in the earlier experiments.

It is evident that walls modeled with CDPM-1, CDPM-5, or CDPM-Segmented exhibit notably similar behavior, with slight discrepancies. However, it is imperative to highlight the stark differences observed when modeling a wall with cast concrete material parameters, represented by CDPM-CAST. This choice can potentially lead to inaccurate estimations of the ultimate load-carrying capacity of the walls. As observed in Figure 5.26-c, the ultimate load capacity of the wall is 208.5 kN.

Focusing on the results from CDPM-1, CDPM-5, and CDPM-Segmented models, the distinctions become more apparent. Figure 5.26-a reveals that CDPM-1 accurately predicts the ultimate load capacity, measuring 115.1 kN in numerical analysis. However, it may not fully capture the initial cracking load, which experimentally occurs in the lower portion of the wall at around 17 kN. On the other hand, CDPM-5 (Figure 5.26-b) accurately represents the initial cracking load but struggles to capture the stiffness post-initial crack formation and the ultimate lateral load capacity, 123.9 kN. Comparatively, the CDPM-Segmented (Figure 5.26-d) model appears to strike a balance. It adeptly captures the initial cracking load and, though slightly lagging behind CDPM-1 in estimating ultimate lateral load capacity as 120.6 kN, outperforms CDPM-5.

However, it's worth noting that walls modeled with CDPM-1 and CDPM-5 exhibit unique characteristics that they continue to bear load after the initiation of one of the dominant cracks, resulting in decreased stiffness. This behavior might be attributed to the nature of the static solver used. To better capture the ultimate load capacity of the wall, using an explicit solver by applying element deletion criterion for the CDPM models is recommended. Consequently, as a criterion for failure in this study, it is assumed that when the tangent stiffness of the wall under the lateral load becomes negative, the wall can be considered to have failed.

Despite the CDPM-Segmented model's commendable performance, it still falls short of perfection in capturing the ultimate load displacement. To refine this, it is suggested that a detailed investigation into changes in wall stiffness and strength along the wall height be conducted. This is crucial, as the assumption that these

parameters change linearly along the wall height, as initially posited, has proven to be imperfect, as evidenced in the results.

It is important to note that the wall analyzed in this study is relatively squat with a height of 1 meter. While it has revealed some insights into the importance of wall parameter changes along its height, the significance of these parameter variations may become more pronounced in taller walls, such as those with a height of 2.5 meters. Further studies involving taller walls are necessary to better understand the extent to which these parameter changes influence the structural response and failure modes.

5.4.2.2 Fracture Mechanism, Crack and Damage Analysis, and Comparison of DIC vs. Numerical Analysis

In Figure 5.27, compressive and tensile damage distributions for different CDPM models are presented as (a) CDPM-1, (b) CDPM-5, (c) CDPM-CAST, and (d) CDPM-Segmented. This figure illustrates the damage distributions at the ultimate lateral load level. Notably, all walls are found to effectively withstand compressive loads at this critical point, with no discernible compressive damage observed. On the other hand, when attention is directed toward the tensile damage distributions in the walls, diagonal tensile damages are observed in all the walls. Following these damages, it is not expected, in practice, for these damaged brittle walls to bear additional loads. Furthermore, the diagonal tensile damage distribution in the walls exhibits only minor differences compared to what is observed in the experiments. Further examination of reason of this minor difference is provided in Figure 5.28, illustrating tensile damage (fracture) propagation during the analysis of Wall-CDPM-Segmented.

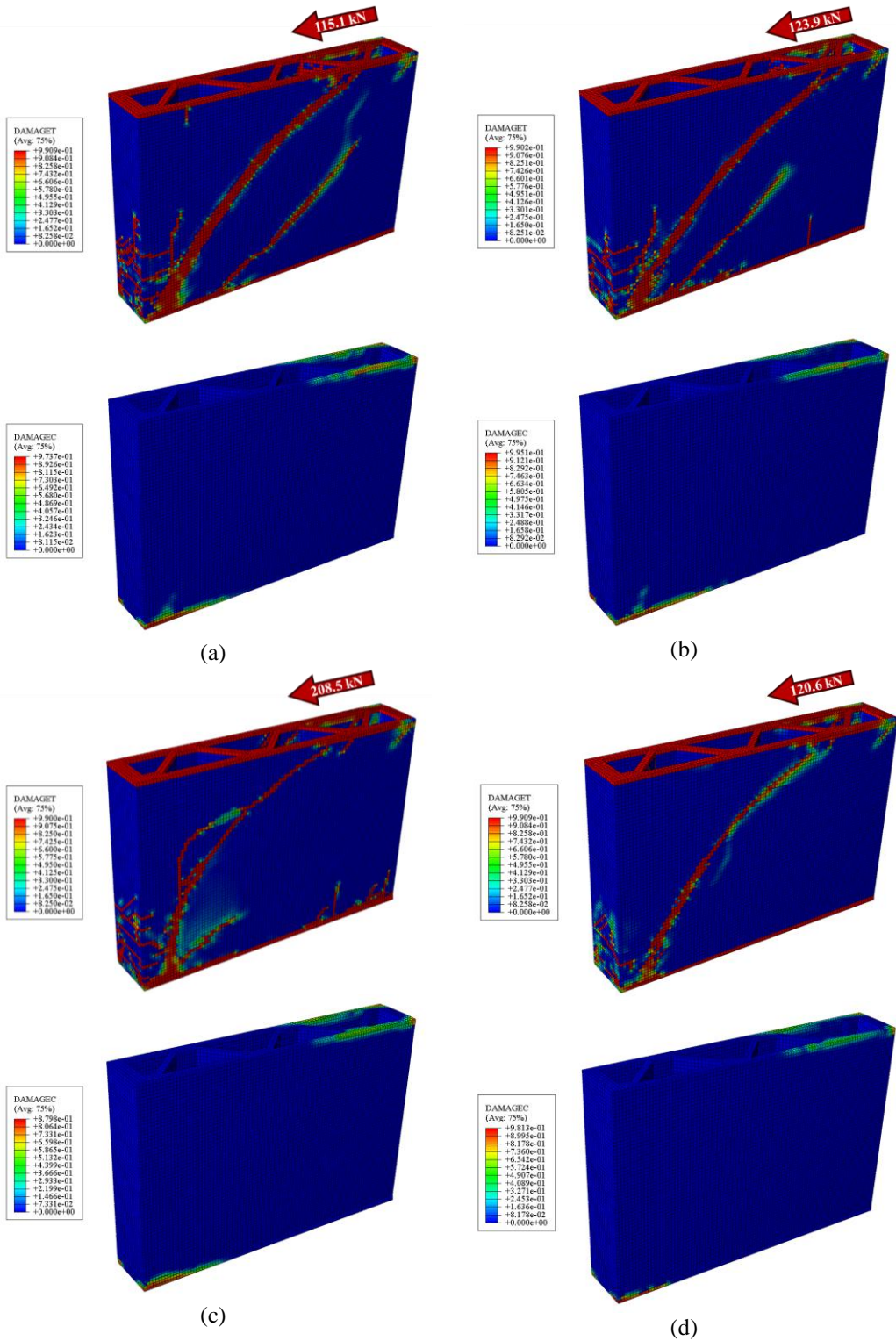


Figure 5.27. Compressive and Tensile Damage Distribution for Different CDPM Walls: (a) CDPM-1, (b) CDPM-5, (c) CDPM-CAST, and (d) CDPM-Segmented

In Figure 5.28, the progressive propagation of tensile damage (fracture) in the Wall-CDPM-Segmented is depicted at various lateral load levels, including 28.1 kN, 44.2 kN, 68.6 kN, and 120.6 kN. The observations in this figure provide valuable insights into the wall's behavior as it approaches its ultimate load-carrying capacity.

At the initial load of 28.1 kN, the tensile damage is primarily concentrated in the bottom portion of the wall. This early damage indicates the onset of structural distress and marks the beginning of the wall's degradation under lateral loading. As the load increases to 44.2 kN, the tensile damage extends at the right top portion of the wall.

Upon reaching a load of 68.6 kN, the left top portion of the wall exhibits tensile damage, although this damage is not prominently observed in the experimental results. The discrepancy between the analysis and experiments in this region is a noteworthy observation, suggesting that the numerical model may not perfectly capture the complex behavior of the wall. This discrepancy can be attributed to the anisotropic mechanical behavior of the 3D printed concrete, which is modeled as isotropic.

Finally, at the maximum load of 120.6 kN, a diagonal tensile damage pattern becomes evident, covering a significant portion of the wall. This diagonal damage indicates the structural failure of the wall, beyond which it is unable to sustain additional loads. However, it is worth mentioning that the observed diagonal crack in the experiment shows only minor differences compared to numerical results. In the experiment, as shown in Figure 5.15 and Figure 5.16, these cracks are more prominent further forward relative to the loading direction. The variations between the analysis and experimental findings may be attributed to the wall's anisotropic behavior and the inherent complexities of its response under lateral loading.

Briefly, Figure 5.28 provides a visual representation of the progressive tensile damage propagation within the Wall-CDPM-Segmented as it approaches its ultimate load capacity. While the numerical analysis captures the overall trends in tensile damage distribution, some discrepancies with experimental observations suggest the

need for further refinement in modeling and the consideration of anisotropic behavior in similar structural analyses.

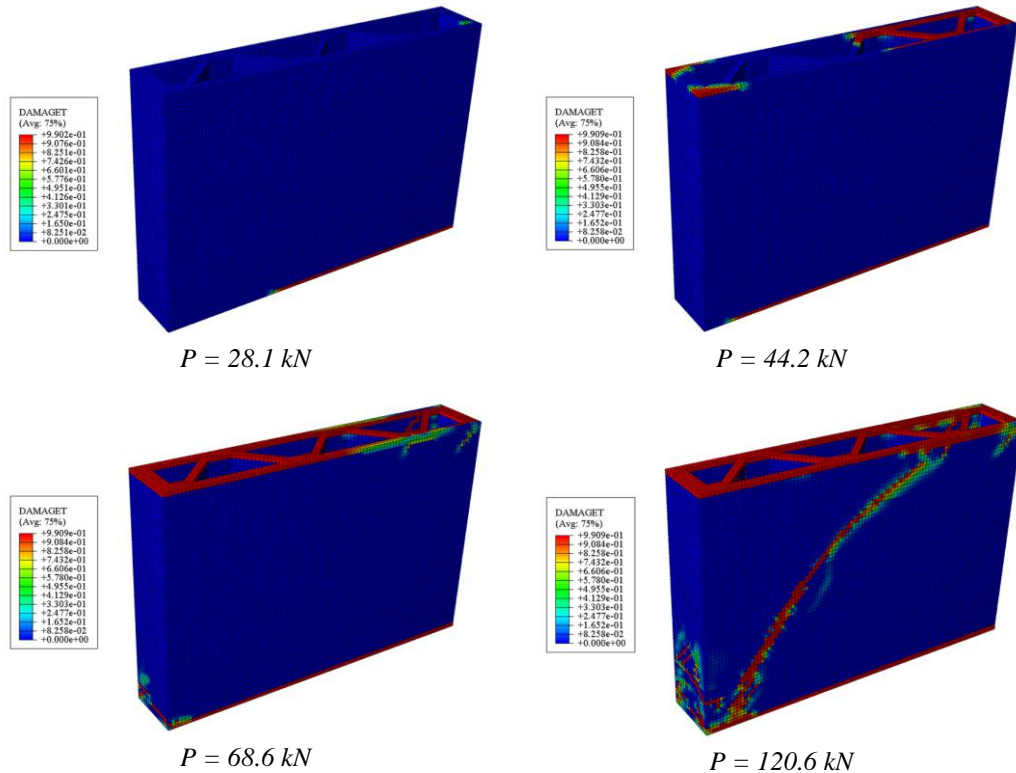


Figure 5.28. Tensile Damage (Fracture) Propagation during the Analysis for the Wall-CDPM-Segmented

Figure 5.29 provides a visual representation of the plastic strain distribution for both the front and back faces of the wall at the ultimate lateral load, 120.6 kN. This distribution of plastic strain is instrumental in understanding the structural behavior and crack patterns that emerge during the wall's response to lateral loading. Plastic strain data are commonly shared in structural analyses to highlight regions of significant deformation and help visualize the progression of damage within the structure. When examining the front side view of the wall in Figure 5.29, the crack pattern closely corresponds to the experimental results displayed in Figure 5.16 and Figure 5.17-b. On the other hand, when considering the back side view of the wall in Figure 5.29, it exhibits similarities to the fracture patterns observed on the back side of the Wall 20-150-100 and 30-150-100, as shown in Figure 5.17-a and Figure

5.17-c. The explanation for these differing patterns will be provided in the shear stress results in the section 5.4.2.3.

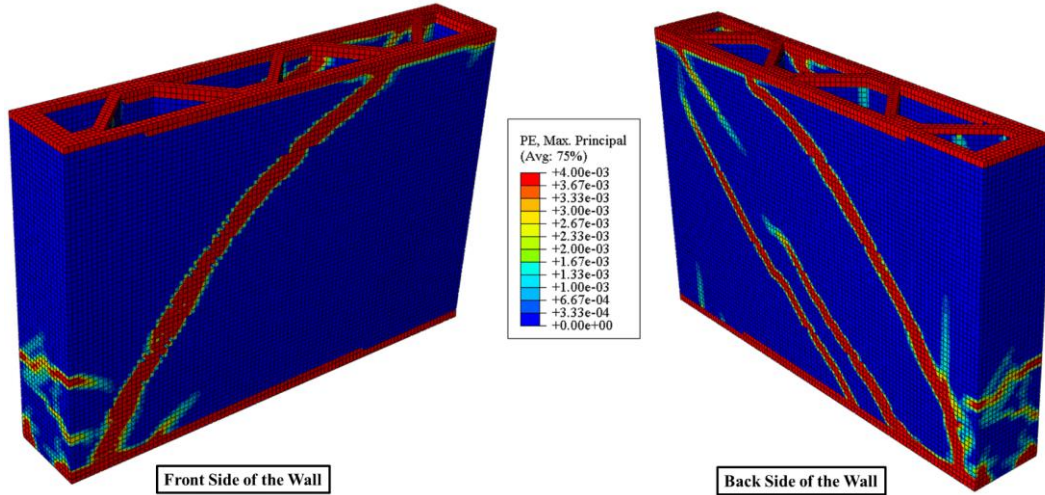


Figure 5.29. Plastic Strain Distribution for the Front and Back Face of the Wall

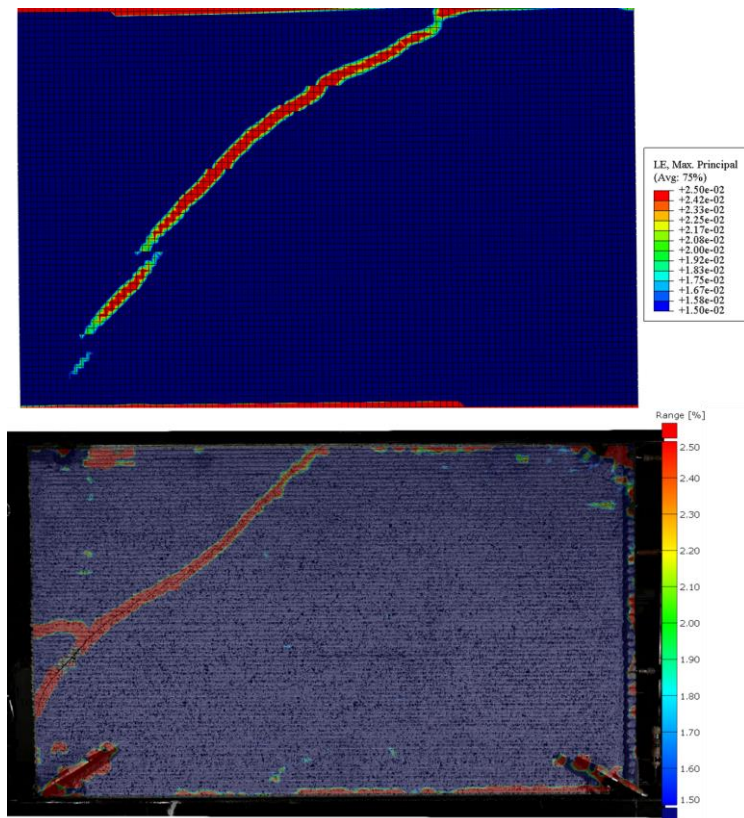


Figure 5.30. Comparison of Numerical Result from ABAQUS and Experimental Result from DIC Considering the Maximum Principal Strain Distribution

In Figure 5.30, a unique perspective is offered, showcasing the comparison between numerical results obtained through ABAQUS simulations and experimental results obtained via DIC. This figure focuses on the distribution of maximum principal strain within the same color spectrum legend boundaries. By presenting the agreement or discrepancies between these two methods, it sheds light on the effectiveness of DIC in capturing fracture patterns and highlights the value it brings to comprehensive analysis. This unconventional comparison underlines the significance of using DIC in capturing detailed fracture mechanisms, enriching our understanding of structural responses beyond conventional numerical simulations.

5.4.2.3 Shear Force Distribution

In this section, a comprehensive analysis of shear force distribution within 3D printed concrete walls under lateral loading is conducted. The distribution of shear stresses across the wall's cross-section is a crucial aspect in understanding its behavior, particularly for walls with complex geometries. As previously discussed, these walls consist of two webs connected by an inner truss, and the interaction between these components significantly influences shear area and stress distribution. The results presented in this section contribute to a deeper understanding of shear behavior in 3D printed concrete walls, especially in the context of complex geometries. Implications for structural integrity and safety, as well as valuable insights for future design and analysis, are provided.

To examine these phenomena, two figures are presented in this section. Figure 5.31 provides a comprehensive view of shear stress distribution contours on the front face of the wall modeled with CDPM-Segmented. The results are displayed at various loading stages, ranging from 5.5 kN (representing the undamaged and fully elastic state) to 120.6 kN, with intermediate stages at 28.1 kN, 44.2 kN, and 68.6 kN. The significance of these loading levels is discussed in Section 5.4.2.2 (Figure 5.28). Each subfigure illustrates distinct phases of the wall's response to lateral loading, depicting the evolution of shear stresses during the process. Additionally, Figure 5.31

provides a unique perspective by presenting shear stress distribution contours on the wall's cross-section at various elevations, including 200, 400, 500, 600, and 800 mm. This approach allows for an examination of how shear stress is distributed across different heights of the wall and provides insights into the development of shear forces within the wall under lateral loading.

As expected, a characteristic progression of shear stress concentrations is witnessed, with shear stress emanating from the top right and traveling towards the bottom left of the wall. This pattern aligns with the anticipated structural response of a loaded wall subjected to lateral forces. Significantly, the inner trusses within the wall appear to bear less shear stress when compared to the web sections. The inner trusses effectively share the applied load with the web portions. This division of labor between the inner trusses and webs contributes to the overall load-bearing capacity and structural integrity of the wall.

Further investigation reveals that Figure 5.31-a, representing the wall in an elastic state, exhibits higher shear stress on the front web compared to the back web. This disparity in shear stress distribution between the front and back web is a critical insight, shedding light on the distribution of shear forces within the wall. The asymmetrical stress distribution highlights the complex load-bearing mechanisms at play and underscores the importance of assessing these variations to ensure structural stability and reliability. This disparity can be attributed to the non-coincidence of the shear center with the geometric center due to the asymmetric inner truss. Conversely, once the wall sustains damage, the shear stress distribution between the front and back webs appears to become nearly identical. This suggests that the wall has reached an equilibrium state after sustaining damage.

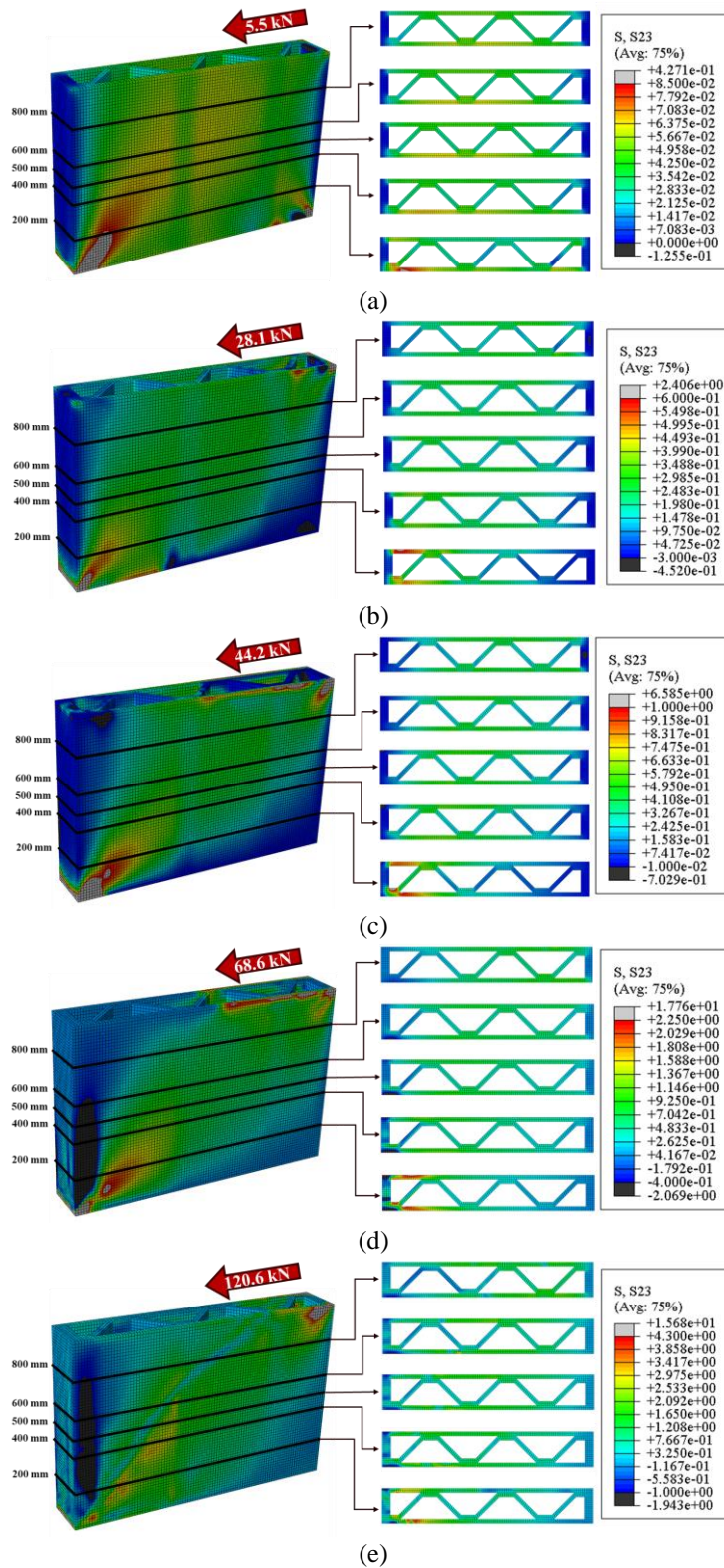


Figure 5.31. Shear Stress Distribution Contour on Wall Cross-Section for Various Load Levels and Elevations

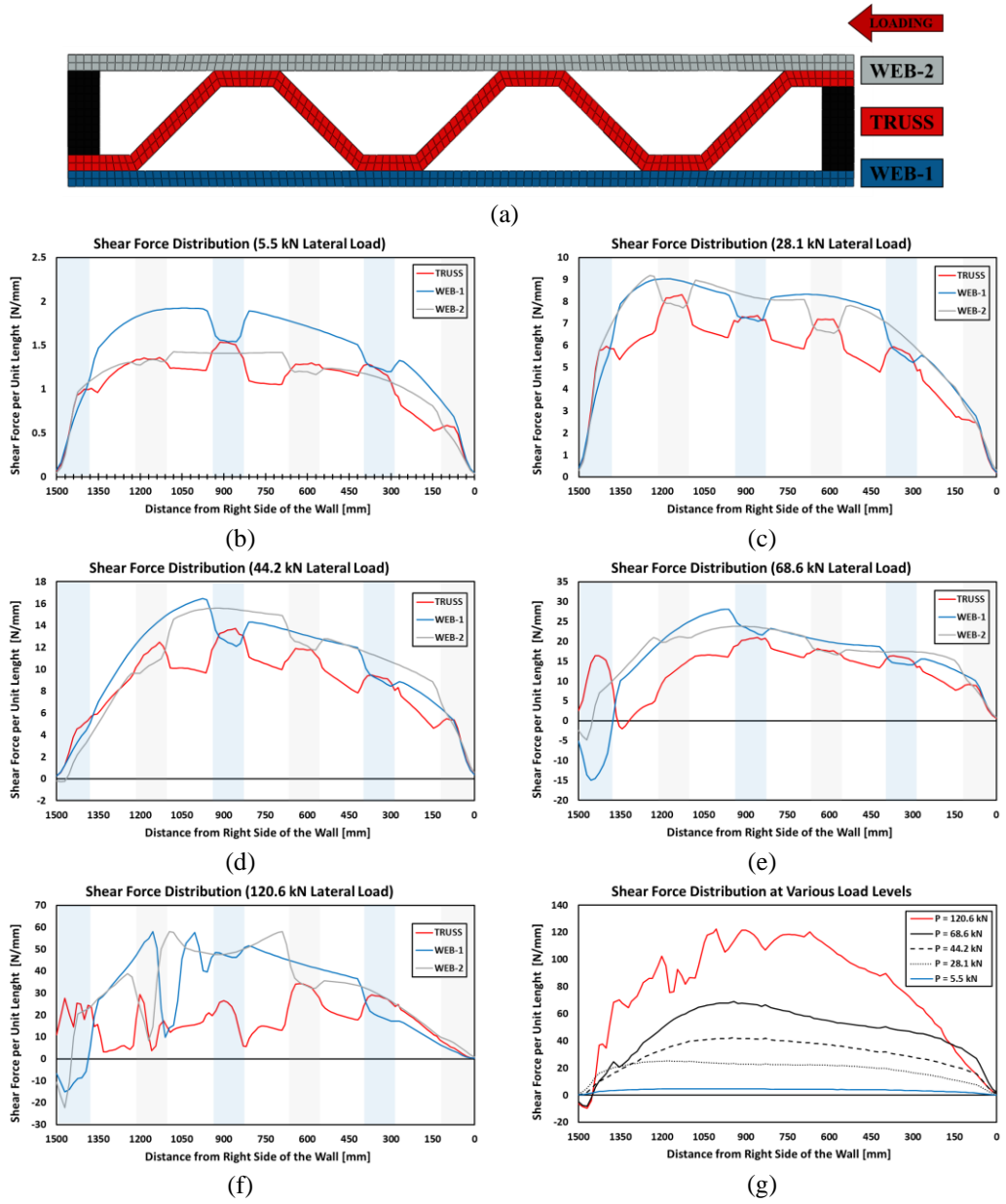


Figure 5.32. Shear Force Distribution and Load Transfer Mechanisms within Mid-Height (500 mm) of Wall-25-150-100 Analyzed using CDPM-Segmented Model

Furthermore, a notable change in shear stress is observed at the junction where the web and inner truss components connect, particularly in Figure 5.31-a. This localized change in shear stress signifies a point of relative structural stability within the wall. It suggests that the connection between the web and inner truss effectively mitigates shear forces in this region. This discovery underscores the significance of examining such nuances in shear stress distribution for a comprehensive understanding of the wall's behavior under varying load conditions.

To delve more deeply into the insights offered by the shear stress distribution discussed in Figure 5.31, Figure 5.32 has been meticulously prepared. This figure comprises seven subfigures labeled (a) through (g), each contributing to a comprehensive understanding of how shear forces are distributed within the mid-height cross-section of the wall analyzed with the CDPM-Segmented model. In Figure 5.32-a, an illustrative cross-section of the wall (25-150-100) is presented, demarcating the regions of interest: WEB-1 (Front web), WEB-2 (Back web), TRUSS, and the loading direction. Subsequent subfigures (b-g) meticulously examine the shear force distribution on WEB-1, WEB-2, and TRUSS for varying loading levels, providing a detailed view of the shear stress dynamics under different lateral loads. In these graphs, the junction where the WEB-1 and inner truss components connect is highlighted in blue, and the junction where the WEB-2 and inner truss components connect is highlighted in grey. This distinction enhances the visualization of shear stress interactions at these critical junctions, revealing that shear forces increase in the truss and decrease in the webs. The primary cause for the increased shear force distribution in the junctions of the truss is their flat orientation as opposed to diagonal. Conversely, when these increases are combined with the decreases in the web, a more parabolic distribution is observed in both the truss and the web. On the other hand, the graphs fluctuate as they approach the collapse load of the wall. This is due to damage evolution on the wall. The culmination in Figure 5.32-g encapsulates the total shear force per unit length, amalgamating the contributions from WEB-1, WEB-2, and TRUSS, offering a holistic perspective on the shear forces acting on the wall at different load levels. The total shear force

distribution exhibits a parabolic pattern, and the inclination of the truss structure on the inside appears to have a negligible impact on this parabolic distribution. Consequently, when determining the web area in accordance with the formulas stipulated in the regulations such as ACI CODE-318 [144] for plain concrete walls, this specific wall type can be treated as a uniform wall. However, it is crucial to note that the effective concrete area must be accurately determined in this context.

After gaining a comprehensive overview from these graphs in Figure 5.32, the subsequent Table 5.5 and graphs in Figure 5.33 have been prepared to enhance the evaluation of the results.

Table 5.5. Applied Load, Members' Reaction Forces and Percentage Contributions

Applied Lateral Load [kN]	Reaction Force [kN]			Percentage Contribution [%]		
	WEB-1	WEB-2	TRUSS	WEB-1	WEB-2	TRUSS
5.5	2.2	1.7	1.6	39.3	30.5	28.9
28.1	10.1	10.1	8.3	36.0	35.8	29.6
44.2	15.8	15.7	13.0	35.7	35.6	29.4
68.6	23.9	25.3	19.4	34.8	36.8	28.3
120.6	44.2	47.7	26.0	36.7	39.6	21.5

In the elastic state, when subjected to an applied lateral load of 5.5 kN, the reaction forces of 2.2 kN, 1.7 kN, and 1.6 kN are observed for WEB-1, WEB-2, and TRUSS, respectively, as tabulated in Table 5.5. The discrepancy in the reaction forces between WEB-1 and WEB-2 (Ratio of reaction forces: WEB-1 to WEB-2 = 1.3) induces a slight rotation in the wall due to the non-coincidence of the shear center and geometric center. This rotation results in torsion, leading to differentiated fractures on the front and back faces of the wall, as evidenced in numerical simulations (Figure 5.29) and experimental observations (Figure 5.16).

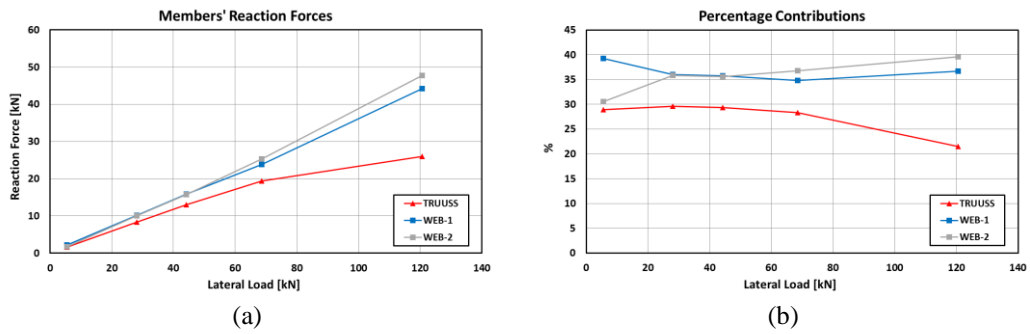


Figure 5.33. The Reaction Forces and Percentage Contributions of Each Member

As the wall is in the inelastic regime (for the loads of 28.1, 44.2, 68.6, and 120.6 kN), structural damage alters the shear distributions among WEB-1, WEB-2, and TRUSS. Following the initiation of the initial crack, shear forces in WEB-1 and WEB-2 become nearly equal until the wall's failure.

Examining the percentage contribution of each member in Figure 5.33, WEB-1, WEB-2, and TRUSS, reveals that, in the elastic regime ($P = 5.5$ kN), the contributions of TRUSS and WEB-2 are approximately equal. However, post-initial crack, the contribution of WEB-1 decreases, while that of WEB-2 increases until equilibrium is reached. A subtle change in Truss's contribution persists until failure, at which point the Truss's contribution diminishes from around 29% to 21.5%, with a simultaneous increase in contributions from WEB-1 and WEB-2.

5.5 Conclusions and Discussion

In Chapter 5, a detailed investigation into the behavior of 3D printed concrete walls under monotonic lateral loads is presented, employing both experimental and numerical methods. The study encompasses five distinct wall types, where the fundamental parameters defining their geometry include width, length, and height, thus influencing the configuration of the inner truss structure.

The ultimate loading limits of the walls under lateral loading were determined experimentally, accompanied by the observation of fracture patterns to provide insights for standard recommendations. To break the walls, two different

experimental setups were employed. Additionally, the lateral displacements of the walls were analyzed using two methods. Displacements were measured using LVDTs in the classical approach, while the more contemporary DIC method was also employed. The successful application of the DIC method significantly contributed to the experiments and served as a valuable tool for comparison in numerical studies.

In the numerical domain, a detailed analysis was conducted on one specific wall, Wall 25-150-100, and a parametric study was undertaken. Material properties were varied along the height of the wall, and cast concrete properties were considered, including compressive strength, tensile strength, elastic modulus, and the relatively insignificant Poisson's ratio. Following the observation that the numerical study's displacement values, fracture patterns, and damage patterns aligned with experimental results, the numerical analysis yielding the best correlation was subjected to a more in-depth examination. This analysis delved into the detailed examination of shear force distributions in the members of the wall.

The key outcomes derived from this comprehensive study are summarized as follows:

- 1. Experimental Investigation:** Ultimate loading limits of 3D printed concrete walls under lateral monotonic loads were determined through experimental testing. The failure loads for Walls 30-150-100, 25-150-100, 20-150-100, and 25-100-100 were found to be 107.5 kN, 97.2 kN, 109.8 kN, and 101.5 kN, respectively. The lowest value observed in Wall 25-150-100, at 97.2 kN, may be attributed to potential unobserved or undetected defects. Notably, the ultimate load for Wall 25-100-150 could not be determined due to limitations in the experimental setup, with the observed maximum load reaching 98.2 kN.

Fracture patterns and failure modes at ultimate load were observed, providing valuable insights for standard recommendations.

2. Measurement Methods: Two methods were employed for lateral displacement analysis: LVDTs for classical measurements and DIC for contemporary measurements. Lateral deformation and wall profiles were captured using LVDT measurements, offering insights into classical deformations. The employment of DIC allowed for the presentation of wall rotation and facilitated the calculation of net lateral deformation, considering sliding and uplift movements. The DIC measurements revealed that the wall with a height of 150 cm exhibited less stiffness compared to others, aligning with expectations. Conversely, the wall with a length of 150 cm was found to be stiffer than its counterparts.

The successful application of the DIC method significantly contributed to the experiments and facilitated comparison with numerical studies. This method played a crucial role in identifying fracture patterns in the walls.

3. Numerical Analysis: The numerical analysis, conducted using the ABAQUS static solver, revealed that the mechanical behavior of the wall is height-dependent considering the top displacement measurements. Utilizing material parameters exclusively from either the top or bottom portion of the wall did not yield optimal results. The segmented wall analysis provided the most accurate representation, although it still demonstrated some limitations. This underscores the importance of a detailed study on the variation of material properties along the wall height. Conversely, the least favorable outcome was observed when employing cast concrete material parameters under lateral load application, indicating its inadequacy for accurate predictions in this context.

4. Comparison of Fracture Patterns between Numerical Simulation and Experimental Results: The fracture pattern derived from numerical simulations closely corresponds to experimental observations. Consequently, the segmented wall, which exhibited the best correlation, underwent a detailed investigation regarding fracture patterns. The examination revealed

crack development at both the bottom and top portions of the wall, culminating in the formation of diagonal cracks. These results were elucidated through the presentation of tensile and compressive damage distribution, as well as plastic strain distribution contours. Intriguingly, the principal strain distribution of the wall exhibited a remarkable alignment with DIC observations, as depicted in Figure 5.30. Notably, when attention was directed to the back face of the wall (not visible during the experiment, as focus was primarily on the front face), a distinct fracture pattern was observed. This fracture type corresponds to the observation in Figure 5.16. Subsequently, a detailed analysis of shear force distribution provided insights into the reasons behind this discrepancy,

- 5. Shear Force Distribution:** To examine shear force distribution on the cross-section of the walls in detail, it is divided into three components: WEB-1, WEB-2, and TRUSS. In the elastic state, characterized by a lateral load of 5.5 kN, the reaction shear force of WEB-1 (front web) exceeded that of WEB-2 and TRUSS, inducing a slight rotation in the wall due to the non-coincidence of the shear center and geometric center. This rotational effect led to torsion, resulting in distinct fractures on the front and back faces of the wall, as evident in both numerical simulations (Figure 5.29) and experimental observations (Figure 5.16). As the wall transitioned into the inelastic regime (for loads of 28.1, 44.2, 68.6, and 120.6 kN), structural damage reshaped the shear distributions among WEB-1, WEB-2, and TRUSS. After the initiation of the initial crack, shear forces in WEB-1 and WEB-2 equalized until the wall's failure. A detailed examination of the percentage contribution of each member in Figure 5.33 reveals that, in the elastic regime ($P = 5.5$ kN), the contributions of TRUSS and WEB-2 are approximately equal. However, post-initial crack, the contribution of WEB-1 decreases, while that of WEB-2 increases until equilibrium is reached. A subtle change in Truss's contribution persists until failure, at which point the Truss's contribution

diminishes from around 29% to 21.5%, accompanied by a simultaneous increase in contributions from WEB-1 and WEB-2.

5.6 Suggestions for future research

While Chapter 3 provides a foundational examination of mechanical property changes along the wall's height, it is acknowledged that this initial study may not fully meet the requirements of the subsequent investigation presented in Chapter 5. The depth and specificity of the analysis conducted in Chapter 3 might not capture all the nuances needed to thoroughly understand the structural behavior revealed in Chapter 5. Specifically, the current study falls short in providing a comprehensive understanding of how these properties evolve across the entire height of the wall, whether they converge to specific values, and the speed of this convergence. The significance of these parameters, potentially more pronounced in taller walls, necessitates a more detailed exploration to ensure a robust understanding of their impact on structural behavior.

In addition to addressing the gaps identified in the current understanding of material property changes along the wall height, future research endeavors should extend the investigation of shear force distribution to encompass a broader spectrum of wall configurations. The current study primarily focuses on a specific wall configuration, and expanding this analysis to include various geometries will provide a more comprehensive understanding of shear force dynamics. This exploration should particularly scrutinize walls with diverse widths, lengths, and heights, as well as those with different truss alignment angles. Such an investigation would shed light on how these geometric variations influence shear force distribution, enabling the derivation of more generalized insights applicable across a wider range of 3D printed concrete walls.

Furthermore, the exploration of anisotropic damage-plastic material model is essential for a more robust analysis of complex 3D geometries. The computational

expense associated with defining interfaces in numerical models, especially for large structures like the walls in our study, highlights the necessity of advancing material models to accurately capture the anisotropic behavior inherent in 3D printed concrete walls.

CHAPTER 6

CONCLUSION

In this thesis, the exploration of 3D printed concrete (3DPC) technology has been a multi-chapter journey. Systematically investigated the performance of 3DPC walls from micro to macro scales addresses a critical gap in the current understanding of this new construction technology.

Chapter 1 initiated the discussion by emphasizing the increasing role of 3DPC in construction and highlighting the necessity for a deeper comprehension of its mechanical properties.

Chapter 2 takes a deep dive into the intricacies of the Continuum Damage Plasticity Model, a crucial component in understanding the cyclic loading behavior of concrete. Here, the plastic-damage model, the evolution of damage and stiffness degradation, and the flow rule and yield function are meticulously expounded. Moving into the realm of numerical implementation, the chapter unveils the stress update algorithm for Continuum Damage Plasticity, shedding light on the intricacies of the computational framework. The return-mapping algorithm and spectral decomposition are detailed, providing a comprehensive view of the numerical tools at play. Linearizing the equations governing damage evolution is a critical aspect discussed in this chapter. The summary of the update algorithm for CDPM encapsulates the essence of the numerical methodology employed throughout the thesis. This chapter is further supplemented by user defined material subroutine in appendixes A and B.

Chapter 3 took a step further, conducting an extensive examination of the physical, mechanical and thermophysical properties of 3DPC across a full-scale wall throughout the height. The key findings of Chapter 3:

- **Scale Dependency:** Properties vary significantly based on elevation in the wall. Extruding concrete against gravity significantly impacts material properties during hydration due to self-weight pressure and increased mix viscosity.
- **Density & Voids:** Lower wall sections are denser due to self-weight pressure and heating, reducing permeability and water penetration. Upper sections are more porous and prone to durability issues.
- **Strength & Stiffness:** Lower sections exhibit significantly higher compressive, tensile, and elastic modulus values compared to upper sections. Anisotropic behavior depends on location, orientation, and loading direction.
- **Failure Modes:** Compressive failure in lower sections resembles cast concrete, while upper sections crack through interlayer interfaces. Splitting tensile tests reveal distinct layer interfaces in upper sections.
- **Thermal Conductivity:** Anisotropic behavior observed, with upper sections having lower conductivity due to increased void presence.

Chapter 4 shifted the focus to the micro and meso-scale, employing Computed Tomography analysis and Finite Element Modeling to dissect interlayer and interstrip porosities and their influence on 3DPC behavior. The key contributions and insights of Chapter 4:

- **Micro-CT Analysis:**
 - Porosity distribution: Right-skewed with distinct differences between cast and printed samples. Cast samples have a wider pore size range.
 - Lower samples: Denser structure with significantly reduced porosity, likely due to self-weight compaction.
 - Overall porosity: No major trend along specimen height, suggesting limited interlayer effect within the studied range.
- **Macro-CT Analysis:**

- Cast vs. printed: Cast samples have larger, irregularly distributed pores. Printed samples show concentrated pores at interlayers and interstrips, with interstrip pores being dominant.
- Upper vs. lower samples: Self-weight and printing time influence porosity, with lower samples exhibiting denser structures.
- Finite Element Analysis:
 - Agreement with experiments: Strong agreement for compressive strength, elastic modulus, and Poisson's ratio.
 - Stress distribution: U_X sample mirrors cast sample, indicating similar response to loads. On the other hand, higher stress intensity observed around localized porosities in other samples, influencing mechanical behavior.
 - Comparing X sample with cast sample, simplified porosities have minimal impact on damage and plastic strain evolution. However, for other samples, Y-S, Y-D, and Z samples, simplified porosities trigger tension damage earlier, leading to strength reductions. Y-S samples (fewer pores compared to Y-D) have higher strength than Y-D. Tension damage in Z samples extending through width of the layers, leading to least strength.
 - Printed samples demonstrate that crack propagation starts within concrete filaments, contrasting with interlayer or interstrip failure under compressive load. Contrary to popular belief, the dominant reason for failure in these samples is localized porosities rather than weak interfaces resulting from the printing process. Experimental and numerical analyses consistently support this conclusion.

The spotlight of Chapter 5 was on the macro/structural level, investigating the structural response and failure mechanisms of unreinforced 3DPC walls under monotonic lateral loads. This chapter provides a comprehensive understanding of 3DPC wall behavior under lateral loads through combined experimental and numerical approaches. Findings offer valuable insights for standard

recommendations and highlight the importance of considering height-dependent material properties and complex shear force distributions. The key findings of Chapter 5:

- Experimental Investigation:
 - Determined ultimate loading capacities of 3DPC walls under lateral loads (ranging from 97.2 kN to 109.8 kN).
 - Observed fracture patterns and failure modes, providing valuable data for standard recommendations.
 - Successfully employed both LVDT and DIC methods for lateral displacement analysis, with DIC revealing insights into wall rotation and net deformation.
 - Confirmed height-dependent behavior, with taller walls exhibiting less stiffness and shorter walls being stiffer.
- Numerical Analysis:
 - Found segmented wall analysis with varied material properties along the height to provide the most accurate representation.
 - Confirmed inadequacy of using cast concrete material parameters for accurate predictions under lateral loads.
 - Demonstrated close correlation between fracture patterns from numerical simulations and experimental observations.
- Shear Force Distribution:
 - Identified distinct shear force contributions from WEB-1, WEB-2, and TRUSS members.
 - Observed torsion and resulting different fracture patterns on front and back faces due to non-coincidence of shear center and geometric center in the elastic state.
 - Showed equalization of shear forces in WEB-1 and WEB-2 after initial crack formation, with contributions from each member shifting until failure.

This research offers significant contributions to the field of 3DPC construction:

- Bridging the knowledge gap: The findings fill a critical gap in our understanding of 3DPC performance under lateral loads, which are crucial for seismic design and safety.
- Informative insights: The study provides detailed insights into the effects of printing parameters, interlayer porosity, and self-weight on material properties and structural behavior.
- Advanced modeling tools: The developed finite element models incorporating material property variations provide valuable tools for accurate predictions of 3DPC performance under lateral loads.
- Standardization support: The findings contribute to the development of standards for 3DPC construction by highlighting the importance of large-scale testing and consideration of material heterogeneity.

While the significant advancements achieved in this thesis, it is crucial to investigate these identified aspects to ensure the long-term success of 3DPC:

- Exploration of anisotropic damage-plastic material model: The exploration of anisotropic damage-plastic material models is essential for a more robust analysis of complex 3D geometries. The computational expense associated with defining interfaces in numerical models, especially for large structures like the walls in our study, highlights the necessity of advancing material models to accurately capture the anisotropic behavior inherent in 3D printed concrete walls.
- Broader investigation of self-weight effect: Given that this study is limited to the characterization and evaluation of a single fiber-reinforced printable concrete mixture, a broader investigation into the self-weight effect for other mixtures is necessary. Understanding how different material compositions

respond to self-weight-induced effects is vital for expanding the applicability of 3DPC in diverse construction scenarios.

- Detailed exploration of material property convergence: The current study falls short in providing a comprehensive understanding of how material properties evolve across the entire height of the wall, whether they converge to specific values, and the speed of this convergence. The significance of these properties necessitates a more detailed exploration to inform precise construction practices.
- Experiments for fracture energy parameters: Suitable experiments for 3DPC related to fracture energy parameters, especially mixed mode, and mode-II, are required. Investigating fracture energy parameters is critical for understanding the material's response to different loading conditions, enabling more accurate predictions of structural performance.
- Extension of shear force distribution analysis: Future research endeavors should extend the investigation of shear force distribution to encompass a broader spectrum of wall configurations. The current study primarily focuses on a specific wall configuration, and expanding this analysis to include various geometries will provide a more comprehensive understanding of shear force dynamics, contributing to the development of standardized design guidelines.
- Reinforcement strategies: Exploration of effective reinforcement techniques for 3DPC walls to improve their structural performance under lateral loads and seismic conditions is essential.
- Large-scale seismic testing: Conducting comprehensive seismic tests on large-scale 3DPC structures incorporating the findings of this study would further validate the developed models and advance the design and implementation of this technology.

REFERENCES

- [1] C.W. Hull, C. Arcadia, United States Patent (19) Hull (54) (75) (73) 21) 22 (51) 52) (58) (56) APPARATUS FOR PRODUCTION OF THREE-DIMENSIONAL OBJECTS BY STEREO THOGRAPHY, (1984).
- [2] S.C. Paul, G.P.A.G. van Zijl, I. Gibson, A review of 3D concrete printing systems and materials properties: current status and future research prospects, *Rapid Prototyp. J.* 24 (2018) 784–798. <https://doi.org/10.1108/RPJ-09-2016-0154>.
- [3] T.D. Ngo, A. Kashani, G. Imbalzano, K.T.Q. Nguyen, D. Hui, Additive manufacturing (3D printing): A review of materials, methods, applications and challenges, *Compos. Part B Eng.* 143 (2018) 172–196. <https://doi.org/10.1016/J.COMPOSITESB.2018.02.012>.
- [4] S.C. Paul, Y.W.D. Tay, B. Panda, M.J. Tan, Fresh and hardened properties of 3D printable cementitious materials for building and construction, *Arch. Civ. Mech. Eng.* 18 (2018) 311–319. <https://doi.org/10.1016/j.acme.2017.02.008>.
- [5] E. Lloret, A.R. Shahab, M. Linus, R.J. Flatt, F. Gramazio, M. Kohler, S. Langenberg, Complex concrete structures: Merging existing casting techniques with digital fabrication, *CAD Comput. Aided Des.* 60 (2015) 40–49. <https://doi.org/10.1016/J.CAD.2014.02.011>.
- [6] K.N. Jha, *Formwork for concrete structures*, 1st editio, MC GRAW HILL INDIA, 2012.
- [7] D.W. Johnston, *Design and construction of concrete formwork*, in: Edward G. Nawy (Ed.), *Concr. Constr. Eng. Handb.*, 2nd editio, CRC Press, 2008.
- [8] M. Batikha, R. Jotangia, M.Y. Baaj, I. Mousleh, 3D concrete printing for sustainable and economical construction: A comparative study, *Autom. Constr.* 134 (2022) 104087.

<https://doi.org/10.1016/J.AUTCON.2021.104087>.

- [9] V. Mechtcherine, R. Buswell, H. Kloft, F.P. Bos, N. Hack, R. Wolfs, J. Sanjayan, B. Nematollahi, E. Ivaniuk, T. Neef, Integrating reinforcement in digital fabrication with concrete: A review and classification framework, *Cem. Concr. Compos.* 119 (2021). <https://doi.org/10.1016/J.CEMCONCOMP.2021.103964>.
- [10] F.P. Bos, C. Menna, M. Pradena, E. Kreiger, W.R.L. da Silva, A.U. Rehman, D. Weger, R.J.M. Wolfs, Y. Zhang, L. Ferrara, V. Mechtcherine, The realities of additively manufactured concrete structures in practice, *Cem. Concr. Res.* 156 (2022) 106746. <https://doi.org/10.1016/j.cemconres.2022.106746>.
- [11] J. Gardiner, Exploring the emerging design territory of construction 3D printing - project led architectural research, Ecuador. (2011) 360, 361.
- [12] J. Green, Jetson Green - 3D Printed Homes Made in China, (2014).
- [13] H. Watkin, World's First 3D Printed Residential Home Erected in Yaroslavl, Russia | All3DP, (2017).
- [14] 3d printed bridge – IAAC Blog, (2019). <https://iaac.net/project/3d-printed-bridge/>.
- [15] A.E. ÇERÇEVİK, Y.C. TOKLU, S.Y. KANDEMİR, M.Ö. YAYLI, 3D BASKI TEKNOLOJİSİ KULLANARAK YAPI ÜRETİMİNİN SON DÖNEM YENİLİKLERİNİN ARAŞTIRILMASI, *Int. J. 3D Print. Technol. Digit. Ind.* 2 (2018) 116–122.
- [16] M. Sakin, Y.C. Kiroglu, 3D Printing of Buildings: Construction of the Sustainable Houses of the Future by BIM, in: *Energy Procedia*, Elsevier Ltd, 2017: pp. 702–711. <https://doi.org/10.1016/j.egypro.2017.09.562>.
- [17] H. Busta, Gensler Completes the World's First 3D-Printed Office Building | Architect Magazine, (2016).

- [18] L. Carolo, 3D Printed House: 20 Most Important Projects | All3DP, (2020).
- [19] T. Page, UAE architects make cement out of salt - CNN Style, (2020).
- [20] M.T. Souza, I.M. Ferreira, E. Guzi de Moraes, L. Senff, A.P. Novaes de Oliveira, 3D printed concrete for large-scale buildings: An overview of rheology, printing parameters, chemical admixtures, reinforcements, and economic and environmental prospects, *J. Build. Eng.* 32 (2020) 101833. <https://doi.org/10.1016/j.jobbe.2020.101833>.
- [21] Apis Cor, GALLERY | Apis Cor, (2017).
- [22] C. Scott, Chinese Construction Company 3D Prints an Entire Two-Story House On-Site in 45 Days - 3DPrint.com | The Voice of 3D Printing / Additive Manufacturing, (2016).
- [23] H. Augur, This On-Site 3D Printed House Took Only 45 Days | All3DP, (2016).
- [24] Automated Construction of Expeditionary Structures (ACES) > Engineer Research and Development Center > Fact Sheet Article View, (2019). <https://www.erd.usace.army.mil/Media/Fact-Sheets/Fact-Sheet-Article-View/Article/1290247/automated-construction-of-expeditionary-structures-aces/>.
- [25] R.J.M. Wolfs, F.P. Bos, T.A.M. Salet, Early age mechanical behaviour of 3D printed concrete: Numerical modelling and experimental testing, *Cem. Concr. Res.* 106 (2018) 103–116. <https://doi.org/10.1016/j.cemconres.2018.02.001>.
- [26] A. D2166, Standard Test Method for Unconfined Compressive Strength of Cohesive Soil, ASTM Int. (2016). <https://www.astm.org/d2166-06.html>.
- [27] D. ASTM, 3080--4: 2004, Standard Test Method for Direct Shear Test of Soils Under Consolidated Drained Conditions, West Conshohocken ASTM Int. (2004). <https://www.astm.org/d3080-04.html>.

- [28] P. Feng, X. Meng, J.-F. Chen, L. Ye, Mechanical properties of structures 3D printed with cementitious powders, *Constr. Build. Mater.* 93 (2015) 486–497. <https://doi.org/10.1016/j.conbuildmat.2015.05.132>.
- [29] GB/T 17671–1999. Method of testing cements: determination of strength. Beijing, (1999).
- [30] R.J.M. Wolfs, F.P. Bos, T.A.M. Salet, Hardened properties of 3D printed concrete: The influence of process parameters on interlayer adhesion, *Cem. Concr. Res.* 119 (2019) 132–140. <https://doi.org/10.1016/j.cemconres.2019.02.017>.
- [31] B. Panda, S.C. Paul, L.J. Hui, Y.W.D. Tay, M.J. Tan, Additive manufacturing of geopolymer for sustainable built environment, *J. Clean. Prod.* 167 (2017) 281–288. <https://doi.org/10.1016/j.jclepro.2017.08.165>.
- [32] N. Ducoulombier, L. Demont, C. Chateau, M. Bornert, J.F. Caron, Additive manufacturing of anisotropic concrete: A flow-based pultrusion of continuous fibers in a cementitious matrix., *Procedia Manuf.* 47 (2020) 1070–1077. <https://doi.org/10.1016/j.promfg.2020.04.117>.
- [33] T. Marchment, J. Sanjayan, Penetration Reinforcing Method for 3D Concrete Printing, *RILEM Bookseries.* 28 (2020) 680–690. https://doi.org/10.1007/978-3-030-49916-7_68/COVER.
- [34] T. Daungwilailuk, P. Pheinsusom, W. Pansuk, Uniaxial load testing of large-scale 3D-printed concrete wall and finite-element model analysis, *Constr. Build. Mater.* 275 (2021) 122039. <https://doi.org/10.1016/j.conbuildmat.2020.122039>.
- [35] B.P. Sinha, K.H. Gerstle, L.G. Tulin, Stress-Strain Relations for Concrete Under Cyclic Loading, *J. Proc.* 61 (1964) 195–212. <https://doi.org/10.14359/7775>.
- [36] Mehta, P.K., Monteiro, P.J.M. (1993) *Concrete Microstructure, Properties,*

and Materials. 2nd Edition, The McGraw- Hill Companies, Inc., (1993).

- [37] A. Journal, O.F. Civil, T. Guwahati, Constitutive modeling of concrete : An overview, (2016).
- [38] A. Saritas, Mixed Formulation Frame Element for Shear Critical Steel and Reinforced Concrete Members, Thesis. (2006) 206. http://books.google.es/books/about/Mixed_Formulation_Frame_Element_for_Shea.html?id=oRyYNwAACAAJ&pgis=1.
- [39] J. Vorel, M. Marcon, G. Cusatis, F. Caner, G. Di Luzio, R. Wan-Wendner, A comparison of the state of the art models for constitutive modelling of concrete, *Comput. Struct.* 244 (2021). <https://doi.org/10.1016/j.compstruc.2020.106426>.
- [40] Jeeho Lee, Gregory L. Fenves, Plastic-Damage Model for Cyclic Loading of Concrete Structures, *J. Eng. Mech.* . 124 (1998) 892–900.
- [41] J. Lubliner, J. Oliver, S. Oller, E. Oñate, A plastic-damage model for concrete, *Int. J. Solids Struct.* 25 (1989) 299–326. [https://doi.org/10.1016/0020-7683\(89\)90050-4](https://doi.org/10.1016/0020-7683(89)90050-4).
- [42] S.H. Ahmad, S.P. Shah, Complete Triaxial Stress-Strain Curves for Concrete., *ASCE J Struct Div.* 108 (1982) 728–742. <https://doi.org/10.1061/jsdeag.0005921>.
- [43] M.Y.H. Bangash, Concrete and concrete structures: numerical modelling and applications, Univ. Manitoba. Master of (1989) 81.
- [44] G. Hofstetter, H.A. Mang, Computational mechanics of reinforced concrete structures, (1995) 366.
- [45] A. Hillerborg, M. Mod er, P.E. Petersson, Analysis of crack formation and crack growth in concrete by means of fracture mechanics and finite elements, *Cem. Concr. Res.* 6 (1976) 773–781. [https://doi.org/10.1016/0008-8846\(76\)90007-7](https://doi.org/10.1016/0008-8846(76)90007-7).

- [46] W.F. Chen, A.F. Saleeb, *Constitutive Equations for Engineering Materials, Volume I: Elasticity and Modeling*, (1994).
- [47] E. Pramono, K. Willam, Fracture EnergyBased Plasticity Formulation of Plain Concrete, *J. Eng. Mech.* 115 (1989) 1183–1204. [https://doi.org/10.1061/\(ASCE\)0733-9399\(1989\)115:6\(1183\)](https://doi.org/10.1061/(ASCE)0733-9399(1989)115:6(1183)).
- [48] J. Lubliner, *Plasticity Theory*, Macmillan Publ. Company, NY. (1990).
- [49] J.C. Simo, T.J.R. Hughes, *Computational Inelasticity*, *Comput. Inelasticity*. (1998). <https://doi.org/10.1007/B98904>.
- [50] W.F. Chen, D.J. Han, *Plasticity for Structural Engineers*, Springer-Verlag, 1988.
- [51] E.N. Dvorkin, A.M. Cuitiño, G. Gioia, A concrete material model based on non-associated plasticity and fracture, (1989).
- [52] D.J. Han, W.F. Chen, Strain-space plasticity formulation for hardening-softening materials with elastoplastic coupling, *Int. J. Solids Struct.* 22 (1986) 935–950. [https://doi.org/10.1016/0020-7683\(86\)90072-7](https://doi.org/10.1016/0020-7683(86)90072-7).
- [53] P.A. Vermeer, R. De Borst, Non-Associated Plasticity for Soils, Concrete and Rock, *HERON*, 29 (3), 1984. (1984).
- [54] E. Oñate, S. Oller, J. Oliver, J. Lubliner, A constitutive model for cracking of concrete based on the incremental theory of plasticity, *Eng. Comput.* 5 (1988) 309–319. <https://doi.org/10.1108/eb023750>.
- [55] N.S. Ottosen, A Failure Criterion for Concrete, *J. Eng. Mech. Div.* 103 (1977) 527–535. <https://doi.org/10.1061/JMCEA3.0002248>.
- [56] J. Lee, *Theory and Implementation of Plastic-Damage Model for Concrete Structures under Cyclic and Dynamic Loading*, (1996).
- [57] J.W. Ju, On energy-based coupled elastoplastic damage theories: Constitutive modeling and computational aspects, *Int. J. Solids Struct.* 25 (1989) 803–833.

[https://doi.org/10.1016/0020-7683\(89\)90015-2](https://doi.org/10.1016/0020-7683(89)90015-2).

- [58] S. Oller, E. Oñate, J. Oliver, J. Lubliner, Finite element nonlinear analysis of concrete structures using a “plastic-damage model,” *Eng. Fract. Mech.* 35 (1990) 219–231. [https://doi.org/10.1016/0013-7944\(90\)90200-Z](https://doi.org/10.1016/0013-7944(90)90200-Z).
- [59] H.W. Reinhardt, *Fracture Mechanics of an Elastic Softening Material like Concrete*, *HERON*, 29 (2), 1984. (1984).
- [60] E. Kuhl, P. Steinmann, I. Carol, A thermodynamically consistent approach to microplane theory. Part II. Dissipation and inelastic constitutive modeling, *Int. J. Solids Struct.* 38 (2001) 2933–2952. [https://doi.org/10.1016/S0020-7683\(00\)00213-4](https://doi.org/10.1016/S0020-7683(00)00213-4).
- [61] I. Carol, M. Jirásek, Z. Bažant, A thermodynamically consistent approach to microplane theory. Part I. Free energy and consistent microplane stresses, *Int. J. Solids Struct.* 38 (2001) 2921–2931. [https://doi.org/10.1016/S0020-7683\(00\)00212-2](https://doi.org/10.1016/S0020-7683(00)00212-2).
- [62] I. Carol, P.C. Prat, Z.P. Bažant, New explicit microplane model for concrete: Theoretical aspects and numerical implementation, *Int. J. Solids Struct.* 29 (1992) 1173–1191. [https://doi.org/10.1016/0020-7683\(92\)90141-F](https://doi.org/10.1016/0020-7683(92)90141-F).
- [63] F.C. Caner, Z.P. Bažant, Microplane Model M4 for Concrete. II: Algorithm and Calibration, *J. Eng. Mech.* 126 (2000) 954–961. [https://doi.org/10.1061/\(ASCE\)0733-9399\(2000\)126:9\(954\)](https://doi.org/10.1061/(ASCE)0733-9399(2000)126:9(954)).
- [64] Z.P. Bažant, F.C. Caner, I. Carol, M.D. Adley, S.A. Akers, Microplane Model M4 for Concrete. I: Formulation with Work-Conjugate Deviatoric Stress, *J. Eng. Mech.* 126 (2000) 944–953. [https://doi.org/10.1061/\(ASCE\)0733-9399\(2000\)126:9\(944\)](https://doi.org/10.1061/(ASCE)0733-9399(2000)126:9(944)).
- [65] Z.P. Bazant, B.H. Oh, Microplane model for fracture analysis of concrete structures, *Proc. Symp. Non-Nucl. Munitions Struct.*, US Air Force Acad. Springs, Co. (1983) 49–55.

- [66] Z.P. Bazant, P.D. Bhat, Endochronic Theory of Inelasticity and Failure of Concrete, *ASCE J Eng Mech Div.* 102 (1976) 701–722. <https://doi.org/10.1061/jmcea3.0002152>.
- [67] Z.P. Bazant, Endochronic inelasticity and incremental plasticity, *Int. J. Solids Struct.* 14 (1978) 691–714. [https://doi.org/10.1016/0020-7683\(78\)90029-X](https://doi.org/10.1016/0020-7683(78)90029-X).
- [68] Z.P. Bažant, Ching-Long Shieh, Endochronic model for nonlinear triaxial behavior of concrete, *Nucl. Eng. Des.* 47 (1978) 305–315. [https://doi.org/10.1016/0029-5493\(78\)90074-2](https://doi.org/10.1016/0029-5493(78)90074-2).
- [69] Simulia Software Company, Abaqus Theory Guide Abacus 6.41, 2014. 6 (2017) 281. <http://50.16.225.63/v6.14/books/stm/default.htm>.
- [70] V.S. Gopalaratnam, S.P. Shah, Softening Response of Plain Concrete in Direct Tension, *J. Proc.* 82 (1985) 310–323. <https://doi.org/10.14359/10338>.
- [71] I.D. Karsan, J.O. Jirsa, Behavior of Concrete Under Compressive Loadings, *J. Struct. Div.* 95 (1969) 2543–2564. <https://doi.org/10.1061/JSDEAG.0002424>.
- [72] V.N. Nerella, V. Mechtcherine, Studying the Printability of Fresh Concrete for Formwork-Free Concrete Onsite 3D Printing Technology (CONPrint3D), in: *3D Concr. Print. Technol.*, Elsevier, 2019: pp. 333–347. <https://doi.org/10.1016/B978-0-12-815481-6.00016-6>.
- [73] S.C. Paul, G.P.A.G. van Zijl, M.J. Tan, I. Gibson, A review of 3D concrete printing systems and materials properties: current status and future research prospects, *Rapid Prototyp. J.* 24 (2018) 784–798. <https://doi.org/10.1108/RPJ-09-2016-0154>.
- [74] M. Mohammad, E. Masad, S.G. Al-Ghamdi, 3D Concrete Printing Sustainability: A Comparative Life Cycle Assessment of Four Construction Method Scenarios, *Build.* 2020, Vol. 10, Page 245. 10 (2020) 245. <https://doi.org/10.3390/BUILDINGS10120245>.

- [75] A. Siddika, M.A. Al Mamun, W. Ferdous, A.K. Saha, R. Alyousef, 3D-printed concrete: applications, performance, and challenges, *J. Sustain. Cem. Mater.* 9 (2020) 127–164. <https://doi.org/10.1080/21650373.2019.1705199/FORMAT/EPUB>.
- [76] A. Perrot, D. Rangeard, A. Pierre, Structural built-up of cement-based materials used for 3D-printing extrusion techniques, *Mater. Struct. Constr.* 49 (2016) 1213–1220. <https://doi.org/10.1617/s11527-015-0571-0>.
- [77] J. Zhang, J. Wang, S. Dong, X. Yu, B. Han, A review of the current progress and application of 3D printed concrete, *Compos. Part A Appl. Sci. Manuf.* 125 (2019). <https://doi.org/10.1016/J.COMPOSITESA.2019.105533>.
- [78] T.T. Le, S.A. Austin, S. Lim, R.A. Buswell, R. Law, A.G.F. Gibb, T. Thorpe, Hardened properties of high-performance printing concrete, *Cem. Concr. Res.* 42 (2012) 558–566. <https://doi.org/10.1016/j.cemconres.2011.12.003>.
- [79] Y. Wei, D. Tay, G. Heng, A. Ting, Y. Qian, B. Panda, L. He, M.J. Tan, Time gap effect on bond strength of 3D-printed concrete, 14 (2019) 104–113. <https://doi.org/10.1080/17452759.2018.1500420>.
- [80] T. Wangler, E. Lloret, L. Reiter, N. Hack, F. Gramazio, M. Kohler, M. Bernhard, B. Dillenburger, J. Buchli, N. Roussel, R. Flatt, Digital Concrete: Opportunities and Challenges, *RILEM Tech. Lett.* 1 (2016) 67–75. <https://doi.org/10.21809/RILEMTECHLETT.2016.16>.
- [81] L. Del Giudice, M.F. Vassiliou, Mechanical properties of 3D printed material with binder jet technology and potential applications of additive manufacturing in seismic testing of structures, *Addit. Manuf.* 36 (2020) 101714. <https://doi.org/10.1016/j.addma.2020.101714>.
- [82] J. Ingaglio, J. Fox, C.J. Naito, P. Bocchini, Material characteristics of binder jet 3D printed hydrated CSA cement with the addition of fine aggregates, *Constr. Build. Mater.* 206 (2019). <https://doi.org/10.1016/j.conbuildmat.2019.02.065>.

- [83] A. V. Rahul, M. Santhanam, H. Meena, Z. Ghani, Mechanical characterization of 3D printable concrete, *Constr. Build. Mater.* 227 (2019). <https://doi.org/10.1016/j.conbuildmat.2019.116710>.
- [84] M.K. Mohan, A. V. Rahul, K. Van Tittelboom, G. De Schutter, Evaluating the Influence of Aggregate Content on Pumpability of 3D Printable Concrete, *RILEM Bookseries*. 28 (2020) 333–341. https://doi.org/10.1007/978-3-030-49916-7_34.
- [85] G. De Schutter, K. Lesage, V. Mechtcherine, V.N. Nerella, G. Habert, I. Agusti-Juan, Vision of 3D printing with concrete — Technical, economic and environmental potentials, *Cem. Concr. Res.* 112 (2018) 25–36. <https://doi.org/10.1016/j.cemconres.2018.06.001>.
- [86] D. Dey, D. Srinivas, B. Panda, P. Suraneni, T.G. Sitharam, Use of industrial waste materials for 3D printing of sustainable concrete: A review, *J. Clean. Prod.* 340 (2022) 130749. <https://doi.org/10.1016/J.JCLEPRO.2022.130749>.
- [87] G. Ma, L. Wang, A critical review of preparation design and workability measurement of concrete material for largescale 3D printing, *Front. Struct. Civ. Eng.* 2017 123. 12 (2017) 382–400. <https://doi.org/10.1007/S11709-017-0430-X>.
- [88] A. Kazemian, X. Yuan, E. Cochran, B. Khoshnevis, Cementitious materials for construction-scale 3D printing: Laboratory testing of fresh printing mixture, *Constr. Build. Mater.* 145 (2017) 639–647. <https://doi.org/10.1016/J.CONBUILDMAT.2017.04.015>.
- [89] S. Klyuev, A. Klyuev, R. Fediuk, M. Ageeva, E. Fomina, M. Amran, G. Murali, Fresh and mechanical properties of low-cement mortars for 3D printing, *Constr. Build. Mater.* 338 (2022) 127644. <https://doi.org/10.1016/J.CONBUILDMAT.2022.127644>.
- [90] M. V. Tran, Y.T.H. Cu, C.V.H. Le, Rheology and shrinkage of concrete using polypropylene fiber for 3D concrete printing, *J. Build. Eng.* 44 (2021) 103400.

<https://doi.org/10.1016/J.JOBE.2021.103400>.

- [91] M.M. Ranjbar, M.H. Beygi, I.M. Nikbin, M. Rezvani, A. Barari, Evaluation of the strength variation of normal and lightweight self-compacting concrete in full scale walls, *Mater. Tehnol.* 45 (2011) 571–577.
- [92] V. Mechtcherine, K. van Tittelboom, A. Kazemian, E. Kreiger, B. Nematollahi, V.N. Nerella, M. Santhanam, G. de Schutter, G. Van Zijl, D. Lowke, E. Ivaniuk, M. Taubert, F. Bos, A roadmap for quality control of hardening and hardened printed concrete, *Cem. Concr. Res.* 157 (2022) 106800. <https://doi.org/10.1016/j.cemconres.2022.106800>.
- [93] ASTM International, ASTM Standard C39/C39M-16, Standard Test Method for Compressive Strength of Cylindrical Concrete Specimens, 2016. https://doi.org/10.1520/C0039_C0039M-20.
- [94] ASTM International, ASTM C78/C78M-22 Standard Test Method for Flexural Strength of Concrete (Using Simple Beam with Third-Point Loading), 2022.
- [95] ASTM International, ASTM Standard C642-13, Standard Test Method for Density, Absorption, and Voids in Hardened Concrete, 2013. <https://doi.org/10.1520/C0642-13>.
- [96] ASTM International, ASTM Standard C1585-20, Standard Test Method for Measurement of Rate of Absorption of Water by Hydraulic-Cement Concretes, 2020. <https://doi.org/10.1520/C1585-20>.
- [97] British Standards Institution, BS EN 12390-8:2009 Testing hardened concrete: Depth of penetration of water under pressure, 2009.
- [98] ASTM International, ASTM Standard C469/C469M, Standard Test Method for Static Modulus of Elasticity and Poisson's Ratio of Concrete in Compression, 2017. https://doi.org/10.1520/C0469_C0469M-14.
- [99] ASTM International, ASTM Standard C496/C496M-17, Standard Test

- Method for Splitting Tensile Strength of Cylindrical Concrete Specimens, West Conshohocken, PA, 2017. https://doi.org/10.1520/C0496_C0496M-17.
- [100] Turkish Standard Institute, TS EN 1052-3 Methods of test for masonry – Part 3 : Determination of initial shear strength, (2009).
- [101] ISO, ISO 22007-2:2015 - Plastics — Determination of thermal conductivity and thermal diffusivity — Part 2: Transient plane heat source (hot disc) method, 2015.
- [102] S.E. Gustafsson, Transient plane source techniques for thermal conductivity and thermal diffusivity measurements of solid materials, *Rev. Sci. Instrum.* 62 (1991) 797–804. <https://doi.org/10.1063/1.1142087>.
- [103] Hot Disk AB, TPS 2500 S Hot Disk Thermal Constants Analyser Brochure, (2017). www.hotdiskinstruments.com.
- [104] B. Adl-zarrabi, A conversion of the measured anisotropic thermal properties by transient plane heat source to the isotropic thermal properties, (2014).
- [105] A.N. Karim, B. Adl-Zarrabi, P. Johansson, A.S. Kalagasidis, Determination of the anisotropic thermal conductivity of an aerogel-based plaster using transient plane source method, *J. Phys. Conf. Ser.* 2069 (2021) 012030. <https://doi.org/10.1088/1742-6596/2069/1/012030>.
- [106] M. van den Heever, A. du Plessis, J. Kruger, G. van Zijl, Evaluating the effects of porosity on the mechanical properties of extrusion-based 3D printed concrete, *Cem. Concr. Res.* 153 (2022) 106695. <https://doi.org/10.1016/j.cemconres.2021.106695>.
- [107] Y. Zhang, H. Qiao, R. Qian, C. Xue, Q. Feng, L. Su, Y. Zhang, G. Liu, H. Du, Relationship between water transport behaviour and interlayer voids of 3D printed concrete, *Constr. Build. Mater.* 326 (2022). <https://doi.org/10.1016/J.CONBUILDMAT.2022.126731>.
- [108] J. Xiao, H. Liu, T. Ding, Finite element analysis on the anisotropic behavior

- of 3D printed concrete under compression and flexure, *Addit. Manuf.* 39 (2021) 101712. <https://doi.org/10.1016/j.addma.2020.101712>.
- [109] E. Keita, H. Bessaies-Bey, W. Zuo, P. Belin, N. Roussel, Weak bond strength between successive layers in extrusion-based additive manufacturing: measurement and physical origin, *Cem. Concr. Res.* 123 (2019) 105787. <https://doi.org/10.1016/J.CEMCONRES.2019.105787>.
- [110] J.G. Sanjayan, B. Nematollahi, M. Xia, T. Marchment, Effect of surface moisture on inter-layer strength of 3D printed concrete, *Constr. Build. Mater.* 172 (2018) 468–475. <https://doi.org/10.1016/J.CONBUILDMAT.2018.03.232>.
- [111] V.N. Nerella, S. Hempel, V. Mechtcherine, Effects of layer-interface properties on mechanical performance of concrete elements produced by extrusion-based 3D-printing, *Constr. Build. Mater.* 205 (2019) 586–601. <https://doi.org/10.1016/J.CONBUILDMAT.2019.01.235>.
- [112] M. van den Heever, F. Bester, M. Pourbehi, J. Kruger, S. Cho, G. van Zijl, Characterizing the Fissility of 3D Concrete Printed Elements via the Cohesive Zone Method, *RILEM Bookseries.* 28 (2020) 489–499. https://doi.org/10.1007/978-3-030-49916-7_50/FIGURES/7.
- [113] B. Panda, S.C. Paul, N.A.N. Mohamed, Y.W.D. Tay, M.J. Tan, Measurement of tensile bond strength of 3D printed geopolymer mortar, *Meas. J. Int. Meas. Confed.* 113 (2018) 108–116. <https://doi.org/10.1016/j.measurement.2017.08.051>.
- [114] H. Kloft, H.W. Krauss, N. Hack, E. Herrmann, S. Neudecker, P.A. Varady, D. Lowke, Influence of process parameters on the interlayer bond strength of concrete elements additive manufactured by Shotcrete 3D Printing (SC3DP), *Cem. Concr. Res.* 134 (2020) 106078. <https://doi.org/10.1016/J.CEMCONRES.2020.106078>.
- [115] J. Van Der Putten, M. Deprez, V. Cnudde, G. De Schutter, K. Van Tittelboom,

- Microstructural Characterization of 3D Printed Cementitious Materials, *Mater.* 2019, Vol. 12, Page 2993. 12 (2019) 2993. <https://doi.org/10.3390/MA12182993>.
- [116] J. Zhang, G. Zhang, S. Liu, Y. Sun, J.-M. Yang, I.-B. Park, H. Lee, H.-K. Kwon, Effects of Nozzle Details on Print Quality and Hardened Properties of Underwater 3D Printed Concrete, *Mater.* 2023, Vol. 16, Page 34. 16 (2022) 34. <https://doi.org/10.3390/MA16010034>.
- [117] L. Yang, S.M.E. Sepasgozar, S. Shirowzhan, A. Kashani, D. Edwards, Nozzle criteria for enhancing extrudability, buildability and interlayer bonding in 3D printing concrete, *Autom. Constr.* 146 (2023) 104671. <https://doi.org/10.1016/J.AUTCON.2022.104671>.
- [118] P. Shakor, S. Nejadi, G. Paul, materials A Study into the Effect of Different Nozzles Shapes and Fibre-Reinforcement in 3D Printed Mortar, (2019). <https://doi.org/10.3390/ma12101708>.
- [119] W. Lao, M. Li, T. Tjahjowidodo, Variable-geometry nozzle for surface quality enhancement in 3D concrete printing, *Addit. Manuf.* 37 (2021) 101638. <https://doi.org/10.1016/J.ADDMA.2020.101638>.
- [120] N. Zhang, J. Sanjayan, Extrusion nozzle design and print parameter selections for 3D concrete printing, *Cem. Concr. Compos.* 137 (2023) 104939. <https://doi.org/10.1016/J.CEMCONCOMP.2023.104939>.
- [121] L. He, W.T. Chow, H. Li, Effects of interlayer notch and shear stress on interlayer strength of 3D printed cement paste, *Addit. Manuf.* 36 (2020) 101390. <https://doi.org/10.1016/J.ADDMA.2020.101390>.
- [122] A. Perrot, D. Rangeard, E. Courteille, 3D printing of earth-based materials: Processing aspects, *Constr. Build. Mater.* 172 (2018) 670–676. <https://doi.org/10.1016/J.CONBUILDMAT.2018.04.017>.
- [123] Y. Zhang, Y. Zhang, L. Yang, G. Liu, Y. Chen, S. Yu, H. Du, Hardened

- properties and durability of large-scale 3D printed cement-based materials, *Mater. Struct. Constr.* 54 (2021) 1–14. <https://doi.org/10.1617/S11527-021-01632-X/FIGURES/11>.
- [124] H. Lee, J.H.J. Kim, J.H. Moon, W.W. Kim, E.A. Seo, Correlation between pore characteristics and tensile bond strength of additive manufactured mortar using X-ray computed tomography, *Constr. Build. Mater.* 226 (2019) 712–720. <https://doi.org/10.1016/J.CONBUILDMAT.2019.07.161>.
- [125] J. Kruger, A. du Plessis, G. van Zijl, An investigation into the porosity of extrusion-based 3D printed concrete, *Addit. Manuf.* 37 (2021) 101740. <https://doi.org/10.1016/j.addma.2020.101740>.
- [126] Y. Chen, O. Çopuroğlu, C. Romero Rodriguez, F.F. d. Mendonca Filho, E. Schlangen, Characterization of air-void systems in 3D printed cementitious materials using optical image scanning and X-ray computed tomography, *Mater. Charact.* 173 (2021) 110948. <https://doi.org/10.1016/J.MATCHAR.2021.110948>.
- [127] M. van den Heever, A. du Plessis, J. Kruger, G. van Zijl, Evaluating the effects of porosity on the mechanical properties of extrusion-based 3D printed concrete, *Cem. Concr. Res.* 153 (2022) 106695. <https://doi.org/10.1016/j.cemconres.2021.106695>.
- [128] C. Liu, R. Zhang, H. Liu, C. He, Y. Wang, Y. Wu, S. Liu, L. Song, F. Zuo, Analysis of the mechanical performance and damage mechanism for 3D printed concrete based on pore structure, *Constr. Build. Mater.* 314 (2022) 125572. <https://doi.org/10.1016/j.conbuildmat.2021.125572>.
- [129] 3D Slicer image computing platform | 3D Slicer, 3D Slicer as an Image Comput. Platf. Quant. Imaging Network. (2012). <https://www.slicer.org/>.
- [130] Rhinoceros Help - Heightfield | Rhino 3-D modeling, (2020). <http://docs.mcneel.com/rhino/6/help/en-us/index.htm#commands/heightfield.htm?Highlight=heightfield>.

- [131] A. Fedorov, R. Beichel, J. Kalpathy-Cramer, J. Finet, J.-C. Fillion-Robin, S. Pujol, C. Bauer, D. Jennings, F. Fennessy, M. Sonka, J. Buatti, S. Aylward, J. V Miller, S. Pieper, R. Kikinis, 3D Slicer as an Image Computing Platform for the Quantitative Imaging Network, *Magn Reson Imaging*. 30 (2012) 1323–1341. <https://doi.org/10.1016/j.mri.2012.05.001>.
- [132] C. Pinter, A. Lasso, G. Fichtinger, Polymorph segmentation representation for medical image computing, *Comput. Methods Programs Biomed.* 171 (2019) 19–26. <https://doi.org/10.1016/J.CMPB.2019.02.011>.
- [133] F. Montero-Chacón, J. Marín-Montín, F. Medina, Mesomechanical characterization of porosity in cementitious composites by means of a voxel-based finite element model, (2014). <https://doi.org/10.1016/j.commat.2014.03.066>.
- [134] L.P. Saenz, discussion of" Equation for the Stress-Strain Curve of Concrete" by Desayi and Krishnan, *J. ACI Proc.* 9 (1964) 1229–1235.
- [135] Dassault Systèmes, *Abaqus Materials Guide*, (2020).
- [136] Y. Dere, Nonlinear FE Modeling of Reinforced Concrete, *Int. J. Struct. Civ. Eng. Res.* 6 (2017) 71–74. <https://doi.org/10.18178/ijscer.6.1.71-74>.
- [137] ABAQUS, *Abaqus Elements Guide*, (2020).
- [138] P.P. Camanho, C.G. Dávila, M.F. De Moura, Numerical simulation of mixed-mode progressive delamination in composite materials, *J. Compos. Mater.* 37 (2003) 1415–1438. <https://doi.org/10.1177/0021998303034505>.
- [139] J. Jagoda, B. Diggs-McGee, M. Kreiger, S. Schuldt, The Viability and Simplicity of 3D-Printed Construction: A Military Case Study, *Infrastructures*. 5 (2020) 35. <https://doi.org/10.3390/infrastructures5040035>.
- [140] X. Han, J. Yan, M. Liu, L. Huo, J. Li, Experimental study on large-scale 3D printed concrete walls under axial compression, *Autom. Constr.* 133 (2022) 103993. <https://doi.org/10.1016/j.autcon.2021.103993>.

- [141] J. Cai, Z. Sheng, X. Wang, Y. Fang, J. Pan, Effect of reinforcement configurations on the flexural behaviors of 3D printed fiber reinforced cementitious composite (FRCC) beams, *J. Build. Eng.* 46 (2022) 103773. <https://doi.org/10.1016/j.jobbe.2021.103773>.
- [142] ŞARTNAME Sikadur®-31 Epoksi Tamir Harcı ile Çatlak Tamiratı Uygulaması, (2019). [https://tur.sika.com/content/dam/dms/tr01/2/Sikadur 31 Epoksi Tamir Harci ile Catlak Tamirati Uygulaması.pdf](https://tur.sika.com/content/dam/dms/tr01/2/Sikadur%2031%20Epoksi%20Tamir%20Harcı%20ile%20Çatlak%20Tamiratı%20Uygulaması.pdf).
- [143] A. Thorenfeldt, E. Tomaszewicz, J. Jensen, Mechanical properties of high-strength concrete and application in design, *Proc. Symp. Util. High Strength Concr.* (1987) 149–159. <https://cir.nii.ac.jp/crid/1571980075083210880>.
- [144] ACI CODE-318-19(22): Building Code Requirements for Structural Concrete and Commentary (Reapproved 2022), (n.d.). https://www.concrete.org/store/productdetail.aspx?ItemID=318U19&Language=English&Units=US_Units.

APPENDICES

A. Concrete Damage Plasticity Model (CDPM) – ABAQUS UMAT

```

1  c Concrete damage-plasticity model (CDPM) _ UMAT for ABAQUS
2  c 28.09.2023 Alper Tunga BAYRAK @ Middle East Technical University
3  c Part of a master thesis study supervised by Prof. Dr. Afsin SARITAS
4  c*****
5
6  c Key references:
7  c [1] Jeeho Lee and Gregory L. Fenves, "Plastic-Damage Model for Cyclic Loading
8  c of Concrete Structures," J. Eng. Mech. , vol. 124, no. 8, pp. 892-900, 1998.
9  c [2] J. Lee, "Theory and Implementation of Plastic-Damage Model," 1996.
10 c [3] A. Saritas, "Mixed Formulation Frame Element for Shear Critical Steel and
    c Reinforced Concrete Members," Thesis, no. January 2006, p. 206, 2006, [Online].
    c Available:
    c http://books.google.es/books/about/Mixed\_Formulation\_Frame\_Element\_for\_Shea.html?
11 c id=oRyYNwAACAAJ&pgis=1
12 c [4] J. Lubliner, J. Oliver, S. Oller, and E. Oñate, "A plastic-damage model for
13 c concrete," Int. J. Solids Struct., vol. 25, no. 3, pp. 299-326, Jan. 1989, doi:
14 c 10.1016/0020-7683(89)90050-4.
15 c*****
16
17 c -----
18 c # of properties (props) = 15
19 c # of state variables (state) = 17
20 c -----
21
22     SUBROUTINE UMAT(STRESS,STATEV,DDSDDE,SSE,SPD,SCD,
23     1 RPL,DDSDDT,DRPLDE,DRPLDT,
24     2 STRAN,DSTRAN,TIME,DTIME,TEMP,DTEMP,PREDEF,DPRED,CMNAME,
25     3 NDI,NSHR,NTENS,NSTATV,PROPS,NPROPS,COORDS,DROT,PNEWDT,
26     4 CELENT,DFGRD0,DFGRD1,NOEL,NPT,LAYER,KSPT,JSTEP,KINC)
27
28     C
29     INCLUDE 'ABA_PARAM.INC'
30
31     C
32     CHARACTER*80 CMNAME
33     DIMENSION STRESS(NTENS),STATEV(NSTATV),
34     1 DDSDDT(NTENS,NTENS),DDSDDT(NTENS),DRPLDE(NTENS),
35     2 STRAN(NTENS),DSTRAN(NTENS),TIME(2),PREDEF(1),DPRED(1),
36     3 PROPS(NPROPS),COORDS(3),DROT(3,3),DFGRD0(3,3),DFGRD1(3,3),
37     4 JSTEP(4)
38
39     C -----
40     C STATEV > history/STATE variable stored there
41     C STRESS > STRESS STORED
42     C DDSDDT > TANGENT MODUL
43     C NPROPS > #OF PROPERTIES DEFINED (15 BENIM MODELDE)
44     C PROPS > DEFINITE PROPERTIES
45     C NSTATV > #OF STATE VARIABLE STORED IN (11 TANE BENDE)
46     C NTENS = 6 (=4 FOR PLANE STRAIN)
47     C NDI = 3 (=2 FOR PLANE STRAIN)
48     C NSHR = 3 (=2 FOR PLANE STRAIN)
49     C STRAN = TOTAL STRAIN
50     C DSTRAN = DELTA EPS
51
52     C -----
53     C     UMAT FOR CONCRETE DAMAGE PLASTICITY MODEL
54     C -----
55
56     PARAMETER third =-0.3333333333333333d0
57     PARAMETER twthird = 0.6666666666666667d0
58     INTEGER i
59     INTEGER j
60     INTEGER k

```

52	INTEGER nitl
53	INTEGER itno
54	INTEGER rono
55	DOUBLE PRECISION K0
56	DOUBLE PRECISION G0
57	DOUBLE PRECISION S0
58	DOUBLE PRECISION alfap
59	DOUBLE PRECISION alfa
60	DOUBLE PRECISION at
61	DOUBLE PRECISION ac
62	DOUBLE PRECISION bt
63	DOUBLE PRECISION bc
64	DOUBLE PRECISION ct
65	DOUBLE PRECISION cc
66	DOUBLE PRECISION ft0
67	DOUBLE PRECISION fc0
68	DOUBLE PRECISION gt
69	DOUBLE PRECISION gc
70	DOUBLE PRECISION phit
71	DOUBLE PRECISION phic
72	DOUBLE PRECISION coht
73	DOUBLE PRECISION cohc
74	DOUBLE PRECISION beta
75	DOUBLE PRECISION Q
76	DOUBLE PRECISION Qp
77	DOUBLE PRECISION xnorm_sg
78	DOUBLE PRECISION xnorm
79	DOUBLE PRECISION I1tr
80	DOUBLE PRECISION EsEnorm
81	DOUBLE PRECISION lam
82	DOUBLE PRECISION Ftr
83	DOUBLE PRECISION H
84	DOUBLE PRECISION cc1
85	DOUBLE PRECISION cc2
86	DOUBLE PRECISION cc3
87	DOUBLE PRECISION cc4
88	DOUBLE PRECISION EI1
89	DOUBLE PRECISION abs1t
90	DOUBLE PRECISION diss
91	DOUBLE PRECISION RS
92	DOUBLE PRECISION ft
93	DOUBLE PRECISION fc
94	DOUBLE PRECISION ftK
95	DOUBLE PRECISION fcK
96	DOUBLE PRECISION EftK
97	DOUBLE PRECISION EfcK
98	DOUBLE PRECISION prmt
99	DOUBLE PRECISION res
100	DOUBLE PRECISION tol
101	DOUBLE PRECISION ddc
102	DOUBLE PRECISION ddt
103	DOUBLE PRECISION, DIMENSION(6) :: e
104	DOUBLE PRECISION, DIMENSION(6) :: ep
105	DOUBLE PRECISION, DIMENSION(6) :: sigtr
106	DOUBLE PRECISION, DIMENSION(6) :: str
107	DOUBLE PRECISION, DIMENSION(3,3) :: P
108	DOUBLE PRECISION, DIMENSION(3,3) :: PT
109	DOUBLE PRECISION, DIMENSION(3) :: Esig
110	DOUBLE PRECISION, DIMENSION(3,3) :: sigEff
111	DOUBLE PRECISION, DIMENSION(3,3) :: EsigEff
112	DOUBLE PRECISION, DIMENSION(3,3) :: dvii
113	DOUBLE PRECISION, DIMENSION(3) :: EsE
114	DOUBLE PRECISION, DIMENSION(3) :: Norm
115	DOUBLE PRECISION, DIMENSION(3) :: Eg
116	DOUBLE PRECISION, DIMENSION(3) :: RSS
117	DOUBLE PRECISION, DIMENSION(2) :: HH
118	DOUBLE PRECISION, DIMENSION(2,2) :: HHK

```

119 DOUBLE PRECISION, DIMENSION(2,3) :: hhh
120 DOUBLE PRECISION, DIMENSION(2,3,3) :: hEsig
121 DOUBLE PRECISION, DIMENSION(3,3) :: EgEsig
122 DOUBLE PRECISION, DIMENSION(2,3) :: HHEsig
123 DOUBLE PRECISION, DIMENSION(3) :: Esiglam
124 DOUBLE PRECISION, DIMENSION(3) :: FEsig
125 DOUBLE PRECISION, DIMENSION(2) :: FK
126 DOUBLE PRECISION, DIMENSION(2) :: lamK
127 DOUBLE PRECISION, DIMENSION(2,2) :: QK
128 DOUBLE PRECISION, DIMENSION(2,2) :: QKinv
129 DOUBLE PRECISION, DIMENSION(2) :: QQ
130 DOUBLE PRECISION, DIMENSION(2) :: DK
131 DOUBLE PRECISION, DIMENSION(11) :: STATEVN
132 DOUBLE PRECISION, DIMENSION(3,3) :: Evector
133 DOUBLE PRECISION, DIMENSION(3) :: Evalue
134 DOUBLE PRECISION, DIMENSION(6) :: xi
135 DOUBLE PRECISION, DIMENSION(3,3) :: devi
136 DOUBLE PRECISION, DIMENSION(3,3) :: bir
137 DOUBLE PRECISION, DIMENSION(2,2) :: br
138 DOUBLE PRECISION, DIMENSION(6, 6) :: xii
139 DOUBLE PRECISION, DIMENSION(6, 6) :: xpp
140 DOUBLE PRECISION, DIMENSION(6, 6) :: dd
141 DOUBLE PRECISION, DIMENSION(6) :: sig
142
143 c... define identity tensors and deviatoric tensors
144 xi = 0.D0
145 devi = 0.D0
146 bir = 0.d0
147 br = 0.d0
148 xii = 0.D0
149 xpp = 0.D0
150 do i = 1,3
151     do j = 1,3
152         xpp(i,j) = third
153         devi(i,j) = third
154     enddo
155 enddo
156 br(1,1) = 1.d0
157 br(2,2) = 1.d0
158
159 do i = 1,3
160     xi (i) = 1.d0
161     devi (i,i) = twotthird
162     bir (i,i) = 1.d0
163     xii(i,i) = 1.D0
164     xii(i+3,i+3) = 1.D0/2.D0
165     xpp (i,i) = twotthird
166     xpp (i+3,i+3) = 1.D0/2.D0
167 enddo
168
169 C##### Start of USER code #####
170
171
172 C... Get the material parameters from DEPVAR
173 K0 = PROPS(1) ! bulk modulus kappa
174 G0 = PROPS(2) ! ground shear modulus G0
175 S0 = PROPS(3) ! tensile stiffness recovery S0
176 alfap = PROPS(4) ! alfap
177 alfa = PROPS(5) ! alfa
178 at = PROPS(6) ! at
179 ac = PROPS(7) ! ac
180 bt = PROPS(8) ! bt
181 bc = PROPS(9) ! bc
182 ct = PROPS(10) ! ct
183 cc = PROPS(11) ! cc
184 ft0 = PROPS(12) ! initial yield stress in tension ft0
185 fc0 = PROPS(13) ! initial yield stress in compres fc0

```

```

186      gt   = PROPS(14) !    tension fracture energy density gt
187      gc   = PROPS(15) !    compres fracture energy density gc
188
189      c..  history variable timestep tn
190      do i = 1, 10
191          STATEVN(i) = STATEV(i)
192      enddo
193      c..  total strain
194      STATEV(12)=STATEV(12) + DSTRAN(1)
195      STATEV(13)=STATEV(13) + DSTRAN(2)
196      STATEV(14)=STATEV(14) + DSTRAN(3)
197      STATEV(15)=STATEV(15) + DSTRAN(4)
198      STATEV(16)=STATEV(16) + DSTRAN(5)
199      STATEV(17)=STATEV(17) + DSTRAN(6)
200      c..  account for Voigt storage
201      STATEV(15) = STATEV(15)/2.D0
202      STATEV(16) = STATEV(16)/2.D0
203      STATEV(17) = STATEV(17)/2.D0
204
205      c..  trace of strains
206      Q  = STATEV(12) + STATEV(13) + STATEV(14)
207      Qp = STATEVN(1) + STATEVN(2) + STATEVN(3)
208      c..  deviator of strains
209      do i = 1,6
210          e(i) = STATEV(i+11) - Q*xi(i)/3.d0
211          ep(i) = STATEVN(i) - Qp*xi(i)/3.d0
212      enddo
213
214      c..  compute the trial state
215      do i = 1,6
216          sigtr(i) = 2.d0*G0*(e(i) - ep(i)) + K0*(Q - Qp)*xi(i)
217      enddo
218      I1tr = sigtr(1) + sigtr(2) + sigtr(3)
219
220      do i=1,6
221          str(i) = sigtr(i) - I1tr*xi(i)/3.d0
222      enddo
223      xnorm = xnorm_sg(6,str,str)
224
225      phit = 1.d0 + at*(2.d0 + at)*STATEVN(7)
226      phic = 1.d0 + ac*(2.d0 + ac)*STATEVN(8)
227      coht =ft0*((1.d0+at-dsqrt(phit))/at)**(1.d0-ct/bt)*dsqrt(phit)
228      cohc =fc0*((1.d0+ac-dsqrt(phic))/ac)**(1.d0-cc/bc)*dsqrt(phic)
229      beta = (cohc/coht) * (1.d0 - alfa) - (alfa + 1.d0)
230
231      c.....Find Eigenvalues (Esig) and Eigenvectors (P)
232      P(1,1) = sigtr(1) ! Voith notation to Matrix
233      P(1,2) = sigtr(4) !
234      P(1,3) = sigtr(6) !
235      P(2,1) = sigtr(4) !      [1,1 1,2 1,3]      [1,1]
236      P(2,2) = sigtr(2) ! P = [2,1 2,2 2,3] & sigtr = [3,3]
237      P(2,3) = sigtr(5) !      [3,1 3,2 3,3]      [1,2]
238      P(3,1) = sigtr(6) !
239      P(3,2) = sigtr(5) !      [2,3]
240      P(3,3) = sigtr(3) !      [1,3]
241
242      ! Call subroutine to compute eigenvalues and eigenvectors
243      call jacobi_eigenvalue (P, 1000, Evector, Evalue, itno, rono)
244      Esig = Evalue
245      P = Evector
246
247      Ftr = alfa*I1tr + dsqrt(3.d0/2.d0)*xnorm - (1.d0-alfa)*cohc
248      1 + beta * (dabs(Esig(3))+Esig(3)) / 2.d0
249      c... CHECK plastic flow
250      if (Ftr.le.1.d-12) then ! ELASTIC STEP
251
252      cccc damage update

```



```

253      EI1 = Esig(1) + Esig(2) + Esig(3)
254      abslt = dabs(Esig(1))+dabs(Esig(2))+dabs(Esig(3))
255      if (abslt.eq.0.D0) abslt = 1.d-5 ! to prevent infinity
256      RS = 1.d0/2.d0 + EI1 / (2.d0*abslt)
257      ddt = 1.d0 - ((1.d0+at-dsqrt(phit))/at)**(ct/bt)
258      ddc = 1.d0 - ((1.d0+ac-dsqrt(phic))/ac)**(cc/bc)
259      STATEV(11) = 1.d0-(1.d0-ddc) * (1.d0-(S0 + (1.d0 - S0)*RS) * ddt)
260
261      cccc
262      do i = 1,6
263          STATEV(i) = STATEVN(i)
264          sig(i) = (1.d0 - STATEV(11)) * sigtr(i)
265      do j = 1,6
266          dd(i,j) = K0*xi(i)*xi(j) + 2.d0*G0*xpp(i,j)
267      enddo
268      enddo
269      DDSDE = (1.d0 - STATEV(11)) * dd
270      STRESS = sig
271      STATEV(7) = STATEVN(7)
272      STATEV(8) = STATEVN(8)
273      STATEV(9) = ddt
274      STATEV(10) = ddc
275      c.. account for Voigt storage
276      STATEV(15) = STATEV(15)*2.D0
277      STATEV(16) = STATEV(16)*2.D0
278      STATEV(17) = STATEV(17)*2.D0
279
280      else ! PLASTIC STEP
281      c
282          tol = 1.d-22
283          lam = 0.d0
284          EsigEff = 0.d0
285          nit1 = 0
286          do i = 1,6
287              STATEV(i) = STATEVN(i)
288          enddo
289          STATEV(7) = STATEVN(7)
290          STATEV(8) = STATEVN(8)
291
292          EsigEff(1,1) = Esig(3)
293          EsigEff(2,2) = Esig(2)
294          EsigEff(3,3) = Esig(1)
295
296          cc1 = -2.d0*G0*I1tr / (3.d0*xnorm) + 3.d0*alfap*K0
297          cc2 = 2.d0*G0/xnorm
298          cc3 = 9.d0*K0*alfap*alfa + dsqrt(6.d0)*G0
299
300          101 continue ! NEWTON_RAPHSON ITERATION
301          nit1 = nit1 + 1
302
303          phit = 1.d0 + at*(2.d0 + at)*STATEV(7)
304          phic = 1.d0 + ac*(2.d0 + ac)*STATEV(8)
305          coht =ft0*(((1.d0+at-dsqrt(phit))/at)**(1.d0-ct/bt))*dsqrt(phit)
306          cohcc =fc0*(((1.d0+ac-dsqrt(phic))/ac)**(1.d0-cc/bc))*dsqrt(phic)
307          beta = (cohcc/coht) * (1.d0 - alfa) - (alfa + 1.d0)
308          H = 0.d0
309          if (EsigEff(1,1).gt.0) H = 1.d0
310          cc4 = alfa*I1tr + dsqrt(3.d0/2.d0)*xnorm - (1.d0-alfa)*cohcc
311
312          lam = (cc4 + beta*H*Esig(3)) / (cc3 + beta*H*(cc2*Esig(3)+cc1))
313          EsigEff(1,1) = Esig(3) - lam*(cc2*Esig(3) + cc1)
314          EsigEff(2,2) = Esig(2) - lam*(cc2*Esig(2) + cc1)
315          EsigEff(3,3) = Esig(1) - lam*(cc2*Esig(1) + cc1)
316          EI1 = EsigEff(1,1) + EsigEff(2,2) + EsigEff(3,3)
317          abslt = dabs(EsigEff(1,1))+dabs(EsigEff(2,2))+dabs(EsigEff(3,3))
318          RS = 1.d0/2.d0 + EI1 / (2.d0*abslt)
319          ft = ft0 * ( (1.d0+at)*dsqrt(phit) - phit ) / at

```

```

320 fc = fc0 * ( (1.d0+ac)*dsqrt(phic) - phic ) / ac
321
322 EsE(1) = EsigEff(1,1) - EI1/3.d0
323 EsE(2) = EsigEff(2,2) - EI1/3.d0
324 EsE(3) = EsigEff(3,3) - EI1/3.d0
325
326 EsEnorm = dsqrt(EsE(1)*EsE(1) + EsE(2)*EsE(2) + EsE(3)*EsE(3))
327
328 Norm(1) = EsE(1) / EsEnorm
329 Norm(2) = EsE(2) / EsEnorm
330 Norm(3) = EsE(3) / EsEnorm
331
332 Eg(1) = Norm(1) + alfab
333 Eg(2) = Norm(2) + alfab
334 Eg(3) = Norm(3) + alfab
335
336 HH(1) = RS * ft * Eg(1) / gt
337 HH(2) = (RS - 1.d0) * fc * Eg(3) / gc
338
339 ftK = ft0*(2.d0 +at) * ((1.d0+at)/(2.d0*dsqrt(phit))-1.d0)
340 fcK = fc0*(2.d0 +ac) * ((1.d0+ac)/(2.d0*dsqrt(phic))-1.d0)
341
342 HHK(1,1) = RS * ftK * Eg(1) / gt
343 HHK(1,2) = 0.d0
344 HHK(2,1) = 0.d0
345 HHK(2,2) = (RS - 1.d0) * fcK * Eg(3) / gc
346
347 hhh = 0.d0
348 hhh(1,1) = RS * ft / gt
349 hhh(2,3) = (RS - 1.d0) * fc / gc
350
351 RSS(1) = dabs(EsigEff(1,1))*(abslt-dabs(EsigEff(1,1)))
352 1 - EsigEff(1,1)*(EI1-EsigEff(1,1))
353 RSS(1) = RSS(1) / (2.d0*dabs(EsigEff(1,1))*(abslt**2.d0))
354 RSS(2) = dabs(EsigEff(2,2))*(abslt-dabs(EsigEff(2,2)))
355 1 - EsigEff(2,2)*(EI1-EsigEff(2,2))
356 RSS(2) = RSS(2) / (2.d0*dabs(EsigEff(2,2))*(abslt**2.d0))
357 RSS(3) = dabs(EsigEff(3,3))*(abslt-dabs(EsigEff(3,3)))
358 1 - EsigEff(3,3)*(EI1-EsigEff(3,3))
359 RSS(3) = RSS(3) / (2.d0*dabs(EsigEff(3,3))*(abslt**2.d0))
360
361
362 hEsig = 0.d0
363 do i = 1,3
364   hEsig(1,1,i) = ft * RSS(i) / gt
365   hEsig(2,3,i) = fc * RSS(i) / gc
366 enddo
367
368 do i = 1,3
369   do j = 1,3
370     EgEsig(i,j) = (1.d0/EsEnorm) * (bir(i,j) - norm(i)*norm(j))
371   enddo
372 enddo
373
374 dvii = MATMUL(EgEsig,devi)
375 EgEsig = dvii
376
377 HHEsig = 0.d0
378 do i = 1,2
379   do j = 1,3
380     do k = 1,3
381       HHEsig(i,j) = HHEsig(i,j) + hEsig(i,k,j)*Eg(k)
382     1 + hhh(i,k) * EgEsig(k,j)
383   enddo
384 enddo
385 enddo
386

```

```

387 Esiglam(1) = -1.d0 * (cc2*Esig(3) + cc1)
388 Esiglam(2) = -1.d0 * (cc2*Esig(2) + cc1)
389 Esiglam(3) = -1.d0 * (cc2*Esig(1) + cc1)
390
391 FEsig(1) = (dsqrt(3.d0/2.d0)*Norm(1)+alfa+beta*H) / (1.d0-alfa)
392 FEsig(2) = (dsqrt(3.d0/2.d0)*Norm(2)+alfa) / (1.d0-alfa)
393 FEsig(3) = (dsqrt(3.d0/2.d0)*Norm(3)+alfa) / (1.d0-alfa)
394
395 EftK = (bt * (at-2.d0*dsqrt(phit))+1.d0) + ct * dsqrt(phit))
396 EftK = Eftk * (2.d0 + at)* ft0 / (2.d0 * bt * dsqrt(phit))
397 Eftk = Eftk * (((at - dsqrt(phit) + 1.d0)/at)**(-1.d0 * ct/bt))
398 EfcK = (bc * (ac-2.d0*dsqrt(phic))+1.d0) + cc * dsqrt(phic))
399 EfcK = EfcK * (2.d0 + ac)* fc0 / (2.d0 * bc * dsqrt(phic))
400 EfcK = EfcK * (((ac - dsqrt(phic) + 1.d0)/ac)**(-1.d0 * cc/bc))
401
402
403 FK(1) = (-1.d0 * cohC*EftK/(coht*coht))
404 FK(1) = FK(1) * ( dabs(EsigEff(1,1)) + EsigEff(1,1) ) / 2.d0
405 FK(2) = ( dabs(EsigEff(1,1)) + EsigEff(1,1) )/(coht*2.d0) - 1.d0
406 FK(2) = FK(2) * EfcK
407
408 prmt = 0.d0
409 do i = 1,3
410   prmt = prmt + FEsig(i)*Esiglam(i)
411 enddo
412
413 lamK(1) = -1.d0 * FK(1) / prmt
414 lamK(2) = -1.d0 * FK(2) / prmt
415
416 QK = 0.d0
417 do i = 1,2
418   do j = 1,2
419     do k = 1,3
420       QK(i,j) = QK(i,j) + lam*HHK(i,j) - br(i,j)
421     1 + (lam*HHEsig(i,k)*Esiglam(k) + HH(i)) * lamK(j)
422   enddo
423 enddo
424 enddo
425
426 QKinv(1,1) = QK(2,2)/(QK(1,1)*QK(2,2)-QK(1,2)*QK(2,1))
427 QKinv(1,2) = -1.d0*QK(1,2)/(QK(1,1)*QK(2,2)-QK(1,2)*QK(2,1))
428 QKinv(2,1) = -1.d0*QK(2,1)/(QK(1,1)*QK(2,2)-QK(1,2)*QK(2,1))
429 QKinv(2,2) = QK(1,1)/(QK(1,1)*QK(2,2)-QK(1,2)*QK(2,1))
430
431 QQ(1) = STATEVN(7) - STATEV(7) + lam * HH(1)
432 QQ(2) = STATEVN(8) - STATEV(8) + lam * HH(2)
433 res = dabs(QQ(1)) + dabs(QQ(2))
434
435 DK = 0.d0
436 do i = 1,2
437   do j = 1,2
438     DK(i) = DK(i) + QKinv(i,j) * QQ(j)
439   enddo
440 enddo
441
442 if ((nit1.lt.500).and.(dabs(res).gt.tol)) then
443   STATEV(7) = STATEV(7) - DK(1)
444   STATEV(8) = STATEV(8) - DK(2)
445   go to 101
446 endif
447 if (nit1.eq.100) write(*,*) '>No Conver! |res|= ', dabs(res)
448 c      END OF THE NEWTON RAPHSON
449
450 Esig(1) = EsigEff(1,1)      ! rearrange the order
451 EsigEff(1,1) = EsigEff(3,3) ! of eigenvalues
452 EsigEff(3,3) = Esig(1)    ! to right order
453

```

```

454 PT = TRANSPOSE( P )
455 sigEff = MATMUL(MATMUL(P,EsigEff), PT)
456
457 ddt = 1.d0 - ((1.d0+at-dsqrt(phit))/at)**(ct/bt)
458 ddc = 1.d0 - ((1.d0+ac-dsqrt(phic))/ac)**(cc/bc)
459 STATEV(9) = ddt
460 STATEV(10) = ddc
461 STATEV(11) = 1.d0-(1.d0-ddc)*(1.d0-(S0 + (1.d0 - S0)*RS) * ddt)
462
463
464 sig(1) = (1.d0 - STATEV(11)) * sigEff(1,1)
465 sig(2) = (1.d0 - STATEV(11)) * sigEff(2,2)
466 sig(3) = (1.d0 - STATEV(11)) * sigEff(3,3)
467 sig(4) = (1.d0 - STATEV(11)) * sigEff(1,2)
468 sig(5) = (1.d0 - STATEV(11)) * sigEff(2,3)
469 sig(6) = (1.d0 - STATEV(11)) * sigEff(1,3)
470
471 do i = 1,6
472   STATEV(i) = STATEV(i) + (lam / xnorm) * (str(i) + alfab*xi(i))
473 do j = 1,6
474   dd(i,j) = K0*xi(i)*xi(j) + 2.d0*G0*xpp(i,j)
475 enddo
476 enddo
477
478 STRESS = sig
479 DDSDE = (1.d0 - STATEV(11)) * dd
480
481 c.. account for Voigt storage
482 STATEV(15) = STATEV(15)*2.D0
483 STATEV(16) = STATEV(16)*2.D0
484 STATEV(17) = STATEV(17)*2.D0
485 endif
486
487 RETURN
488 END SUBROUTINE
489
490
491 function xnorm_sg(ndms,a,b)
492 implicit none
493 INTEGER jj
494 INTEGER ndms
495 DOUBLE PRECISION xnorm_sg
496 DOUBLE PRECISION, DIMENSION(ndms) :: a
497 DOUBLE PRECISION, DIMENSION(ndms) :: b
498 DOUBLE PRECISION, DIMENSION(6) :: f
499
500 do jj = 1, 3
501   f(jj) = 1.d0
502   f(jj+3) = 2.d0
503 enddo
504
505 xnorm_sg = 0.d0
506 do jj = 1,ndms
507   xnorm_sg = xnorm_sg + a(jj)*b(jj)*f(jj)
508 enddo
509 xnorm_sg = dsqrt(xnorm_sg)
510 return
511 end
512
513
514 subroutine jacobi_eigenvalue ( a, it_max, v, d, it_num, rot_num)
515 implicit none
516
517 integer,parameter:: n=3
518 double precision a(n,n), bw(n), c, d(n), g, gapq, h
519 integer i, it_max,it_num, j, k, l, m, p, q, rot_num
520

```

```

521     double precision s, t, tau, term, termq, theta
522     double precision thresh, v(n,n), w(n), zw(n)
523
524
525     cc JACOBI_EIGENVALUE carries out the Jacobi eigenvalue iteration.
526     c
527     c Discussion:
528     c
529     c This function computes the eigenvalues and eigenvectors of a
530     c real symmetric matrix, using Rutishauser's modifications of the classical
531     c Jacobi rotation method with threshold pivoting.
532     c
533     c Licensing:
534     c
535     c This code is distributed under the GNU LGPL license.
536     c
537     c Modified:
538     c
539     c 17 September 2013
540     c September 2023 by Alper Tunga BAYRAK
541     c
542     c Author:
543     c
544     c FORTRAN77 version by John Burkardt
545     c
546     c Parameters:
547     c
548     c Input, integer N, the order of the matrix.
549     c
550     c Input, double precision A(N,N), the matrix, which must be square, real,
551     c and symmetric.
552     c
553     c Input, integer IT_MAX, the maximum number of iterations.
554     c
555     c Output, double precision V(N,N), the matrix of eigenvectors.
556     c
557     c Output, double precision D(N), the eigenvalues, in descending order.
558     c
559     c Output, integer IT_NUM, the total number of iterations.
560     c
561     c Output, integer ROT_NUM, the total number of rotations.
562     c
563
564
565     do j = 1, n
566         do i = 1, n
567             v(i,j) = 0.0D+00
568         end do
569         v(j,j) = 1.0D+00
570     end do
571
572     do i = 1, n
573         d(i) = a(i,i)
574     end do
575
576     do i = 1, n
577         bw(i) = d(i)
578         zw(i) = 0.0D+00
579     end do
580
581     it_num = 0
582     rot_num = 0
583
584 10 continue
585
586     if ( it_num .lt. it_max ) then
587

```

```

588     it_num = it_num + 1
589     c
590     c The convergence threshold is based on the size of the elements in
591     c the strict upper triangle of the matrix.
592     c
593     thresh = 0.0D+00
594     do j = 1, n
595         do i = 1, j - 1
596             thresh = thresh + a(i,j) ** 2
597         end do
598     end do
599
600     thresh = sqrt ( thresh ) / dble ( 4 * n )
601
602     if ( thresh .eq. 0.0D+00 ) then
603         go to 20
604     end if
605
606     do p = 1, n
607         do q = p + 1, n
608
609             gapq = 10.0D+00 * abs ( a(p,q) )
610             termq = gapq + abs ( d(p) )
611             termq = gapq + abs ( d(q) )
612         c
613         c Annihilate tiny offdiagonal elements.
614         c
615         if (4.lt.it_num.and.termq.eq.abs(d(p)).and.termq.eq.abs(d(q)))then
616
617             a(p,q) = 0.0D+00
618         c
619         c Otherwise, apply a rotation.
620         c
621         else if ( thresh .le. abs ( a(p,q) ) ) then
622
623             h = d(q) - d(p)
624             term = abs ( h ) + gapq
625
626             if ( term .eq. abs ( h ) ) then
627                 t = a(p,q) / h
628             else
629                 theta = 0.5D+00 * h / a(p,q)
630                 t = 1.0D+00 / ( abs ( theta ) + sqrt ( 1.0D+00 + theta * theta))
631                 if ( theta .lt. 0.0D+00 ) then
632                     t = - t
633                 end if
634             end if
635
636             c = 1.0D+00 / sqrt ( 1.0D+00 + t * t )
637             s = t * c
638             tau = s / ( 1.0D+00 + c )
639             h = t * a(p,q)
640         c
641         c Accumulate corrections to diagonal elements.
642         c
643             zw(p) = zw(p) - h
644             zw(q) = zw(q) + h
645             d(p) = d(p) - h
646             d(q) = d(q) + h
647
648             a(p,q) = 0.0D+00
649         c
650         c Rotate, using information from the upper triangle of A only.
651         c
652         do j = 1, p - 1
653             g = a(j,p)
654             h = a(j,q)

```

```

655     a(j,p) = g - s * ( h + g * tau )
656     a(j,q) = h + s * ( g - h * tau )
657 end do
658
659 do j = p + 1, q - 1
660     g = a(p,j)
661     h = a(j,q)
662     a(p,j) = g - s * ( h + g * tau )
663     a(j,q) = h + s * ( g - h * tau )
664 end do
665
666 do j = q + 1, n
667     g = a(p,j)
668     h = a(q,j)
669     a(p,j) = g - s * ( h + g * tau )
670     a(q,j) = h + s * ( g - h * tau )
671 end do
672 c
673 c Accumulate information in the eigenvector matrix.
674 c
675 do j = 1, n
676     g = v(j,p)
677     h = v(j,q)
678     v(j,p) = g - s * ( h + g * tau )
679     v(j,q) = h + s * ( g - h * tau )
680 end do
681
682 rot_num = rot_num + 1
683
684 end if
685
686 end do
687 end do
688
689 do i = 1, n
690     bw(i) = bw(i) + zw(i)
691     d(i) = bw(i)
692     zw(i) = 0.0D+00
693 end do
694
695 go to 10
696
697 end if
698
699 20 continue
700 c
701 c Restore upper triangle of input matrix.
702 c
703 do j = 1, n
704     do i = 1, j - 1
705         a(i,j) = a(j,i)
706     end do
707 end do
708 c
709 c Ascending sort the eigenvalues and eigenvectors.
710 c
711 do k = 1, n - 1
712
713     m = k
714
715     do l = k + 1, n
716         if ( d(l) .lt. d(m) ) then
717             m = l
718         end if
719     end do
720
721     if ( m .ne. k ) then

```

```
722
723     t    = d(m)
724     d(m) = d(k)
725     d(k) = t
726
727     do i = 1, n
728         w(i) = v(i,m)
729         v(i,m) = v(i,k)
730         v(i,k) = w(i)
731     end do
732
733     end if
734
735 end do
736
737 return
738
739 end subroutine jacobi_eigenvalue
740
741
742
```


B. Concrete Damage Plasticity Model (CDPM) – FEAP UMAT

```

1  c$id: umat1.f,v 1.1 2004/01/11 19:11:33 rlt Exp $
2      subroutine umat1(type,vv, d, ud, n1,n3)
3
4      c      * * F E A P * * A Finite Element Analysis Program
5
6      c.... Copyright (c) 1984-2004: Regents of the University of California
7      c                      All rights reserved
8
9      c-----[--.....+-----+-----]
10     c      Purpose: Dummy user material model routine
11
12     c      Inputs:
13     c          type - Name of material model
14     c          vv(5) - Command line real data
15     c          d(*) - Program material parameter data
16
17     c      Outputs:
18     c          ud(*) - Material parameter data for model
19     c          n1 - Number of history items/point (time dependent)
20     c          n3 - Number of history items/point (time independent)
21     c-----[--.....+-----+-----]
22     implicit none
23
24     include 'iofile.h'
25     logical pcomp, pinput, errck
26     character type*15
27     integer n1,n3, ii
28     real*8 vv(5),d(*),ud(*)
29
30     c      Set command name
31     if(pcomp(type,'mat1',4)) then ! Default form: DO NOT CHANGE
32         type = 'CDPMUPSUB' ! Specify new 'name'
33     c      Input user data and save in ud(*) array
34     else ! Perform input for user data
35         n1 = 11
36         errck = pinput(ud(1),15)
37         write( *,2000) n1
38         write(iow,2000) n1
39         write( *,2001) (ud(ii), ii=1,15)
40         write(iow,2001) (ud(ii), ii=1,15)
41     endif
42     2000 format(
43     * 10x,'MATERIAL MODEL FOR FEAP ----- (c) A.T. Bayrak, METU '/
44     * 10x,'[ ] [ ] CDPM gibi!!! from Lee thesis '/
45     * 10x,'[ ] [ ] UMAT1..... Version 05/11/2013'/
46     * 10x,'[ ] [n1 ] material history variables .....',i12)
47     2001 format(
48     * 10x,'[ 1] [ K0] e:          bulk modulus K0 = ', e12.5/
49     * 10x,'[ 2] [ G0] e:          shear modulus G0 = ', e12.5/
50     * 10x,'[ 3] [ S0] p: tension stiffness recovery S0 = ', e12.5/
51     * 10x,'[ 4] [alfap] p:          alfap = ', e12.5/
52     * 10x,'[ 5] [ alfa] p:          alfa = ', e12.5/
53     * 10x,'[ 6] [ at] p:          at = ', e12.5/
54     * 10x,'[ 7] [ ac] p:          ac = ', e12.5/
55     * 10x,'[ 8] [ bt] p:          bt = ', e12.5/
56     * 10x,'[ 9] [ bc] p:          bc = ', e12.5/
57     * 10x,'[10] [ ct] p:          ct = ', e12.5/
58     * 10x,'[11] [ cc] p:          cc = ', e12.5/
59     * 10x,'[12] [ ft0] p: initial yield str in Tens ft0 = ', e12.5/
60     * 10x,'[13] [ fc0] p: initial yield str in Comp fc0 = ', e12.5/

```

```

61      * 10x,'[14] [   gt] p: Tens Frctre energy density gt =   ', e12.5/
62      * 10x,'[15] [   gc] p: Comp Frctre energy density gc =   ', e12.5)
63      c
64      return
65      end
66      c
67      c
68      c
69      subroutine umat11(eps,theta,td,d,ud,hn,h1,nh,ii,istrt, sig,dd,isw)
70
71      c-----[---+---+---+-----]
72      c Purpose: User Constitutive Model
73
74      c Input:
75      c     eps(*) - Current strains at point (small deformation)
76      c     theta - Deformation gradient at point (finite deformation)
77      c     theta - Trace of strain at point
78      c     td - Determinant of deformatiom gradient
79      c     td - Temperature change
80      c     d(*) - Program material parameters (nnd)
81      c     ud(*) - User material parameters (nud)
82      c     hn(nh) - History terms at point: t_n
83      c     h1(nh) - History terms at point: t_n+1
84      c     nh - Number of history terms
85      c     ii - Current point number
86      c     istrt - Start state: 0 = elastic; 1 = last solution
87      c     isw - Solution option from element
88
89      c Output:
90      c     sig(*) - Stresses at point.
91      c     N.B. 1-d models use only sig(1)
92      c     dd(6,*) - Current material tangent moduli
93      c     N.B. 1-d models use only dd(1,1) and dd(2,1)
94      c-----[---+---+---+-----]
95      implicit none
96      include 'tdata.h'
97      include 'pmod2d.h'
98      c
99      integer nh,istrt,isw, ii
100     real*8 td
101     real*8 eps(*),theta(*),d(*),ud(*),hn(nh),h1(nh), sig(*),dd(6,*)
102     c
103     integer i, j, k, nitl, info, itno, rono
104     real*8 xi(6), bir(3,3), xii(6,6), xpp(6,6), third, twothird
105     real*8 work(8)
106     real*8 K0, G0, S0, alfap, alfa
107     real*8 at, ac, bt, bc, ct, cc, ft0, fc0, gt, gc
108     real*8 phit, phic, coht, cohc, beta
109     real*8 Q, Qp, e(6), ep(6), Evector(3,3), Evalue(3)
110     real*8 sigtr(6), I1tr, str(6), xnorm_sg, xnorm
111     real*8 P(3,3), PT(3,3), Esig(3), sigEff(3,3), EsigEff(3,3)
112     real*8 EsE(3), EsEnorm, Norm(3), Eg(3), lam, devi(3,3),dvii(3,3)
113     real*8 Ftr, H, cc1, cc2, cc3, cc4, EI1, abslt, diss
114     real*8 RS, RSS(3), ft, fc, ftK, fcK, EftK, EfcK
115     real*8 HH(2), HHK(2,2), hhh(2,3), hEsig(2,3,3), EgEsig(3,3)
116     real*8 HHEsig(2,3), Esiglam(3), FEsig(3), FK(2), prmt, lamK(2)
117     real*8 QK(2,2), QKinv(2,2), QQ(2), DK(2), br(2,2), res, tol
118     real*8 ddc, ddt
119
120     c Compute and output stress (sig) and (moduli)
121     c... define identity tensors
122
123     parameter ( third =-0.3333333333333333d0,
124     & twothird = 0.66666666666666667d0)
125     data xi/1.d0, 1.d0, 1.d0, 0.d0, 0.d0 ,0.d0/
126     data devi/twothird, third , third,
127     & third , twothird, third,

```

```

128 &      third  , third  , twothird/
129   data bir/1.d0, 0.d0, 0.d0,
130 &      0.d0, 1.d0, 0.d0,
131 &      0.d0, 0.d0, 1.d0/
132   data br/1.d0, 0.d0,
133 &      0.d0, 1.d0/
134   data xii/1.d0, 0.d0, 0.d0, 0.d0, 0.d0, 0.d0,
135 &      0.d0, 1.d0, 0.d0, 0.d0, 0.d0, 0.d0,
136 &      0.d0, 0.d0, 1.d0, 0.d0, 0.d0, 0.d0,
137 &      0.d0, 0.d0, 0.d0, 5.d-1,0.d0, 0.d0,
138 &      0.d0, 0.d0, 0.d0, 0.d0, 5.d-1,0.d0,
139 &      0.d0, 0.d0, 0.d0, 0.d0, 0.d0, 5.d-1/
140
141   data xpp/twothird,  third,  third,  0.d0,  0.d0,  0.d0,
142 &      third, twothird,  third,  0.d0,  0.d0,  0.d0,
143 &      third,  third, twothird,  0.d0,  0.d0,  0.d0,
144 &      0.d0,  0.d0,  0.d0,  5.d-1,  0.d0,  0.d0,
145 &      0.d0,  0.d0,  0.d0,  0.d0,  5.d-1,  0.d0,
146 &      0.d0,  0.d0,  0.d0,  0.d0,  0.d0,  5.d-1/
147
148 C
149 C... Get the material parameters from ud-field
150 K0 = ud(1) ! bulk modulus kappa
151 G0 = ud(2) ! ground shear modulus G0
152 S0 = ud(3) ! tensile stiffness recovery S0
153 alfap = ud(4) ! alfap
154 alfa = ud(5) ! alfa
155 at = ud(6) ! at
156 ac = ud(7) ! ac
157 bt = ud(8) ! bt
158 bc = ud(9) ! bc
159 ct = ud(10) ! ct
160 cc = ud(11) ! cc
161 ft0 = ud(12) ! initial yield stress in tension ft0
162 fc0 = ud(13) ! initial yield stress in compres fc0
163 gt = ud(14) ! tension fracture energy density gt
164 gc = ud(15) ! compres fracture energy density gc
165
166 c
167 c.. trace of strains
168 Q = eps(1) + eps(2) + eps(3)
169 Qp = hn(1) + hn(2) + hn(3)
170 c.. account for Voigt storage
171 eps(4) = eps(4)/2.d0
172 eps(5) = eps(5)/2.d0
173 eps(6) = eps(6)/2.d0
174
175 c.. deviator of strains
176 do i = 1,6
177   e(i) = eps(i) - Q*xi(i)/3.d0
178   ep(i) = hn(i) - Qp*xi(i)/3.d0
179 enddo
180
181 c.. compute the trial state
182 do i = 1,6
183   sigtr(i) = 2.d0*G0*(e(i) - ep(i)) + K0*(Q - Qp)*xi(i)
184 enddo
185 I1tr = sigtr(1) + sigtr(2) + sigtr(3)
186
187 do i=1,6
188   str(i) = sigtr(i) - I1tr*xi(i)/3.d0
189 enddo
190 xnorm = xnorm_sg(6,str,str)
191
192 phit = 1.d0 + at*(2.d0 + at)*hn(7)
193 phic = 1.d0 + ac*(2.d0 + ac)*hn(8)
194 coht =ft0*(((1.d0+at-dsqrt(phit))/at)**(1.d0-ct/bt))*dsqrt(phit)
195 cohc =fc0*(((1.d0+ac-dsqrt(phic))/ac)**(1.d0-cc/bc))*dsqrt(phic)

```

```

195     beta = (cohc/coht) * (1.d0 - alfa) - (alfa + 1.d0)
196
197     c.....Find Eigenvalues (Esig) and Eigenvectors (P)
198     P(1,1) = sigtr(1) ! Voith notation to Matrix
199     P(1,2) = sigtr(4) !
200     P(1,3) = sigtr(6) !
201     P(2,1) = sigtr(4) !      [1,1 1,2 1,3]
202     P(2,2) = sigtr(2) ! P = [2,1 2,2 2,3] & sigtr = [3,3]
203     P(2,3) = sigtr(5) !      [3,1 3,2 3,3]
204     P(3,1) = sigtr(6) !
205     P(3,2) = sigtr(5) !
206     P(3,3) = sigtr(3) !
207
208
209     call jacobi_eigenvalue (P, 1000, Evector, Evalue, itno, rono)
210     Esig = Evalue
211     P = Evector
212
213     Ftr = alfa*I1tr + dsqrt(3.d0/2.d0)*xnorm - (1.d0-alfa)*cohc
214     & + beta * ((dabs(Esig(3))+Esig(3)) / 2.d0)
215     c... CHECK plastic flow
216     if (Ftr.le.0.d0) then ! ELASTIC STEP
217
218
219     EI1 = Esig(1) + Esig(2) + Esig(3)
220     abslt = dabs(Esig(1))+dabs(Esig(2))+dabs(Esig(3))
221     if (abslt.eq.0.D0) abslt = 1.d-5 ! to prevent infinity
222     RS = 1.d0/2.d0 + EI1 / (2.d0*abslt)
223     ddt = 1.d0 - ((1.d0+at-dsqrt(phit))/at)**(ct/bt)
224     ddc = 1.d0 - ((1.d0+ac-dsqrt(phic))/ac)**(cc/bc)
225     h1(11) = 1.d0-(1.d0-ddc) * (1.d0-(S0 + (1.d0 - S0)*RS) * ddt)
226
227
228     do i = 1,6
229     h1(i) = hn(i)
230     sig(i) = (1.d0 - h1(11)) * sigtr(i)
231     do j = 1,6
232     dd(i,j) = (1.d0 - h1(11)) * (K0*xi(i)*xi(j) + 2.d0*G0*xpp(i,j))
233     enddo
234     enddo
235     h1(7) = hn(7)
236     h1(8) = hn(8)
237     h1(9) = hn(9)
238     h1(10) = hn(10)
239
240     else ! PLASTIC STEP
241
242     c
243     tol = 1.d-10
244     lam = 0.0d0
245     EsigEff = 0.d0
246     nitl = 0
247     do i = 1,6
248     h1(i) = hn(i)
249     enddo
250     h1(7) = hn(7)
251     h1(8) = hn(8)
252
253     EsigEff(1,1) = Esig(3)
254     EsigEff(2,2) = Esig(2)
255     EsigEff(3,3) = Esig(1)
256
257     cc1 = -2.d0*G0*I1tr / (3.d0*xnorm) + 3.d0*alfap*K0
258     cc2 = 2.d0*G0/xnorm
259     cc3 = 9.d0*K0*alfap*alfa + dsqrt(6.d0)*G0
260
261     101 continue

```

```

262 nitl = nitl + 1
263
264 phit = 1.d0 + at*(2.d0 + at)*h1(7)
265 phic = 1.d0 + ac*(2.d0 + ac)*h1(8)
266 coht =ft0*((1.d0+at-dsqrt(phit))/at)**(1.d0-ct/bt))*dsqrt(phit)
267 cohc =fc0*((1.d0+ac-dsqrt(phic))/ac)**(1.d0-cc/bc))*dsqrt(phic)
268 beta = (cohc/coht) * (1.d0 - alfa) - (alfa + 1.d0)
269 H = 0.d0
270 if (EsigEff(1,1).gt.0) H = 1.d0
271 cc4 = alfa*I1tr + dsqrt(3.d0/2.d0)*xnorm - (1.d0-alfa)*cohc
272
273 lam = (cc4 + beta*H*Esig(3)) / (cc3 + beta*H*(cc2*Esig(3)+cc1))
274 EsigEff(1,1) = Esig(3) - lam*(cc2*Esig(3) + cc1)
275 EsigEff(2,2) = Esig(2) - lam*(cc2*Esig(2) + cc1)
276 EsigEff(3,3) = Esig(1) - lam*(cc2*Esig(1) + cc1)
277 EI1 = EsigEff(1,1) + EsigEff(2,2) + EsigEff(3,3)
278 abslt = dabs(EsigEff(1,1))+dabs(EsigEff(2,2))+dabs(EsigEff(3,3))
279 RS = 1.d0/2.d0 + EI1 / (2.d0*abslt)
280 ft = ft0 * ( (1.d0+at)*dsqrt(phit) - phit ) / at
281 fc = fc0 * ( (1.d0+ac)*dsqrt(phic) - phic ) / ac
282
283 EsE(1) = EsigEff(1,1) - EI1/3.d0
284 EsE(2) = EsigEff(2,2) - EI1/3.d0
285 EsE(3) = EsigEff(3,3) - EI1/3.d0
286
287 EsEnorm = dsqrt(EsE(1)*EsE(1) + EsE(2)*EsE(2) + EsE(3)*EsE(3))
288
289 Norm(1) = EsE(1) / EsEnorm
290 Norm(2) = EsE(2) / EsEnorm
291 Norm(3) = EsE(3) / EsEnorm
292
293 Eg(1) = Norm(1) + alfap
294 Eg(2) = Norm(2) + alfap
295 Eg(3) = Norm(3) + alfap
296
297 HH(1) = RS * ft * Eg(1) / gt
298 HH(2) = (RS - 1.d0) * fc * Eg(3) / gc
299
300 ftK = ft0*(2.d0 +at) * (((1.d0+at)/(2.d0*dsqrt(phit)))-1.d0)
301 fcK = fc0*(2.d0 +ac) * (((1.d0+ac)/(2.d0*dsqrt(phic)))-1.d0)
302
303 HHK(1,1) = RS * ftK * Eg(1) / gt
304 HHK(1,2) = 0.d0
305 HHK(2,1) = 0.d0
306 HHK(2,2) = (RS - 1.d0) * fcK * Eg(3) / gc
307
308 hhh = 0.d0
309 hhh(1,1) = RS * ft / gt
310 hhh(2,3) = (RS - 1.d0) * fc / gc
311
312 RSS(1) = dabs(EsigEff(1,1))*(abslt-dabs(EsigEff(1,1)))
313 & - EsigEff(1,1)*(EI1-EsigEff(1,1))
314 RSS(1) = RSS(1) / (2.d0*dabs(EsigEff(1,1))*(abslt**2.d0))
315 RSS(2) = dabs(EsigEff(2,2))*(abslt-dabs(EsigEff(2,2)))
316 & - EsigEff(2,2)*(EI1-EsigEff(2,2))
317 RSS(2) = RSS(2) / (2.d0*dabs(EsigEff(2,2))*(abslt**2.d0))
318 RSS(3) = dabs(EsigEff(3,3))*(abslt-dabs(EsigEff(3,3)))
319 & - EsigEff(3,3)*(EI1-EsigEff(3,3))
320 RSS(3) = RSS(3) / (2.d0*dabs(EsigEff(3,3))*(abslt**2.d0))
321
322
323 hEsig = 0.d0
324 do i = 1,3
325 hEsig(1,1,i) = ft * RSS(i) / gt
326 hEsig(2,3,i) = fc * RSS(i) / gc
327 enddo
328

```

```

329 do i = 1,3
330 do j = 1,3
331   EgEsig(i,j) = (1.d0/EsEnorm) * (bir(i,j) - norm(i)*norm(j))
332 enddo
333 enddo
334
335 dvii = MATMUL(EgEsig,devi)
336 EgEsig = dvii
337
338 HHESig = 0.d0
339 do i = 1,2
340 do j = 1,3
341 do k = 1,3
342   HHESig(i,j) = HHESig(i,j) + hEsig(i,k,j)*Eg(k)
343 &      + hhh(i,k) * EgEsig(k,j)
344 enddo
345 enddo
346 enddo
347
348 Esiglam(1) = -1.d0 * (cc2*Esig(3) + cc1)
349 Esiglam(2) = -1.d0 * (cc2*Esig(2) + cc1)
350 Esiglam(3) = -1.d0 * (cc2*Esig(1) + cc1)
351
352 FEsig(1) = (dsqrt(3.d0/2.d0)*Norm(1)+alfa+beta*H) / (1.d0-alfa)
353 FEsig(2) = (dsqrt(3.d0/2.d0)*Norm(2)+alfa) / (1.d0-alfa)
354 FEsig(3) = (dsqrt(3.d0/2.d0)*Norm(3)+alfa) / (1.d0-alfa)
355
356 EftK = (bt * (at-2.d0*dsqrt(phit)+1.d0) + ct * dsqrt(phit))
357 EftK = EftK * (2.d0 + at)* ft0 / (2.d0 * bt * dsqrt(phit))
358 Eftk = EftK * (((at - dsqrt(phit) + 1.d0)/at)**(-1.d0 * ct/bt))
359 Efck = (bc * (ac-2.d0*dsqrt(phic)+1.d0) + cc * dsqrt(phic))
360 Efck = Efck * (2.d0 + ac)* fc0 / (2.d0 * bc * dsqrt(phic))
361 Efck = Efck * (((ac - dsqrt(phic) + 1.d0)/ac)**(-1.d0 * cc/bc))
362
363
364 FK(1) = (-1.d0 * cohk*EftK/(coht*coht))
365 FK(1) = FK(1) * ( dabs(EsigEff(1,1)) + EsigEff(1,1) ) / 2.d0
366 FK(2) = ( dabs(EsigEff(1,1)) + EsigEff(1,1) )/(coht*2.d0) - 1.d0
367 FK(2) = FK(2) * Efck
368
369 prmt = 0.d0
370 do i = 1,3
371   prmt = prmt + FEsig(i)*Esiglam(i)
372 enddo
373
374 lamk(1) = -1.d0 * FK(1) / prmt
375 lamk(2) = -1.d0 * FK(2) / prmt
376
377 QK = 0.d0
378 do i = 1,2
379 do j = 1,2
380 do k = 1,3
381   QK(i,j) = QK(i,j) + lam*HHK(i,j) - br(i,j)
382 &      + (lam*HHESig(i,k)*Esiglam(k) + HH(i)) * lamK(j)
383 enddo
384 enddo
385 enddo
386
387 QKinv(1,1) = QK(2,2)/(QK(1,1)*QK(2,2)-QK(1,2)*QK(2,1))
388 QKinv(1,2) = -1.d0*QK(1,2)/(QK(1,1)*QK(2,2)-QK(1,2)*QK(2,1))
389 QKinv(2,1) = -1.d0*QK(2,1)/(QK(1,1)*QK(2,2)-QK(1,2)*QK(2,1))
390 QKinv(2,2) = QK(1,1)/(QK(1,1)*QK(2,2)-QK(1,2)*QK(2,1))
391
392 QQ(1) = hn(7) - h1(7) + lam * HH(1)
393 QQ(2) = hn(8) - h1(8) + lam * HH(2)
394 res = dabs(QQ(1)) + dabs(QQ(2))
395

```

```

396     DK = 0.d0
397     do i = 1,2
398     do j = 1,2
399         DK(i) = DK(i) + QKinv(i,j) * QQ(j)
400     enddo
401     enddo
402
403
404 c... check the convergence
405 c     write(*,'(a10,e12.5,a10,i5,a10,e12.5)')
406 c     & "time=", ttim," iter=",nit1, " res=", res
407 c     if ((nit1.lt.100).and.(dabs(res).gt.tol)) then
408         h1(7) = h1(7) - DK(1)
409         h1(8) = h1(8) - DK(2)
410         go to 101
411     endif
412     if (nit1.eq.100) write(*,*) '>No Conver! |res|=', dabs(res)
413 c
414
415     Esig(1) = EsigEff(1,1)           ! rearrange the order
416     EsigEff(1,1) = EsigEff(3,3)     ! of eigenvalues
417     EsigEff(3,3) = Esig(1)         ! to right order
418
419     PT = TRANSPOSE( P )
420     sigEff = MATMUL(MATMUL(P,EsigEff), PT)
421
422     ddt = 1.d0 - (((1.d0+at-dsqrt(phit))/at)**(ct/bt))
423     ddc = 1.d0 - (((1.d0+ac-dsqrt(phic))/ac)**(cc/bc))
424     h1(9) = ddt
425     h1(10) = ddc
426     h1(11) = 1.d0 - (1.d0-ddc) * (1.d0 - (S0 + (1.d0 - S0)*RS) * ddt)
427
428
429     sig(1) = (1.d0 - h1(11)) * sigEFF(1,1)
430     sig(2) = (1.d0 - h1(11)) * sigEFF(2,2)
431     sig(3) = (1.d0 - h1(11)) * sigEFF(3,3)
432     sig(4) = (1.d0 - h1(11)) * sigEFF(1,2)
433     sig(5) = (1.d0 - h1(11)) * sigEFF(2,3)
434     sig(6) = (1.d0 - h1(11)) * sigEFF(1,3)
435
436     do i = 1,6
437         h1(i) = hn(i) + (lam / xnorm) * (str(i) + alfab*xi(i))
438     do j = 1,6
439         dd(i,j) = (1.d0 - h1(11)) * (K0*xi(i)*xi(j) + 2.d0*G0*xpp(i,j))
440     enddo
441     enddo
442
443     endif
444
445
446
447 c... store the plastic arc length as sig(3) for post-processing
448     if (isw.eq.8) then
449         sig(1) = h1(7)
450         sig(2) = h1(8)
451         sig(3) = h1(9)
452     !     sig(4) = h1(10)
453         sig(4) = h1(11)
454     endif
455     end
456
457
458     function xnorm_sg(ndms,a,b)
459     implicit none
460     integer ndms
461     double precision a(ndms),b(ndms),xnorm_sg
462

```

```

463 integer jj
464 double precision f(6)
465 data f/1.d0,1.d0,1.d0,2.d0,2.d0,2.d0/
466 c
467 xnorm_sg = 0.d0
468 do jj = 1,ndms
469 xnorm_sg = xnorm_sg + a(jj)*b(jj)*f(jj)
470 enddo
471 xnorm_sg = dsqrt(xnorm_sg)
472 return
473 end function xnorm_sg
474 c
475 c
476
477
478
479 subroutine jacobi_eigenvalue ( a, it_max, v, d, it_num, rot_num)
480 implicit none
481
482 integer,parameter:: n=3
483
484 double precision PPP(9), a(n,n), bw(n), c, d(n), g, gapq, h
485 integer i, it_max,it_num, j, k, l, m, p, q, rot_num
486 double precision s, t, tau, term, termq, theta
487 double precision thresh, v(n,n), w(n), zw(n),eige(12)
488
489
490 c ! it_max = 1000 let say
491 c ! n, the order of matrix
492 c ! a, nxn matrix
493 c ! v, eigenvector, nxn
494 c ! d, eigenvalue descending order, n
495 c !
496
497 cc JACOBI_EIGENVALUE carries out the Jacobi eigenvalue iteration.
498 c
499 c Discussion:
500 c
501 c This function computes the eigenvalues and eigenvectors of a
502 c real symmetric matrix, using Rutishauser's modifications of the classical
503 c Jacobi rotation method with threshold pivoting.
504 c
505 c Licensing:
506 c
507 c This code is distributed under the GNU LGPL license.
508 c
509 c Modified:
510 c
511 c 17 September 2013
512 c September 2023 by Alper Tunga BAYRAK
513 c
514 c Author:
515 c
516 c FORTRAN77 version by John Burkardt
517 c
518 c Parameters:
519 c
520 c Input, integer N, the order of the matrix.
521 c
522 c Input, double precision A(N,N), the matrix, which must be square, real,
523 c and symmetric.
524 c
525 c Input, integer IT_MAX, the maximum number of iterations.
526 c
527 c Output, double precision V(N,N), the matrix of eigenvectors.
528 c
529

```



```

530 c   Output, double precision D(N), the eigenvalues, in descending order.
531 c
532 c   Output, integer IT_NUM, the total number of iterations.
533 c
534 c   Output, integer ROT_NUM, the total number of rotations.
535 c
536
537
538     do j = 1, n
539         do i = 1, n
540             v(i,j) = 0.0D+00
541         end do
542         v(j,j) = 1.0D+00
543     end do
544
545     do i = 1, n
546         d(i) = a(i,i)
547     end do
548
549     do i = 1, n
550         bw(i) = d(i)
551         zw(i) = 0.0D+00
552     end do
553
554     it_num = 0
555     rot_num = 0
556
557 10  continue
558
559     if ( it_num .lt. it_max ) then
560
561         it_num = it_num + 1
562     !c
563     !c The convergence threshold is based on the size of the elements in
564     !c the strict upper triangle of the matrix.
565     !c
566         thresh = 0.0D+00
567         do j = 1, n
568             do i = 1, j - 1
569                 thresh = thresh + a(i,j) ** 2
570             end do
571         end do
572
573         thresh = sqrt ( thresh ) / dble ( 4 * n )
574
575         if ( thresh .eq. 0.0D+00 ) then
576             go to 20
577         end if
578
579         do p = 1, n
580             do q = p + 1, n
581
582                 gapq = 10.0D+00 * abs ( a(p,q) )
583                 termq = gapq + abs ( d(p) )
584                 termq = gapq + abs ( d(q) )
585             !c
586             !c Annihilate tiny offdiagonal elements.
587             !c
588             if (4.lt.it_num.and.termq.eq.abs(d(p)).and.termq.eq.abs(d(q)))then
589
590                 a(p,q) = 0.0D+00
591             !c
592             !c Otherwise, apply a rotation.
593             !c
594             else if ( thresh .le. abs ( a(p,q) ) ) then
595
596

```

```

597     h = d(q) - d(p)
598     term = abs ( h ) + gapq
599
600     if ( term .eq. abs ( h ) ) then
601         t = a(p,q) / h
602     else
603         theta = 0.5D+00 * h / a(p,q)
604         t = 1.0D+00 / ( abs ( theta ) + sqrt ( 1.0D+00 + theta * theta))
605         if ( theta .lt. 0.0D+00 ) then
606             t = - t
607         end if
608     end if
609
610         c = 1.0D+00 / sqrt ( 1.0D+00 + t * t )
611         s = t * c
612         tau = s / ( 1.0D+00 + c )
613         h = t * a(p,q)
614 !c
615 !c Accumulate corrections to diagonal elements.
616 !c
617         zw(p) = zw(p) - h
618         zw(q) = zw(q) + h
619         d(p) = d(p) - h
620         d(q) = d(q) + h
621
622         a(p,q) = 0.0D+00
623 !c
624 !c Rotate, using information from the upper triangle of A only.
625 !c
626         do j = 1, p - 1
627             g = a(j,p)
628             h = a(j,q)
629             a(j,p) = g - s * ( h + g * tau )
630             a(j,q) = h + s * ( g - h * tau )
631         end do
632
633         do j = p + 1, q - 1
634             g = a(p,j)
635             h = a(j,q)
636             a(p,j) = g - s * ( h + g * tau )
637             a(j,q) = h + s * ( g - h * tau )
638         end do
639
640         do j = q + 1, n
641             g = a(p,j)
642             h = a(q,j)
643             a(p,j) = g - s * ( h + g * tau )
644             a(q,j) = h + s * ( g - h * tau )
645         end do
646 !c
647 !c Accumulate information in the eigenvector matrix.
648 !c
649         do j = 1, n
650             g = v(j,p)
651             h = v(j,q)
652             v(j,p) = g - s * ( h + g * tau )
653             v(j,q) = h + s * ( g - h * tau )
654         end do
655
656         rot_num = rot_num + 1
657
658     end if
659
660 end do
661 end do
662
663 do i = 1, n

```

```

664         bw(i) = bw(i) + zw(i)
665         d(i) = bw(i)
666         zw(i) = 0.0D+00
667     end do
668
669     go to 10
670
671     end if
672
673 20    continue
674 !c
675 !c Restore upper triangle of input matrix.
676 !c
677     do j = 1, n
678         do i = 1, j - 1
679             a(i,j) = a(j,i)
680         end do
681     end do
682 !c
683 !c Ascending sort the eigenvalues and eigenvectors.
684 !c
685     do k = 1, n - 1
686
687         m = k
688
689         do l = k + 1, n
690             if ( d(l) .lt. d(m) ) then
691                 m = l
692             end if
693         end do
694
695         if ( m .ne. k ) then
696
697             t = d(m)
698             d(m) = d(k)
699             d(k) = t
700
701             do i = 1, n
702                 w(i) = v(i,m)
703                 v(i,m) = v(i,k)
704                 v(i,k) = w(i)
705             end do
706
707         end if
708
709     end do
710
711     return
712 end subroutine jacobi_eigenvalue
713

```